Universitat de Girona

CHARACTERIZATION OF THE TRANSLAMINAR COHESIVE LAW

Adrián Ortega Novillo

Per citar o enllaçar aquest document:
Para citar o enlazar este documento:
Use this url to cite or link to this publication:
http://hdl.handle.net/10803/406960

http://creativecommons.org/licenses/by-sa/4.0/deed.ca

Aquesta obra està subjecta a una llicència Creative Commons Reconeixement-CompartirIgual

Esta obra está bajo una licencia Creative Commons Reconocimiento-CompartirIgual

This work is licensed under a Creative Commons Attribution-ShareAlike licence

Universitat
de Girona

Doctoral Thesis

Characterization of the Translaminar Cohesive Law

Adrián Ortega Novillo

2017

Universitat
de Girona

Escola Politècnica Superior

Doctoral Thesis

Characterization of the Translaminar Cohesive Law

Adrián Ortega Novillo

2017

Doctoral Program in Technology

Advisors:

Dr. Pere Maimí Vert	Dr. Emilio V. González Juan
Universitat de Girona	Universitat de Girona

Thesis submitted to the University of Girona for the degree of Doctor of Philosophy

Adrián Ortega Novillo
Characterization of the Translaminar Cohesive Law
Doctoral Thesis, 2017
Doctoral Program in Technology
Advisors: Dr. Pere Maimí Vert and Dr. Emilio V. González Juan

Universitat de Girona
AMADE Research Group
Escola Politècnica Superior
Dept. d’Enginyeria Mecànica i de la Construcció Industrial
Carrer Universitat de Girona, 4
17003 Girona

Al meus pares,
Juan Luis i Librada

> *Notice that the stiffest tree is most easily cracked, while the bamboo or willow survives by bending with the wind.*
>
> — **Bruce Lee**

Acknowledgement

First, I would like to express my gratitude to my advisors, Pere Maimí and Emilio González, for their continuous support and for encouraging my research. Their guidance has helped me enormously in the development of this thesis.

Secondly, I would like to thank the research group AMADE, for bringing me the opportunity and support to accomplish this thesis during these four years.

I would also like to thank Professor M.R. Wisnom and Dr. X. Xu, from the University of Bristol, for their insightful discussions and for sharing with us their experimental findings.

També m'agradaria agrair a tots els amics i companys amb els quals he compartit molts bons moments durant aquest temps. En especial a en Gerard i l'Albert Carrillo, amb qui vaig començar el màster ara fa ja més de 4 anys. També agrair a moltíssims companys del grup de recerca, com ara en Pere Badalló, amb qui tants donettes i triangles de xocolata he compartit al bar; a la fila d'AMADE formada per la Magda, la Laura i en Jordi, que m'han aguantat durant totes les tardes d'avorriment, quan posava cançons i vídeos a la sala de doctorant mentres ells intentaven treballar; a en Yi i l'Aravind, que tantes paraules i frases útils en khmer i hindi m'han ensenyat. Tampoc em vull oblidar de la Irene, en Santi i l'Adrià Quintanes, i la resta de membres que formen i han passat per AMADE.

Per útim, vull agrair especialment a la meva família, pel seu suport incondicional durant tots aquests anys.

The work contained in this Ph. D thesis was concluded in the AMADE research group (Department of Mechanical Engineering and Industrial Construction, University of Girona, Spain). The thesis was carried out, in part, under the pre-doctorate grant with reference BR2013/35, and was partially funded by the Spanish Government through the *Ministerio de Economía y Competitividad*, under contracts MAT2013-46749-R and MAT2015-69491-C3-1-R.

List of Publications

The present Ph. D. thesis has been prepared as a compendium of peer-reviewed journal papers, according to the regulations of the Universitat de Girona. The thesis is comprised of the following papers:

- A. Ortega, P. Maimí, E. V. González, Ll. Ripoll. Compact tension specimen for orthotropic materials. *Composites Part A: Applied Science and Manufacturing* 2014; 63:85-93.
  doi:10.1016/j.compositesa.2014.04.012
  ISSN: 1359-835X, Impact Factor: 3.012, ranked 2/39 in the category of *Engineering, Manufacturing* and ranked 3/24 in the category of *Materials Science, Composites* (1^{st} quartile)[1].

- A. Ortega, P. Maimí, E. V. González, D. Trias. Characterization of the translaminar fracture cohesive law. *Composites Part A: Applied Science and Manufacturing* 2016; 91(2):501-509.
  doi:10.1016/j.compositesa.2016.01.019
  ISSN: 1359-835X, Impact Factor: 3.071, ranked 2/40 in the category of *Engineering, Manufacturing* and ranked 4/24 in the category of *Materials Science, Composites* (1^{st} quartile)[2].

---

[1] According to the 2013 Journal Citation Reports

[2] According to the 2014 Journal Citation Reports

- A. Ortega, P. Maimí, E. V. González, D. Trias. Specimen geometry and specimen size dependence of the $\mathcal{R}$-curve and the Size Effect Law from a Cohesive Model point of view. *Accepted in International Journal of Fracture* 2017.
  ISSN: 0376-9429, Impact Factor: 1.566, ranked 51/137 in the category of *Mechanics* (2nd quartile)[3].

- A. Ortega, P. Maimí, E. V. González, J. R. Sainz de Aja, F. M. de la Escalera, P. Cruz. Translaminar fracture toughness of interply hybrid laminates under tensile and compressive loads. *Submitted to Composites Science and Technology* 2016.
  ISSN: 0266-3538, Impact Factor: 3.897, ranked 1/24 in the category of *Materials Science, Composites* (1st quartile)[4].

Attended conferences

- A. Ortega, P. Maimí, E. V. González. Characterization of the intralaminar fracture cohesive law. 7th International Conference on Composites Testing and Model Identification (CompTest 2015). Madrid (Spain).
  International Conference. Oral presentation.

- A. Ortega, P. Maimí, E. V. González, J. R. Sainz de Aja, F. M de la Escalera. Effect of the ply stacking sequence on the translaminar fracture cohesive law. 17th European Conference on Composite Materials (ECCM17). Munich (Germany).
  International Conference. Oral presentation.

---

[3] According to the 2014 Journal Citation Reports

[4] According to the 2015 Journal Citation Reports

Universitat
de Girona

Dr. Pere Maimí Vert, Associate Professor at Universitat de Girona,

and

Dr. Emilio V. González Juan, Lecturer at Universitat de Girona,

hereby CERTIFY that

The work entitled *Characterization of the Translaminar Cohesive Law*, submitted for the doctoral degree by Adrián Ortega Novillo, has been conducted under their supervision and that it fulfills the requirements to aim for the *International Mention*.

Girona, February 2017.

Pere Maimí Vert	Emilio V. González Juan
Universitat de Girona	Universitat de Girona

List of Figures

1.1 Stress-strain diagrams for typical fibers used in composites (Vasiliev and Morozov, 2007). 2

2.1 Infinite plane subjected to a tensile stress with a central crack. 11
2.2 σ_{yy} stress profile for $\theta = 0$ near the crack tip 12
2.3 Irwin's plastic correction zone: (a) first order plastic correction, (b) second order plastic correction, (c) elasto-plastic stresses distribution near the crack tip. 15
2.4 Dugdale's (a) and Barenblatt's (b) cohesive zone models. 18
2.5 Concept of FPZ and tension-softening in concrete: (a) FPZ in front of an open crack and (b) tension-softening inside FPZ. 20
2.6 Typical load-deformation relation of a notched beam under bending and development of the FPZ in front of the notch. 21
2.7 Common Cohesive Law: (a) Constant, (b) linear and (c) exponential shapes. 22
2.8 Bilinear Cohesive Law shape, with G_1 as the fracture energy related to the initial slope H_1. 22
2.9 Integration path Γ and normal traction vector t for the J-integral. . . . 24
2.10 Size effect law for (a) notched and (b) unnotched structures. 25

3.1 Problems during the CL determination from a tensile test: (a) Multiple cracks in tensile specimens. (b) Rotation of crack faces in pre-cracked specimens. (c) Crack overlapping. 29

3.2 Bilinear Cohesive Law proposed for concrete, with the defining characteristics σ_u, G_c, G_1 and ω_G. 30
3.3 Uniaxial tensile test (left) and split-cylinder test (right) 31
3.4 Linear approximation of the initial part of the Cohesive Law. 34
3.5 FPZ translation along the symmetry plane, until the ligament is only held by the cohesive stresses defined by the last part of the Cohesive Law. 35
3.6 DCB specimen subjected to: (a) a bending moment M in pure mode I loading and (b) a pair of bending moments M_1 and M_2 in mixed mode I/II loading. 37
3.7 Optimization approach to measure the CL. 41
3.8 Rectangular plate with lateral crack subjected to a remotely applied stress σ and Cohesive stresses σ_c inside the FPZ. 42
3.9 Rectangular finite plate with a fracture process zone expressed as a lineal superposition problem. 43
3.10 Discretized traction nodes along the crack plane 45

4.1 Fracture mechanics specimens. 51
4.2 Compact Tension (CT) Specimen Geometry, subjected to a controlled displacement u and measured load P and with the principal directions represented by x_1 and x_2. 55

5.1 Representation of the Failure Process Zone. 60
5.2 (a) Tension-softening inside the Fracture Process Zone. (b) Typical Cohesive Law on the material. 61
5.3 Compact Tension (CT) specimen with a FPZ expressed as a superposition of linear problems. 63
5.4 (a) Finite Element model of a Compact Tension specimen, using cohesive elements to model the Fracture Process Zone. (b) Comparison of the displacement (u) and load (P) curves obtained with the author's methodology and using a Finite Element model. 64

5.5 Comparison of the normalized (a) cohesive crack openings and (b) cohesive stresses inside the FPZ obtained with the author's proposed methodology and with a Finite Element model, for a Compact Tension specimen with a normalized characteristic length of $\bar{\ell}_M = 1$. 65

5.6 Depiction of three states (1-3) during the FPZ growth: (a) the P-u position, (b) the FPZ stress and crack openings and (c) the dissipated energy inside the CL. The cracks openings ω_1, ω_2 and ω_3 are measured at the initial crack position a_0. 67

5.7 P-u curve for the two hybrid specimens and the corresponding smoothed average curve. (b) Three different CL obtained from three different sets of points. 69

5.8 (a) Three $\mathcal{R}$-$\Delta a_{eq}/\ell_M$ curves with a linear CL for $\bar{\ell}_M = 0.05$, 0.5 and 1. (b) Three $\mathcal{R}$-curves with a linear, constant and exponential CL and with $\bar{\ell}_M = 0.04$. 71

5.9 Propagation values of $\mathcal{R}$ for several values of $\bar{\ell}_M$. 72

6.1 Measured Cohesive Law and proposed simplified shape for the Laminate L04. 78

6.2 X-ray of the laminates L06 and L07 for the CT specimens. Several matrix cracks can be observed in the laminate L07. 79

7.1 Over-height Compact Tension (OCT) specimen geometry, with all dimensions defined with respect to the size W, where the dashed line represents the crack path. 82

7.2 Experimental (solid lines) and fitted (dashed lines) load displacement curves. The marks represent the points selected in order to fit the Cohesive Law for each specimen. 84

7.3 Measured Cohesive Law obtained from each OCT specimen, along the simplified trilinear Cohesive Law (solid line). 85

7.4 (a) Center Cracked Specimen (CCS) and (b) Open Hole specimen (OH) geometry, with all dimensions defined with respect to the half of the notch size R. 86

7.5 Predicted nominal strength σ_N of the Open Hole and Center Cracked specimens with respect to half of the notch length R, considering the CL of Fig. 7.3, along with some experimental results. 87

8.1 Comparison between FE and fitted (a) $\bar{C}$ and (b) $\bar{K}$ curves for three examples of orthotropic materials. 92
8.2 Comparison of the displacement (u) and load (P) curves obtained with the author's methodology and using a Finite Element model. 95
8.3 P-u curve for the two hybrid specimens and the corresponding smoothed average curve. (b) Three different CL obtained from three different sets of points. 96
8.4 Measured Cohesive Law obtained from each OCT specimen, along the simplified trilinear Cohesive Law (solid line). 97
8.5 Predicted nominal strength σ_N of the Open Hole and Center Cracked specimens with respect to half of the notch length R, considering the CL of Fig. 7.3, along with some experimental results. 98

List of Tables

4.1 Values of λ and ρ for seven different materials. 53

6.1 Ply properties of each composite material, where C is woven carbon fabric, G is woven glass fabric and UC is unidirectional carbon tape. . 76
6.2 Hybrid laminates stacking sequences, where C is woven carbon fabric, G is woven glass fabric and UC is unidirectional carbon tape. The 0^o direction is aligned with the loading direction. 77
6.3 Simplified Cohesive Law parameters for each laminate. 80

7.1 Laminate properties. 83

Contents

1 Introduction **1**

1.1 Background 1

1.1.1 Fibre-reinforced composite materials 1

1.1.2 Translaminar failure 3

1.2 Motivation 3

1.3 Objectives 4

1.4 Thesis structure 4

I Literature Review **7**

2 Introduction to the cohesive law. History and concepts **9**

2.1 Linear Elastic Fracture Mechanics 9

2.1.1 Griffith. Fracture mechanics based on energy balance 10

2.1.2 Stress field near the crack tip 11

2.1.3 Relation between G and K 13

2.1.4 Irwin's plastic correction 14

2.2 Crack-bridging models 17

2.2.1 Dugdale's and Barenblatt's cohesive zone models 17

2.2.2 Generalized cohesive model 19

2.2.3 Rice's J-integral 23

2.2.4 Size effect on structural strength according to the Crack-bridging models 24

3 Existing literature on determining the cohesive law 27
3.1 Experimental measure from a tensile test 27
3.2 Obtaining characteristic values of the Cohesive Law from experimental test 29
3.3 The J-integral method 35
3.4 Optimization techniques 39
3.4.1 Null crack tip intensity factor 41
3.4.2 Tractions at the failure plane 43
3.4.3 FE method 45

II Translaminar fracture toughness **47**

4 Linear Elastic Fracture Mechanics 49
4.1 Literature Review: specimens and standard procedures 49
4.2 Stress field of a planar orthotropic solid 52
4.3 The Compact Tension specimen for orthotropic materials 54
4.3.1 Specimen Compliance and Stress Intensity Factor 55
4.3.2 Undesired failure modes: back-end compression failure and excessive bearing at the holes 56

5 Non Linear Fracture Mechanics: Fracture Process Zone and Cohesive Law 59
5.1 Literature Review: Fracture Process Zone, $\mathcal{R}$-curve and the Cohesive Law 59
5.2 Direct method: Dugdale's condition 62
5.3 Inverse problem 66
5.4 Discussion 69

III The Cohesive Law as a material property **73**

6 Translaminar Cohesive Law of interply hybrid laminates 75

6.1 Materials and laminates 75
6.2 Results and discussion 76

7 Cohesive Law independence of the specimen size and geometry 81
7.1 How the specimen size influences the measured Cohesive Law . . . 81
7.2 Predicting the nominal strength of other geometries 85

IV Concluding remarks **89**

8 Results and discussion 91
8.1 Compact Tension specimen for orthotropic materials 91
8.2 Determination of the translaminar Cohesive Law 93
8.3 The translaminar Cohesive Law as a material property 95
8.4 Effects of the stacking sequence on the measured Cohesive Law . . 98

9 Conclusions 101

10 Perspective and future work 105
10.1 Extension of the Cohesive Zone Model for orthotropic laminates . . 105
10.2 Translaminar Cohesive Law and damage mechanisms relationship . 106
10.3 Study on the interlaminar Cohesive Law 107
10.4 Application to other materials 107

V Bibliography **109**

Bibliography 111

VI Appendices **123**

A Appendix A: Polynomial fitting functions 125

VII Generated papers **127**

Abstract

The outstanding stiffness and strength properties, with respect to their weight, of fibre-reinforced polymers have led to an increase of their usage in structures that needed a weight reduction. This has been specially the case of the aerospace industry, where the use of light materials has a significant effect on the fuel consumption of aircraft structures, resulting in two direct benefits: first reducing the economic costs of flights, and second, reducing the gas emission that causes the greenhouse effect.

When a fibre-reinforced composite laminate is subjected to traction or compression, it develops a relatively large Fracture Process Zone where material toughening mechanisms such as matrix cracking, fibre-bridging and fibre pull-outs take place. The damage onset and damage propagation are well defined from a cohesive model point of view, although no standard procedure has been yet developed to characterize the translaminar Cohesive Law. The present Ph.D. thesis proposes an objective inverse method for obtaining the Cohesive Law from a single Compact Tension test.

First, the usage of the Compact Tension specimen for determining the fracture properties of orthotropic laminates has been studied. As a result, a Stress Intensity Factor function has been developed, for the mentioned geometry, applicable to a wide range of materials orthotropies. Additionally, some test recommendations are given taking into account the material properties.

Second, a semi-analytic model has been developed for a Compact Tension specimen subjected to a controlled displacement and corresponding load within a cohesive model framework. The model is able to capture the material response while the Fracture Process Zone is being developed, obtaining the evolution of multiple variables such as the crack opening and the cohesive stresses, for any given arbitrary Cohesive Law shape.

Third, with the aid of the aforementioned model, an algorithm has been developed capable of obtaining the translaminar Cohesive Law from a single Compact Tension test. The methodology to solve the inverse problem consists on defining a piecewise unknown Cohesive Law. The segments widths and slopes are found in order to best fit the experimental curve.

Last, the proposed inverse method has been used to perform an in-depth discussion of the Cohesive model. First, the Cohesive Law has been measured for several interply hybrid laminates, in order to study the influence of the stacking sequence on the resulting curve. Secondly, the method has been applied to show the invariability of the obtained Cohesive Law for different geometries and specimen sizes.

Resum

L’excel·lent rigidesa i resistència, respecte al seu pes, dels polímers reforçats amb fibres han portat a un augment del seu ús en estructures que necessiten una reducció de pes. Aquest ha estat especialment el cas de la indústria aeroespacial, on l’ús de materials lleugers afecta significativament el consum de combustible dels avions, resultant en dos avantatges directes: primer la reducció dels costos económics dels vols, i segon, la reducció de l’emissió dels gasos causants de l’efecte hivernacle.

Quan un laminat compost de polímer reforçat amb fibres és sotmès a tracció o compressió, aquest desenvolupa una Zona de Procés de Fractura relativament gran, on mecanismes d’enduriment com ara l’esquerdament de la matriu, bridging i pull-out de fibres tenen lloc. La iniciació i propagació del dany estan ben definits des del punt de vista del model cohesiu, tot i que actualment encara no hi ha cap procediment estàndard per caracteritzar la Llei Cohesiva translaminar. La present tesi doctoral proposa un mètode invers per a l’obtenció de la Llei Cohesiva utilitzant unicament un assaig de la proveta Compact Tension.

En primer lloc, s’ha estudiat l’ús de la proveta Compact Tension per determinar les propietats de fractura de laminats ortotrópics. D’aquest estudia ha sorgit una funció del Factor d’Intensitat de Tensions, aplicable a una àmplia gamma de materials ortotrópics. A més, s’han donat algunes recomanacions per a la correcta realització de l’assaig, tenint en compte les propietats del material.

En segon lloc s’ha desenvolupat un model semi-analític capaç de reproduir el comportament d’una proveta Compact Tension sotmesa a un desplaçament controlat i a una càrrega corresponent, dins el marc del model cohesiu. El model és capaç de capturar el comportament del material mentre es desenvolupa la Zona de Procés de Fractura, així com obtenir l’evolució de múltiples variables com ara l’obertura d’esquerda i les tensions cohesives, per a qualsevol forma de la Llei cohesiva donada.

En tercer lloc, amb l'ajuda del model anteriorment esmentat, s'ha desenvolupat un algoritme capaç d'obtenir la Llei cohesiva d'un laminat, a partir d'un únic assaig de la proveta Compact Tension. La metodologia per resoldre el problema invers consisteix a definir la Llei cohesiva a mesurar com una funció definida a trossos, composta per trams lineals. L'ample i el pendent de cada tram es varia fins que la corba força-desplaçament s'ajusta millor a la mesurada en l'assaig.

Finalment, el mètode proposat del problema invers s'ha utilitzat per dur a terme una discussió del model cohesiu. En primer lloc, la Llei Cohesiva de diferents laminats híbrids ha estat mesurada, per tal d'estudiar la influència de la seqüència d'apilament en la forma de la Llei Cohesiva obtinguda. En segon lloc, el mètode ha estat aplicat per mostrar la invariabilitat de la Llei cohesiva obtinguda de diferents geometries i mides de provetes.

Resumen

La excelente rigidez y resistencia, con respecto a su peso, de los polímeros reforzados con fibras han llevado a un aumento de su uso en estructuras que necesitan una reducción de peso. Esto ha sido especialmente el caso de la industria aeroespacial, donde el uso de materiales ligeros afecta significativamente el consumo de combustible de los aviones, lo que resulta en dos ventajas directas: primero reducir los costes económicos de los vuelos, y segundo, la reducción de la emisión de gases causantes del efecto invernadero.

Cuando un laminado compuesto de polímero reforzado con fibras es sometido a tracción o compresión, éste desarrolla una Zona de Proceso de Fractura relativamente grande, donde mecanismos de endurecimiento tales como agrietamiento de la matriz, fibre-bridging y fibre pull-out tienen lugar. La iniciación y propagación del daño están bien definidos desde el punto de vista del modelo de cohesivo, aunque en la actualidad todavía no existe ningún procedimiento estándar para caracterizar la Ley Cohesiva translaminar. La presente tesis doctoral propone un método inverso para la obtención de la Ley Cohesiva utilizando únicamente un ensayo de la probeta Compact Tension.

En primer lugar, se ha estudiado el uso de la probeta Compact Tension para determinar las propiedades de fractura de laminados ortotrópicos. Como resultado, se ha desarrollado una función del Factor de Intensidad de Tensiones, aplicable a una amplia gama de materiales ortotrópicos. Además, se han dado algunas recomendaciones para la correcta realización del ensayo, teniendo en cuenta las propiedades del material.

En segundo lugar, se ha desarrollado un modelo semi-analítico capaz de reproducir el comportamiento de una probeta Compact Tension sometida a un desplazamiento controlado y a su carga correspondiente dentro del marco del modelo cohesivo. El modelo es capaz de capturar el comportamiento del material mientras se desarrolla la Zona de Proceso de Fractura, así como la evolución de múltiples variables tales

como la apertura de grieta y tensiones cohesivas, para cualquier forma de la Ley Cohesiva.

En tercer lugar, con la ayuda del modelo anteriormente mencionado, se ha desarrollado un algoritmo capaz de obtener la Ley Cohesiva de un laminado, a partir de un único ensayo de la probeta Compact Tension. La metodología para resolver el problema inverso consiste en definir la Ley Cohesiva a medir como una función definida a trozos, compuesta por tramos lineales. El ancho y la pendiente de cada tramo se modifica hasta que la curva fuerza-desplazamiento se ajusta mejor a la medida en el ensayo.

Por último, el método propuesto para el problema inverso se ha utilizado para llevar a cabo una discusión del modelo cohesivo. En primer lugar, la Ley Cohesiva de distintos laminados híbridos se ha medido, con el fin de estudiar la influencia de la secuencia de apilamiento en la forma de la Ley Cohesiva obtenida. En segundo lugar, el método ha sido aplicado para mostrar la invariabilidad de la Ley Cohesiva obtenida de diferentes geometrías y tamaños de probetas.

Introduction

1

1.1 Background

The outstanding stiffness and strength properties, with respect to their weight, of fibre-reinforced polymers have led to an increase of their usage in structures that needed a weight reduction. This has been specially the case of the aerospace industry, where the use of light materials has a significant effect on the fuel consumption of aircraft structures, resulting in two direct benefits: first reducing the economic costs of flights, and second, reducing the gas emissions that cause the greenhouse effect.

The effort lead by researchers, development and design communities over the last four decades has led to a better understanding of the failure mechanisms of fibre-reinforced composite materials and how these mechanisms can impact the performance of structural components. Although this has carried more efficient structural designs, there is still room to push the boundaries of damage tolerant components. In order to achieve this, methods for predicting the onset and subsequent propagation of damage in composite components are, therefore, highly desirable.

1.1.1 Fibre-reinforced composite materials

A composite material is any material that consists of two or more components with different properties and distinct boundaries between them. Concretely, Fibre-Reincorced polymers (FRP) refer to the family of composite materials made of a polymer matrix reinforced with fibres. The fibers are usually made of glass or carbon, and are the basic components of these composite materials, as they provide the high strength and stiffness required in structural applications. The volume fraction of the polymer matrix is usually lower than 50$\%$.

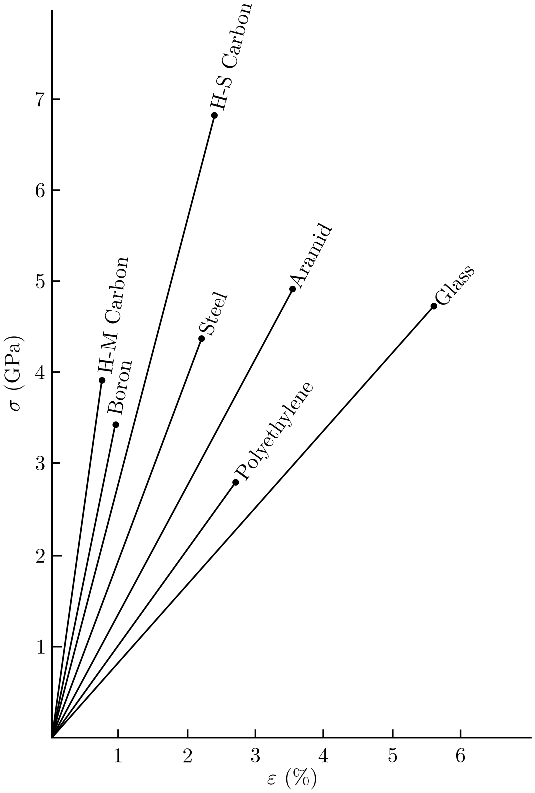

Fig. 1.1.: Stress-strain diagrams for typical fibers used in composites (Vasiliev and Morozov, 2007).

Glass fibers are characterized by having a high strength and relatively low stiffness, high chemical and biological resistance, and low cost. On the other hand, carbon fibres are much stiffer than the glass fibres, with modern carbon fibres capable of reaching elastic modulus of about four times the modulus of steel. Fig. 1.1 shows typical stress-strain diagrams for high-modulus (H-M) and high-strength (H-S) carbon fibres. Carbon fibers are also characterized by providing high chemical and biological resistance, electric conductivity and very low coefficient of thermal expansion.

In order to create a monolithic composite material capable of withstanding the required strength and stiffness, the fibres are bounded in a matrix material. These provide the final shape of the composite structure and govern the parameters of the manufacturing process. The resulting combination is a ply or lamina of FRP composite, with high structural properties in one direction (along the fibre direction), but of poor quality on the other directions. By joining several of these plies, oriented in different directions, it is possible to create a laminate, in order to provide the required engineering properties, such as the in-plane stiffness, bending stiffness and strength.

1.1.2 Translaminar failure

Most structural components are subjected to several combinations of tensile, compressive and bending loads that may cause the failure of a FRP laminate in different manners: matrix cracking induced delamination, tensile failure of a ply, free-edge delaminations, translaminar crack, etc.

The present thesis focuses on translaminar failure. This phenomenon is described when a crack appears across the whole thickness of the laminate, breaking all the plies. It is a very catastrophic failure mode, as it requires a relatively high amount of energy to start propagating, that is suddenly released upon reaching a critical load. This type of failure can appear in structural elements with stress concentrations at discontinuities such as holes and pins.

1.2 Motivation

Multiple theories exist in the literature to model a translaminar crack of a FRP composite, ranging from Linear Elastic Fracture Mechanics (LEFM), through more complex models such as the Critical Distances Theory and the Cohesive Zone model. Although some simple theories reproduce effectively these kind of crack for a very limited range of geometries (LEFM needs the presence of a crack to be applied), they fail when trying to extrapolate the laboratory results to larger structures.

The Cohesive Zone model is capable of reproducing this kind of fracture for a wide range of specimen sizes and geometries, even for unnotched structures. The key ingredient of this approach is the Cohesive Law of the material, which is assumed to be a property for a given laminate. The main disadvantage of the Cohesive Zone model is the lack of robust and objective tools, and procedures to meaure the Cohesive Law.

1.3 Objectives

The present thesis aims to deepen into the analysis of the translaminar crack formation and growth of fibre-reinforced composite materials, from a Cohesive Model point of view, particularly on developing a robust tool to measure the translaminar Cohesive Law. In order to achieve this main goal, several specific objectives are proposed, such as developing an analytical solution to the Cohesive Zone, an proposing and algorithm that measures the translaminar Cohesive Law.

1.4 Thesis structure

The present thesis has been developed as a compendium of publications, with a reproduction of the generated manuscripts at the end of this document. Instead of copying the whole text of each publication within the body of the thesis, we have decided to write the document as a whole, including some parts of the publications when necessary, while adding information and results not published elsewhere. This decision gives the opportunity to the reader to completely follow the conducted research during the writing of this thesis, but at the same time, when interested, to consult the details available in the full-text versions of the published manuscripts.

With this in mind, the document has been divided in three blocks. The first part consists of a wide literature review, composed of Chapters 2 and 3. The former is focused on a brief introduction and basis of fracture mechanics, from the very fundamental concepts of Linear Fracture Mechanics to the introduction of the more complex Cohesive Zone model. On the other hand, the latter is an in-depth literature review of the current available methods to measure the Cohesive Law.

The second block is focused on the analysis of the fracture toughness of a fibre-reinforced composite laminate, composed of Chapters 4 and 5. In Chapter 4 the Compact Tension specimen is studied and some LEFM tools have been introduced to use this specimen for any laminate orthotropy, as well as giving some design recommendations. The results of this research have generated the PAPER A. Chapter 5 studies the translaminar fracture from the Cohesive Model point of view, introducing a methodology to measure the laminate Cohesive Law. The results of this research have generated the documents PAPER B and PAPER C.

The third block consists of Chapters 6 and 7, and is focused on the applicability of the developed methodology. Chapter 6 attempts to relate how the used ply stacking sequence affects the resulting Cohesive Law, generating the document PAPER D. Chapter 7 discusses the fundamental hypothesis of the Cohesive Zone model: is the translaminar Cohesive Law a material property?

The concluding remarks are found in the fourth block, with Chapter 8 based on the general results and discussion of the thesis, Chapter 9 consists of the general conclusions, and finally, Chapter 10 introduces some lines of future research.

Part I

Literature Review

2

Introduction to the cohesive law. History and concepts

Traditionally, structural designs were based on the limits imposed by the material's ultimate tensile and compressive strengths. By using these design criteria, the structures would never suffer from loads that would cause the collapse throughout their life. However, many structures failed even though they never exceeded the calculated critical loads: these collapses were produced by the inherent defects of the material present in the structure, or because of the growth of the defects up to a critical dimension.

This chapter aims to summarize the different theories that helped to develop the concept of the cohesive Fracture Process Zone (FPZ) and the Cohesive Law (CL), from the appearance of the fracture mechanics proposed by Griffith to the emergence of the general cohesive model proposed by Hillerborg.

2.1 Linear Elastic Fracture Mechanics

Firstly introduced by Griffith, the principles of fracture mechanics were based on an energy balance. Subsequently several authors delved into the stress state near the crack tip. This section contains the main concepts of Linear Elastic Fracture Mechanics (LEFM) that may be found in many fracture mechanics books (Bažant and Planas, 1998; Sharpe and William N., 2008; Zihai Shi, 2009).

2.1.1 Griffith. Fracture mechanics based on energy balance

Griffith (Griffith, 1921; Griffith, 1924) theorized that the maximum load that a structure can withstand depends not only on the strength of the material, but also on the size of the defects that may exist in the structural element. Given a linear elastic material and of unitary thickness, that contains a crack of length a, the total energy E of the system can be divided into two components: the potential energy Π stored in the system and the energy associated with crack surface U_s:

$$E = \Pi + U_s \tag{2.1}$$

The potential energy Π is the summation of the work done by the external forces applied to the sample, stored in the form of elastic energy. Assuming the material has a unitary thickness, all the acting forces can be considered to be applied per unit thickness too. The energy associated with crack surface, U_s, can be understood as the free surface energy plus the plastic energy dissipated while creating new crack surface, again per unit crack area. If the problem is considered to be almost static (otherwise the inertial forces should be taken into account), the energy of the system is in equilibrium when is minimal. Therefore the equilibrium condition $\mathrm{d}E/\mathrm{d}A = 0$ is applied, where A represents the crack surface, which per unit thickness is equal to the crack length a. G is defined as the potential energy release rate (ERR) per unit crack surface area, and G_c is defined as the fracture resistance per unit surface area as:

$$G(a) \equiv -\frac{\mathrm{d}\Pi}{\mathrm{d}a} \quad ; \quad G_c \equiv \frac{\mathrm{d}U_s}{\mathrm{d}a} \tag{2.2}$$

In this manner, if the available potential energy is lower than the fracture resistance, the the crack will not grow. Otherwise, the crack growth condition is verified:

$$G\left(a\right) = G_c \tag{2.3}$$

The fracture resistance G_c is considered to be a material property that must be obtained experimentally and Griffith defined it as constant value. This is generally true for brittle materials, although in practice most materials show a dependence

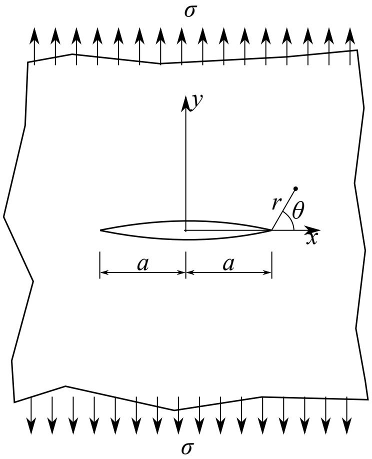

Fig. 2.1.: Infinite plane subjected to a tensile stress with a central crack.

of G_c as the crack grows. The function $G\left(a\right)$ can be obtained either analytically or numerically.

2.1.2 Stress field near the crack tip

The study of the stress field around the crack tip was formulated in parallel with the developments of Griffith, by Inglis (Inglis, 1913), Irwin (Irwin, 1957) and other authors (Muskhelishvili, 1954; Williams, 1957). Consider a sheet made of an isotropic linear elastic material of infinite extent with a central crack of length $2a$ subjected to tension σ perpendicular to the crack direction, defined in Fig. 2.1. Given the polar coordinates r and θ centred at the crack tip, the stress field is defined:

$$\sigma_{ij} = \frac{K}{\sqrt{2\pi r}} f_{ij}\left(r,\theta\right) \tag{2.4}$$

where σ_{ij} is the stress defined in the coordinates x and y shown in Fig. 2.1, and $f_{ij}\left(r,\theta\right)$ is a non-dimensional function. Observing the stress field defined in Eq. 2.4, two characteristics stand out. First, the stress suffered by the material increases infinitely as the point being considered is closer to the crack tip, independently of

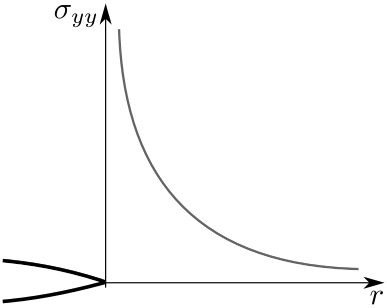

Fig. 2.2.: σ_{yy} stress profile for $\theta = 0$ near the crack tip

the remote stress σ applied, as long as it is not null. This phenomenon is known as a singularity of stresses at the crack tip, represented in Fig. 2.2.

$$\lim_{r \to 0} \sigma_{ij} \to \infty \tag{2.5}$$

Second, for a given configuration, the whole stress field is completely defined by a single scalar K, known as the Stress Intensity Factor (SIF). Although being a scalar, the K value varies in function of the applied load, the geometry of the structure and the crack length as:

$$K = \sigma \sqrt{\pi a} \cdot g \tag{2.6}$$

where g is a non-dimensional geometric function. For the illustrated case of a plate of infinite extension (Fig. 2.1), the value of g is equal to 1. The function g has been tabulated for multiple geometries and loading configurations and can be found in numerous Handbooks (Tada et al., 2000). Observing Eq. 2.6, K is directly proportional to the applied remote stress σ and proportional to the square root of the crack length a.

Likewise the crack growth condition defined by Eq. 2.3, it is possible to define a crack growth condition from the stress field around the crack tip as:

$$K\left(a\right) = K_c \tag{2.7}$$

where K_c is the material fracture toughness, a material property that must be determined experimentally.

2.1.3 Relation between G and K

So far two parameters related to fracture have been introduced: the Stress Intensity Factor K and the rate of energy release G. As already mentioned, the first parameter defines the stress and displacement around the crack while the second accounts for the released elastic energy as the crack grows. Irwin (Irwin, 1957) deduced the relationship between these two parameters.

Suppose the same sheet of material defined in Fig. 2.1. Because the load is applied in mode I loading configuration, the SIF and the fracture energy are denoted as K_I and G_I, respectively. Within the LEFM framework and assuming that the work necessary to close the crack at the tip is equal to zero, the energy release rate can be calculated as the work required to close the crack an infinitesimal length δa. The vertical displacement u_y is computed as:

$$u_y = \frac{2\sigma}{E}\sqrt{a^2 - x^2} = \frac{2K_I}{E}\sqrt{\frac{a^2 - x^2}{\pi a}} \tag{2.8}$$

where x and r are defined in Fig. 2.1. The crack closing stress is defined in Eq. 2.4, that for $\theta = 0$ and $f = 1$ (infinite extension sheet) becomes:

$$\sigma_{yy} = \frac{K_I}{\sqrt{2\pi r}} \tag{2.9}$$

Once the crack surface displacement and the stress profile have been defined, computing the work to close the crack an infinitesimal crack extension δa leads to the expression

$$G_I = \frac{K_I^2}{E'} \tag{2.10}$$

where E' is the effective elastic modulus (E for plane stress and $E/\left(1-\nu^2\right)$ for plane strain). It can be demonstrated that for mode II and III, the relationships between G and K are:

$$G_{II} = \frac{K_{II}^2}{E'} \tag{2.11}$$

$$G_{III} = \frac{1}{1-\nu}\frac{K_{III}^2}{E'} \tag{2.12}$$

Eqs. 2.10-2.12 define the relationship between G and K for an isotropic material given the crack grows in the x direction defined in Fig. 2.1. For an an orthotropic material, the relationship is extended:

$$G_I = \frac{K_I^2}{E'}\left(\frac{2\lambda^{3/2}}{1+\rho}\right)^{-1/2} \tag{2.13}$$

where λ and ρ are two non-dimensional scalars that define the orthotropy of the material:

$$\lambda = \frac{E_{yy}}{E_{xx}} \quad , \quad \rho = \frac{\sqrt{\lambda}}{2G_{xy}}\left(E_{xx} - 2\nu_{xy}G_{xy}\right) \tag{2.14}$$

where E_{xx} and E_{yy} are the elastic moduli, G_{xy} is the shear modulus and ν_{xy} is the Poisson's ratio, defined by the material principal axes. In the plane strain case, λ and ρ are obtained by replacing E_{xy}, E_{xy} and ν_{xy} in Eq. 2.14:

$$E'_{xx} = \frac{E_{xx}}{1-\nu_{xz}\nu_{zx}}, \quad E'_{yy} = \frac{E_{yy}}{1-\nu_{yz}\nu_{zy}}, \quad \nu'_{xy} = \frac{\nu_{xy}+\nu_{xz}\nu_{zy}}{1-\nu_{xz}\nu_{zx}} \tag{2.15}$$

The relationship between the fracture toughness and the fracture energy is likewise defined:

$$G_c = \frac{K_c^2}{E'}\left(\frac{2\lambda^{3/2}}{1+\rho}\right)^{-1/2} \tag{2.16}$$

2.1.4 Irwin's plastic correction

Although LEFM is suitable for predicting the crack growth and the stress distribution around the crack tip in a simple manner (Section 2.1.2), it also introduces an

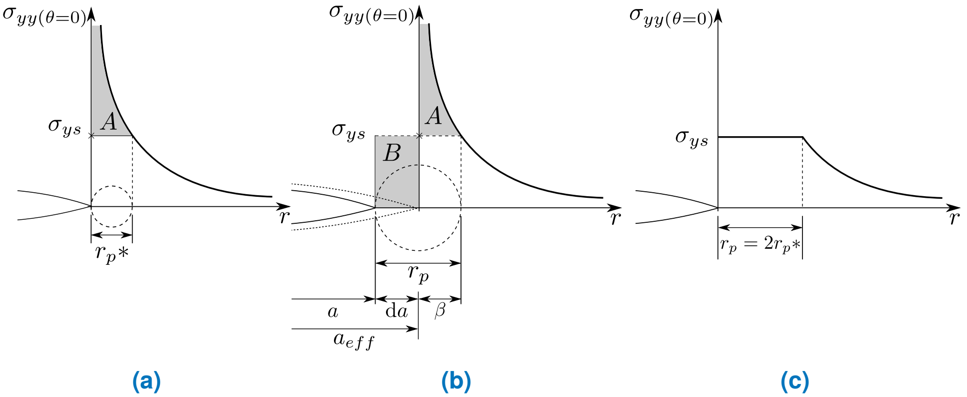

Fig. 2.3.: Irwin's plastic correction zone: (a) first order plastic correction, (b) second order plastic correction, (c) elasto-plastic stresses distribution near the crack tip.

inaccuracy for any material: the presence of a stress singularity at the crack tip. Because no material is capable of withstanding an infinite stress, it is necessary to consider that it contains a non-linear region. Metals develop a plastic region where the stress exceeds their yield strength and quasi-brittle materials form a Fracture Process Zone (FPZ). The extension of this region was first estimated by Irwin (Irwin, 1957; Irwin, 1961), known as Irwin's plastic correction.

The first order plastic correction length r_p^* is found as the zone where the material exceeds its yield strength σ_{ys} (metals) or its tensile strength σ_u (quasi-brittle). Fig. 2.3(a) shows the stress distribution near the crack tip $\sigma_{yy}(r, \theta = 0)$ as $\sigma_{yy}(r) = K_I/\sqrt{2\pi r}$. For perfect plastic materials, the first order plastic correction length can be simply obtained by imposing that the stress $\sigma_{yy}(r)$ in this region is equal to the material yield stress σ_{ys}. Imposing this condition, the length in terms of the applied remote stress σ is obtained:

$$r_p^* = \frac{K_I^2}{2\pi\sigma_{ys}^2} = \frac{\sigma^2 a}{2\sigma_{ys}^2} \tag{2.17}$$

The new distribution of stresses neglects the tensions greater than σ_{ys}, denoted with an A in Fig. 2.3(a). Because of that, the force balance is not satisfied with the first order correction defined in Eq. 2.17. Irwin (Irwin, 1957; Irwin, 1961) suggested a methodology to estimate a new plastic correction zone r_p by introducing an equivalent crack length a_{eff}. The increase in crack length is defined as $\mathrm{d}a$ and the new inelastic zone length is $r_p = \mathrm{d}a + \beta$. In this manner, the inelastic region is increased, redistributing the stresses as shown in Fig. 2.3(b). The fictitious increase of crack length is then obtained by imposing $A = B$:

$$\mathrm{d}a = r_p^* \quad \text{or} \quad r_p = \mathrm{d}a + \beta = 2r_p^* = \frac{K_I^2}{\pi\sigma_{ys}^2} \tag{2.18}$$

Resulting in a second order correction length r_p twice as the length r_p^*. For a perfectly plastic material the resulting stress distribution is shown in Fig. 2.3c. The effective SIF is obtained:

$$K_{I,eff} = \sigma\sqrt{\pi a_{eff}} = \sigma\sqrt{\pi(a + r_p)} = \sigma\sqrt{\pi a\left(1 + \frac{\sigma^2}{2\sigma_{ys}^2}\right)} \tag{2.19}$$

Under plane strain, the plastic region is formed under a triaxial stress state, and the Irwin's plastic correction then becomes:

$$r_p^* = \frac{K_I^2}{6\pi\sigma_{ys}^2} \tag{2.20}$$

which is lower than the plane stress state first order correction by a factor of 3.

The plastic zone development causes the fracture energy G_c or the fracture toughness K_c to be a function of the crack growth. Therefore, Eq. 2.3 and Eq. 2.7 can be rewritten:

$$G\left(a_{eff}\right) = \mathcal{R}\left(\Delta a\right), \quad K\left(a_{eff}\right) = K_{\mathcal{R}}\left(\Delta a\right) \tag{2.21}$$

where $\mathcal{R}\left(\Delta a\right) = K_{\mathcal{R}}^2\left(\Delta a\right)/E'$ is the resistance curve of the material. It is defined as a function that grows as the plastic zone is being developed, achieving a plateau value equal to G_c as soon as the crack growth becomes self-similar.

2.2 Crack-bridging models

Linear Elastic Fracture Mechanics are suitable when the material non-linearities are confined to a very small region at the crack tip, compared to other problem dimensions. When a large Fracture Process Zone is present, more elaborated fracture models are needed in order to capture properly the energy dissipation mechanisms.

2.2.1 Dugdale's and Barenblatt's cohesive zone models

Dugdale (Dugdale, 1960) and Barenblatt (Barenblatt, 1959; Barenblatt, 1962), proposed, independently, a cohesive zone model where closure stresses are present at the crack tip, in order to capture the non-linear behaviour of the material in the formation of new crack surface. Likewise Irwin, Dugdale's and Barenblatt's models also introduced the concept of the effective crack, with a length of $2a + 2\ell_{\mathrm{Dug}}$, as shown in Fig. 2.4. The cohesive or closure forces acting in the non-linear zone represent the material resistance to fracture when it is subjected to external forces, and therefore eliminating the stress singularity at the crack tip.

These models take into account the non-linear behaviour at the crack tip by introducing cohesive forces at the surface of the crack. The main difference between the two is that in the case of Dugdale's model, the closure stresses of the material are constant and equal to the yield strength of the material σ_{ys}. On the other hand, Barenblatt's model stresses represent the forces of molecular cohesion of the material, and these vary throughout the plastic zone defined by a function $q\left(x\right)$.

In order to determine the length of the non-linear zone, Dugdale's condition may be applied: the stress singularity at the crack tip must disappear under the combined action of the remote stress σ and the cohesive forces at the crack tip. Based on

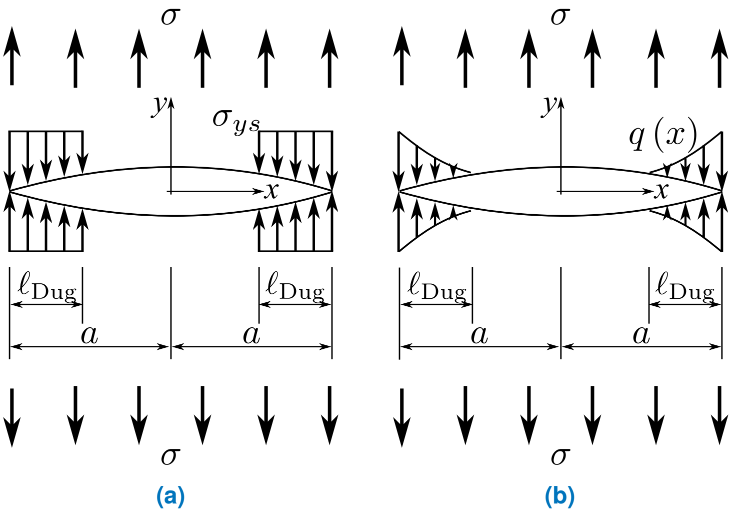

Fig. 2.4.: Dugdale's (a) and Barenblatt's (b) cohesive zone models.

the superposition principle, the global SIF must be null, obtained by adding the K caused by each acting load:

$$K_I = K_I^{\text{remote}} + K_I^{\text{cohes}} = 0 \tag{2.22}$$

where K_I^{remote} is the SIF caused by the remote stress σ for an infinite sheet of material of crack length $a + \ell_{\text{Dug}}$, and K_I^{cohes} is the SIF caused by the closure stress applied over a length ℓ_{Dug}. Assuming a constant closure distribution equal to σ_{ys} (Dugdale's cohesive zone model), the plastic zone length is found by solving Eq. 2.22:

$$\ell_{\text{Dug}} = \frac{\pi^2 \sigma^2 a}{8\sigma_{ys}^2} = \frac{\pi K_I^2}{8\sigma_{ys}^2} \tag{2.23}$$

Barenblatt's cohesive zone model can be solved analogously, but replacing the SIF K_I^{cohes} by the one caused by the stress distribution $q\,(x)$. Comparing Dugdale's plastic zone length with Irwin's one:

$$\frac{r_p}{\ell_{\text{Dug}}} = \frac{8}{\pi^2} = 0,81 \tag{2.24}$$

As it can be seen, the relative difference between both solutions differs less than 20%.

Although the cohesive zone models introduced by Dugdale and Barenblatt have been able to eliminate the stress singularity at the crack tip and have provided a way to estimate the length of the material non-linear region, they have also caused the failure criterion based on the K_{Ic} to be no longer applicable.

2.2.2 Generalized cohesive model

Heterogeneous materials such as concrete or composite materials fracture under complicated mechanisms due the fact that they are composed of various components bonded together (cement and aggregates in the case of concrete, and reinforcement and matrix in the case of composite materials). Under these circumstances, when such materials are subjected to tension, a Fracture Process Zone forms near the crack tip, where inelastic fracture mechanisms take place, such as micro-cracking and bridging (Mai, 2006), as seen in Fig. 2.5(a).

A generalized cohesive zone model for non-linear fracture problems was introduced by Hillerborg (Hillerborg et al., 1976), which is an extension of the model of Dugdale and Barenblatt. Similar to other cohesive models, he introduced the concept of a fictitious crack that takes place inside the FPZ, capable of transferring closure tension between its surfaces. The relationship between the cohesive stress profile as the Crack Opening Displacement (COD) opens is governed by the Cohesive Law (CL) or tension-softening law of the material. It describes a tension-softening phenomenon, illustrated in Fig. 2.5(b). It is generally considered to be a material property (Elices et al., 2002).

Fig. 2.6 shows a three-point bending notched beam subjected to a controlled displacement (u) and corresponding load (P), while reproducing the FPZ formation and growth based on the generalized cohesive zone model. In order to capture a stable crack formation the load is applied under controlled displacement until the specimen splits completely. The initial slope of the load-displacement curve

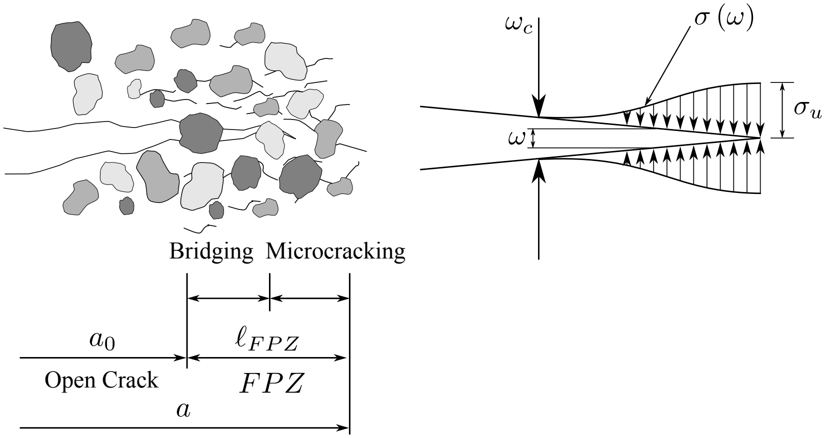

(a) **(b)**

Fig. 2.5.: Concept of FPZ and tension-softening in concrete: (a) FPZ in front of an open crack and (b) tension-softening inside FPZ.

is defined by the elastic compliance of the specimen for the given geometry and initial notch. The Fracture Process Zone is initialized as soon as the stress at the crack tip reaches the material tensile strength σ_u, represented as the point A in Fig. 2.6. This usually occurs for low values of P, because of the presence of the stress singularity at the notch. The FPZ initializes its development with a null length and a cohesive crack opening equal to zero. As the displacement is increased, the FPZ grows as well as the cohesive crack, with the stresses being defined by the CL. The maximum load the structure can withstand is reached at point B, while the FPZ is still being developed. At point C the FPZ has been fully developed, and the COD at the initial crack position has reached the critical opening ω_c. From this moment the FPZ starts to translate along the crack plane and while the crack growth becomes self-similar. When the last portion of the specimen has reached the critical opening ω_c, the specimen splits in half, at point D. As just seen, the pre-peak and early post-peak non-linearity is controlled by the Cohesive Law of the material, and cannot be described completely with a single parameter such as G_c or K_c.

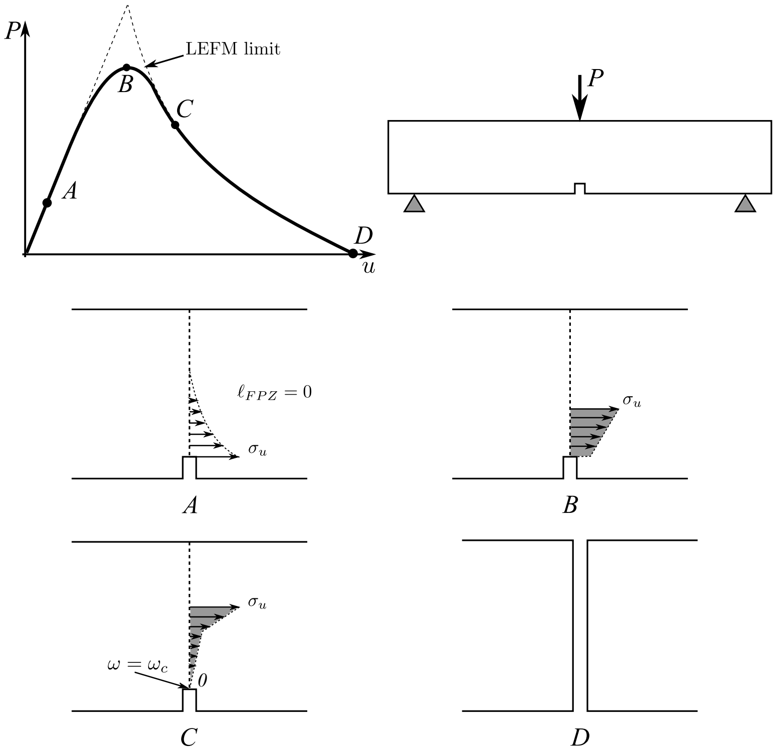

Fig. 2.6.: Typical load-deformation relation of a notched beam under bending and development of the FPZ in front of the notch.

Some commonly used CL shapes can be seen in Fig. 2.7. Although a unique curve can be defined for every material, some characteristics are common among all the softening laws. For instance, the area under the curve must be equal to the material fracture energy G_c, to ensure the correct energy dissipation when the FPZ is fully developed. The onset point of the Cohesive Law matches the tensile strength σ_u, and the FPZ is totally developed once the COD at the initial crack tip has reached the critical value ω_c. Lastly, to ensure a localized crack, it is necessary that $\partial\sigma/\partial\omega \leq 0$, i.e. the softening function must be a non-increasing function, or, at least, that its local maxima are lower than σ_u. Otherwise, after the first crack had appeared, other crack would appear at neighbouring points (Elices et al., 2002).

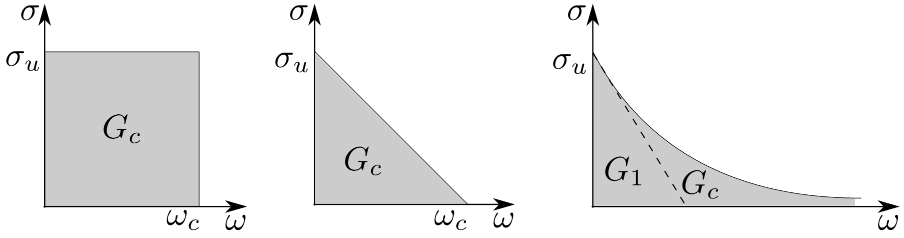
σ
σ_u
G_c
ω_c
ω
σ
σ_u
G_c
ω_c
ω
σ
σ_u
G_1
G_c
ω

(a) **(b)** **(c)**

Fig. 2.7.: Common Cohesive Law: (a) Constant, (b) linear and (c) exponential shapes.

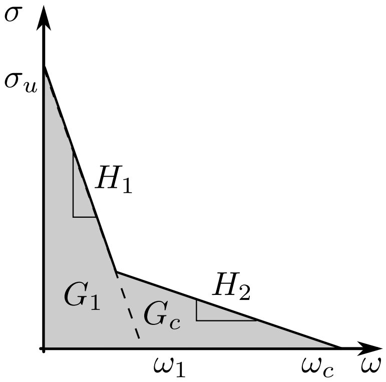
σ
σ_u
H_1
H_2
G_1
G_c
ω_1
ω_c
ω

Fig. 2.8.: Bilinear Cohesive Law shape, with G_1 as the fracture energy related to the initial slope H_1.

Metallic or polymer structures have their nominal strength and structural response well enough predicted with the use of a constant (Fig. 2.7a) or linear (Fig. 2.7b) Cohesive Laws. For such shapes, only two parameters are needed to be fully described, usually being σ_u and G_c. Concrete or fibre-reinforced composite materials do not have their energy dissipation mechanisms well enough represented with these curves. Exponential CL shapes (Fig. 2.7c) with an initial linear part are capable of capturing properly the damage mechanisms of concrete (Planas et al., 2003), whereas Bilinear cohesive laws (Fig. 2.8) provide optimal solutions for both concrete and fibre-reinforced composite materials (Elices et al., 2009).

Bilinear laws need four parameters to fully describe the shape, being σ_u and G_c two of them. Two additional values are needed to describe the CL: the slopes of the branches H_1 and H_2, the fracture energy G_1 associated with the first part of the CL, the abscissa centroid of the area under the curve, etc. Unfortunately, such softening laws have their measurement not well established by the researchers. Chapter 3 delves on the methodologies to obtain the CL shape available in the literature.

2.2.3 Rice's J-integral

The LEFM definition of the Energy Release Rate assumes the existence of a sharp crack a. Within the framework of a cohesive zone model, the crack length looses its definition, due to the existence of the FPZ. An alternative to measure the energy dissipated inside the FPZ without any LEFM assumptions was proposed by Rice (1968). Ideally, one would like to measure the strain and stress field of the specimen during the whole crack formation and propagation. Then, it would be possible to directly apply the J definition

$$J = \int_{\Gamma} \left(\Phi dx_1 - t_i \frac{\partial u_i}{\partial x_2} ds \right) \tag{2.25}$$

where J is the energy being dissipated at a given instant inside the FPZ, Φ is the elastic strain density, t_i is the surface traction vector and u_i is the displacement vector. The surface traction vector is obtained as $t_i = \sigma_{ij} n_j$, where n_j is a unitary vector normal to the path Γ and σ_{ij} is the stress tensor.

The J defined in Eq. 2.25 is a path-independent integral, meaning that the measured energy that is being dissipated is invariant regardless of the path Γ, provided it encloses the FPZ, as seen in Fig. 2.9. Moreover, when the FPZ is small enough compared to other problem dimensions and small-scale yielding (SSY) or bridging (SSB) can be assumed, the J-integral equals to the Energy Release Rate G defined in Eq. 2.3.

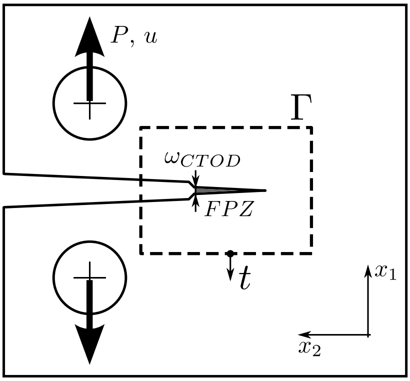

Fig. 2.9.: Integration path Γ and normal traction vector t for the J-integral.

When shrinking the integral path Γ to just include de boundaries of the FPZ, Eq. 2.9 becomes:

$$J = \int_{0}^{w_{CTOD}} \sigma\left(w\right) dw \tag{2.26}$$

where $\sigma\left(\omega\right)$ is the CL function and ω_{CTOD} is the Crack Tip Opening Displacement, i.e., the crack opening measured at the initial notch position. Eq. 2.26 establishes a direct relation between J and the CL. While the FPZ is being developed, J is always lower than G_c and as soon as $J = G_c$ the FPZ becomes completely developed. At this point the crack growth becomes self-similar. The definition of Eq. 2.9 does not require the measurement of the crack length while also not making any approximation.

2.2.4 Size effect on structural strength according to the Crack-bridging models

The phenomenon known in the literature as Size Effect accounts for the dependence of the structural strength on the specimen size. The structural or nominal strength σ_N is defined as the maximum load the specimen withstands divided by some measure of specimen size (W). The specimen size W may be arbitrarily defined by

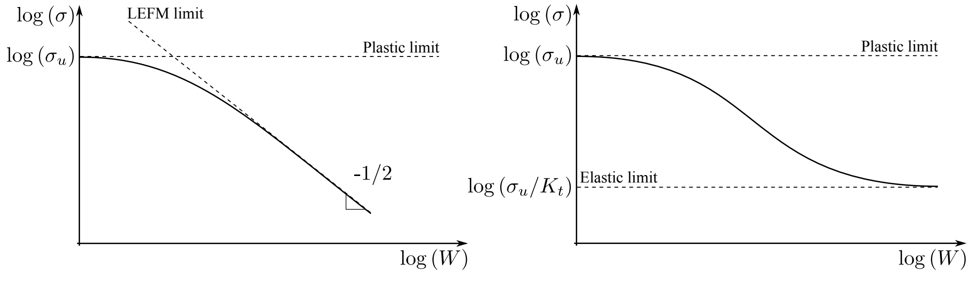

(a) **(b)**

Fig. 2.10.: Size effect law for (a) notched and (b) unnotched structures.

any dimension, given all tested specimens remain geometry invariant. The typical response for notched and unnotched structures is shown in Fig. 2.10.

The generalized cohesive zone model is able to capture the Size Effect as:

$$\left(\frac{\sigma_u}{\sigma_N}\right)^2 = \phi\left(\frac{W}{\ell_M}\right) \tag{2.27}$$

where

$$\ell_M = \frac{EG_c}{\sigma_u^2} \tag{2.28}$$

is a characteristic length of the material. The function ϕ is generally unknown, but can be computed using numerical simulations (Bažant and Planas, 1998; Cusatis and Schauffert, 2009; Maimí et al., 2012) for a given specimen geometry and Cohesive Law shape.

For small specimen sizes, notched or unnotched, the nominal strength tends to the plastic limit, i.e., the nominal stress σ_N calculated through purely plastic analysis, where the whole stress profile located at the failure plane is equal to σ_u. In this case, the nominal strength is achieved before the FPZ has been completely developed, hence not experiencing any large softening. In that manner, the nominal strength is fully controlled by the first slope of the softening curve (Mai and Hakeem, 1984). The plastic limit tends to a horizontal line for the logarithmic variables $\log(\sigma_N) - \log(W)$ for $\lim_{W\to 0}$, as seen in Fig. 2.10. On the other hand, for large notched specimens, the σ_N follows the LEFM limit, where the response tends to a line with a slope of $-1/2$ (see Fig. 2.10(b)). In this case, the ℓ_{FPZ} is very small compared to the other problem dimensions, with the Fracture Process Zone completely developed when the nominal strength is reached. Therefore σ_N is controlled uniquely by G_c while assuming LEFM. Lastly, for large specimens without stress singularities or blunt notches, such as the Open Hole, σ_N tends to the material elastic limit, controlled by the stress concentration factor K_t (see Fig. 2.10(a)).

3

Existing literature on determining the cohesive law

The determination of the Cohesive Law has been a problem of increasing interest for the scientific community over the last three decades. An overwhelming number of literature resources delve with this topic: several specimen geometries, materials, loading configurations and methodologies have been studied. Historically introduced for concrete materials, the prime problem of the cohesive zone modelling is the determination of the softening law itself. With the increasing presence of fibre-reinforced composites materials in aeronautical and automotive applications, several new approaches have been suggested by researchers to accomplish this measure. This chapter deals with the most common methodologies to measure the Cohesive Law, classified by the nature of the procedures.

3.1 Experimental measure from a tensile test

The most direct methodology to obtain the Cohesive Law is from a stable traction test (Cornelissen et al., 1986; Hordijk et al., 1987). In this manner it is possible to obtain the entire softening curve $\sigma - \omega$ as a direct measure of a single experiment. However, approaching the problem with this methodology may lead to some difficulties or even the impossibility to finalize the test or validate the data (Elices et al., 2002).

- **Crack instability:** The most common problem when approaching the CL measure in this manner derives from the instability of the crack growth. Usually, tensile specimens store a high amount of elastic energy prior to the crack onset, causing a sudden crack growth that results in the inability to properly measure the $\sigma - \omega$ curve. The use of smaller specimens may reduce the stored elastic energy, although most quasi-brittle materials would require an extremely small specimen in order to achieve a stable crack growth, even for laboratory standards. Generally, the stable crack growth condition, i.e, the absence of a snap-back of the load-displacement curve, is checked with $L < E/H$, where L is the specimen length and H is the maximum slope of the Cohesive Law, as seen in Fig. 2.8. Because of this, in practice, this method has only been used for concrete.

- **Multiple cracks:** To direct measure the softening law, a single crack perpendicular to the loading direction must form across the section of the specimen. However, many ceramic and cementitious materials develop more than one cohesive crack during the experiment. Additionally, the location of the crack is unknown before the test (Fig. 3.1a).

- **Crack rotation and crack overlapping:** The inclusion of small notches to force the crack location may provoke the fracture to become asymmetric: both cracks do not grow at the same rate, resulting in the rotation of the specimen (shown in Fig. 3.1b). When stiffer testing machines are used to avoid this phenomenon, the specimen itself rotates internally, making the cracks at each side of the specimen to overlap and preventing the formation of a single crack (shown in Fig. 3.1c).

Because of the mentioned difficulties in the direct determination of the softening law from a tensile test, some indirect methods have been developed by multiple researchers. This chapter includes a classification of the available procedures, ranging from experimental test to obtain characteristic values of the CL to parametric fitting using analytic or Finite Element models, through more sophisticated methods such as the J-integral method.

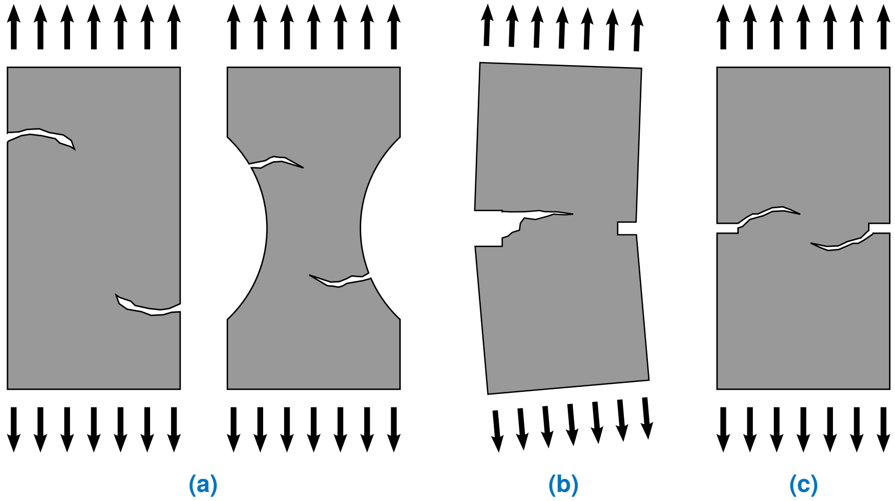

Fig. 3.1.: Problems during the CL determination from a tensile test: (a) Multiple cracks in tensile specimens. (b) Rotation of crack faces in pre-cracked specimens. (c) Crack overlapping.

3.2 Obtaining characteristic values of the Cohesive Law from experimental test

An alternative to measuring the entire Cohesive Law from a single fracture test was proposed by (Planas and Elices, 1999). Their approach was developed for concrete, assuming a bilinear CL shape. This methodology consists on performing several independent experiments in order to determine the parameters that define the softening law, separately. The four chosen parameters to be determined from this method are: the ultimate tensile strength σ_u, the total fracture energy G_c, the fracture energy related with the first part slope G_1 and the abscissa of the centroid of the curve ω_G. The chosen parameters are depicted in Fig. 3.2. It should be mentioned that, although the methodology is intended to be used for concrete, it could be adapted for fibre-reinforced composite materials.

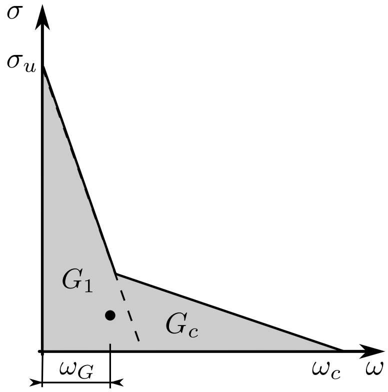

Fig. 3.2.: Bilinear Cohesive Law proposed for concrete, with the defining characteristics σ_u, G_c, G_1 and ω_G.

Ultimate tensile strength σ_u

The ultimate tensile strength of the material can be obtained from a uniaxial tensile test, where the maximum load (P_u) that the specimen withstands is recorded (Mier and Vliet, 2002), as seen in Fig. 3.3. The stress distribution at the failure plane tends to the material tensile strength σ_u at the critical load. In order to successfully record σ_u, the specimen must not have any notch or holes to prevent any stress concentration to appear. Otherwise, the average stress distribution at the failure plane would be altered. Taking this into account, σ_u can be determined with Eq. 3.1:

$$\sigma_u = \frac{P_u}{A} \tag{3.1}$$

where A is the area of the failure plane, perpendicular to the loading direction.

A tensile test is normally sufficient to measure the σ_u of many quasi-brittle materials. In the case of FRP, the tensile test is accurate enough, as long as undesired failure modes, such as the failure at the end tabs, are avoided. However, some materials, like concrete, show a low repeatability of σ_u recorded by a tensile test (Planas et al., 2003). This behavior is caused by the inherent defects of the material, such as cavities and micro-cracks between the cement and the aggregates, with sizes

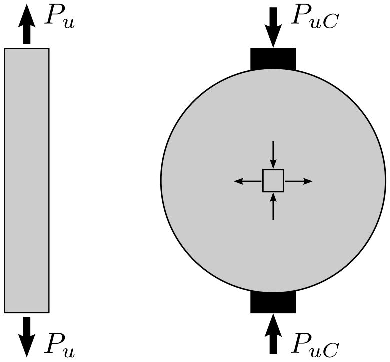

Fig. 3.3.: Uniaxial tensile test (left) and split-cylinder test (right)

that are not negligible with respect to other problem dimensions. Because of the randomness of the defects at this scale, stress concentrations take place at the defect surfaces, altering the average stress at the failure plane between specimens of the same size. In order to increase the repeatability of the measured tensile strength, an alternative approach is to use the split-cylinder test (Elices et al., 2002; Planas and Elices, 1999). In this experiment, a concrete cylinder is subjected to a compression load, shown in Fig. 3.3. The cylinder is loaded until it splits in two halves under the action of a compressive load P_{uC}. At the failure plane, which is oriented along the loading direction, the stress distribution is almost constant an equal to σ_u. Small areas next to the load application points are submitted to compression, although they influence on the average stress at the failure plane can be neglected.

The repeatability of the recorded σ_u is increased by using the split-cylinder tests at the cost of a significant inconvenient: the measure is size-dependent. The size effect law for the tensile strength obtained from a split-cylinder test can be written in the form:

$$\sigma_u \phi_C \left(\ell_{M,1}\right) = \frac{2P_{uC}}{\pi D_C L_C} \tag{3.2}$$

where ϕ_C is the size effect function related to the cylinder test and D_C and L_C are the cylinder diameter and length respectively. The $\ell_{M,1}$ is a characteristic length of the material related to G_1, the fracture energy related to the first part of the Cohesive Law and shown in Fig. 3.4

$$\ell_{M,1} = \frac{G_1 E}{\sigma_u^2} \tag{3.3}$$

The size effect function ϕ_C can be obtained by carrying out several experiments on different size specimens with similar geometries or it can be computed numerically (Camanho et al., 2007; Maimí et al., 2012). When split-cylinder testing laboratory sized specimens of concrete, the size effect law can be approximated to 1 (Elices et al., 2002). Hence, σ_u is computed as:

$$\sigma_u \approx \frac{2P_{uC}}{\pi D_C L_C} \tag{3.4}$$

When ϕ_C can not be assumed as 1, at least two experiments must be carried out in order to compute it numerically, while obtaining the σ_u and at the same time $\ell_{M,1}$ (see Section Initial shape of the cohesive law).

Fracture Energy G_c

The total fracture energy G_c is measured from a stable fracture test, such as the Compact Tension test for fibre-reinforced composite materials or the notched three point bending test for concrete. In general, any stable fracture test is sufficient as long as the Fracture Process Zone is fully developed prior to the end of the test.

During a quasi-static fracture test, if the kinetic energy is neglected, the work done on the specimen is equal to the product of the load force (P) and load application point displacement (u). Assuming that the external work W_F has been spent solely on creating new crack area until the specimen has been split in two, the specific fracture energy is obtained from dividing the external work W_F by the ligament area.

Alternatively, to measure G_c it is possible to just assume LEFM for the given specimen, and take the total fracture energy as the plateau value of the obtained $\mathcal{R}$-curve, i.e., when the FPZ has been completely developed.

In these experiments, the specimens are loaded to create a macro-crack that grows in a quasi-static state, until the specimens are split completely. For specimens with positive geometries (the vast majority of specimen geometries), the test must be displacement-controlled in order to achieve a stable crack growth and to capture the entire P-u curve. For negative geometries the test can be either loading or displacement controlled.

Initial shape of the cohesive law

As mentioned in Section 2.2.2, the maximum load a structure can withstand is achieved while the FPZ is still being developed. Therefore, the initial shape of the CL plays a key role in the prediction of the structural nominal strength. For a bilinear CL, the initial part of the curve is defined by σ_u and G_1. The latter parameter expresses the fracture energy dissipated by the first slope of the softening function as $G_1 = \sigma_u \omega_1 / 2$. The ω_1 is the crack opening obtained at the intersection of the abscissa axis and the projection of the first slope, as shown in Fig. 3.4. G_1 can also be expressed by means of the characteristic length $\ell_{M,1}$ as $G_1 = \sigma_u^2 \ell_{M,1} / E$, introduced in Eq. 3.3.

To experimentally obtain G_1, it is necessary to perform a series of tests of different size specimens with similar geometries, in order to capture the Size Effect:

$$P_u = \sigma_u \phi \left(\frac{W}{\ell_{M,1}} \right) \tag{3.5}$$

where P_u is the structural ultimate load and W is the specimen's size. Elices et al. (2002) solved the Size Effect function ϕ for a notched three point bending test while assuming a linear initial part of the softening law. If the tensile strength σ_u is known (measured from the split-cylinder test for concrete), ω_1 can be determined with:

$$\frac{\omega_1}{\sigma_u} = \left(1 - \alpha_0^{1.45}\right) \frac{D_B}{E'} \left[\frac{26,22}{(x-1)^2} + \frac{5,36}{x} \right] \tag{3.6}$$

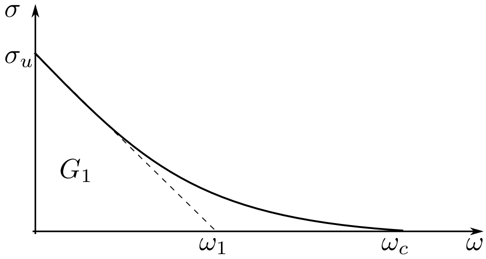

Fig. 3.4.: Linear approximation of the initial part of the Cohesive Law.

where D_B is the beam depth and α_0 is the initial crack to depth ratio $\alpha_0 = a_0/D_B$. The variable x is defined as:

$$x = \left[3\left(1-\alpha_0\right)^2 \frac{2B_B D_B^2 \sigma_u}{3P_u S_B} \right] \tag{3.7}$$

where B_B is the beam thickness and S_B is the loading span.

The same procedure can be applied for other specimen geometries and materials, as long as σ_u is determined independently, and the nominal strength of the chosen specimen is influenced by the Size Effect. The ϕ can be obtained for other geometries by fitting numerical simulations.

Last part of the cohesive law shape

As already mentioned in Section 2.2.2, the crack growth becomes self-similar as soon as the FPZ has been fully developed. During this phase, the FPZ moves along the symmetry plane. During the last moments before the specimen splits in two, the only cohesive forces that are sticking the two parts of the specimen together are defined by the second slope of the softening law. Fig. 3.5 schematically represents this behaviour.

Elices et al. (Elices et al., 2002) suggested to describe the final shape of the cohesive law by using the abscissa centroid coordinate of the softening curve area ω_G, as

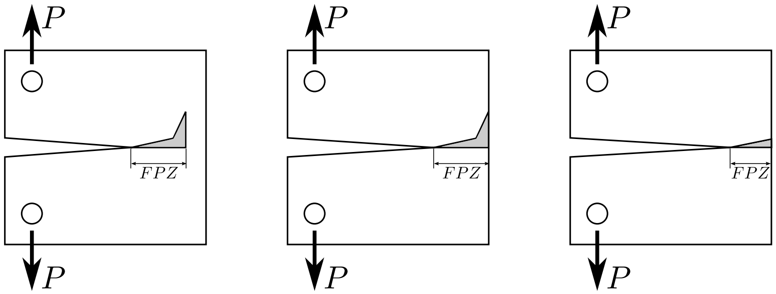

Fig. 3.5.: FPZ translation along the symmetry plane, until the ligament is only held by the cohesive stresses defined by the last part of the Cohesive Law.

shown in Fig. 2.8. Again for a notched three point bending test, the final part of the P-u curve tends to the asymptotic solution

$$P \approx \frac{S_B B_B \omega_G G_c}{4u^2} \tag{3.8}$$

where u is displacement of the applied load. In order to determine ω_G, it needs to be best fitted with the experimental points of the curve. It may be solved by an iterative method while minimizing the error between the computed and experimental values. It should be mentioned that this method was proposed to measure the CL of concrete, which has a high compressive strength. Applying this approach to FRP may lead to undesired failure modes such as buckling or compressive failure.

3.3 The J-integral method

This methodology takes advantage of the existing relationship between the J-integral and the material CL. As previously stated in Section 2.2.3, both parameters are directly related, as one is the integral of the other. When applying Rice's J-integral definition around a FPZ, the energy being dissipated inside the non-linear region is computed correctly, even when Large-Scale Bridging is present, as no LEFM assumptions are made.

In order to obtain the material softening function, the J must be recorded as a function of the Crack Tip Opening Displacement ω_{CTOD} during the whole crack formation and propagation. Then, the CL is obtained by differentiating the curve J-ω_{CTOD} (Li. et al., 1987; Sørensen and Jacobsen, 2003; Lindhagen and Berglund, 2000):

$$\sigma = \mathrm{d}J/\mathrm{d}\omega_{CTOD} \tag{3.9}$$

As the expression of J does not depend on the integration path Γ, it does not need to be traced to just include the FPZ boundary, but can be obtained from any arbitrary path, as long as the whole FPZ is enclosed. This property is highly useful, as it allows to obtain the softening law virtually from any specimen geometry.

Although the procedure to measure the CL from the J-ω_{CTOD} is simple enough, provided the curve has been obtained, in reality the difficulty arises when trying to evaluate the J-integral. Many strategies exist in the literature on how to accomplish this measure. This Section includes the most spread approaches adopted by different researchers.

In order to compute J, ideally one would like to measure the strain and stress field of the specimen during the whole crack formation and propagation. Then, it would be possible to directly apply the J definition given in Eq. 2.25. In reality, the only procedure to measure the whole strain and stress field of a specimen during a test is by using the Digital Image Correlation (DIC) technique. This technique follows the relative displacement of several spots printed on the specimen face. As a result, the strain field is recorded where the material is continuous, provided that the measurement is done sufficiently away from the FPZ (Catalanotti et al., 2010; Bergan et al., 2014). The stress field is then obtained from the strain field by knowing the material elastic properties. For some particular Specimen Geometries (SG) and loading configurations, an explicit form of Eq. 2.25 can be found, i.e. the closed form solution. Hence, the J-integral can analytically expressed, resulting in only needing to measure some output variables such as the acting load or certain displacements, instead of measuring the stress and strain field. For instance, when evaluating J in a Double Cantilever Beam (DCB) subjected to a bending moment

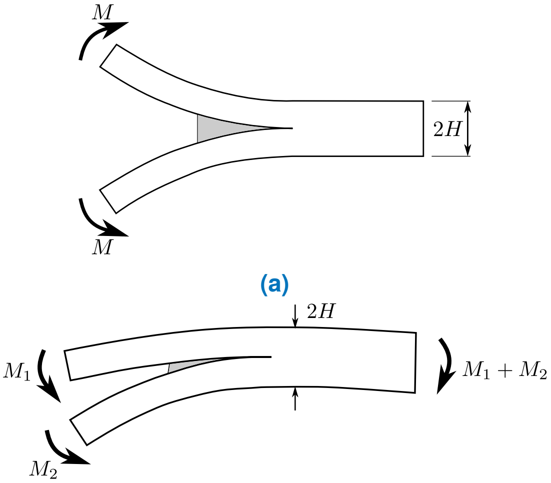

(a)

(b)

Fig. 3.6.: DCB specimen subjected to: (a) a bending moment M in pure mode I loading and (b) a pair of bending moments M_1 and M_2 in mixed mode I/II loading.

M in pure mode I loading, as seen in Fig. 3.6(a), the expression turns (Suo et al., 1992):

$$J = \frac{12M^2}{E'H} \tag{3.10}$$

with only needing to record the bending moment that is being applied as the FPZ progresses. Similarly, J can be expressed analytically for a DCB subjected to a pair of bending moments M_1 and M_2 in mixed mode I/II loading, shown in Fig. 3.6(b), J is expressed (Sørensen et al., 2006):

$$J = \frac{21\left(M_1^2 + M_2^2\right) - 6M_1M_2}{4B^2H^3E} \quad \text{for} \quad |M_1| < M_2 \tag{3.11}$$

again with only needing to record the applied bending moments. In a similar way, when applying a point load P in pure mode I loading, the expression is simplified as $J\left(P, \theta\right)$, where θ is the rotated angle at the loading end (Paris and Paris, 1988; Olsson and Stigh, 1989), meaning that in addition to measure P, θ needs also to be recorded experimentally (Andersson and Stigh, 2004).

When studying the fracture toughness and the though-the-thickness crack propagation in fibre-reinforced composite materials, the most commonly tested specimens are the Compact Tension (CT) and the Overheight Compact Tension (OCT) specimens. Unfortunately, closed-form J-integral expressions do not exist for these geometries. The only way to measure J would be by means of the more difficult and expensive DIC technique. Because the computation of J with DIC can be very time consuming, an alternative was proposed by Bergan et al. (2016). In this case, they measured the J-integral curve for a CT specimen assuming that J=G, and thus, equalling the $\mathcal{R}$-ω_{CTOD} to J-ω_{CTOD}. The Crack Tip Opening Displacement was still tracked with DIC. Lastly, the parameters that defined the bilinear CL were best fitted from the measured $\mathcal{R}$-ω_{CTOD} function. In their study, they also compared, from a FE test, the J and $\mathcal{R}$ curves for three Compact Tension specimens of different sizes with a bilinear cohesive law. While the $\mathcal{R}$-ω_{CTOD} were influenced by the specimen size, they assumed the discrepancies could be ignored, even for laboratory sized specimens.

Lastly, instead of measuring the J-ω_{CTOD} curve for the whole experiment, it is possible to obtain the CL shape from a single frame of the test, by means of the experimental measure of the function $\sigma - \omega$. Ideally, it could be obtained as the evolution of the stress measured at the initial crack tip a_0 position as the crack opens, similarly to the method applied to composite materials proposed by Zobeiry et al. (2014). In this method, the displacement field of the specimen is measured through the use of the Digital Image Correlation (DIC) technique, and the FPZ boundary is estimated where the material does not behave linear-elastically. The cohesive stresses are obtained by assuming the stress in the loading direction across the damaged material to be uniform and equal to the stress of the undamaged material adjacent to the FPZ. Finally, an optimization algorithm is used in order to find a softening function that best fits the experimental curves. Despite the fact that this method is time-consuming, it is capable of measuring any arbitrary CL during the FPZ formation as well as during the self-similar crack growth. In practice, some problems arise when trying to perform this experimental measurement. For instance, it is not feasible to measure the strain inside an heterogeneous region such as the FPZ, where a material discontinuity is taking place, e.g. matrix cracking, fibre bridging and fibre pull-out. On the other hand, the crack opening could be measured with a displacement transducer placed at the initial crack tip or with the use of the DIC, although the obtained data would probably suffer from high scattering.

3.4 Optimization techniques

As seen through this Chapter, the direct measure of the CL variables is very difficult, if not impossible, for most materials. For instance, it is not feasible to measure the stresses inside an heterogeneous region such as the FPZ, where a material discontinuity takes place. On the other hand, the crack opening profile inside the FPZ could be measured with a displacement transducer placed at the initial crack tip or with the use of the more sophisticated DIC. Additionally, the closed-form solutions for the J-integral are only available for a handful of geometries, but in many other cases, such solutions may not exist. Under these circumstances, an additional family of methodologies to determine the CL have emerged. These are called optimization techniques (Que and Tin-Loi, 2002; Silva et al., 2014; Ortega et al., 2015; Roelfstra and Wittmann, 1986; Steiger et al., 1995; Bolzon et al., 2002; Ortega et al., 2016; Cox and Marshall, 1991; Lindhagen et al., 2000).

In the optimization techniques group, the softening law is found through the use of an optimization algorithm capable of solving the inverse problem. The inverse problem consists of predicting the CL by changing its shape in a numeric simulation until it fits the experimental results, as depicted in Fig. 3.7. All the methodologies based on solving the inverse problem are usually composed of three key ingredients:

- First, an experimental test is carried out where the P-u curve is recorded. Other variables such as the Crack Tip Opening Displacement can also be recorded, depending which variables are going to be fitted. When addressing the problem in this fashion it is important to perform a stable fracture test and to choose the correct specimen size W. The specimen needs to be sufficiently large to guarantee that at the end of the experiment the FPZ has been completely developed, while at the same time, it must be sufficiently small so that its response differs enough from the LEFM one, allowing to properly capture the CL shape.

- Second, it is necessary to develop a computer simulation test that virtually reproduces the experimental one, where the parameters that define the CL can be freely altered. This computation can be performed by FE analysis, or other numerical or analytic methods, as will be further discussed.

- Last, the optimization algorithm is performed in order to find the CL parameters. To do so, a suitable norm which quantifies the discrepancy between experimental data and the corresponding values provided by the computer simulation is minimized, with respect to the mentioned parameters.

During a fracture test, usually the recorded variables are the load and some sort of displacement measure, such as the load-pin displacement or the Crack Opening Displacement. These are the output variables that are normally best fitted in order to measure the Cohesive Law. These variables are easily recorded during the experiment, but can only be applied to measure the CL if they are recorded during the whole FPZ formation, and not just during the auto-similar crack growth. An alternative approach was proposed by Cox and Marshall (1991) and Lindhagen et al. (2000), where the complete crack opening profile is experimentally determined and the Cohesive Law is numerically found until the numerical crack profile fits to the experimental results. The accuracy of this method depends on the measured crack openings that in multiaxial composites appears to be difficult. On the other hand, it is possible to measure the cohesive law in self-similar crack regime. Similarly, Stutz et al. (2011b), Stutz et al. (2011a), and Sørensen et al. (2008b), tested a DCB specimen with a Bragg fibre placed in the interface. This fibre is capable of obtaining the strain distribution along its length, thus measuring the stress inside the totally formed FPZ. The CL was fitted in order that it would adjust the strain distribution.

Several methodologies can be found in the literature to solve the inverse problem by this approach. This section delves in the methodologies to execute the computer simulations of the virtual test, and will not focus on the optimization techniques in order to find the optimum solution.

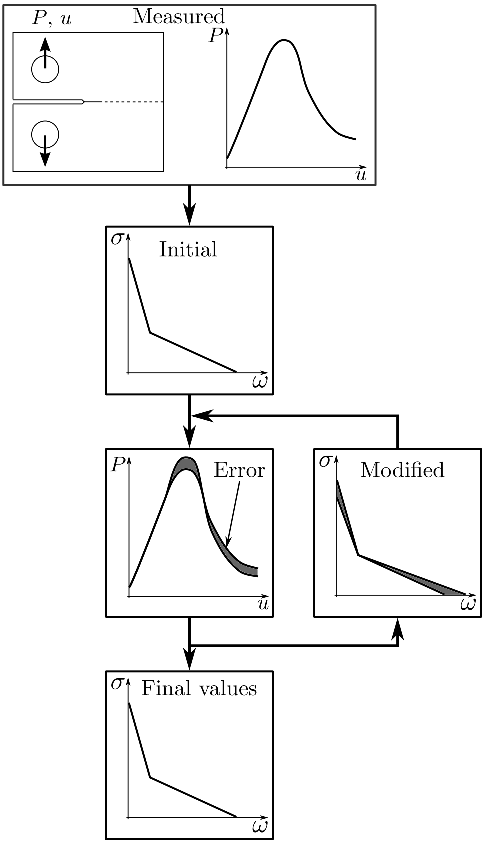
P, u
Measured
P
u
σ
Initial
ω
P
Error
u
σ
Modified
ω
σ
Final values
ω

Fig. 3.7.: Optimization approach to measure the CL.

3.4.1 Null crack tip intensity factor

This methodology derives from Dugdale's cohesive zone model highlighted in Section 2.2.1. Let's consider a rectangular plate with an initial notch of length R, subjected to a controlled displacement and corresponding tension σ normal to the initial crack, as seen in Fig. 3.8.

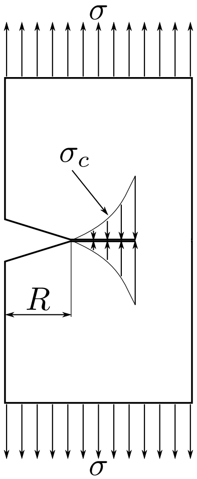

Fig. 3.8.: Rectangular plate with lateral crack subjected to a remotely applied stress σ and Cohesive stresses σ_c inside the FPZ.

To obtain the load-displacement curve of the given specimen, while taking into account the non-linearities of the Cohesive Zone, Dugdale's condition is applied, i.e, the global Stress Intensity Factor at the crack tip must be zero:

$$K = K^{\sigma} + K^{\sigma_c} = 0 \tag{3.12}$$

where K^{σ} is the SIF caused by the applied stress σ and K^{σ_c} is the SIF caused by the whole cohesive stress profile σ_c. If the Cohesive Stress profile inside the FPZ is known, there is only one value for σ that satisfies Eq. 3.12. Although σ_c is unknown and may change during the FPZ development, it can be discretized as a series of small constant stresses of value equal to σ_i applied at the crack surface. The non-linear problem expressed as a superposition of linear problems is shown in Fig. 3.9. In order to solve the cohesive stress profile inside the FPZ, the crack opening profile must also be found. It is possible to express the set of openings ω_i as a superposition of the openings caused by each acting load

$$\omega_i = \omega_i^{\sigma} + \omega_i^{\sigma_c} \tag{3.13}$$

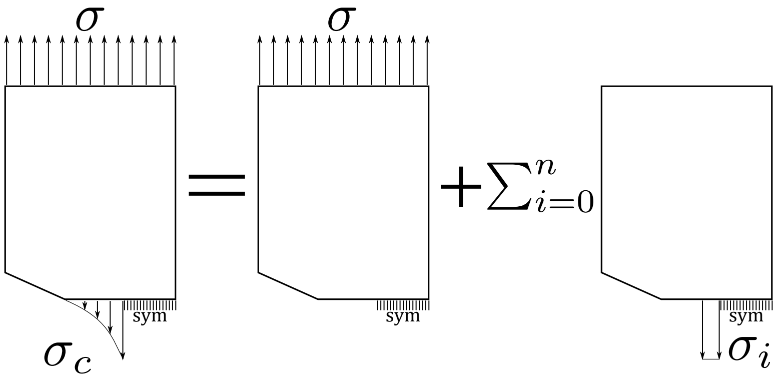

Fig. 3.9.: Rectangular finite plate with a fracture process zone expressed as a lineal superposition problem.

where ω_i, ω_i^{σ} and $\omega_i^{\sigma_c}$ are the total crack opening, the crack opening caused by the point load P and the crack openings caused by the cohesive stress profile σ_c, respectively. The solution to the Eq. 3.13 is obtained from an iterative process and for a given CL. As a result, the stress profile and the crack openings at the FPZ are obtained. Lastly, the load P is obtained by means of Eq. 3.12. The displacement is determined, again, by the superposition of the displacement due to external load (σ) and the cohesive stresses.

This methodology can be applied on other geometries (Newman, 1983; Williams et al., 2011; Maimí et al., 2012), and will be further described in Section 5.2, where it is applied for a Compact Tension specimen.

3.4.2 Tractions at the failure plane

In this case, the cohesive problem is approached from the study of the traction distribution of the material at the crack plane. Again, the considered geometry is a rectangular plate with an initial notch of length R, subjected to a controlled displacement and corresponding tension σ normal to the initial crack, as seen in Fig. 3.8. The goal is to reproduce analytically the whole non-linear solution of the P-u curve. An analogous procedure can be applied to solve other geometries.

The solution is found by obtaining the tractions at the crack plane, again by using the superposition principle. The whole stress distribution is acquired as the superposition of the stresses caused by each acting load: the tension σ corresponding to the applied displacement and the inelastic response of the cohesive stresses inside the FPZ (Que and Tin-Loi, 2002; Que, 2003).

Dividing the crack plane in n intervals, as shown in Fig. 3.10, the traction at each point is evaluated:

$$t_i = \sum_{i=1}^{n} Z_{ij}\omega_j + t_i^e \tag{3.14}$$

where t_i is the traction vector of the discretized crack plane points when a displacement u is applied, t_i^e is the traction due the linear elastic response of the material, ω_j is the fictitious crack opening profile vector along the crack plane and Z_{ij} is the influence coefficient matrix, that describes the traction at position i imposed by a unitary opening at position j.

Observing Eq. 3.14, if no point is bearing a tension greater than σ_u, the cohesive crack opening is null, and therefore the traction distribution becomes the linear elastic response of the material t_i^e. On the other hand, if any point experiences an elastic stress greater than σ_u, the cohesive crack starts to open and the bearing stress must lie on the Cohesive Law. Taking this into account, it can be seen that the traction vector t_i must satisfy:

$$t_i = \sigma\left(\omega_i\right) \tag{3.15}$$

where $\sigma\left(\omega_i\right)$ are the cohesive stresses at each discretized crack opening obtained from the Cohesive Law. It should be mentioned that the elastic stress solution t_i^e also lies in the Cohesive Law (at the vertical branch of zero cohesive crack opening).

In order to solve the problem, it is necessary to obtain the crack opening profile ω_j that satisfies Eq. 3.14 and Eq. 3.15 at the same time. This is normally achieved

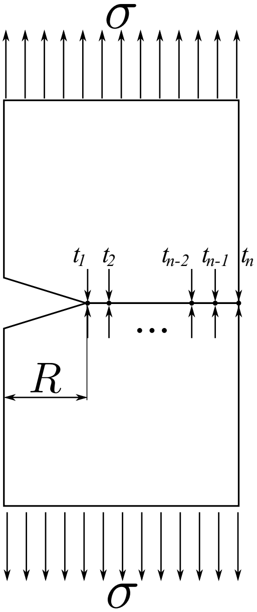

Fig. 3.10.: Discretized traction nodes along the crack plane

from an iterative process. Once ω_j and t_i are known, the load of the structure for the given displacement P is computed

$$P = X_j \omega_j + P^e \tag{3.16}$$

where P^e is the load necessary to create a displacement u in the structure if only an elastic response is considered, and X_j is a vector that relates the load necessary to open the crack at the node j by unity.

3.4.3 FE method

Lastly, another used method to obtain the softening law of the material is the Finite Element (FE) method (Mihashi and Nomura, 1996; Tschegg et al., 1993). As in both previous cases, the objective is to reproduce a crack initiation and development of an specimen with an unknown Cohesive Law, but instead of trying to obtain the P-u from analytic approaches, it is obtained with the use of a FE model.

Basically two approaches to solve the problem are generally used. The first one consist of modelling the geometry with elastic elements in conjunction with cohesive elements (Turon et al., 2006). In this case the crack propagation plane must be known a priori, placing cohesive elements along the crack path. The behaviour of the FPZ is governed by the cohesive law of the element. The second approach is to use continuum damage model elements with tension softening (Maimí et al., 2007a; Maimí et al., 2007b). In this case the crack propagation plane does not need to be known beforehand, because the damage model used in the elements is capable of reproduce the cohesive crack that may appear in any place of the geometry. A drawback with this type of element is experienced when a crack is not propagating perpendicular to one of the side of the element. In order to solve the problem, the geometry would need to be re-meshed to orientate the elements perpendicularly to the crack.

Part II

Translaminar fracture toughness

4

Linear Elastic Fracture Mechanics

The translaminar fracture toughness accounts for the energy dissipated when developing and propagating a crack that spans all the plies of a laminate, i.e, a though-the-thickness crack. This kind of fracture involves complicated fracture mechanisms such as fibre-matrix debonding, fibre breaking and fibre pull-out, resulting in large amounts of energy being dissipated. During the crack onset and crack propagation, the fracture energy G_c associated to this kind of fracture takes into account all these damage mechanisms indistinctly.

The present chapter focuses on the determination of the fracture toughness associated with a translaminar crack growth under mode I tension. A literature review has been performed to establish the available standard procedures and specimen geometries in order to measure the critical strain energy release rate for fibre-reinforced composite laminates. Next, the Stress Intensity Factor (SIF) and Compliance (C) analytic functions for a Compact Tension are formulated, in order to take into account the material orthotropy. Additionally, some experimental recommendations are given to measure the fracture toughness from a Compact Tension specimen, while avoiding undesirable failure modes. Lastly, a new geometry is proposed in order to prevent or delay undesired failure mechanisms during the experimental testing.

4.1 Literature Review: specimens and standard procedures

The translaminar fracture toughness is a key parameter in the prediction of the nominal strength of load-bearing structures. For that reason, the determination of this property is of high interest for the scientific community (Laffan et al., 2012b). The translaminar toughness is usually used in numerous models in order to define the strength of composite structures when loaded in tension (Whitney and Nuismer, 1974; Tan, 1988; Soutis et al., 1991; Taylor, 2007; Taylor, 2008; Maimí et al., 2012; Maimí et al., 2013). Therefore, reliable methods to obtain the laminate G_c or the resistance curve are needed in order to feed numerical (Maimí et al., 2007a; Maimí et al., 2007b; Camanho et al., 2007) or analytic models (Whitney and Nuismer, 1974; Tan, 1988; Soutis et al., 1991; Taylor, 2007; Taylor, 2008; Maimí et al., 2012; Maimí et al., 2013).

Over the last four decades, numerous fracture mechanics test specimens have been proposed in order to obtain the translaminar fracture toughness of composite laminates. The most common ones are shown in Fig. 4.1. In general, the most accepted and used geometry is the Compact Tension specimen, adapted from metallic materials (ASTM, 1997), as it has been used in multiple studies (Slepetz and Carlson, 1975; Parhizgar et al., 1982; Cowley and Beaumont, 1997; Minnetyan and Chamis, 1996; Underwood and Kortschot, 1993; Garg, 1985; Masters, 1997; Poe and Reeder, 2001; Jose et al., 2001; Pinho et al., 2006; Laffan et al., 2010a; Laffan et al., 2010b; Laffan et al., 2011; Catalanotti et al., 2010; Gutkin et al., 2011; Ortega et al., 2014; Blanco et al., 2014a; Blanco et al., 2014b; Zobeiry et al., 2014; Underwood et al., 1995). The Extended Compact Tension (ECT), also proposed for metallic materials, has been also used for composite laminates in numerous occasions (Underwood et al., 1995; Poe and Reeder, 2001; Haj-Ali and El-Hajjar, 2003; Haj-Ali et al., 2006; El-Hajjar and Haj-Ali, 2005; Piascik and Newman, 1995; Piascik et al., 1997). Another variant of the CT specimen is the Over-height Compact Tension (OCT) (Kongshavn, 1996; Kongshavn and Poursartip, 1999; Floyd, 2004; Li et al., 2009; Zobeiry et al., 2014; Xu et al., 2015) , designed for composite laminates with large failure process zones. Other specimens used are the Three Point Bending (TPB) (Garg, 1985; Underwood et al., 1995; Sket et al., 2012) and Four Point Bending (FPB) (Connell et al., 1994; Laffan et al., 2012a). Lastly, a set of unstable specimens have also been used in some works, such as the Center Cracked Specimen (CCS) (Daniel, 1978; Garg, 1985; Masters, 1997; Poe and Reeder, 2001), the Double Edge Notched (DEN) (Bažant et al., 1996; Catalanotti

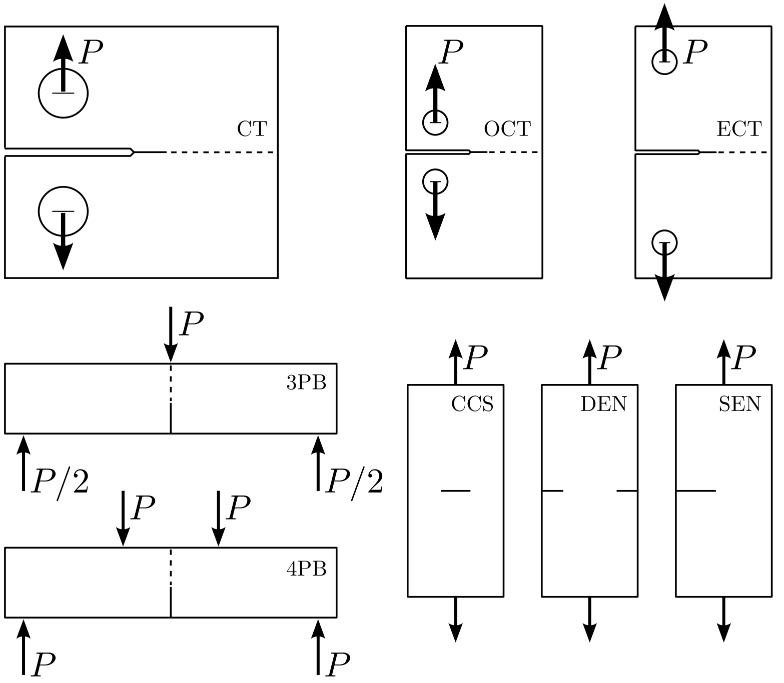

Fig. 4.1.: Fracture mechanics specimens.

et al., 2014a; Catalanotti et al., 2014b) and Single End Notched (SEN) (Bažant et al., 1996; Masters, 1997) specimens.

Despite the existing interest in determining the G_c associated with the laminate mode I opening, only one standard procedure exists that is applicable to composite materials. This standard is the ASTM E1922-04 (ASTM, 2015), designed for the ECT specimen. Other ASTM standards originally developed for metallic materials, such as the ASTM E399-09 (ASTM, 1997) for a Compact Tension specimen, have been applied for laminated composites, in conjunction with special recommendations such as the load displacement and the notch radius.

4.2 Stress field of a planar orthotropic solid

Given a general anisotropic material with a linear constitutive relation, in a bi-dimensional problem, the stress-strain relation can be expressed as:

$$\varepsilon_i = \sum_{j=1,2,6} b_{ij}\sigma_j, i = 1, 2, 6 \tag{4.1}$$

where:

$$b_{ij} = \begin{cases} s_{ij}, \text{ for plane stress} \\ s_{ij} - s_{i3}s_{j3}/s_{33}, \text{ for plane strain} \end{cases} \quad i, j = 1, 2, 6. \tag{4.2}$$

It is known that for any anisotropic material, the solution of the differential equation that defines the stress state depends on the roots of the characteristic polynomial (Lekhnitskii, 1963):

$$b_{11}p^4 - 2b_{16}p^3 + (2b_{12} + b_{66})p^2 - 2b_{26}p + b_{22} = 0 \tag{4.3}$$

with four complex roots in p. It is possible to define a subset of anisotropic materials, defined as orthotropic materials, if their mechanical properties are unique and independent according to three mutually perpendicular directions. For a planar orthotropic material with the principal directions x_1-x_2 defined by its two principal axes, only four independent elastic constants are needed: b_{11}, $b_{12} = b_{21}$, b_{22} and b_{66}, since $b_{16} = b_{26} = 0$. Hence, Eq. (4.3) is reduced to:

$$\lambda p^4 + 2\rho\sqrt{\lambda}p^2 + 1 = 0 \tag{4.4}$$

where p_1 and p_2 are the roots with positive imaginary parts and:

$$\lambda = \frac{b_{11}}{b_{22}} \quad , \quad \rho = \frac{2b_{12} + b_{66}}{2\sqrt{b_{11}b_{22}}} \tag{4.5}$$

In the plane stress case, λ and ρ are expressed as:

$$\lambda = \frac{E_{22}}{E_{11}} \quad , \quad \rho = \frac{\sqrt{\lambda}}{2G_{12}}(E_{11} - 2\nu_{12}G_{12}) \tag{4.6}$$

Material	λ	ρ
T300/920 unidirectional lamina (Laffan et al., 2010a)	0.0657	3.7326
T300/920 [0, $\pm$60]$_s$ isotropic	1.0	1.0
T300/920 [0, 90]$_s$ cubic	1.0	7.9302
Western White Pine wood (Green et al., 1999)	0.0380	1.9635
Northern White Cedar wood (Green et al., 1999)	0.0810	0.6642
Cu (FCC) (Suo, 1990)	1.0	0.03
Fe (BCC) (Suo, 1990)	1.0	0.20

Tab. 4.1.: Values of λ and ρ for seven different materials.

where E_{11} and E_{22} are the elastic moduli, G_{12} is the shear modulus, and ν_{12} is the Poisson's ratio. In the plane strain case, λ and ρ are obtained by replacing E_{11}, E_{22} and ν_{12} in Eq. (4.6) by:

$$E'_{11} = \frac{E_{11}}{1-\nu_{13}\nu_{31}}\ , \qquad E'_{22} = \frac{E_{22}}{1-\nu_{23}\nu_{32}}\ , \qquad \nu'_{12} = \frac{\nu_{12}+\nu_{13}\nu_{32}}{1-\nu_{13}\nu_{31}} \tag{4.7}$$

To ensure the positive definiteness of the strain energy, it must be ensured that:

$$\lambda > 0 \quad \text{and} \quad \rho > -1 \tag{4.8}$$

The anisotropy of the material is easily described by the parameters λ and ρ. For an isotropic material, the parameters take the values $\lambda = \rho = 1$. However, for a cubic material, it only needs to be ensured that $\lambda = 1$ and that $\rho \neq 1$. Table 4.1 contains the values of λ and ρ for a number of materials. From the point of view of composite laminates, the laminate anisotropy is determined by the lay-up sequence; an in-plane isotropic lay-up may have its principals axis oriented in any direction by definition. Some examples of laminate sequences that satisfy this condition are [0, $\pm$60]$_s$, [0,$\pm$45,90]$_s$ or [0,$\pm$36,$\pm$72]$_s$. On the other hand, cubic materials have a principal axis every 45 degrees. An example of cubic laminate sequence is a cross-ply laminate.

Assuming the material behavior to be linear elastic, that the specimen undergoes small displacements and assuming Linear Elastic Fracture Mechanics, the Stress Intensity Factor (SIF) caused by the bearing load P and Compliance functions can be expressed in the form:

$$K_I = \frac{P}{h}\sqrt{\frac{\bar{a}}{W}}\bar{K}_I\left(\bar{a}, \mathrm{SG}, \lambda, \rho\right) \quad ; \quad C = \frac{1}{hE}\bar{C}\left(\bar{a}, \mathrm{SG}, \lambda, \rho\right) \tag{4.9}$$

where P is the applied load, h is the specimen thickness, W is a measure related to the in-plane specimen size, $\bar{a}$ is the normalized crack length defined as $\bar{a} = a/W$ and E is the material elastic modulus of any principal direction, for example E_{11}. The non-dimensional functions $\bar{K}_I$ and $\bar{C}$ define the specimen SIF and compliance, respectively. These are functions that depend on $\bar{a}$, the Specimen Geometry (SG) and two dimensionless parameters λ and ρ that define the anisotropy of the material, introduced in Section 2.1.3 and detailed in the next subsection.

4.3 The Compact Tension specimen for orthotropic materials

The non-dimensional SIF and compliance functions defined in Equation 4.9 have been obtained for a Compact Tension specimen, taking into account the material orthotropy, defined by the variables λ and ρ. In order to do so, a parametric FE model was created using Python scripting together with ABAQUS/Standard 6.11-1 FEM software. To obtain the compliance for a given λ and ρ, a load of 1 N was applied at the loading pin, while the crack nodes were released gradually along the crack plane. The displacement u was captured at the loading line. Also, the Virtual Crack Closure Technique (VCCT) was applied along the crack nodes to compute the SIF. The non-dimensional functions were then found by fitting the results obtained form the FE simulations. The details of the FE model, as well as its validation and the procedure used to fit results can be found in the PAPER A included in this document. Both functions are applicable for $0.03162 \leq \lambda \leq 10.0$ and $0.1 \leq \rho \leq 10$.

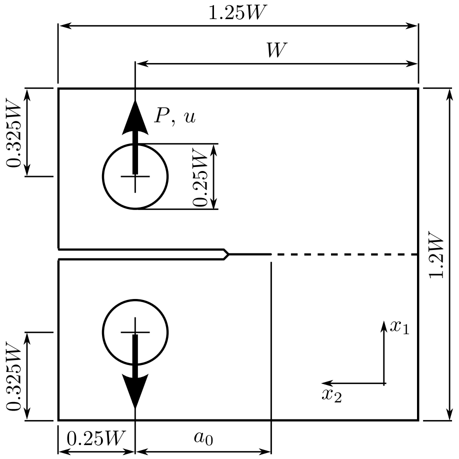

Fig. 4.2.: Compact Tension (CT) Specimen Geometry, subjected to a controlled displacement u and measured load P and with the principal directions represented by x_1 and x_2.

4.3.1 Specimen Compliance and Stress Intensity Factor

The dependence of the dimensionless compliance $\bar{C}$ with respect to $\bar{a}$, λ and ρ can be approximated by a function of the form:

$$\bar{C}\left(\bar{a}, \lambda, \rho\right) = q(\bar{a}, \lambda, \rho) \cdot \lambda^{B} \cdot (1 + 0.22698 \cdot \rho)^{0.53527} \cdot \left(\frac{1+\bar{a}}{1-\bar{a}}\right)^{2} \tag{4.10}$$

where $q(\bar{a}, \lambda, \rho)$ is a fourth order polynomial of $\bar{a}$, in which its coefficients depend on λ and ρ, and B is a polynomial that depends on the normalized crack length $\bar{a}$ and ρ. The coefficients can be found in Appendix A. Note that Eq. 4.10 is dimensionless and can be used for any specimen size W as long as the CT geometry of Fig. 4.2 is respected.

The $\bar{K_I}$ interpolating function is defined:

$$\bar{K_I}\left(\bar{a},\lambda,\rho\right) = p(\bar{a},\lambda,\rho)\cdot\lambda^{D}\cdot\left(1+0.006689\cdot\rho\right)^{0.47151}\cdot\frac{2\left(2+\bar{a}\right)}{\left(1-\bar{a}\right)^{3/2}}\cdot\frac{1}{\sqrt{\bar{a}}}\cdot\left(\frac{2\lambda^{3/2}}{1+\rho}\right)^{1/4} \tag{4.11}$$

where $p(\bar{a},\lambda,\rho)$ is a fourth order polynomial of $\bar{a}$, with coefficients that depend on λ and ρ, and D is a polynomial dependent on the normalized crack length $\bar{a}$ and ρ. The coefficients are also found in Appendix A. Again, Eq. 4.11 is applicable to any specimen size W.

4.3.2 Undesired failure modes: back-end compression failure and excessive bearing at the holes

Some undesired failure mechanisms may appear when testing a CT specimen, preventing the experiment from being performed properly. Such failure modes include failure under compression at the back end of the specimen or at the pin holes due the bearing load. In this section, we present a proposal of failure criteria which take into account the orthotropy of the material, the specimen size W and the initial crack length a_0.

The first contemplated failure mode considers the compressive stresses at the back end of the Compact Tension specimen. These compressive stresses usually appear while the fracture test is carried out, and tend to increase as the crack grows. This may cause the specimen to collapse under compression at the back end before it has been completely split (Laffan et al., 2010b). For some composite materials this failure can occur in the form of ply delamination. Such phenomena have also been observed in some tougher materials with large initiation or propagation loads and also in low compression strength materials. The failure criterion considering the back end compression (f_{BE}) can be expressed as:

$$\frac{\sigma_{uC}\sqrt{W}}{K_{Ic}} > f_{BE} \tag{4.12}$$

where σ_{uC} is the ultimate compressive stress of the laminate, obtained as $f_{BE} = r\left(\bar{a}, \lambda, \rho\right)/\sqrt{\bar{a}}$, and where $r(\bar{a}, \lambda, \rho)$ is the dimensionless back end compression stress function. This stress-based failure criterion predicts the initiation of the material failure at the back face of the specimen. For some materials, the failure may be controlled by a stable process due the formation of a Fracture Process Zone. When dealing with composite materials, the back end failure normally appears in the form of a kink-band. Hence, the failure criterion expressed in Eq. 4.12 is a conservative prediction of the failure. It should be mentioned that, in order to use this type of failure criteria, the material toughness K_{Ic} must be known beforehand. To overcome this problem, it is possible to simply use an approximate expected fracture toughness of the specimen being tested. The dimensionless back end stress $r(\bar{a}, \lambda, \rho)$ was obtained by fitting the results of the FEM models for a wide range of material orthotropies with the least-squares method. The function is defined as a fourth order polynomial of $\bar{a}$, with coefficients that depend on λ and ρ.

The second undesired failure mode is failure under compression at the load-bearing holes of the specimen. When the crack length is very small, the bearing load required to propagate the crack may be so high that it causes the collapse under compression in the area surrounding the loading holes. The stress at the hole due to the bearing pin can be defined as:

$$\sigma_{bearing} = \frac{P}{hd} < \alpha\sigma_{uC} \tag{4.13}$$

where d is the hole diameter and α is a parameter that depends on the stress distribution between the pin and the hole. The value of α is normally considered to be equal to 1 or $4/\pi$. The standard procedure recommends a hole diameter of $d = 0.25W$. Hence, the diameter can be defined as $d = w/n$ (with $n = 4$ in the standard recommendations). The failure criterion taking into account the bearing load ($f_{bearing}$) is then defined as:

$$\frac{\sigma_{uC}\sqrt{w}}{K_{Ic}} > f_{bearing} \tag{4.14}$$

where:

$$f_{bearing} = \frac{n}{\alpha\bar{K}_{Ic}\sqrt{\bar{a}}} \tag{4.15}$$

5

Non Linear Fracture Mechanics: Fracture Process Zone and Cohesive Law

5.1 Literature Review: Fracture Process Zone, $\mathcal{R}$-curve and the Cohesive Law

During crack nucleation and crack growth in a continuum solid, most materials develop a relatively large Fracture Process Zone (FPZ) where energy is dissipated. Fig. 5.1 schematically describes the FPZ present between the traction free crack (between points a and b) and the elastic solid (beyond point d). This area is divided in two regions based on the nature of the dissipation mechanisms. The first region (bounded by points c and d) is located ahead of the crack tip, where non-linear material hardening takes place. Also known as intrinsic dissipation, it is typical of metals and other ductile materials. The second region (bounded by b and c) is located behind the crack tip, where material softening or extrinsic dissipation occurs. The latter region is typical of quasi-brittle materials, such as concrete, composite materials and advanced ceramics (Ritchie, 2011). Depending on the relative sizes of these two zones and of the structure, one may distinguish between ductile behaviour (intrinsic dissipation is dominant), quasi-brittle behavior (extrinsic dissipation is dominant) or brittle fracture (the FPZ is very small compared to the structure size). The present work focuses on quasi-brittle materials.

Linear Elastic Fracture Mechanics (LEFM) considers that the entire FPZ (bounded by the points b and d in Fig. 5.1) lies at a single point at the crack tip while the rest of the solid behaves elastically, i.e., considers a brittle fracture. In reality this zone must have some finite size. Irwin estimated the FPZ length (ℓ_{FPZ}) using the

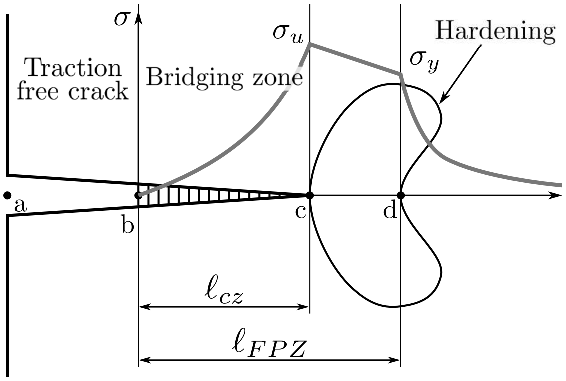

Fig. 5.1.: Representation of the Failure Process Zone.

elastic stress distribution around the crack tip, by assuming that the ℓ_{FPZ} is equal to the zone over which the tensile strength has been exceeded (Irwin, 1960). Irwin also introduced the term equivalent crack length: a fictitious increase of the crack in order to maintain the force balance when assuming the new stress distribution inside the FPZ.

A common practice is to take into account the non-linearities that take place at the crack tip while the FPZ is being developed by using LEFM in conjunction with an $\mathcal{R}$-curve that defines the apparent increase of fracture toughness as the crack grows. Instead of using a LEFM fracture criterion $G = G_{Ic}$, the crack growth condition is computed with a variable toughness provided by the $\mathcal{R}$-curve. This methodology is widely used to predict the crack growth of quasi-brittle materials, although its application range is unclear, and will be latter addressed in the thesis.

An alternative approach to describe the Fracture Process Zone formation is through the use of the cohesive model. In this framework, the FPZ is initialized as soon as a point of the specimen reaches a stress equal to the material ultimate strength σ_u, where a fictitious crack starts to develop, still capable of transferring stresses between its surfaces. This tension-softening phenomenon is represented in Fig. 5.2a. The relationship between these closure or cohesive stresses and the crack openings is known as the Cohesive Law (CL) of the material. A typical CL shape

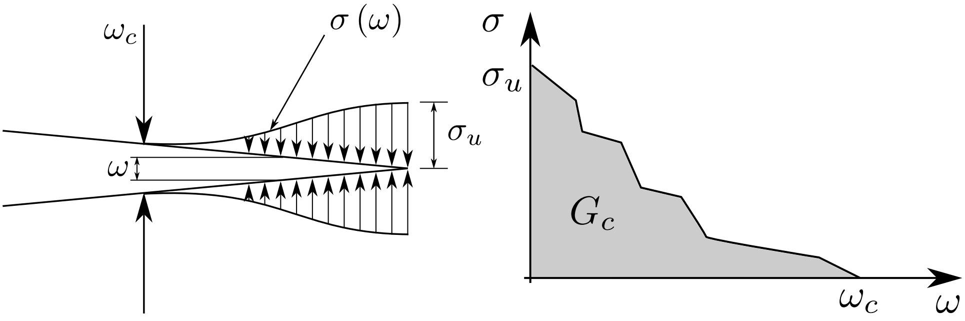

(a) **(b)**

Fig. 5.2.: (a) Tension-softening inside the Fracture Process Zone. (b) Typical Cohesive Law on the material.

is illustrated in Fig. 5.2b. The FPZ is still formed as the crack is opened, until the crack opening measured at the beginning of the FPZ a_0 reaches a critical value ω_c. At this precise instant the crack growth enters a steady state, i.e., it dissipates a constant fracture energy Gc, while the FPZ moves along the crack path. During the steady state growth the cohesive crack opening profile and cohesive stress profile remain almost constant. This methodology goes back to the Dugdale's strip yield model (Dugdale, 1960), who introduced a constant stress inside the FPZ, and Barenblatt (Barenblatt, 1962), who introduced a stress function with respect to the crack opening, and those implemented later with finite elements by Hillerborg by using cohesive elements (Hillerborg et al., 1976) and Bažant in a smeared way (Bažant and Oh, 1983). It should be mentioned that Dugdale's strip yield model was developed for perfect plasticity, although, in fact, the model is more suitable for quasi-brittle fracture: the energy dissipation is confined in a plane (bridging stresses) instead of taking up a volume (material hardening). The use of the CL accounts for the extrinsic energy dissipation mechanisms typical of quasi-brittle materials, by introducing a relationship between bridging stresses and the crack opening.

This chapter is structured as follows: Section 5.2 proposes a new methodology to solve the FPZ formation while taking into account the cohesive stresses and the CL shape; Section 5.3 describes an algorithm capable of solving the Inverse problem in order to experimentally measure the CL from a fracture test; lastly, Section 5.4

presents a discussion on the Cohesive Model itself and the incompatibility with $\mathcal{R}$-curve based fracture mechanics.

5.2 Direct method: Dugdale's condition

As seen in the Literature Review, most methodologies to obtain the CL of a material involve sophisticated experimental setups to measure the required variables (Digital Image Correlation to measure the displacement field, inclinometers to measure rotation angles, ...). On the contrary, inverse problem approaches only need to monitor easy-to-record variables, such as the applied load and the displacement. However, they also need a quick enough tool to virtually reproduce the test for any assumed CL shape, i.e., a tool capable of solving the direct method. The approach to solve the direct method used in this thesis is described below.

A standard CT specimen of size W, shown in Fig. 4.2, is subjected to the action of a controlled displacement (u) and corresponding load (P) applied at the pin holes. The analytic solution is capable of predicting the FPZ development as a crack grows in pure mode-I along the symmetry plane. The starting point of the problem solution comes from the Dugdale's condition, i.e., the global Stress Intensity Factor (SIF) of the problem, K, must be null (Dugdale, 1960; Barenblatt, 1959; Barenblatt, 1962):

$$K = K^P + K^{\sigma_c} = 0 \tag{5.1}$$

where K^P is the SIF caused by the point load P and K^{σ_c} is the SIF caused by the whole cohesive stress profile σ_c. Although the σ_c is unknown and may change during the FPZ development, it can be discretized as a series of small constant stresses of value equal to σ_i applied at the crack surface. The non-linear problem expressed as a superposition of linear problems is shown in Fig. 5.3.

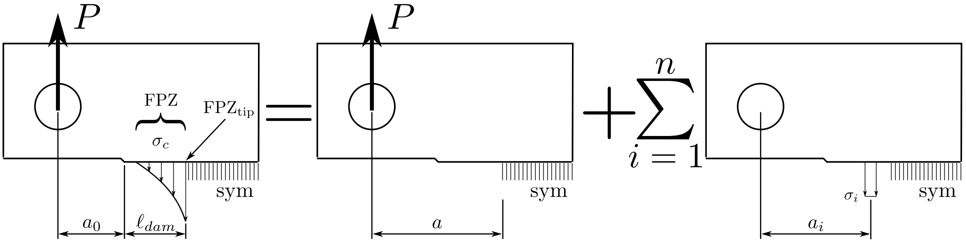

Fig. 5.3.: Compact Tension (CT) specimen with a FPZ expressed as a superposition of linear problems.

In order to solve the cohesive stress profile inside the FPZ, the crack opening profile must also be found. It is possible to express the set of openings ω_i as a superposition of the openings caused by each acting load

$$\omega_i = \omega_i^P + \omega_i^{\sigma_c} \tag{5.2}$$

where ω_i, ω_i^P and $\omega_i^{\sigma_c}$ are the total crack opening, the crack opening caused by the point load P and the crack openings caused by the cohesive stress profile σ_c, respectively.

Eq. 5.2 is solved from an iterative process for a given CL. As a result, the stress profile and the crack openings at the FPZ are obtained. Lastly, the load P is obtained by means of Eq. 5.1, and the displacement u is determined as the crack opening measured at $a_i = 0$, using again Eq. 5.2.

The detailed solutions to Eq. 5.1 and Eq. 5.2 can be found in PAPER B. However, some features of the model are worth mentioning. The solution to the direct method allows to determine the load, the displacement, the FPZ length, the crack opening profile and the cohesive stress profile during the whole crack growth and propagation. The resulting system of equations obtained from applying Eq. 5.1 and Eq. 5.2 can be expressed as a system of non-linear algebraic equations. These have been implemented in a Matlab® script, solving the problem in about 1 second of computational time, using a Desktop computer with an Intel i5 processor running at 3.2 Ghz.

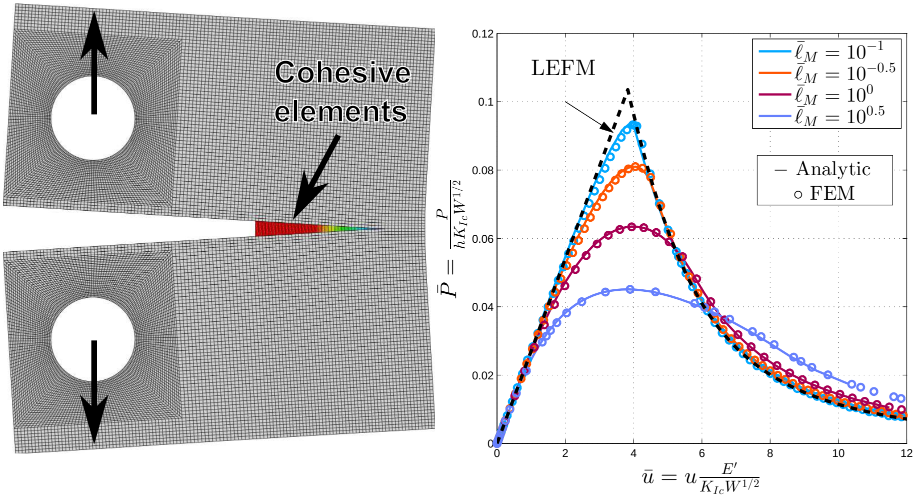

(a) **(b)**

Fig. 5.4.: (a) Finite Element model of a Compact Tension specimen, using cohesive elements to model the Fracture Process Zone. (b) Comparison of the displacement (u) and load (P) curves obtained with the author's methodology and using a Finite Element model.

Any obtained output associated with the problem can be expressed as

$$\chi(\bar{u}, \bar{\ell}_M, CL, SG, MP) \tag{5.3}$$

where $\bar{u} = u\dfrac{E'}{K_{Ic}W^{1/2}}$ is the normalized displacement, CL is the Cohesive Law shape, SG is the Specimen Geometry, and MP are the non-dimensional variables associated with the material anisotropy λ and ρ, with the principal directions aligned with the crack, introduced in Section 4.2. Following the same approach, the load can be normalized as $\bar{P} = \dfrac{P}{hK_{Ic}W^{1/2}}$.The variable $\bar{\ell}_M$ is the normalized characteristic length defined as:

$$\bar{\ell}_M = \frac{\ell_M}{W} \quad \text{where} \quad \ell_M = \frac{G_{Ic}E'}{\sigma_u^2} \tag{5.4}$$

This normalized characteristic length indicates how relevant are the material non-linearities with respect to the specimen size.

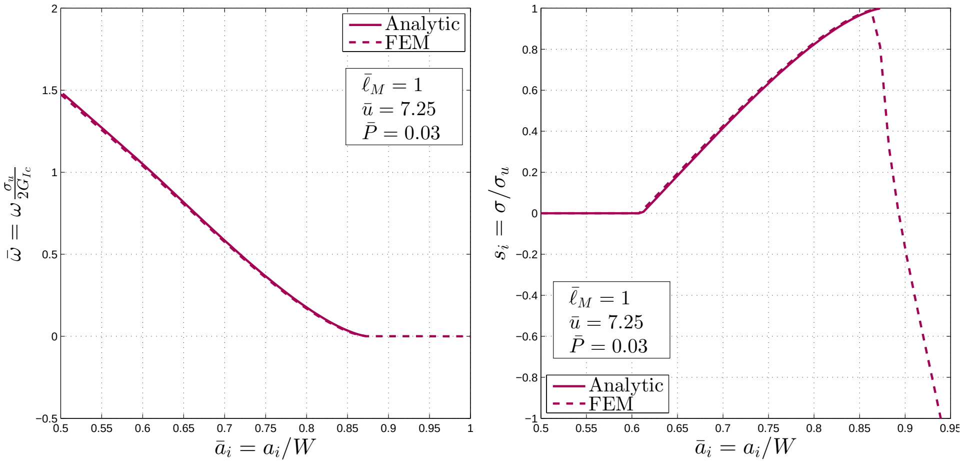

(a) **(b)**

Fig. 5.5.: Comparison of the normalized (a) cohesive crack openings and (b) cohesive stresses inside the FPZ obtained with the author's proposed methodology and with a Finite Element model, for a Compact Tension specimen with a normalized characteristic length of $\bar{\ell}_M = 1$.

In order to validate the proposed methodology, a Finite Element model has been created using Python scripting together with ABAQUS/Standard 6.11-1 FEM software. The 4-node plane stress elements with reduced integration (CPS4R) were used to mesh the model. The FPZ has been modelled by placing Cohesive Elements along the symmetry plane of the specimen (Turon et al., 2006), as seen in Fig. 5.4a, assuming a linear CL shape. A comparison of the displacement and load outputs obtained by both the FE model and the proposed author's methodology is found in Fig. 5.4b, for several normalized material characteristic lengths $\bar{\ell}_M$. As it can be seen in the Figure, the response for small $\bar{\ell}_M$ (large specimen size W) tends to the LEFM particular solution, marked with dashed lines.

Additionally, Fig. 5.5 contains a comparison of the normalized cohesive crack openings and cohesive stresses inside the FPZ for both the FE outputs and the proposed direct method. As it can be appreciated, both solutions are in good agreement, hence validating the authors proposed methodology satisfactorily.

5.3 Inverse problem

Once the algorithm to solve the direct method has been validated, it is time to continue with the solution to the inverse problem. The inverse problem, i.e., the determination of the Cohesive Law shape from a fracture test, is solved in three steps: first, a u-P curve is obtained from an experimental test; second, a computer simulation of the test must be carried out in order to find the parameters that define the Cohesive Law; lastly, it is necessary to perform a minimization of a suitable norm which quantifies the discrepancy between experimental data and the corresponding values provided by the computer simulation, with respect to the mentioned parameters. In the present work, the computer simulation is performed by using the author's proposed methodology to solve the direct method (Ortega et al., 2016).

The understanding of the FPZ formation within a cohesive crack model is needed in the development of the inverse method presented in this paper. The FPZ is initialized as soon as a point of the specimen reaches a stress equal to the material strength. Once the σ_u is reached, the FPZ grows as the displacement is increased, opening the cohesive crack and changing the cohesive stress profile in relation with the laminate CL. When the crack opening at $a = a_0$ reaches the critical opening ω_c, the FPZ ends its development. At this precise point the crack growth enters a steady state, meaning that it dissipates a constant energy G_c, while the FPZ moves along the crack path. During this steady state growth the cohesive crack opening profile and cohesive stress profile remain almost constant.

Since the peak load is reached while the FPZ is still being formed, the analysis of the cohesive stresses inside the FPZ along the crack growth is of great interest in predicting the nominal strength of structures. Fig. 5.6 gives some more accurate insight, as it depicts the progress of the FPZ growth, and its relation with the CL. Given the Point 1 of the P-u curve, the cohesive stresses range from σ_u at the FPZ tip (next to the undamaged material), where the crack opening is $\omega = 0$, to $\sigma = \sigma_1$ at a crack opening ω_1 measured at the end of the FPZ (next to the traction free crack), i.e., at a distance a_0 measured from the load line. In other words, to describe the crack growth and the FPZ development until the Point 1, only a part of

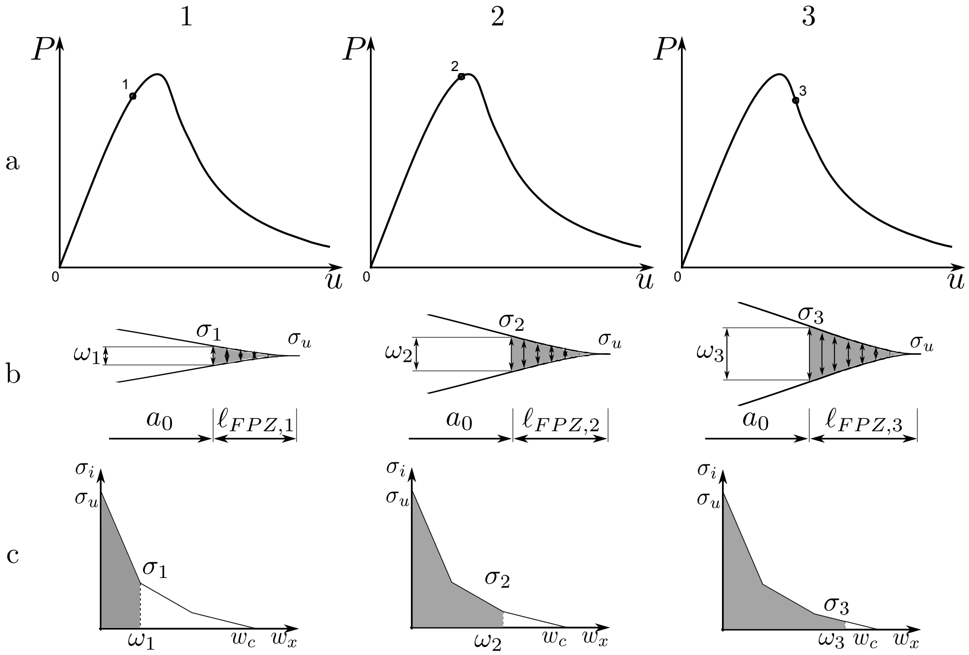

Fig. 5.6.: Depiction of three states (1-3) during the FPZ growth: (a) the P-u position, (b) the FPZ stress and crack openings and (c) the dissipated energy inside the CL. The cracks openings ω_1, ω_2 and ω_3 are measured at the initial crack position a_0.

the CL needs to be known, i.e, the CL shape beyond the point ω_1-σ_1 is not needed. Observing Point 2, now the cohesive crack opening increases to ω_2 and the cohesive stress decreases to σ_2. In this case, to define the crack growth and the FPZ, the CL must be known up to ω_2-σ_2. The same can be applied to Point 3, and to every displacement increase. If all the cohesive model variables are known during the crack growth, each point of the P-u curve has a unique corresponding FPZ state, with the cohesive stresses defined between $0 \leq \omega \leq \omega_i$, where ω_i is the Crack Tip Opening Displacement (CTOD). In other words, every infinitesimal FPZ development increase needs an additional infinitesimal portion of the CL. This property allows to define a piecewise CL by fitting consecutive points in the P-u curve.

The inverse method takes advantage of the progressive FPZ development process, being able to determine the CL from a single CT fracture test, that is, there is no need to test other SG or sizes. An algorithm is proposed in order to solve the inverse problem, with the following strategy: first, some points from the experimental u-P curve are selected around the peak load, while the FPZ is still being developed, that will be used to fit the curve. The algorithm is initialized by defining a Cohesive Law with a single linear branch. The first branch of the CL is found by modifying its slope until the predicted load at the first selected point matches the experimental value. When the slope is found, the width of the first branch is found by determining the cohesive crack opening at the initial crack tip a_0 at the given displacement. The algorithm continues by adding as many branches as number of experimental points are going to be fitted, consecutively finding an additional linear branch of the CL.

As an example of the usability of this method, the CL has been measured using the proposed approach to solve the inverse problem. A Compact Tension specimen of size $W = 51$ mm and with an initial crack length of $a_0 = 26$ mm has been tested. The used material is an hybrid laminate made of woven Carbon fabric (C) and woven Glass fabric (G) with a stacking sequence $[(0^C/45^C)_2/0^G/60^G/-60^G]$ (laminate L02 of Chapter 6). Fig. 5.7a shows the u-P curves of two specimens and the corresponding smoothed average. For the sake of ensuring the objectivity of this method, the CL has been measured three times for the same laminate, each time fitting a different set of points. Concretely, the CL has been obtained by fitting six (□), eight ($\triangledown$) and nine ($\times$) points from the smooth average curve. Each set is observed in Fig. 5.7a. The measured CL for each set is shown in Fig. 5.7b. As it can be seen, for the tested laminates, the general shape of the CL remains unchanged regardless the used set of points. Additionally, the total fracture energy G_{Ic} measured from each CL is 105.0 N/mm, 103.8 N/mm and 105.0 N/mm respectively, providing more evidence of the objectivity of the proposed approach to solve the inverse problem, at least, for the shown specimen.

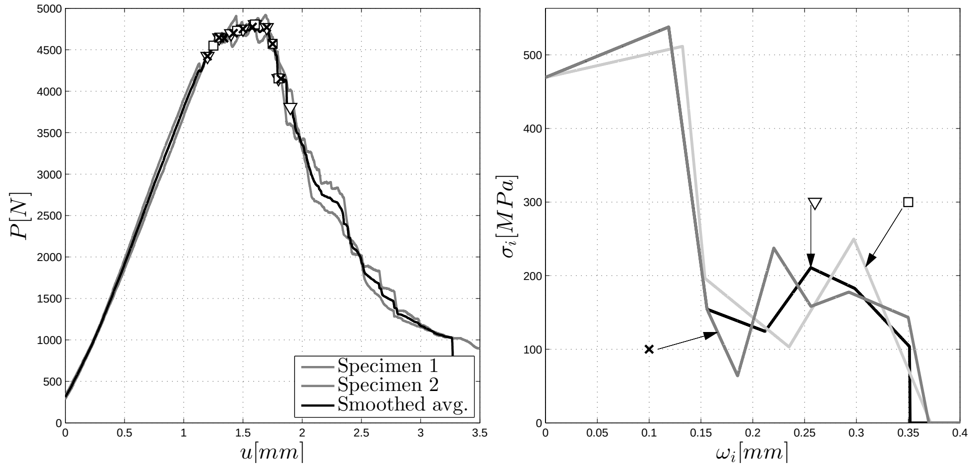

(a) **(b)**

Fig. 5.7.: P-u curve for the two hybrid specimens and the corresponding smoothed average curve. (b) Three different CL obtained from three different sets of points.

5.4 Discussion

An extensive discussion of the applicability of the Cohesive Zone Modelling and the incompatibility with LEFM based theories can be found in PAPER C, although a brief summary of discussion is hereby exposed. When dealing with quasi-brittle materials in the presence of large-scale bridging (LSB), the stress field differs greatly form the LEFM one, as the FPZ takes a considerably large portion of the specimen. Under this scenario, the Energy Release Rate (ERR) is not well defined assuming LEFM. Additional problems also appear when trying to measure the crack length a. Typically, in LEFM, the crack tip is defined as a sharp through-the-thickness edge perpendicular to the crack growth direction. In reality, even for brittle materials, the crack tip profile is not straight, and its shape usually depends on the specimen thickness. Additionally, taking the cohesive model as background, the crack tip location is not well-defined, since there is no clear transition between the bulk material and the free-edge crack, because of the presence of the FPZ.

Therefore, the use of $\mathcal{R}$-curve to predict the crack growth should only be applied under small-scale bridging (SSB) conditions for quasi-brittle materials or under small-scale yielding (SSY) for ductile materials, i.e., when the ℓ_{FPZ} is small compared to other problem dimensions, particularly when compared to the crack length. This limitation is obvious for laboratory sized specimens (Bažant, 1992), and becomes especially true for some natural materials such as human bone (Yan et al., 2007; Koester et al., 2008a) or human dentin (Koester et al., 2008b), whose natural size limits the specimen dimensions. This restriction is also present in some newly developed materials such as metallic-glasses and bio-inspired ceramics (Bloyer et al., 1998; Bouville et al., 2014; Demetriou et al., 2011) where the specimen size is limited by the manufacturing processes. Furthermore, the methodologies to predict the structural strength based on the $\mathcal{R}$-curve are only applicable for notched specimens, as they are not able to predict crack nucleation on smoothed surfaces.From a cohesive model point of view, the apparent increase of the fracture toughness of the material descried by the $\mathcal{R}$-curve can be understood as the formation and propagation of the FPZ (Suo et al., 1992; Jacobsen and Sørensen, 2001). The increase of G_{Ic} takes place while the FPZ is growing. During this process, the cohesive zone is being developed with the cohesive stresses and crack openings being related by the CL. As a consequence, the Cohesive Law shape plays an important role on the $\mathcal{R}$-curve output. Additionally, the FPZ formation and its development are also influenced by the loading conditions and the Specimen Geometry, hence resulting in very diverse $\mathcal{R}$-curves depending on those variables. For theses reasons, the $\mathcal{R}$-curve should not be considered a material property (Bao and Suo, 1992; Suo et al., 1992; Sørensen et al., 2008a; Sørensen and Jacobsen, 1998).

Some $\mathcal{R}$-curves have been obtained in order to illustrate the specimen size ($\bar{\ell}_M$) and CL dependence. To obtain the curves, the output variables u and P have been obtained for a CT specimen with a linear CL for $\bar{\ell}_M = 0.05$, 0.5 and 1, using the analytic cohesive model defined in Section 5.2. First, the compliance obtained from the direct method is equalled to the elastic compliance of a Compact Tension specimen (Bažant and Planas, 1998), in order to infer the equivalent crack length a_{eq}. Then, the fracture toughness is obtained from the LEFM definition of the stress intensity factor K_I^P, found in (Bažant and Planas, 1998).

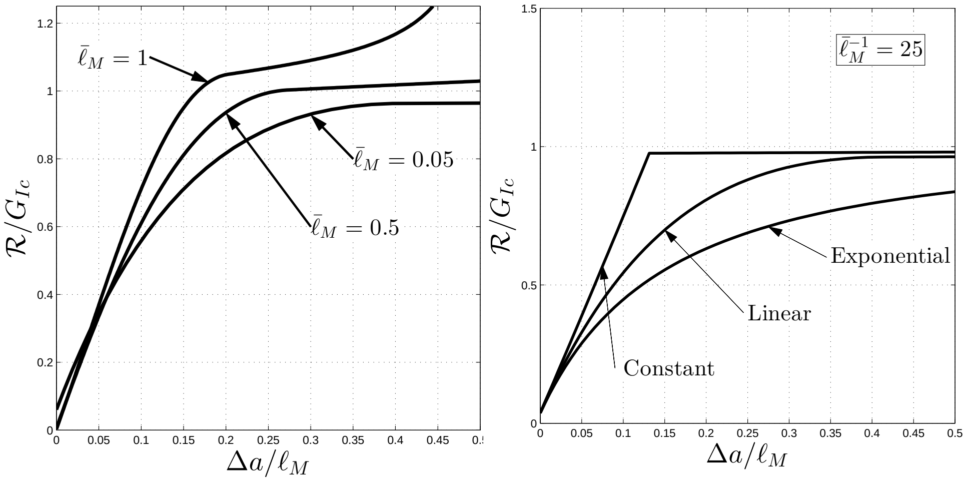

(a) **(b)**

Fig. 5.8.: (a) Three $\mathcal{R}$-$\Delta a_{eq}/\ell_M$ curves with a linear CL for $\bar{\ell}_M = 0.05$, 0.5 and 1. (b) Three $\mathcal{R}$-curves with a linear, constant and exponential CL and with $\bar{\ell}_M = 0.04$.

The curves of Fig. 5.8a have been obtained for a linear CL. As it can be appreciated, the measured $\mathcal{R}$ is heavily dependent on the $\bar{\ell}_M$, obtaining more distorted outputs as the material non-linearities become more relevant. To be able to discern when large-scale bridging and small-scale bridging assumptions can be made, an additional plot has been obtained, observed in Fig. 5.9. In this case the propagation values of $\mathcal{R}$, i.e. the maximum value $\mathcal{R}_{\text{max}}$, has been obtained for several $\bar{\ell}_M$ values. As it can be observed in Fig. 5.9, the $\bar{\ell}_M$ values for which the assumption of SSB is correct (and therefore LEFM is applicable) are influenced by the CL shape. When comparing the self-similar crack growth for a constant CL against a linear CL, the former exhibits a shorter FPZ length. Therefore, the assumption of SSB will be possible for small values of $\bar{\ell}_M$ (larger specimens). In general, the longer the tail of the CL shape is, the longer the fully developed FPZ length will be. On the other hand, as $\bar{\ell}_M$ increases, the $\mathcal{R}$ value becomes distorted when LEFM assumptions are made, as seen in the left region of Fig. 5.9.

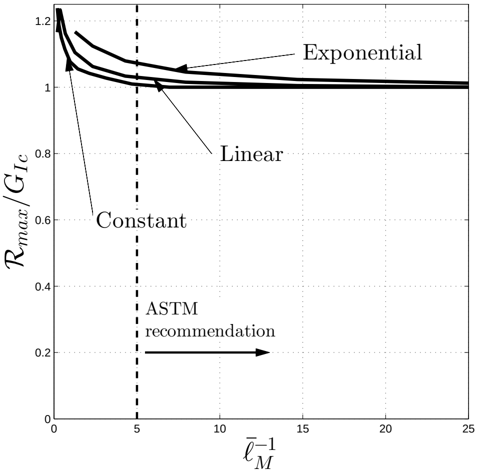

Fig. 5.9.: Propagation values of $\mathcal{R}$ for several values of $\bar{\ell}_M$.

Specifically, the standard procedure for the determination of the fracture toughness of metallic materials ASTM E399 (ASTM, 1997) and of plastic materials ASTM D5045 (ASTM, 1999) states that the procedure to determine the $\mathcal{R}$ can only be applied for $\bar{\ell}_M < 0.4\,(1 - \bar{a}_0)$, then for the CT specimen presented $\bar{\ell}_M^{-1} > 5$. As it can be seen in Fig. 5.9, for large enough specimens, it is correct to assume SSB, resulting in an $\mathcal{R}$-curve that is not size dependant. Fig. 5.8b shows three $\mathcal{R}$-curves for a linear, constant and exponential CL, for $\bar{\ell}_M^{-1} = 25$, in which case SSB can be assumed. In conclusion, it has been shown that the $\mathcal{R}$-curve is a property incompatible with the Cohesive Law. This disagreement is mainly caused by the use of LEFM assumptions in the $\mathcal{R}$-curve definition.

Part III

The Cohesive Law as a material property

6

Translaminar Cohesive Law of interply hybrid laminates

The use of hybrid materials is of high interest for the materials science research field as well for industrial applications. These kind of composites may benefit from advantages of each separate material, e.g, improving the damage tolerance, delaying some failure mechanism or even decreasing the total economic cost by using inexpensive materials. This Section studies the translaminar Cohesive Law of several interply hybrid laminates, and how the stacking sequence and ply material can influence the total laminate traction-separation law. The studied interply hybrid laminates have been obtained by combining two materials of a total set of three type of plies: Unidirectional Carbon (UC) tape, woven Carbon fabric (C) and woven Glass fabric (G). For each combination of two materials several stacking sequences have been studied. Concretely, how the location of certain plies can modify the overall translaminar Cohesive Law.

6.1 Materials and laminates

The three composite materials that have been tested in the experimental campaign are the same ones defined in the work of González et al. (González et al., 2014), where one is unidirectional carbon tape and the other two are woven fabrics. The three materials have been supplied by Hexcel®. The fabric materials use HexFlow® RTM 6 mono-component epoxy system. All composites have been supplied with epoxy binders on both sides (with the binder representing about 5% of the total fabric weight). The woven fabrics plies are Carbon (C) fabric type G0926 (5HS, 6K, 370 gsm), and Glass (G) fabric type S2 (style 6781, Z-6040, 303 gsm), while the UC is type G1157 (UD, 6 K, 270 gsm). The elastic properties of each lamina are found in Table 6.1. The ply thickness of each material C, G and UC are 0.353 mm,

Tab. 6.1.: Ply properties of each composite material, where C is woven carbon fabric, G is woven glass fabric and UC is unidirectional carbon tape.

Material	E_1 (GPa)	E_2 (GPa)	G_{12} (GPa)	ν_{12}	σ_u (MPa)
C	59.54	54.95	5.21	0.03	804.1
G	19.65	19.24	3.93	0.09	557.8
UC	116.73	8.31	4.67	0.26	1477.1

0.229 mm and 0.247 mm, respectively. The thickness has been obtained from an average of 6 measurements of cured non-hybrid laminates.

The interply hybrid laminates have been divided in three sets by combining two different materials per laminate: C-G, C-UC and G-UC. The translaminar CL has been obtained from a CT specimen subjected to a controlled displacement and corresponding load again using the methodology proposed in Section 5.3. The stacking sequences are summarized in Table 6.2, with the fibre direction of 0° aligned with the loading direction, shown in Fig. 4.2. In order being able to compare the laminates of each set, the ply stacking sequences have been chosen to be symmetric, balanced and in-plane quasi-isotropic. The number of plies of each material has also been kept constant. As a result, the resultant in-plane stiffness are constant among each set, although the bending stiffness may vary from laminate to laminate. The C-G laminates are made of $n = 14$ plies, with a cured laminate thickness h of 4.31 mm. In the case of the C-UC laminates $n = 14$ and $h = 4.22$ mm, whereas for the G-UC, $n = 18$ and $h = 4.22$ mm.

6.2 Results and discussion

The measured CL for the laminate L04 is shown in Fig. 6.1. Observing the shape of traction-separation law, it can be appreciated that, for small crack openings (about $\omega \approx 0.15$), the FPZ still has a relatively high capacity of transferring stresses. The measured CL also features a long tail that transfers low stress levels at larger

Tab. 6.2.: Hybrid laminates stacking sequences, where C is woven carbon fabric, G is woven glass fabric and UC is unidirectional carbon tape. The 0° direction is aligned with the loading direction.

Materials	Laminates
C-G	L01: $[0^{\text{G}}/60^{\text{G}}/-60^{\text{G}}/(0^{\text{C}}/45^{\text{C}})_2]_{\text{S}}$ L02: $[(0^{\text{C}}/45^{\text{C}})_2/0^{\text{G}}/60^{\text{G}}/-60^{\text{G}}]_{\text{S}}$ L03: $[0^{\text{G}}/(45^{\text{C}}/0^{\text{C}})_2/60^{\text{G}}/-60^{\text{G}}]_{\text{S}}$
C-UC	L04: $[90^{\text{UC}}/-30^{\text{UC}}/30^{\text{UC}}/(0^{\text{C}}/45^{\text{C}})_2]_{\text{S}}$ L05: $[(0^{\text{C}}/45^{\text{C}})_2/90^{\text{UC}}/-30^{\text{UC}}/30^{\text{UC}}]_{\text{S}}$
G-UC	L06: $[90^{\text{UC}}/-45^{\text{UC}}/0^{\text{UC}}/45^{\text{UC}}/(0^{\text{G}}/45^{\text{G}})_2/0^{\text{G}}]_{\text{S}}$ L07: $[(0^{\text{G}}/45^{\text{G}})_2/0^{\text{G}}/-45^{\text{UC}}/90^{\text{UC}}/45^{\text{UC}}/0^{\text{UC}}]_{\text{S}}$ L08: $[90^{\text{UC}}/-45^{\text{UC}}/0^{\text{G}}/45^{\text{G}}/0^{\text{UC}}/45^{\text{UC}}/0^{\text{G}}/45^{\text{G}}/0^{\text{G}}]_{\text{S}}$ L09: $[0^{\text{G}}/45^{\text{G}}/0^{\text{G}}/0^{\text{UC}}/45^{\text{UC}}/0^{\text{G}}/45^{\text{G}}/90^{\text{UC}}/-45^{\text{UC}}]_{\text{S}}$

crack openings. Although not included in this document, the rest of the measured laminates all present a similar softening-law shapes. In order to objectively compare the CL features of each laminate, a simplified cohesive law has been proposed, capable of reproducing the behaviour described above: the transfer of high stresses at low crack openings and low stress levels for large crack openings. The simplified CL consists of a linear branch defined by σ_u and G_1, a sudden drop of stresses located at ω_1, and a second linear branch defined by σ_1 and $G_c - G_1$. This simplified shape is also shown in Fig. 6.1. The total energy fracture G_c and the critical crack opening ω_c are maintained from the experimentally measured CL. Hence, only 4 out of the 6 parameters need to be found in order to completely define the simplified CL (σ_u, σ_1, ω_1, and G_1). These have been obtained by means of a least square fitting. Table 6.3 showcases the best fitted parameters for each laminate. Having the translaminar CL expressed in this manner, it is possible to objectively compare each laminate, and also analyse how the material used at the ply level modifies the overall laminate behaviour.

Observing the laminates made of Carbon fabric and Glass fabric (C-G), the position of each material has no effect on the onset fracture energy G_1, although the propagation fracture energy G_c values are slightly increased when the Carbon

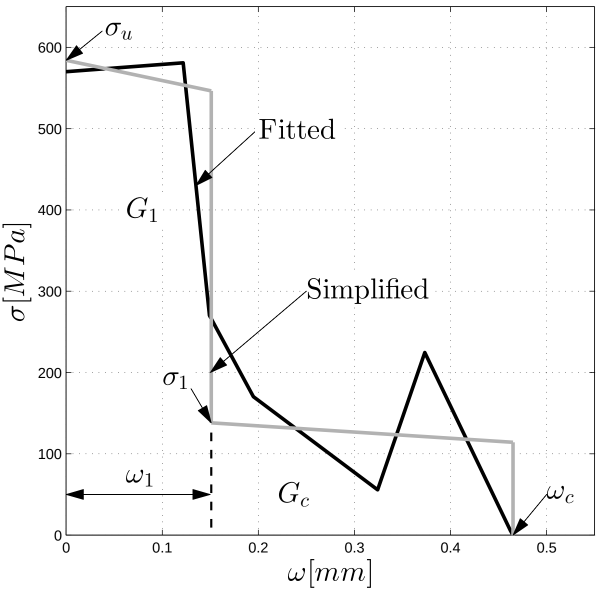

Fig. 6.1.: Measured Cohesive Law and proposed simplified shape for the Laminate L04.

fabric plies are located in the outer faces of the laminate. Moving to the Carbon fabric and Unidirectional Carbon tape laminates (C-UC), placing the UC plies in the outer faces increases the G_c about a 15 $\%$, while placing them in the middle increases G_1 a 15 $\%$. The third group of laminates are the ones made with the most contrasting materials: Glass fabric and unidirectional Carbon tape (G-UC). In this case, the effects of the material position on the fracture energy are more evident than in the previous studied laminates. One laminate stands out with respect to the other three, the L07. Observing closely the stacking sequences of both L06 and L07, it can be appreciated that both have the same layup, but with the plies of G and UC with switched positions. The stacking sequence of L07 has a ply clustering in the 0° in the center of the laminate, resulting in outstanding performance, mainly caused be two phenomena. First, it is known that the fiber pull-out contributes to the laminate energy dissipation, being a desired failure mode when a translaminar crack is present. It is also known that thicker plies cause the fiber pull-out length to be increased, hence dissipating more energy (Laffan et al., 2010b), as is in the

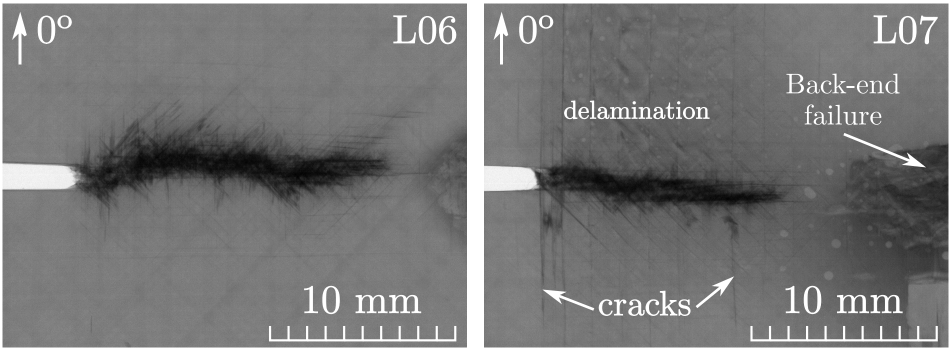

(a)

(b)

Fig. 6.2.: X-ray of the laminates L06 and L07 for the CT specimens. Several matrix cracks can be observed in the laminate L07.

case of L07. The second damage mechanism phenomenon is the appearance of larger amounts of matrix cracks and delaminations in the presence of thicker plies (Li et al., 2009). Fig. 6.2 shows the X-ray image of both laminates L06 and L07. In the case of L07, the damage zone is characterized by having larger matrix cracks and larger delaminations which are not present in the case of L06. These matrix cracks have two impacts during the damage process: first the matrix crack growth itself, which adds to the laminate fracture energy, although its contribution may be negligible compared to other fracture mechanisms such as fiber pull-out (Cooper and Kelly, 1970). Secondly, the presence of numerous matrix cracks in the laminate may cause a crack blunting effect, which leads to a reduction of the energy release rate of the specimen. It should be pointed out that the Cohesive Laws have been obtained assuming that all the dissipation mechanisms are confined in the fracture plane. This hypothesis does not hold true for the laminate L07, where these matrix cracks and delaminations take place far from the fracture plane. Hence, the results for this case should be considered only qualitatively.

Moving to laminates L08 and L09, the same phenomena can be observed. Both laminates have the same stacking sequence but with the plies of G and UC with switched positions. In this case the discrepancy of energy is not as remarkable as

Tab. 6.3.: Simplified Cohesive Law parameters for each laminate.

Material	Laminate	G_c [N/mm]	G_1 [N/mm]	ω_1 [mm]	ω_c [mm]
C-G	L01	98	70	0.17	0.57
	L02	106	70	0.17	0.37
	L03	98	72	0.15	0.53
C-UC	L04	123	87	0.15	0.49
	L05	111	99	0.17	0.45
G-UC	L06	102	87	0.17	0.43
	L07	166	99	0.16	0.52
	L08	94	70	0.10	0.54
	L09	113	83	0.16	0.50

in the case of laminates L06 and L07, since L09 only dissipates about 24% more energy than L08. This may be explained by the laminate L09 having a ply clustering of UC in the -45°, instead of the 0°. However, thicker plies, even at -45°, may still result in higher pull-out lengths and fibre breakage.

The increase of the dissipated energy observed in the specimens where more transverse matrix is visible can be mainly explained by three phenomena. The first one being the transverse crack propagation itself. Although the matrix fracture energy may be negligible compared to the fibre fracture energy, the contribution of all the matrix cracking events can significantly add to the total translaminar fracture energy of the laminate. The second phenomenon may be related to the matrix cracking induced delamination. This is apparent in the laminate L07, shown in Fig. 6.2 where some small delaminations near the initial crack tip can be observed. Finally, the third phenomenon can be explained by the reduction of the Stress Intensity Factor of the whole laminate at the crack tip, caused by the presence of transverse matrix cracking. Hence requiring more energy to propagate the translaminar crack.

An in-depth description of the data reduction of each laminate is included in PAPER D. It also includes the characterization of the laminates under compressive loads, obtained from the Compact Compression specimen.

7

Cohesive Law independence of the specimen size and geometry

The Cohesive Zone model has been applied throughout this document to model the translaminar fracture, meaning that it can only be applied in laminates where the damage mechanisms are almost localized in a plane. Laminates that experiment large delaminations could not be benefited from this approach. The Cohesive Zone model presents many advantages over the LEFM-based models. To begin with, it is applicable to predict the nominal strength of structures in the absence of cracks. Also, it is capable of capturing the size effect of structures with the same geometry (more details can be found in PAPER C).

One of the main hypothesis of the Cohesive Zone model is that it assumes the Cohesive Law to be a material property, i.e, it does not depend on the specimen size or the specimen geometry. The main objective of this Section is to check the foundation of this hypothesis. This will be confirmed in two steps: first, it will be studied how the change in specimen size influences the measured CL. Second, it will be studied how well the same CL can predict the nominal strength of multiple geometries.

7.1 How the specimen size influences the measured Cohesive Law

As previously mentioned, the first step is to study how the specimen size influences the obtained CL using the methodology of Section 5.3. To do so, the CL has been measured for three Over-height Compact Tension (OCT) specimens of different

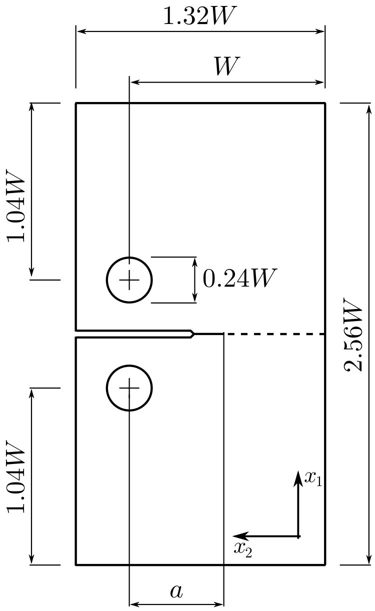

Fig. 7.1.: Over-height Compact Tension (OCT) specimen geometry, with all dimensions defined with respect to the size W, where the dashed line represents the crack path.

sizes for the same laminate. The Over-height Compact Tension (Kongshavn, 1996; Kongshavn and Poursartip, 1999; Floyd, 2004; Li et al., 2009; Zobeiry et al., 2014; Xu et al., 2015) was designed to measure translaminar fracture toughness of composite laminates with a large Failure Process Zone. Fig. 7.1 shows the geometry of the specimen with respect to the size W. As the proposed methodology to determine the CL only needs to experimentally register the load and displacement outputs, the curves are taken from the results published by Xu et al. (2015). In this publication, the experimental load, displacement and damage evolution of three different OCT specimens of size $W = 40.3$, 80.6 and 161.2mm are presented. The laminate material is IM7/8552, a carbon-epoxy pre-preg provided by Hexcel HexPly®, with a nominal ply thickness of 0.125 mm. The stacking sequence is quasi-isotropic $[45/90/-45/0]_{4s}$. The elastic properties of the laminate are found in Table 7.1.

Stacking sequence	W [mm]	a_0 [mm]	h [mm]	E [MPa]	σ_u [MPa]
$[45, 90, -45, 0]_{4s}$	40.3/80.6/161.2	0.4W	4	61645	990

Tab. 7.1.: Laminate properties.

The experimental P-u curves of each specimen size are shown in Figure 7.2. The solid lines represent the experimental curves, while the dashed ones have been obtained from applying a Gaussian smooth, in order to reduce the experimental scatter. This technique averages the values around a given point weighted according to a Gaussian function, such that the end points at the data window have less influence on the averaged value than the ones near the centre. For each specimen curve, some points were used in order to apply the inverse method. For the scaled-down specimen ($W = 40.3$ mm), 12 points were used, marked with $*$. For the base-line ($W = 80.6$ mm) and scaled-up ($W = 161.2$ mm) specimens, 20 points were fitted, marked with a $+$ and a $\times$, respectively.

The obtained CL shapes for the three specimen sizes are shown in Fig. 7.3. The initial point of the curve, $\sigma_u = 990$ MPa, is taken from the laminate strength, and has not been obtained from the inverse problem solution. Observing the results, it is possible to identify a similar trend for the three CL: first, a steep drop in stresses, followed second smooth drop up until a crack opening around $\omega \approx 0.7$ mm. This type of curve is usually expected in order to reproduce the translaminar fracture of carbon-reinforced composites. The first drop of stresses may be related to the high amounts of energy suddenly released when fibre-breakage takes place. The second slope can be related with fibre-bridging and fibre pull-out, taking place at wider crack openings. Is is worth mentioning that none of the three specimens have fully developed their FPZ when the experiment was finished. This is easily observed in two aspects: firstly, none of the P-u curves never follow the typical LEFM response at any point in the experiment, and secondly, none of the obtained CL are closed curves.

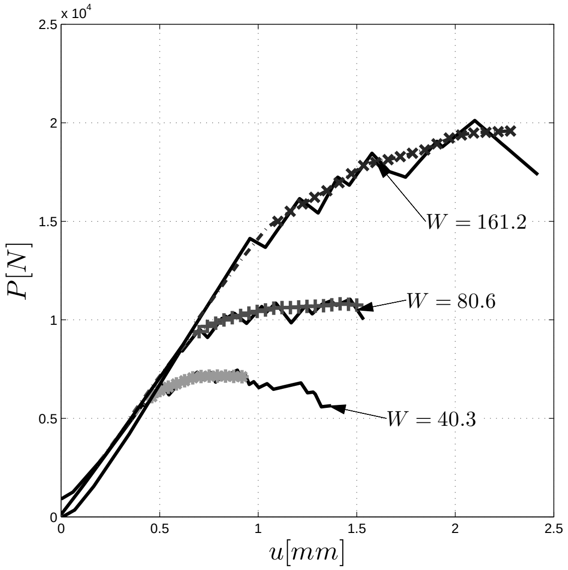

Fig. 7.2.: Experimental (solid lines) and fitted (dashed lines) load displacement curves. The marks represent the points selected in order to fit the Cohesive Law for each specimen.

Observing the measured shapes, one may assume that they describe the same general trend, and therefore, the CL property is not influenced by the specimen size, at least, for the range of tested sizes and for the given geometry. The discrepancies can be attributed to the experimental scatter and to the material heterogeneity. In order to see how well the measured CL can predict the strength other geometries, a simplified CL is proposed, marked with a solid line in Fig. 7.3. The proposed piecewise curve is defined as a trilinear CL, defined by the points $\sigma(\omega) = [990(0); 250(0.0893); 175(0.7); 0(0.7)]$. The cut-off observed in $\omega = 0.7\ \mathrm{mm}$ has been introduced as no information was obtained for greater crack openings. The area under the curve corresponds to a fracture energy of $G_{Ic} = 185\ \mathrm{N/mm}$ or a critical SIF of $K_{Ic} = 3377\ \mathrm{MPa}\sqrt{\mathrm{mm}}$.

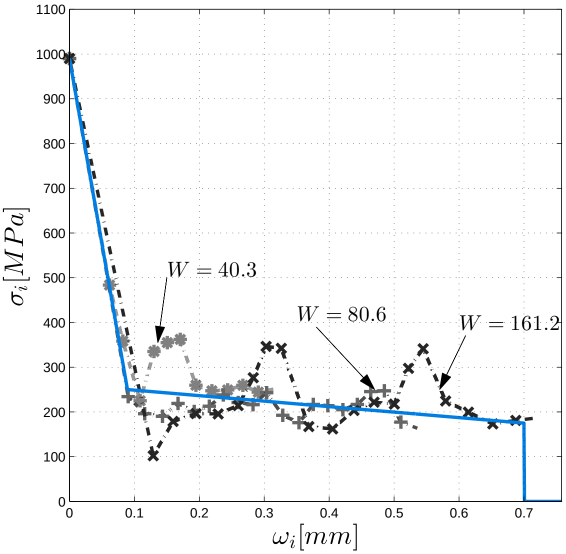

Fig. 7.3.: Measured Cohesive Law obtained from each OCT specimen, along the simplified trilinear Cohesive Law (solid line).

7.2 Predicting the nominal strength of other geometries

In order to verify if the CL is modified by the specimen geometry, the proposed simplified CL has been used to predict the nominal strength of two specimens: the Center Cracked (CCS) and Open Hole (OH) specimens. Fig. 7.4 shows the geometry of both specimens, with all the dimensions specified with respect to the half the notch length R. The nominal strength, σ_N, is defined as the average stress of the net section at the maximum load, and has been predicted by solving the direct method, as described in Section 5.2, for both geometries. A wide range of sizes have been studied, with values of $R =$ 1.5875, 3.175, 6.35, 12.7 and 25.4 mm. For

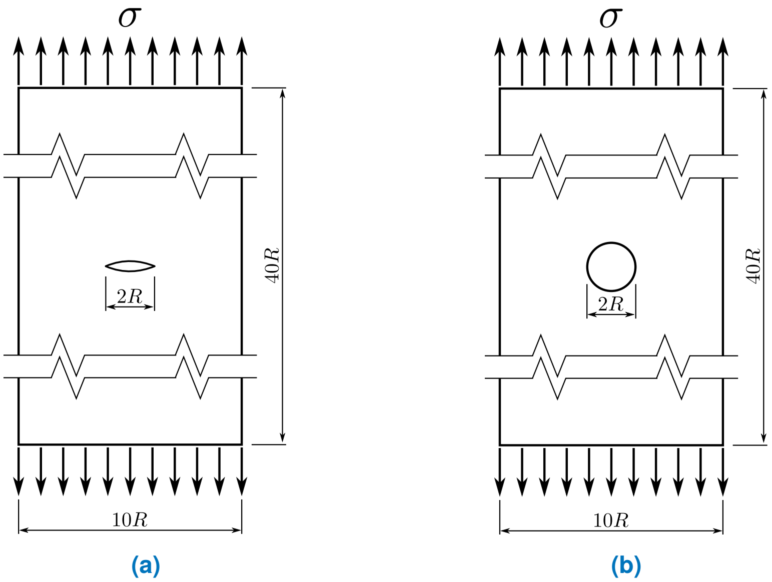

Fig. 7.4.: (a) Center Cracked Specimen (CCS) and (b) Open Hole specimen (OH) geometry, with all dimensions defined with respect to the half of the notch size R.

all the specimens, the considered laminate is the same used in the OCT, with the properties summarized in Table 7.1.

The results of the predictions are found in Fig. 7.5, along some experimental ones. These have been obtained from the published results in Xu et al. (2014). Some characteristics of the plot of Fig. 7.5 are worth mentioning. The line labelled as plastic limit references to the particular case in which the net section is subjected to a constant stress distribution equal to the laminate strength σ_u. This limit is reached for extremely small specimens in both the CCS and OH, where the FPZ length takes the whole section. As the specimen size increases, the σ_N tends to two particular solutions for $R \to \infty$, depending on the geometry considered. For the OH specimen, the solution follows the elastic solution determined by the stress concentration factor. On the other hand, for the CCS, the solution follows the LEFM determined by the stress intensity factor or the energy release rate. As it can be seen, in general, the predictions using the proposed CL are in good agreement with the experimental

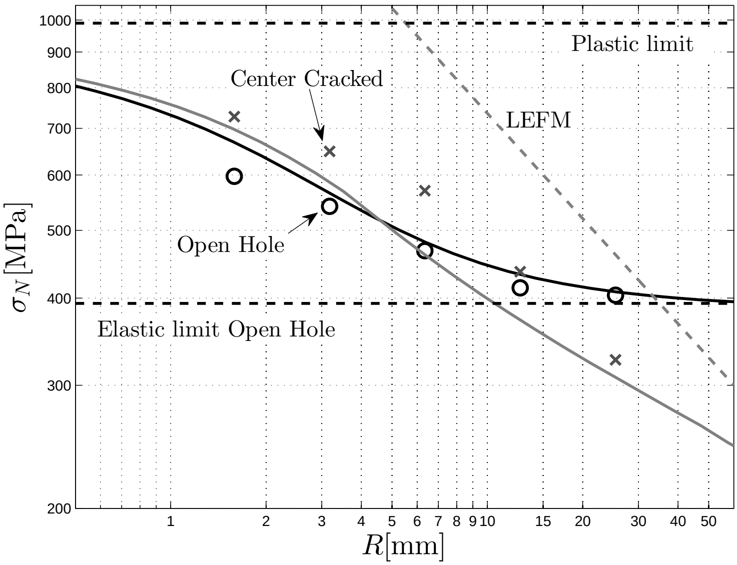

Fig. 7.5.: Predicted nominal strength σ_N of the Open Hole and Center Cracked specimens with respect to half of the notch length R, considering the CL of Fig. 7.3, along with some experimental results.

results, even some of them being in excellent agreement. The obtained predictions follow the expected aforementioned particular solutions, by solving the direct method and only changing the specimen size. More concretely, the nominal strength of the Center Cracked Specimen is slightly underpredicted, being the most critical case about a 20$\%$ lower for $R = 6.35$ mm. On the other hand, the σ_N is slightly overpredicted for the Open Hole specimen, being the most critical case about a 12$\%$ greater for $R = 1.5875$ mm. These results suggest that, for the CCS, the nucleation and crack growth requires more energy than the determined by the OCT. However, the OH specimen seems to require less energy than OCT specimen.

Part IV

Concluding remarks

Results and discussion

8

This chapter summarizes the results of the developed work as a whole and discusses them in accordance with four different building blocks: the extension of the Compact Tension specimen for orthotropic materials (Chapter 4), the determination of the translaminar Cohesive Law (Chapter 5), the verification of the Cohesive Law as a material property (Chapter 7), and how the stacking sequence can influence the measured CL (Chapter 6).

8.1 Compact Tension specimen for orthotropic materials

When facing the problem of measuring the total fracture energy G_{Ic} or the associated critical Stress Intensity Factor K_{Ic} of an orthotropic laminate, it is necessary to have a function of the form

$$K_{Ic}\left(\bar{a}, \lambda, \rho\right) \tag{8.1}$$

that takes into account the orthotropy of the material defined by the non-dimensional variables λ and ρ. The available existing methodologies consisted on obtaining Eq. 8.1 from a FE for a particular laminate. The writing of this Ph.D. thesis has contributed to the problem by introducing an analytic expression of Eq. 8.1 for a wide range of material orthotropies. The function has been obtained from fitting the results obtained from FE simulations, and has been contrasted with the tabulated isotropic solution available in the literature, as well as with particular orthotropic solutions also found in the literature. The function computes the SIF with a maximum error of 2.37% with respect to the FE simulations.

Likewise, when measuring the crack length a, basically two approaches exist: one being measuring a optically, and the other one by equalling the experimental com-

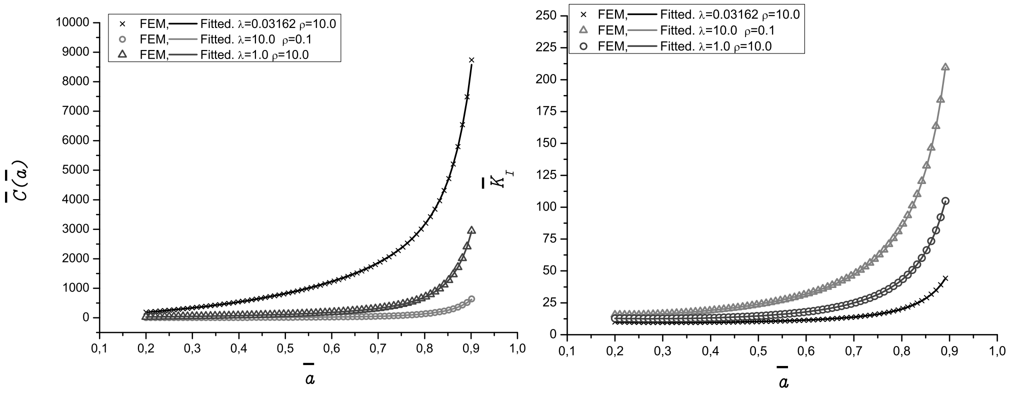

(a) **(b)**

Fig. 8.1.: Comparison between FE and fitted (a) $\bar{C}$ and (b) $\bar{K}$ curves for three examples of orthotropic materials.

pliance with the elastic one and thus obtaining the equivalent elastic crack length. The former is not an objective methodology when large Fracture Process Zone are present, as the crack tip location is not well defined, specially for fibre-reinforced composite materials. The latter method relies on having an expression of the form

$$C\left(\bar{a}, \lambda, \rho\right) \tag{8.2}$$

Researchers would typically obtain Eq. 8.2 from a FE model for every particular laminate needed to be tested. The present thesis has also introduced a general analytic expression for Eq. 8.2 for the CT specimen. Again, the function has been obtained from fitting the results obtained from FE simulations, and has been contrasted with the tabulated isotropic solution, as well as with particular orthotropic solutions, both found in the literature. The function computes the elastic Compliance of the CT specimen with a maximum error of 2.29% with respect to the FE simulations.

Both general expressions for the Compliance and the SIF introduced in this thesis facilitate the measurement of the translaminar fracture energy for a wide range of orthotropies, without the need of doing a FE analysis for each particular tested laminate. These are valid for $0.03162 \leq \lambda \leq 10.0$ and $0.1 \leq \rho \leq 10.0$, covering virtually all the orthotropies that can be found in existing materials. The details on how these functions have been obtained and their benchmarks can be found in PAPER A. As an illustrative example, Fig. 8.1 shows the excellent agreement between the proposed functions and the simulations obtained from the FE method.

8.2 Determination of the translaminar Cohesive Law

Although the previous Section introduced general tools for measuring G_{Ic} and the associated SIF for a wide range of orthotropies, in reality, the measurement of the total fracture energy and Stress Intensity Factor are not sufficient for predicting the nominal strength of structures when large Fracture Process Zone are present, with respect to other problem dimensions. In these cases, during the FPZ initiation and growth, the apparent fracture energy grows with the applied displacement. Once the FPZ has been fully developed the apparent fracture energy achieves a plateau value equal to G_{Ic}. This apparent increase of fracture energy is known as the $\mathcal{R}$-curve of the material. Using the Linear Elastic Fracture Mechanics reduction methods, it could be possible to record the whole $\mathcal{R}$-curve as a function of the crack length, although this would only suffice to reproduce the exact same experiment from which it was recorded, as the $\mathcal{R}$-curve cannot be extrapolated to other geometries or sizes. This is a consequence of the $\mathcal{R}$ not being a material property, as it depends on the specimen size and geometry. LEFM assumes that the energy dissipation is localized within a very small volume at the crack tip and, as a consequence, the stress field can be defined by a single parameter K_I. Hence, LEFM based theories can deliver wrong predictions of structural strengths when large FPZ are present, as is in the case of fibre-reinforced composite materials. Numerous studies are available in the literature that support this statement, as introduced in Section 5.4, an discussed in-depth in PAPER C.

On the other hand, more complex fracture models such as the Cohesive Zone Model (Section 5.1), can properly predict the change in size and geometry by assuming the CL as the true material property. This defines the relation between the closing stresses and the crack openings inside the FPZ. Two main drawbacks appear with this approach. First, the Cohesive Zone Modelling crack growth is predicted by a set of non-linear equations that are usually complex to solve. Secondly, the measurement of the translaminar CL itself is still an unresolved problem despite the many attempts by the scientific community (a wide review can be found in Chapter 3).

The present thesis has improved the aforementioned problems related with the Cohesive Zone Model (CZM) in two aspects. First, a semi-analytic solution has been proposed to predict the P-u curve of a Compact Tension specimen along all the FPZ related outputs, for any random CL shape. The method is able to obtain many outputs during the crack growth, such as the cohesive crack openings ω_i, cohesive stresses σ_i and the FPZ length ℓ_{FPZ}. The non-linear problem has been solved by applying the superposition principle in order to describe the SIF of the whole problem for a given instant during the crack growth, and by solving the Dugdale's condition. This is fulfilled by ensuring that the total SIF is null due to the presence of the cohesive stresses inside the FPZ. This approach has proven to be a reliable and fast tool to solve all the variables related to the FPZ, as presented in Section 5.2. The results obtained in this manner are in perfect agreement with those that can be obtained by the Finite Elements approach, in just a fraction of the computational cost. Fig. 8.2 shows the excellent agreement between the proposed analytic model and the FE simulations, for a linear Cohesive Law shape. The procedure presented in this thesis is easily applicable to other geometries.

This thesis has also proposed a methodology to measure the translaminar Cohesive Law from a single fracture test of a Compact Tension specimen. The CL is defined as a piecewise linear function, initially with segments of unknown slopes and widths. Each segment is adjusted so that the predicted P-u curve best fits some selected points from the experimental curve. This methodology has proven to be objective enough, as the obtained CL does not depend on the selected points of the curve,

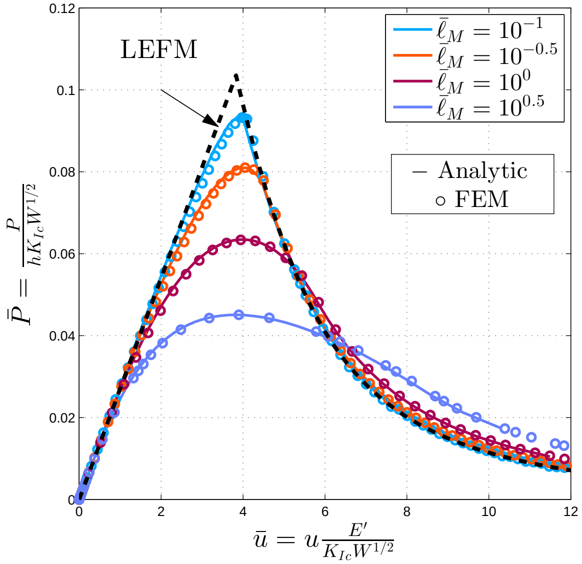

Fig. 8.2.: Comparison of the displacement (u) and load (P) curves obtained with the author's methodology and using a Finite Element model.

as shown in Fig. 8.3. The details of the methodology are found in Section 5.3 and can also be found in detail in PAPER B.

8.3 The translaminar Cohesive Law as a material property

Is the translaminar CL a material property? The Cohesive Zone model assumes this as a fact, but there is no experimental evidence to support this due to the lack resources for measuring it. The present thesis tries to answer this question with the aid of the introduced method to obtain the CL. The property has been checked in two phases. In the first phase, the translaminar CL has been measured for three Over-height Compact Tension specimens of different sizes while maintaining the same laminate. The three specimens are geometrically identical, but with rescaled

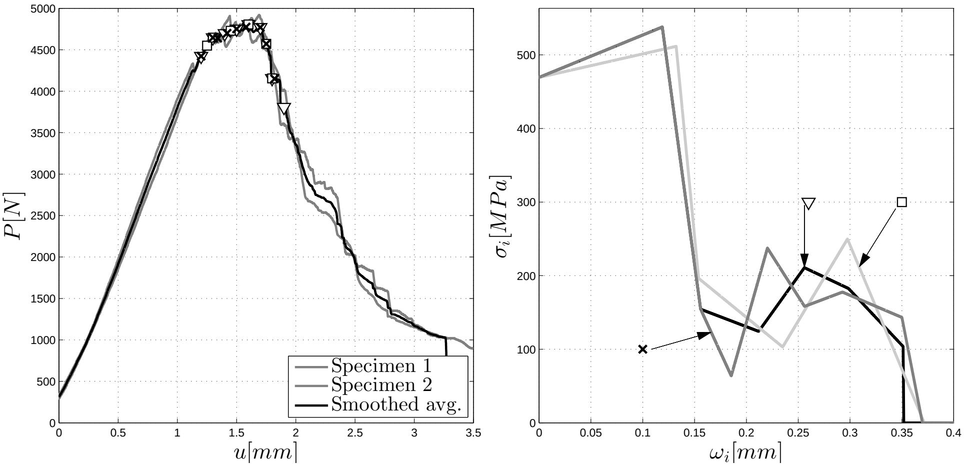

(a) **(b)**

Fig. 8.3.: P-u curve for the two hybrid specimens and the corresponding smoothed average curve. (b) Three different CL obtained from three different sets of points.

dimensions. The results show that the general shape of the measured CL remains unaffected by the specimen size. The obtained CL for each specimen size is shown in Fig. 8.4.

The second phase in order to check whether the CL is a material property consists in using the obtained curve from the OCT specimens to predict the nominal strength of other geometries and sizes. To do so, first, a simplified CL shape is proposed, used to predict the nominal strength of the geometries. This general shape is shown as a solid line in Fig. 8.4. The other geometries that are predicted are the Open Hole and the Center Cracked specimens. The predicted nominal strengths are in good agreement with the experimental ones, as can be appreciated in Fig. 8.5. For some of the cases, the predicted values are in excellent agreement with the experimental ones. The details on the followed procedure, used materials, stacking sequence and obtained results can be found detail in Chapter 7.

When defining the translaminar fracture of fibre reinforced composites, the Cohesive Law takes into account several dissipation mechanisms indistinctly, such as fibre

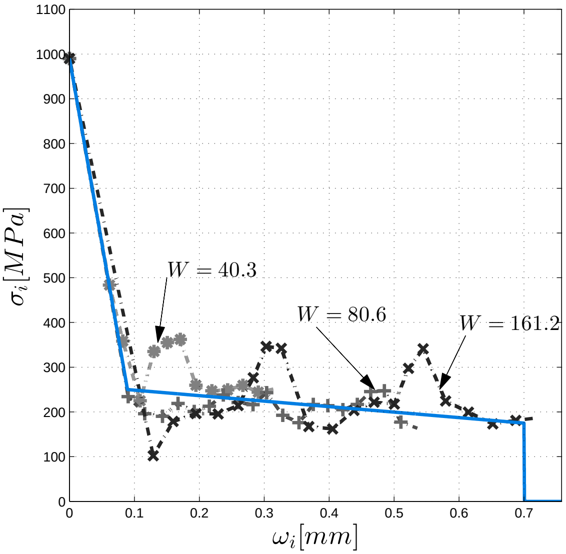

Fig. 8.4.: Measured Cohesive Law obtained from each OCT specimen, along the simplified trilinear Cohesive Law (solid line).

breaking, matrix cracking, fibre bridging and fibre pull-out. Assuming the CL as a material property implies that these series of events that take place inside the FPZ during the crack initiation and growth are the same and dissipate the same energy regardless the considered geometry or the size of the structure. This might be a harsh assumption, as it is difficult to believe that a notched and an unnotched structures undergo the same fracture damage mechanisms. Even so, in view of the results, it seems plausible to assume the CL as a material property that remains constant, at least, macroscopically speaking, for the ranged size of specimens.

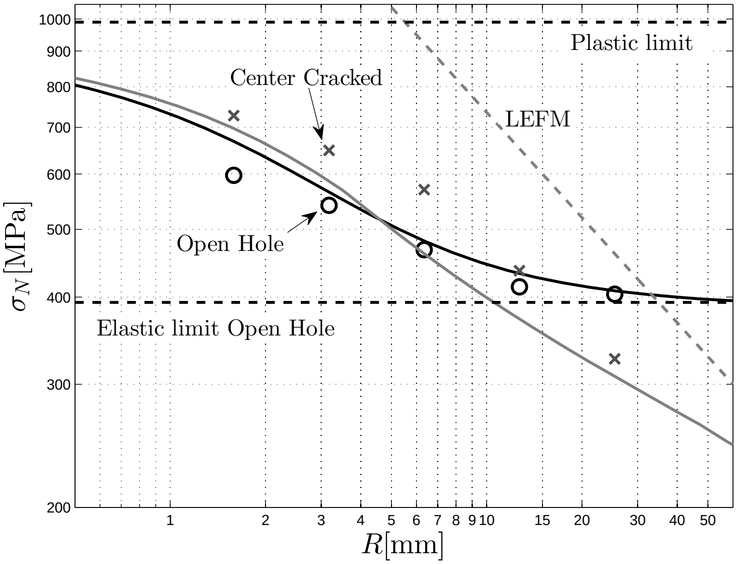

Fig. 8.5.: Predicted nominal strength σ_N of the Open Hole and Center Cracked specimens with respect to half of the notch length R, considering the CL of Fig. 7.3, along with some experimental results.

8.4 Effects of the stacking sequence on the measured Cohesive Law

As previously mentioned, the CL accounts for several energy dissipation mechanisms during the FPZ formation and growth. In the case of fibre-reinforced composite materials, most of these damage mechanisms depend of the fibre and matrix properties as well as the laminate properties. In the presence of a translaminar crack, the CL accounts for the whole laminate. In such cases, the used stacking sequence may influence the fracture events during the crack formation, even for laminates with the same in-plane properties, causing a significant influence in the resultant translaminar fracture energy.

In order to study the influence of the stacking sequence on the measured translaminar CL, some interply hybrid laminates were tested, combining two materials of a total set of three type of plies: Unidirectional Carbon (UC) tape, woven Carbon fabric (C) and woven Glass fabric (G). For each combination of two materials several stacking sequences have been studied. The laminates have been chosen in order to accomplish that, for each set, the in-plane properties and the laminate thickness remained as constant as possible.

The measured CL for each laminate show that the stacking sequence does have an impact on the total fracture energy as well as the CL shape. The results show that, at least for the tested materials, ply-clusters made of laminae perpendicular to the crack growth dissipate more energy than those laminates without ply-clustering.

9

Conclusions

The present thesis deals with the data reduction analysis of pure mode I translaminar cracks of fibre-reinforced composite laminates, i.e, a crack that grows along the laminate submitted to tension, breaking all the plies. The work focuses first on the Linear Elastic Fracture Mechanics data reduction methods, extended to consider any material orthotropy. It is followed by more complex approaches based on the Cohesive Zone Model. The main conclusions of this work are grouped according to five main blocks, found below.

The first contribution of the present work is the introduction of several data reduction methods and design tools. These tools, based on the Linear Elastic Fracture Mechanics theory, have been developed for the Compact Tension specimen, but have been extended in order to account for the orthotropic behavior of the laminate.

- An analytic function of the form $C\left(a, \bar{\lambda}, \rho\right)$ for the elastic compliance of a Compact Tension specimen has been proposed, taking into account the material orthotropy.

- An analytic function of the form $K_I\left(a, \bar{\lambda}, \rho\right)$ for the Stress Intensity Factor of a Compact Tension specimen subjected to a mode I loading at the pin holes has been proposed, taking into account the material orthotropy.

- Both functions have been obtained from a wide range of FE simulations, providing an excellent agreement with the tabulated isotropic solution as well as for some particular orthotropic solutions available in the literature.

- A failure criteria has been proposed for the Compact Tension specimen, taking into account the laminate orthotropy. The strength-based criteria accounts for compression failure at the specimen back-end and by the bearing load at the holes.

- The failure criteria have been checked with two laminates, again resulting in good agreement with the experimental results.

Linear Elastic Fracture Mechanics are not sufficient to properly predict this kind of fracture in the presence of a large Fracture Process Zone, as is normally the case of fibre-reinforced composite materials. Thus, the present thesis approaches this kind of fracture by considering the Cohesive Zone Model point of view.

- An analytic cohesive model has been proposed in order to solve the fracture problem of a Compact Tension specimen subjected to a controlled displacement and corresponding load. The model obtains the whole load-displacement curve for a given translaminar Cohesive Law, while obtaining the cohesive crack openings, cohesive stresses and the Fracture Process Zone length.

- The model has been validated with several FE simulations, assuming a linear CL, while changing the specimen size. The results are in excellent agreement with the simulations, while only taking fraction of the computing time with respect to the FE simulations.

- With the use of the model, Linear Elastic Fracture Mechanics reduction methods have been put to test. The results of this study prove that the $\mathcal{R}$-curve is incompatible with the Cohesive Zone Modelling, resulting in a property that depends on the specimen size and geometry.

An indispensable ingredient of the Cohesive Zone Model is the Cohesive Law of the laminate. Several sophisticated attempts to measure this property are found in the literature. The present work proposes a simple and objective methodology to measure this property from a single fracture test.

- A methodology has been proposed to measure the translaminar Cohesive Law from a single Compact Tension fracture test by solving the inverse problem. The method obtains softening law by best fitting some points of the experimental load-displacement curve using the analytic cohesive model.

- The algorithm is initialized with an unknown CL shape, defined as a piecewise linear function, with unknown slopes and widths. Each segment is adjusted in order that the predicted load-displacement curve best fits the selected experimental points.

- The proposed methodology has proven to be efficient, as the obtained Cohesive Laws shape do not depend on the selected points in the fitting process, at least for the tested materials, laminates and geometries.

The next step has been to study how the stacking sequence can influence the Cohesive Law shape.

- Several interply hybrid Compact Tension specimens were tested to study the effect of the ply stacking sequence on the measured translaminar Cohesive Law. The laminates were obtained by combining two materials of a total of three type of plies: Unidirectional Carbon, woven Carbon fabric and woven Glass fabric.

- For each set of two materials, the laminates and stacking sequences were chosen in order to maintain the in-plane elastic modulus and the laminate thickness as constant as possible.

- The obtained Cohesive Laws showed that the laminates with ply clustering dissipate more energy than the ones with more dispersed plies.

- The increase of the translaminar fracture toughness on the laminates with ply clustering aligned perpendicular to the principal crack growth may be mainly attributed to larger amounts of fibre pull-out and longer fibre pull-out lengths. Some other fracture mechanisms that may add to the total fracture energy are: the growth of transverse cracks, transverse cracking induced delamination and blunting of the crack tip caused by the presence of the transverse matrix cracks.

The main hypothesis assumed in the Cohesive Zone Model approach is that the Cohesive Law is a material property. This thesis has provided some evidence for the tested laminates.

- In order test how the specimen size affects the measured CL, it has been measured from three geometrically identical Over-height Compact Tension, tested by the University of Bristol. All the specimens were obtained from the same laminate, maintaining the same geometry while varying the size.

- The measured CL for each specimen are almost identical, following a unique general shape for the given laminate, regardless the tested size.

- The obtained Cohesive Law was then used to predict the nominal strength of two additional geometries: the Center Cracked and Open Hole Specimen, again made of the same laminate.

- The predicted strengths are in good agreement with the existing experimental results. It is plausible to assume the translaminar Cohesive Law a material property, at least, for the tested range of specimen sizes.

- The hypothesis may hold true only when the damage mechanisms are localized in the fracture plane at the crack tip. If other typologies of damage, such a large delaminations, take place away from the crack tip, the Cohesive model is not be suitable to model them.

Perspective and future work

10

This chapter presents some possible lines of future research and extension of the work developed in this thesis.

10.1 Extension of the Cohesive Zone Model for orthotropic laminates

The semi-analytic solution for the Compact Tension specimen introduced in Section 5.2, capable of solving the Cohesive Zone problem of a specimen subjected to a controlled displacement and corresponding load, can only be applied for in-plane quasi-isotropic laminates. This limitation is a consequence of the lack of availability of the Stress Intensity Factor functions that consider other material orthotropies.

In order to analytically solve the problem to consider non quasi-isotropic laminates, the algorithm needs to be fed with three different SIF functions that take into account the material orthotropy:

- SIF caused by the bearing load applied at the pin holes.
- SIF caused by a constant cohesive stress applied over a small surface inside the Fracture Process Zone.
- SIF caused by a point load applied over a small surface inside the Fracture Process Zone.

Of the three SIF, the first one has already been obtained for a wide range of orthotropies, as presented in Section 4.3. The other two remaining SIF could be obtained by means of parametric FE model using Python scripting together with ABAQUS.

10.2 Translaminar Cohesive Law and damage mechanisms relationship

The translaminar Cohesive Law of a fibre-reinforced laminate accounts for several energy dissipation mechanisms during the Fracture Process Zone formation and growth. These damage mechanisms can account for fibre breakage, matrix cracking, fibre bridging, fibre pull-out and even small delaminations between plies around the crack tip.

With the aid of the introduced means to measure the translaminar Cohesive Law, the next logic step is to explore the relationship between the observed damage mechanisms and the obtained softening law shape. For example, in the case of laminates with large fibre-bridging regions, the tail of the measured CL is longer, as this involves larger Fracture Process Zones. Having a better understanding this relationship can lead to a better laminate design, benefiting certain damage mechanisms over the others, depending on the required applications. Although this research has begun during the writing of the present thesis, as exposed in Chapter 6, an in-depth research needs yet to be accomplished.

In order to research this relationship, a test campaign should be carried out with several laminates, modifying the layup sequences to influence the development of the different failure mechanisms. For each tested laminate the Cohesive Law should be measured, and the specimens inspected in order to determine the damage mechanisms it has experienced. The inspection can be performed on post-mortem specimens, but also in the middle of the test if non-destructive techniques are used to inspect the specimen. For instance, it is a known fact that thicker plies causes more fibre pull-out at the perpendicular-to-the-crack-growth plies (Pinho et al., 2006), with larger pull-out length as the distance to the interface is increased. Other example is the effect of the ply clustering on the matrix cracking, as briefly observed in Chapter 6.

10.3 Study on the interlaminar Cohesive Law

The proposed method to obtain the translaminar Cohesive Law could be implemented for studying the interlaminar behaviour of fibre-reinforced composite laminates. An ideal specimen candidate to carry this study is the Double Cantilever Beam (DCB), as the required Stress Intensity Factor functions to analytically solve the cohesive problem are already available in the literature (Massabò et al., 2003).

The procedure of obtaining the interlaminar Cohesive Law could be carried out analogously to the procedure described in Chapter 5.3, by just needed to record the load-displacement curve on the experimental test. Further, multiple DCB tests have been accomplished by the scientific community during the last 50 years, resulting in multiple available experimental curves waiting to be fitted.

10.4 Application to other materials

In the present work, the proposed methodology to measure the Cohesive Law has only been applied to fibre-reinforced polymers. In reality, such methodology could be applied to any quasi-brittle material provided the damage mechanisms are located within the Fracture Process Zone plane.

The Cohesive Law could be measured from various quasi-brittle materials such as: concrete, numerous types of woods, a wide range of polymer materials, metallic-glasses, bone and dentin and also other bio-materials.

Part V

Bibliography

Bibliography

Andersson T. and Stigh U. (2004). The stress-elongation relation for an adhesive layer loaded in peel using equilibrium of energetic forces. In: *International Journal of Solids and Structures* 41, pp. 413–434 (cit. on p. 37).

ASTM (1997). E399-90. Standard test method for plane-strain fracture toughness of metallic materials. In: *1991 Annual Book of ASTM Standards* 3.Reapproved, pp. 451–485 (cit. on pp. 50, 51, 72).

ASTM (1999). D5045-99. Standard test methods for plane-strain fracture toughness and strain energy release rate of plastic materials. In: *West Conshohocken, PA* (cit. on p. 72).

ASTM (2015). E1922-04. Standard Test Method for Translaminar Fracture Toughness of Laminated and Pultruded Polymer Matrix Composite Materials. In: *West Conshohocken, PA* (cit. on p. 51).

Bao G. and Suo Z. (1992). Remarks on crack-bridging concepts. In: *Applied Mechanics Reviews* 45.8, pp. 355–366 (cit. on p. 70).

Barenblatt G. I. (1959). The formation of equilibrium cracks during brittle fracture: general ideas an hypotheses, axially-symmetric cracks. In: *Journal of Applied Mathematics and Mechanics* 23, pp. 622–636 (cit. on pp. 17, 62).

Barenblatt G. I. (1962). The Mathematical Theory of Equilibrium Cracks in Brittle Fracture. In: *Advances In Applied Mechanics*. Advances in Applied Mechanics 7. Ed. by Dryden, H. L. and Von Kármán, T. and Kuertim G. and Van Den Dungen, F. H. and Howarth, L., pp. 55–129 (cit. on pp. 17, 61, 62).

Bažant Z. P. (1992). Fracture Mechanics of Concrete. In: *First International Conference on Fracture Mechanics of Concrete Structures* (cit. on p. 70).

Bažant Z. P. and Oh B. H. (1983). Deformation of Cracked Net-Reinforced Concrete Walls. In: *Journal of Structural Engineering* 109.2, pp. 93–108 (cit. on p. 61).

Bažant Z. P. and Planas J. (1998). Fracture and Size Effect in Concrete and Other Quasibrittle Materials. Boca Raton and London: CRC Press (cit. on pp. 9, 25, 70).

Bažant Z. P., Daniel I. M. and Li Z. (1996). Size effect and fracture characteristics of composite laminates. In: *Journal of Engineering Materials and Technology* 118, pp. 317–324 (cit. on pp. 50, 51).

Bergan A. C., Dávila C. G., Leone F. A., Awerbuch J. and Tan T. (2014). Mode I Cohesive Law Characterization of Through-Crack Propagation in a Multidirectional Laminate. In: *Proceedings of the American Society for Composites 2014-Twenty-ninth Technical Conference on Composite Materials* (cit. on p. 36).

Bergan A. C., Dávila C. G., Leone F. A., Awerbuch J. and Tan T. (2016). A Mode I cohesive law characterization procedure for through-the-thickness crack propagation in composite laminates. In: *Composites Part B: Engineering* 94, pp. 338–349 (cit. on p. 38).

Blanco N., Trias D., Pinho S. T. and Robinson P. (2014a). Intralaminar fracture toughness characterisation of woven composite laminates. Part I: Design and analysis of a compact tension (CT) specimen. In: *Engineering Fracture Mechanics* 131, pp. 349–360 (cit. on p. 50).

Blanco N., Trias D., Pinho S. T. and Robinson P. (2014b). Intralaminar fracture toughness characterisation of woven composite laminates. Part II: Experimental characterisation. In: *Engineering Fracture Mechanics* 131, pp. 361–370 (cit. on p. 50).

Bloyer D. R., Venkateswara Rao K. T. and Ritchie R. O. (1998). Fracture toughness and R-curve behavior of laminated brittle-matrix composites. In: *Metallurgical and Materials Transactions A: Physical Metallurgy and Materials Science* 29.10, pp. 2483–2496 (cit. on p. 70).

Bolzon G., Fedele R. and Maier G. (2002). Parameter identification of a cohesive crack model by Kalman filter. In: *Computer Methods in Applied Mechanics and Engineering* 191.25-26, pp. 2847–2871 (cit. on p. 39).

Bouville F., Maire E., Meille S., et al. (2014). Strong, tough and stiff bioinspired ceramics from brittle constituents. In: *Nature Materials* 13.5, pp. 508–514 (cit. on p. 70).

Camanho P. P., Maimí P. and Dávila C. G. (2007). Prediction of size effects in notched laminates using continuum damage mechanics. In: *Composites Science and Technology* 67.13, pp. 2715–2727 (cit. on pp. 32, 50).

Catalanotti G., Camanho P. P., Xavier J., Dávila C. G. and Marques A. (2010). Measurement of resistance curves in the longitudinal failure of composites using digital image correlation. In: *Composites Science and Technology* 70.13, pp. 1986–1993 (cit. on pp. 36, 50).

Catalanotti G., Arteiro A., Hayati M. and Camanho P. P. (2014a). Determination of the mode I crack resistance curve of polymer composites using the size-effect law. In: *Engineering Fracture Mechanics* 118, pp. 49–65 (cit. on p. 50).

Catalanotti G., Xavier J. and Camanho P. P. (2014b). Measurement of the compressive crack resistance curve of composites using the size effect law. In: *Composites Part A: Applied Science and Manufacturing* 56, pp. 300–307 (cit. on p. 51).

Connell S., Zok F., Du Z. and Suo Z. (1994). On the tensile properties of a fiber reinforced titanium matrix composite - II. Influence of notches and holes. In: *Acta Metallurgica et Materialia* 42.10, pp. 3451–3461 (cit. on p. 50).

Cooper G. and Kelly A. (1970). The contribution to the work of fracture of a composite material of pull-out of fibers. In: *Mechanics of Composite Materials*. Ed. by F. Wendt, H. Liebowitz and N. Perrone. Pergamon, pp. 653 –661 (cit. on p. 79).

Cornelissen H. A. W., Hordijk D. A. and Reinhardt H. W. (1986). *Experimental determination of crack softening characteristics of normalweight and lightweight concrete* (cit. on p. 27).

Cowley K. and Beaumont P. (1997). The interlaminar and intralaminar fracture toughness of carbon-fibre/polymer composites: The effect of temperature. In: *Composites Science and Technology* 57.11, pp. 1433–1444 (cit. on p. 50).

Cox B. N. and Marshall D. B. (1991). Stable and unstable solutions for bridged cracks in various specimens. In: *Acta Metallurgica et Materialia* 39.4, pp. 579–589 (cit. on pp. 39, 40).

Cusatis G. and Schauffert E. A. (2009). Cohesive crack analysis of size effect. In: *Engineering Fracture Mechanics* 76.14, pp. 2163–2173 (cit. on p. 25).

Daniel I. M. (1978). Strain and Failure Analysis of Graphite/Epoxy Plates with Cracks. In: *Experimental Mechanics* 18.July, pp. 246–252 (cit. on p. 50).

Demetriou M. D., Launey M. E., Garrett G., et al. (2011). A damage-tolerant glass. In: *Nature Materials* 10.2, pp. 123–128 (cit. on p. 70).

Dugdale D. (1960). Yielding of steel sheets containing slits. In: *Journal of Mechanics Physics of Solids* 8, pp. 100–104 (cit. on pp. 17, 61, 62).

El-Hajjar R. and Haj-Ali R. (2005). Mode-I fracture toughness testing of thick section FRP composites using the ESE(T) specimen. In: *Engineering Fracture Mechanics* 72.4, pp. 631–643 (cit. on p. 50).

Elices M., Guinea G. V., Gómez J. and Planas J. (2002). The cohesive zone model: advantages, limitations and challenges. In: *Engineering Fracture Mechanics* 69.2, pp. 137–163 (cit. on pp. 19, 21, 27, 31–34).

Elices M., Rocco C. and Roselló C. (2009). Cohesive crack modelling of a simple concrete: Experimental and numerical results. In: *Engineering Fracture Mechanics* 76.10, pp. 1398–1410 (cit. on p. 22).

Floyd A. M. (2004). An engineering approach to the simulation of gross damage development in composite laminates, Ph.D. Thesis. University of British Columbia (cit. on pp. 50, 82).

Garg A. (1985). Fracture Behavior of Cross-Ply Graphite-Epoxy Laminates. In: *Engineering Fracture Mechanics* 22.6, pp. 1035–1985 (cit. on p. 50).

González E. V., Maimí P., Sainz de Aja J. R., Cruz P. and Camanho P. P. (2014). Effects of interply hybridization on the damage resistance and tolerance of composite laminates. In: *Composite Structures* 108.0, pp. 319–331 (cit. on p. 75).

Green D. W., Winandy J. E. and Kretschmann D. E. (1999). Mechanical properties of wood. Wood handbook: wood as an engineering material. Madison; WI: USDA Forest Service, pp. 4.1–4.45 (cit. on p. 53).

Griffith A. A. (1924). The Theory of Rupture. In: *1st International Congress on Applied Mechanics*. Ed. by C. B. Bienzano and J. M. Burgers. Tech. Boekhandel en Drukkerij, pp. 54–63 (cit. on p. 10).

Griffith A. (1921). The Phenomena of Rupture and Flow in Solids. In: *Philosophical Transactions of the Royal Society of London. Series A, Containing Papers of a Mathematical or Physical Character* 221, pp. 163–198 (cit. on p. 10).

Gutkin R., Laffan M. L., Pinho S. T., Robinson P. and Curtis P. T. (2011). Modelling the R-curve effect and its specimen-dependence. In: *International Journal of Solids and Structures* 48.11-12, pp. 1767–1777 (cit. on p. 50).

Haj-Ali R. and El-Hajjar R. (2003). Crack propagation analysis of mode-I fracture in pultruded composites using micromechanical constitutive models. In: *Mechanics of Materials* 35.9, pp. 885–902 (cit. on p. 50).

Haj-Ali R., El-Hajjar R. and Muliana A. (2006). Cohesive fracture modeling of crack growth in thick-section composites. In: *Engineering Fracture Mechanics* 73.15, pp. 2192–2209 (cit. on p. 50).

Hillerborg A., Modéer M. and Petersson P. E. (1976). Analysis of crack formation and crack growth in concrete by means of fracture mechanics and finite elements. In: *Cement and Concrete Research* 6.6, pp. 773–781 (cit. on pp. 19, 61).

Hordijk D. A., Reinhardt H. W. and Cornelissen H. A. W. (1987). Fracture mechanics parameters of concrete from uniaxial tensile tests as influenced by specimen length. In: *Fracture of Concrete and Rock*. Ed. by S. P. Shah and S. E. Swartz. Bethel: SEM-RILEM, pp. 138–149 (cit. on p. 27).

Inglis C. E. (1913). Stress in a plate due to the presence of cracks and sharp corners. In: *Proc. Inst. Naval Architect.* 55, pp. 219–241 (cit. on p. 11).

Irwin G. R. (1960). Fracture mechanics. In: *Structural mechanics*. London: Pergamon Press (cit. on p. 60).

Irwin G. R. (1957). Analysis of stresses and strains near the end of a crack traversing a plate. In: *Journal of Applied Mechanics* 24.9, pp. 361–364 (cit. on pp. 11, 13, 15, 16).

Irwin G. R. (1961). Plastic Zone Near a Crack and Fracture Toughness. In: *Sagamore Research Conference Proceeding* 4, pp. 63–78 (cit. on pp. 15, 16).

Jacobsen T. K. and Sørensen B. F. (2001). Mode I intra-laminar crack growth in composites - modelling of R-curves from measured bridging laws. In: *Composites Part A: Applied Science and Manufacturing* 32, pp. 1–11 (cit. on p. 70).

Jose S., Ramesh Kumar R., Jana M. K. and Venkateswara Rao G. (2001). Intralaminar fracture toughness of a cross-ply laminate and its constituent sub-laminates. In: *Composites Science and Technology* 61.8, pp. 1115–1122 (cit. on p. 50).

Koester K. J., Ager J. W. and Ritchie R. O. (2008a). The true toughness of human cortical bone measured with realistically short cracks. In: *Nature Materials* 7.8, pp. 672–677 (cit. on p. 70).

Koester K. J., Ager J. W. and Ritchie R. O. (2008b). The effect of aging on crack-growth resistance and toughening mechanisms in human dentin. In: *Biomaterials* 29, pp. 1318–1328 (cit. on p. 70).

Kongshavn I. and Poursartip A. (1999). Experimental investigation of a strain-softening approach to predicting failure in notched fibre-reinforced composite laminates. In: *Composites Science and Technology* 59.1, pp. 29–40 (cit. on pp. 50, 82).

Kongshavn I. A. (1996). Experimental Investigation of a Strain Softening Approach to Predicting Failure of Notched Composite Laminates, Ph.D. Thesis. P. 149 (cit. on pp. 50, 82).

Laffan M. J., Pinho S. T., Robinson P. and Iannucci L. (2010a). Measurement of the in situ ply fracture toughness associated with mode I fibre tensile failure in FRP. Part I: Data reduction. In: *Composites Science and Technology* 70.4, pp. 614–621 (cit. on pp. 50, 53).

Laffan M. J., Pinho S. T., Robinson P. and Iannucci L. (2010b). Measurement of the in situ ply fracture toughness associated with mode I fibre tensile failure in FRP. Part II: Size and lay-up effects. In: *Composites Science and Technology* 70.4, pp. 614–621 (cit. on pp. 50, 56, 78).

Laffan M. J., Pinho S. T., Robinson P. and McMillan A. (2011). Translaminar fracture toughness: The critical notch tip radius of 0^o plies in CFRP. In: *Composites Science and Technology* 72.1, pp. 97–102 (cit. on p. 50).

Laffan M. J., Pinho S. T., Robinson P., Iannucci L. and McMillan A. J. (2012a). Measurement of the fracture toughness associated with the longitudinal fibre compressive failure mode of laminated composites. In: *Composites Part A: Applied Science and Manufacturing* 43.11, pp. 1930–1938 (cit. on p. 50).

Laffan M. J., Pinho S. T., Robinson P. and McMillan a. J. (2012b). Translaminar fracture toughness testing of composites: A review. In: *Polymer Testing* 31.3, pp. 481–489 (cit. on p. 50).

Lekhnitskii S. G. (1963). Theory of elasticity of an anisotropic body. Holdenday (cit. on p. 52).

Li. V. C., Chan C.-M. and Leung C. K. (1987). Experimental determination of the tension-softening relations for cementitious composites. In: *Cement and Concrete Research* 17, pp. 441–452 (cit. on p. 36).

Li X., Hallett S. R., Wisnom M. R., et al. (2009). Experimental study of damage propagation in Over-height Compact Tension tests. In: *Composites Part A: Applied Science and Manufacturing* 40.12, pp. 1891–1899 (cit. on pp. 50, 79, 82).

Lindhagen J. E., Gamstedt E. K. and Berglund L. A. (2000). Application of bridging-law concepts to short-fibre composites. Part 3: Bridging law derivation from experimental crack profiles. In: *Composites Science and Technology* 60.16, pp. 2883–2894 (cit. on pp. 39, 40).

Lindhagen J. and Berglund L. (2000). Application of bridging-law concepts to short-fibre composites. Part 1: DCB test procedures for bridging law and fracture energy. In: *Composites Science and Technology* 60.6, pp. 871–883 (cit. on p. 36).

Mai Y. W. (2006). Cohesive zone and crack-resistance (R)-curve of cementitious materials and their fibre-reinforced composites. In: *Engineering Fracture Mechanics* 69.2002, pp. 219–234 (cit. on p. 19).

Mai Y. W. and Hakeem M. I. (1984). Slow crack growth in bleached cellulose fibre cements. In: *Journal of Materials Science Letters* 3.2, pp. 127–130 (cit. on p. 25).

Maimí P., Camanho P. P., Mayugo J. and Dávila C. G. (2007a). A continuum damage model for composite laminates: Part I: Constitutive model. In: *Mechanics of Materials* 39.10, pp. 897–908 (cit. on pp. 46, 50).

Maimí P., Camanho P. P., Mayugo J. and Dávila C. G. (2007b). A continuum damage model for composite laminates: Part II: Computational implementation and validation. In: *Mechanics of Materials* 39.10, pp. 909–919 (cit. on pp. 46, 50).

Maimí P., Trias D., González E. and Renart J. (2012). Nominal strength of quasi-brittle open hole specimens. In: *Composites Science and Technology* 72.10, pp. 1203–1208 (cit. on pp. 25, 32, 43, 50).

Maimí P, González E. V., Gascons N and Ripoll L. (2013). Size Effect Law and Critical Distance Theories to Predict the Nominal Strength of Quasibrittle Structures. In: *Applied Mechanics Reviews* 65, pp. 1–16 (cit. on p. 50).

Massabò R., Brandinelli L. and Cox B. N. (2003). Mode I weight functions for an orthotropic double cantilever beam. In: *International Journal of Engineering Science* 41.13-14, pp. 1497–1518 (cit. on p. 107).

Masters J. E. (1997). Translaminar Fracture Toughness of a Composite Wing Skin Made of Stitched Warp-knit Fabric. In: *Nasa Contractor Report* November (cit. on pp. 50, 51).

Mier J. G. M. van and Vliet M. R. A. van (2002). Uniaxial tension test for the determination of fracture parameters of concrete: state of the art. In: *Engineering Fracture Mechanics* 69, pp. 235–247 (cit. on p. 30).

Mihashi H and Nomura N (1996). Correlation between characteristics of fracture process zone and tension-softening properties of concrete. In: *Nuclear Engineering and Design* 165, pp. 359–376 (cit. on p. 45).

Minnetyan L. and Chamis C. C. (1996). The C(T) Specimen in Laminated Composites Testing. In: *Nasa Technical Memorandum* NASA-Technical Memorandum 4712 (cit. on p. 50).

Muskhelishvili N. (1954). Some Basic Problems in the Theory of Elasticity. 4th Edition. Noordhoff, Leyden (cit. on p. 11).

Newman J. (1983). A nonlinear fracture mechanics approach to the growth of small cracks. In: *AGARD*. Vol. 5, No. 328, 6.1–6.26 (cit. on p. 43).

Olsson P. and Stigh U. (1989). On the determination of the constitutive properties of thin interphase layers - An exact inverse solution. In: *International Journal of Fracture* 41.1, pp. 71–76 (cit. on p. 37).

Ortega A., Maimí P., González E. and Ripoll L. (2014). Compact tension specimen for orthotropic materials. In: *Composites Part A: Applied Science and Manufacturing* 63, pp. 85–93 (cit. on p. 50).

Ortega A, Maimí P and González E. V. (2015). Characterization of the intralaminar fracture cohesive law. In: *7th International Conference on Composite Testing and Model Identification COMPTEST 2015* (cit. on p. 39).

Ortega A., Maimí P., González E. V. and Trias D. (2016). Characterization of the translaminar fracture cohesive law. In: *Composites Part A: Applied Science and Manufacturing* (cit. on pp. 39, 66).

Parhizgar S., Zachary L. W. and Sun C. T. (1982). Application of the principles of linear fracture mechanics to the composite materials. In: *International Journal of Fracture* 20.1, pp. 3–15 (cit. on p. 50).

Paris A. J. and Paris P. C. (1988). Instantaneous Evaluation of J and C*. In: *International Journal of Fracture* 38, pp. 19–21 (cit. on p. 37).

Piascik R. S. and Newman J. C. (1995). An extended compact tension specimen for fatigue crack growth and fracture testing. In: *International Journal of Fracture* 76.3, R43–R48 (cit. on p. 50).

Piascik R. S., Newman J. C. and Underwood J. H. (1997). The extended compact tension specimen. In: *Fatigue & Fracture of Engineering Materials & Structures* 20.4, pp. 559–563 (cit. on p. 50).

Pinho S. T., Robinson P. and Iannucci L. (2006). Fracture toughness of the tensile and compressive fibre failure modes in laminated composites. In: *Composites Science and Technology* 66.13, pp. 2069–2079 (cit. on pp. 50, 106).

Planas J and Elices M. (1999). Size effect and inverse analysis in concrete fracture. In: 19, pp. 367–378 (cit. on pp. 29, 31).

Planas J., Elices M., Guinea G. V., et al. (2003). Generalizations and specializations of cohesive crack models. In: *Engineering Fracture Mechanics* 70.14, pp. 1759–1776 (cit. on pp. 22, 30).

Poe C. C. and Reeder J. R. (2001). Fracture Behavior of a Stitched Warp-Knit Carbon Fabric Composite. May (cit. on p. 50).

Que N. S. (2003). Identification of cohesive crack fracture parameters using mathematical programming. PhD thesis (cit. on p. 44).

Que N. S. and Tin-Loi F (2002). An optimization approach for indirect identification of cohesive crack properties. In: *Computer & Structures* 80, pp. 1383–1392 (cit. on pp. 39, 44).

Rice J. R. (1968). A Path Independent Integral and the Approximate Analysis of Strain Concentration by Notches and Cracks. In: 35, pp. 379–386 (cit. on p. 23).

Ritchie R. O. (2011). The conflict between strength and toughness. In: *Nature materials* 10, pp. 817–822 (cit. on p. 59).

Roelfstra P. E. and Wittmann F. H. (1986). Numerical method to link strain softening with failure of concrete. In: *Fracture Toughness and Fracture Energy of Concrete*. Ed. by F. H. Wittmann. B. V., Amsterdam: Elsevier Science Publishers, pp. 163–175 (cit. on p. 39).

Sharpe J. and William N. (2008). Springer Handbook of Experimental Solid Mechanics. 1st Edition. Springer, p. 1128 (cit. on p. 9).

Silva F. G., Xavier J., Pereira F. A., et al. (2014). Determination of cohesive laws in wood bonded joints under mode II loading using the ENF test. In: *International Journal of Adhesion and Adhesives* 51.8, pp. 54–61 (cit. on p. 39).

Sket F., Seltzer R., Molina-Aldareguía J. M., Gonzalez C. and Llorca J. (2012). Determination of damage micromechanisms and fracture resistance of glass fiber/epoxy cross-ply laminate by means of X-ray computed microtomography. In: *Composites Science and Technology* 72.2, pp. 350–359 (cit. on p. 50).

Slepetz J. M. and Carlson L. (1975). Fracture of Composite Compact Tension Specimens. In: *Fracture Mechanics of Composites*. Ed. by G. P. Sendeckyj. March. ASTM STP 593 (cit. on p. 50).

Sørensen B. F. and Jacobsen T. K. (1998). Large-scale bridging in composites: R-curves and bridging laws. In: *Composites Part A: Applied Science and Manufacturing* 29.11, pp. 1443–1451 (cit. on p. 70).

Sørensen B. F. and Jacobsen T. K. (2003). Determination of cohesive laws by the J integral approach. In: *Engineering Fracture Mechanics* 70, pp. 1841–1858 (cit. on p. 36).

Sørensen B. F., Jørgensen K., Jacobsen T. K. and Østergaard R. C. (2006). DCB-specimen loaded with uneven bending moments. In: *International Journal of Fracture* 141, pp. 163–176 (cit. on p. 37).

Sørensen B. F., Gamstedt E. K., Østergaard R. C. and Goutianos S. (2008a). Micromechanical model of cross-over fibre bridging - Prediction of mixed mode bridging laws. In: *Mechanics of Materials* 40.4-5, pp. 220–234 (cit. on p. 70).

Sørensen L., Botsis J., Gmür T. and Humbert L. (2008b). Bridging tractions in mode I delamination: Measurements and simulations. In: *Composites Science and Technology* 68.12, pp. 2350–2358 (cit. on p. 40).

Soutis C., Fleck N. A. and Smith P. A. (1991). Failure Prediction Technique for Compression Loaded Carbon Fibre-Epoxy Laminate with Open Holes. In: *Journal of Composite Materials* 25.11, pp. 1476–1498 (cit. on p. 50).

Steiger T., Sadouki H. and Wittmann F. H. (1995). Simulation and Observation of the Fracture Process Zone. In: *Proc. of Fracture Mechanics of Concrete Structures, FRAMCOS II*. Vol. II, pp. 157–168 (cit. on p. 39).

Stutz S., Cugnoni J. and Botsis J. (2011a). Crack - fiber sensor interaction and characterization of the bridging tractions in mode I delamination. In: *Engineering Fracture Mechanics* 78.6, pp. 890–900 (cit. on p. 40).

Stutz S., Cugnoni J. and Botsis J. (2011b). Studies of mode I delamination in monotonic and fatigue loading using FBG wavelength multiplexing and numerical analysis. In: *Composites Science and Technology* 71.4, pp. 443–449 (cit. on p. 40).

Suo Z (1990). Delamination Specimens for Orthotropic Materials. In: *Journal of Applied Mechanics-Transactions of the Asme* 57.3, pp. 627–634 (cit. on p. 53).

Suo Z, Bao G and Fan B. (1992). Delamination R-curve phenomena due to damage. In: *Journal of the Mechanics and Physics of Solids* 40.1, pp. 1–16 (cit. on pp. 37, 70).

Tada H., Paris P. C. and Irwin G. R. (2000). The stress analysis of cracks handbook. New York: ASME Press, pp. 62–63 (cit. on p. 12).

Tan S. C. (1988). Effective Stress Fracture Models for Unnotched and Notched Multidirectional Laminates. In: *Journal of Composite Materials* 22, pp. 322–340 (cit. on p. 50).

Taylor D. (2008). The theory of critical distances. In: *Engineering Fracture Mechanics* 75.7, pp. 1696–1705 (cit. on p. 50).

Taylor D. (2007). The Theory of Critical Distances, a New Perspective in Fracture Mechanics. Elsevier (cit. on p. 50).

Tschegg E. K., Humer K. and Weber H. W. (1993). Fracture tests in Mode I on fibre-reinforced plastics. In: *Journal of Materials Science* 28.9, pp. 2471–2480 (cit. on p. 45).

Turon A., Camanho P. P., Costa J. and Dávila C. G. (2006). A damage model for the simulation of delamination in advanced composites under variable-mode loading. In: *Mechanics of Materials* 38.11, pp. 1072–1089 (cit. on pp. 46, 65).

Underwood J. and Kortschot M. (1993). Notch-tip Damage and Translaminar Fracture Toughness Measurements from Carbon/Epoxy Laminates. In: *Proceedings of 2nd International Conference on Deformation and Fracture of Composites* (cit. on p. 50).

Underwood J., Kortschot M., Lloyd W., et al. (1995). Translaminar Fracture Toughness Test Methods and Results from Interlaboratory Tests of Carbon/Epoxy Laminates. In: *National symposium on fracture mechanics*. ASTM (cit. on p. 50).

Vasiliev V. V. and Morozov E. V. (2007). Advanced Mechanics of Composite Materials (Second Edition). Ed. by V. V. Vasiliev and E. V. Morozov. Second Edition. Oxford: Elsevier Science Ltd (cit. on p. 2).

Whitney J. and Nuismer R. (1974). Stress Fracture Criteria for Laminated Composites Containing Stress Concentrations. In: *Journal of Composite Materials* 8.3, pp. 253–265 (cit. on p. 50).

Williams M. L. (1957). On the stress distribution at the base of a stationary crack. In: *Journal of Applied Mechanics* 24.1, pp. 109–114 (cit. on p. 11).

Williams T. N., Newman Jr J. C. and Gullett P. M. (2011). Crack-surface displacements for cracks emanating from a circular hole under various loading conditions. In: *Fatigue & Fracture of Engineering Materials & Structures* 34.4, pp. 250–259 (cit. on p. 43).

Xu X., Wisnom M. R., Mahadik Y. and Hallett S. R. (2014). An experimental investigation into size effects in quasi-isotropic carbon/epoxy laminates with sharp and blunt notches. In: *Composites Science and Technology* 100, pp. 220–227 (cit. on p. 86).

Xu X., Wisnom M. R., Mahadik Y. and Hallett S. R. (2015). Scaling of fracture response in overheight compact tension tests. In: *Composites Part A: Applied Science and Manufacturing* 69, pp. 40–48 (cit. on pp. 50, 82).

Yan J., Mecholsky J. J. and Clifton K. B. (2007). How tough is bone? Application of elasticplastic fracture mechanics to bone. In: *Bone* 40.2, pp. 479–484 (cit. on p. 70).

Zihai Shi (2009). Crack Analysis in Structural Concrete: Theory and Applications. 1 st. Butterworth-Heinemann, p. 344 (cit. on p. 9).

Zobeiry N., Vaziri R. and Poursartip A. (2014). Characterization of Strain-Softening Behaviour and Failure Mechanisms of Composites under Tension and Compression. In: *Composites Part A: Applied Science and Manufacturing* 68, pp. 29–41 (cit. on pp. 38, 50, 82).

Part VI

Appendices

A

Appendix A: Polynomial fitting functions

The polynomial function $q(\bar{a}, \lambda, \rho)$ of Eq. 4.10 can be expressed in matrix form as follows:

$$q(\bar{a}, \lambda, \rho) = \begin{bmatrix} 1 \\ \bar{\lambda} \\ \bar{\rho} \\ \bar{\lambda}^2 \\ \bar{\lambda}\bar{\rho} \\ \bar{\rho}^2 \\ \bar{\lambda}^3 \\ \bar{\lambda}^2\bar{\rho} \\ \bar{\lambda}\bar{\rho}^2 \end{bmatrix}^T \begin{bmatrix} 1.6128 & 8.9466 & -20.688 & 18.786 & -5.5381 \\ -3.2808 & 32.523 & -94.902 & 116.73 & -51.736 \\ 0.71078 & 8.4546 & -11.629 & -3.8438 & 8.454 \\ 0.34995 & 1.2604 & 15.834 & -37.624 & 20.129 \\ -2.1383 & 12.246 & -29.195 & 37.859 & -18.884 \\ -0.46023 & 15.616 & -34.155 & 25.156 & -7.1906 \\ -1.4802 & 12.872 & -33.187 & 30.728 & -8.6936 \\ -0.57399 & 7.1987 & -34.221 & 54.132 & -26.768 \\ -3.0283 & 23.403 & -54.343 & 41.271 & -6.7808 \end{bmatrix} \begin{bmatrix} 1 \\ \bar{a} \\ \bar{a}^2 \\ \bar{a}^3 \\ \bar{a}^4 \end{bmatrix} \tag{A.1}$$

where:

$$\bar{\lambda} = \log\lambda \quad , \quad \bar{\rho} = \log(\rho + 1) \tag{A.2}$$

The polynomial function B of Eq. 4.10 is:

$$B = -0.24216 + 1.4018\bar{\bar{a}} - 0.003505\bar{\rho} + 1.4908\bar{\bar{a}}^2 - 0.058317\bar{\bar{a}}\bar{\rho} \tag{A.3}$$

where $\bar{\bar{a}}$ is:

$$\bar{\bar{a}} = \log\bar{a} \tag{A.4}$$

The polynomial function $p(\bar{a}, \lambda, \rho)$ of Eq. 4.11 can be expressed in matrix form as follows:

$$p(\bar{a}, \lambda, \rho) = \begin{bmatrix} 1 \\ \bar{\lambda} \\ \bar{\rho} \\ \bar{\lambda}^2 \\ \bar{\lambda}\bar{\rho} \\ \bar{\rho}^2 \\ \bar{\lambda}^3 \\ \bar{\lambda}^2\bar{\rho} \\ \bar{\lambda}\bar{\rho}^2 \end{bmatrix}^T \begin{bmatrix} 0.30817 & 2.1609 & -5.72 & 6.2711 & -2.4512 \\ 0.61118 & -4.5341 & 12.698 & -14.428 & 5.5896 \\ 0.098042 & 2.3871 & -8.6206 & 10.742 & -4.3791 \\ 0.1443 & 0.098426 & 0.47793 & -2.5788 & 1.9266 \\ -1.2451 & 8.9848 & -22.996 & 26.09 & -11.037 \\ 0.85309 & -3.104 & 7.3777 & -9.0334 & 4.0197 \\ -0.14716 & 1.752 & -6.0346 & 7.7217 & -3.3098 \\ -0.16912 & 0.82943 & -2.7216 & 4.5667 & -2.6053 \\ 0.12556 & -0.35037 & -0.53346 & 0.90753 & -0.042327 \end{bmatrix} \begin{bmatrix} 1 \\ \bar{a} \\ \bar{a}^2 \\ \bar{a}^3 \\ \bar{a}^4 \end{bmatrix} \tag{A.5}$$

The polynomial function D of Eq. 4.11 is defined as:

$$D = -0.066112 + 0.75681\bar{\bar{a}} - 0.015\bar{\rho} + 0.58136\bar{\bar{a}}^2 - 0.08451\bar{\bar{a}}\bar{\rho} \tag{A.6}$$

The polynomial function $r(\bar{a}, \lambda, \rho)$ of Eq. 4.12 can be expressed in matrix form as follows:

$$r(\bar{a}, \lambda, \rho) = \begin{bmatrix} 1 \\ \bar{\lambda} \\ \bar{\rho} \\ \bar{\lambda}^2 \\ \bar{\lambda}\bar{\rho} \\ \bar{\rho}^2 \\ \bar{\lambda}^3 \\ \bar{\lambda}^2\bar{\rho} \\ \bar{\lambda}\bar{\rho}^2 \end{bmatrix}^T \begin{bmatrix} 6.7195 & -47.349 & 129.7 & -150.03 & 66.291 \\ -0.15366 & 4.1923 & -7.3129 & 1.6292 & 3.1257 \\ -1.1389 & 6.2549 & -12.787 & 14.461 & -7.2961 \\ 2.2165 & -14.813 & 32.255 & -28.591 & 9.0782 \\ -3.0204 & 16.775 & -40.317 & 44.5 & -18.129 \\ -1.4327 & 11.786 & -35.032 & 43.226 & -19.277 \\ -0.25291 & 0.48823 & 1.7188 & -4.258 & 2.329 \\ -3.2837 & 24.238 & -60.512 & 63.226 & -23.799 \\ 4.5281 & -30.891 & 78.302 & -85.562 & 33.658 \end{bmatrix} \begin{bmatrix} 1 \\ \bar{a} \\ \bar{a}^2 \\ \bar{a}^3 \\ \bar{a}^4 \end{bmatrix} \tag{A.7}$$

Part VII

Generated papers

PAPER A

Compact tension specimen for orthotropic materials

A. Ortega [a], P. Maimí [a], E.V. González [a], Ll. Ripoll [a]

[a]AMADE, Mechanical Engineering and Industrial Construction Department, Universitat de Girona, Campus Montilivi s/n, Girona, Spain

The paper has been published in *Composites Part A: Applied Science and Manufacturing Vol. 63 (2014) 85-93.*

Composites: Part A 63 (2014) 85–93

Contents lists available at ScienceDirect

Composites: Part A

journal homepage: www.elsevier.com/locate/compositesa

Compact tension specimen for orthotropic materials

A. Ortega *, P. Maimí, E.V. González, Ll. Ripoll

AMADE, Mechanical Engineering and Industrial Construction Department, Universitat de Girona, Campus Montilivi s/n, Girona, Spain

ARTICLE INFO

Article history:
Received 10 July 2013
Received in revised form 3 April 2014
Accepted 17 April 2014
Available online 26 April 2014

Keywords:
B. Anisotropy
B. Fracture
B. Fracture toughness
D. Mechanical testing

ABSTRACT

A solution for a Compact Tension (CT) specimen is proposed in order to obtain the *linear elastic fracture toughness*, the *stress intensity factor* and the *compliance at the load line*. The solution applies for any orthotropic material whose principal directions are defined by the crack direction, assuming that the crack grows along the symmetry plane of the specimen. Given two dimensionless parameters, λ and ρ, that define the orthotropy of the material, the elastic response is unique. With the aid of a parameterized Finite Element Model (FEM), a solution is obtained for any orthotropic material. The results are fitted into an interpolating function, which shows excellent agreement with simulated data. Additionally, the initial crack length required to produce a stable crack growth under displacement control is studied for various material orthotropies. Finally, some failure criteria are introduced regarding the failure at the holes of the CT and at the back end face of the specimen. Some design recommendations are given after analyzing the failure mechanisms.

© 2014 Elsevier Ltd. All rights reserved.

1. Introduction

When Linear Elastic Fracture Mechanics (LEFM) were first developed, metallic materials were the most widely used in industry and this remains the case today. Since metals are considered to be mainly isotropic, most standardized methods [1–4] for obtaining the fracture properties, such as the critical fracture energy G_{Ic} or the stress intensity factor (SIF) K_{Ic} are developed considering isotropic materials. Despite this, most of the other materials used in industrial applications are anisotropic in nature. Woods and advanced materials, such as fiber reinforced composites, have been used increasingly in recent years. Such materials are far from satisfying the expectations of isotropy and, therefore, current standardized methods cannot be applied [5–7]. This situation means new tools and procedures need to be developed in order to measure the fracture properties of anisotropic materials.

From an LEFM point of view, and assuming that there are no inelastic energy dissipation mechanisms (except for those occurring at the crack tip), the critical fracture toughness can be seen as the elastic Energy Release Rate (ERR) per new unit area created. In the case of the CT specimen, the crack length is normalized as $\bar{a} = a/w$, where a is the crack length measured from the load application point and w is the span between the load point and the back end face of the specimen, as seen in Fig. 1. Even though the standard CT specimen has a normalized size of $w = 51$ mm, the formulation and the methodology here presented can be used for other sizes of w as long as the CT geometry is respected. With the principal directions defined as x_1 parallel to the loading direction and x_2 aligned to the symmetry plane, and assuming that the crack grows along the x_2 direction, a unique relation between the specimen compliance (C) and the normalized crack length exists. When this relation is known, it is possible to infer the crack length from the experimental compliance curve and, in conjunction with the load - load application point displacement (P_i–u_i), it is possible, ultimately, to obtain G_{Ic} or K_{Ic}. This procedure cannot be applied if the crack does not propagate along the x_2 direction, as occurs in the case of some composite materials where the majority of the plies are aligned in a direction different to x_2 [8].

Up to now, the general function $C(\bar{a})$ has only been obtained for isotropic materials [3,4]. For other types of anisotropy, current methods involve optically measuring the crack tip length during the test [7], measuring the crack tip location with the aid of the Digital Image Correlation technique [6], or the use of a Finite Element Method program [5,6,9]. Using the SIF isotropic solution on orthotropics materials can lead to significant error. For example, when computing the K_I of a T300/913 carbon epoxy cross-ply composite material with a laminate sequence of $(90,0)_{8s}$ with the standard isotropic solution, an error of 11% results with respect to that obtained by a FEM model, taking into account the orthotropy of the laminate [9]. The aim of this paper is to obtain analytical expressions of the linear elastic fracture toughness, the stress intensity factor and the compliance of the CT geometry while taking into account the orthotropy of the material. It is important to note that

---

* Corresponding author.
E-mail address: adri.ort@gmail.com (A. Ortega).

http://dx.doi.org/10.1016/j.compositesa.2014.04.012
1359-835X/© 2014 Elsevier Ltd. All rights reserved.

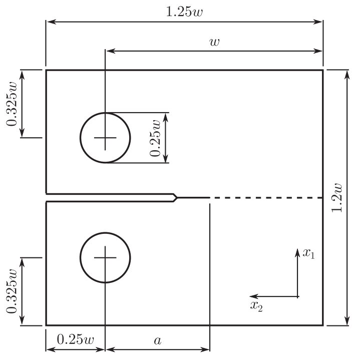

Fig. 1. Compact Tension (CT) specimen geometry, with all dimensions defined with respect to the size *w*, where the dashed line represents the crack path.

the same methodology described here may be used to determine the compliance and SIF functions of other specimen geometries, although the equations and results presented are only valid for the geometry of Fig. 1.

Expressions such as the ones presented here are useful to obtain G_{Ic} or K_{Ic} from experimental results. As previously stated, they can be found in many Fracture Mechanics handbooks [3,4] and in standardized procedures [1,2] only for the isotropic case. Obtaining the expressions for the orthotropic case may improve the level of standardization on how to obtain fracture properties of non-isotropic materials, instead of computing a particular FEM solution for every different material that needs to be tested. Also, in some cases, an explicit expression of the SIF in terms of the crack length is needed when solving more complicated Fracture Mechanics problems, such as crack-bridging models and cohesive models. A linear FEM is not enough to solve this type of problems, and non-linear constitutive models are needed, which require high computational time and resources. The use of explicit expressions, like the ones presented in this paper, can help to reduce the computing times drastically.

This paper is structured as follows: Section 2 defines the stress field of a planar orthotropic solid as a function of two dimensionless parameters, λ and ρ, which define the orthotropy of the material. Section 3 presents the procedure and assumptions of the FEM models. Section 4 contains a parametric function of the compliance and the SIF for a wide range of orthotropies. In Section 5, the stability of the crack growth is studied from a linear elastic point of view. Section 6 presents some design recommendations based on the proposed material failure criteria. Finally, Section 7 summarizes the conclusions and describes the relevance of this work.

2. Stress field of a planar orthotropic solid

In a bi-dimensional problem defined by the x_1–x_2 plane, the stress state of an elastic body with its boundary conditions (BCs) prescribed only by tractions depends solely on the BCs, the geometry and two dimensionless parameters that define the anisotropy of the material [10]. Consequently, for any given isotropic material, these values remain constant and, therefore, the stress state does not depend on the material. This property of the stress state means it is relatively simple to generate $C(\bar{a})$ and stress intensity factor curves.

Given a general anisotropic material with a linear constitutive relation, in a bi-dimensional problem, the stress–strain relation can be expressed as:

$$\varepsilon_i = \sum_{j=1,2,6} b_{ij}\sigma_j, \quad i = 1,2,6 \tag{1}$$

where:

$$b_{ij} = \begin{cases} s_{ij}, \text{for plane stress} \\ s_{ij} - s_{i3}s_{j3}/s_{33}, \text{for plane strain} \end{cases} \quad i,j = 1,2,6. \tag{2}$$

It is known that for any anisotropic material, the solution of the differential equation that defines the stress state depends on the roots of the characteristic polynomial [10]:

$$b_{11}p^4 - 2b_{16}p^3 + (2b_{12} + b_{66})p^2 - 2b_{26}p + b_{22} = 0 \tag{3}$$

with four complex roots in p. If the material is orthotropic with the principal directions x_1–x_2 defined by the principal axes of the material, only four independent elastic constants are needed: $b_{11},\ b_{12} = b_{21},\ b_{22}$ and b_{66}, since $b_{16} = b_{26} = 0$. Hence, Eq. (3) is reduced to:

$$\lambda p^4 + 2\rho\sqrt{\lambda}p^2 + 1 = 0 \tag{4}$$

where p_1 and p_2 are the roots with positive imaginary parts and:

$$\lambda = \frac{b_{11}}{b_{22}}, \quad \rho = \frac{2b_{12} + b_{66}}{2\sqrt{b_{11}b_{22}}} \tag{5}$$

In the plane stress case, λ and ρ are expressed as:

$$\lambda = \frac{E_{22}}{E_{11}}, \quad \rho = \frac{\sqrt{\lambda}}{2G_{12}}(E_{11} - 2\nu_{12}G_{12}) \tag{6}$$

where E_{11} and E_{22} are the elastic moduli, G_{12} is the shear modulus, and ν_{12} is the Poisson's ratio. In the plane strain case, λ and ρ are obtained by replacing $E_{11},\ E_{22}$ and ν_{12} in Eq. (6) by:

$$E'_{11} = \frac{E_{11}}{1 - \nu_{13}\nu_{31}}, \quad E'_{22} = \frac{E_{22}}{1 - \nu_{23}\nu_{32}}, \quad \nu'_{12} = \frac{\nu_{12} + \nu_{13}\nu_{32}}{1 - \nu_{13}\nu_{31}} \tag{7}$$

To ensure the positive definiteness of the strain energy, it must be ensured that:

$$\lambda > 0 \quad \text{and} \quad \rho > -1 \tag{8}$$

The anisotropy of the material is easily described by the parameters λ and ρ. For an isotropic material, the parameters take the values $\lambda = \rho = 1$. However, for a cubic material, it only needs to be ensured that $\lambda = 1$ and that $\rho \neq 1$. Table 1 contains the values of λ and ρ for a number of materials. From the point of view of composite laminates, the laminate anisotropy is determined by the lay-up sequence; an in-plane isotropic lay-up may have its principals axes oriented in any direction by definition. Some examples of laminate sequences that satisfy this condition are $[0, \pm60]_s, [0, \pm45, 90]_s$ or $[0, \pm36, \pm72]_s$. On the other hand, cubic materials have a principal axis every 45°. An example of cubic laminate sequence is a cross-ply laminate.

Table 1
Values of λ and ρ for seven different materials.

Material	λ	ρ
T300/920 unidirectional lamina [19]	0.0657	3.7326
T300/920 $[0, \pm60]_s$ isotropic	1.0	1.0
T300/920 $[0, 90]_s$ cubic	1.0	7.9302
Western White Pine wood [20]	0.0380	1.9635
Northern White Cedar wood [20]	0.0810	0.6642
Cu (*FCC*) [21]	1.0	0.03
Fe (*BCC*) [21]	1.0	0.20

The relation between the applied load P and the load application point displacement u is expressed by the compliance C which depends on the normalized crack length $\bar{a}$, λ and ρ:

$$u = P \cdot C \tag{9}$$

The compliance C can be expressed in terms of a dimensionless function:

$$C = \frac{\overline{C}(\bar{a}, \lambda, \rho)}{h \cdot E_{11}} \tag{10}$$

where $\overline{C}$ is the normalized compliance, h is the specimen thickness and E_{11} is the elastic modulus of the material along the loading direction. This normalization has also been used by other authors [3]. The normalized compliance $\overline{C}$ is unique for a given material orthotropy and a normalized crack length.

The energy release rate is obtained as follows:

$$G_I = \frac{1}{h}\frac{\partial U}{\partial a} = \frac{1}{2}\frac{P^2}{h^2 E_{11} w}\frac{\partial \overline{C}}{\partial \bar{a}} \tag{11}$$

where $\partial U/\partial a$ is the rate of change of the stored elastic energy U with respect to the crack length a and $\partial \overline{C}/\partial \bar{a}$ is the rate of change in the dimensionless compliance of the specimen with respect to the normalized crack length $\bar{a}$. Finally, for an orthotropic material, the relation between the SIF and G_I is defined as [11]:

$$K_I^2 = G_I E_{11}\sqrt{\frac{2\lambda^{3/2}}{1+\rho}} \tag{12}$$

3. Numerical simulations

A parametric FEM model was created using Python scripting together with ABAQUS/Standard 6.11-1 FEM software. The 4-node bi-linear quadrilateral with reduced integration and hourglass control plane stress element (CPS4R) was used to mesh the model. This type of element has been shown to properly capture the bending properties when it is used as with a rectangular shape aligned with the principal axes of bending [12]. Compared to other types of elements, the results obtained with CPS4R elements were the ones that best matched the tabulated isotropic solution, which is based on the Boundary Collocation Method analysis [3]. Three different average element sizes of 1.0 mm, 0.5 mm and 0.25 mm were considered for the coarse mesh, resulting in differences of less than 1% for the computed compliance. An average element size of 0.5 mm was chosen for the rest of the simulations. The geometry of Fig. 1 was respected, with $w = 51$ mm. Four different pin loading configurations, depicted in Fig. 2, were considered: uniformly distributed stress, uniform radial stress, pin modeled as a rigid body with contact interaction and a point load applied at the upper edge of the hole. The resultant vertical forces were the same in all cases. As already stated by other authors [13,14], the differences in the compliance and SIF for the different loading configurations were insignificant for $\bar{a} > 0.4$. Despite this, for the rest of the numerical simulations, the point load case was the one used because it gave the smallest compliance error with respect to the isotropic case [3]. One half of the unit thickness CT specimen was modeled and symmetric conditions were assumed as can be seen in Fig. 3.

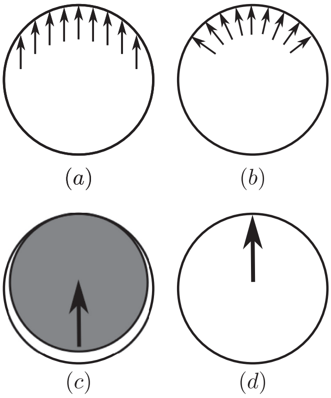

Fig. 2. Pin hole loading configurations: (a) uniformly distributed, (b) uniform radial stress, (c) contact interaction between pin and hole, (d) point load.

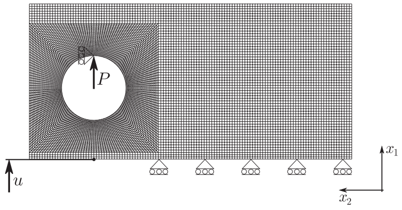

Fig. 3. Model mesh of half of the CT specimen and the applied boundary conditions, with an average element size of 0.5 mm at the coarse mesh.

To obtain the compliance for a given λ and ρ, a load of 1 N was applied at the loading pin, while the crack nodes were released gradually along the crack plane. The displacement u was captured at the loading line. Also, the Virtual Crack Closure Technique (VCCT) was applied along the crack nodes to compute the SIF.

To ensure accuracy and to validate the model, the compliance obtained with FEM was compared with the CT isotropic solution that can be found in various handbooks [3]. The model shows excellent agreement with the known solution, as seen in Fig. 4, with an error of less than 0.57%. In addition to the isotropic case,

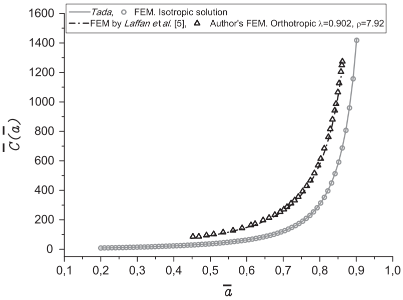

Fig. 4. $\overline{C}(\bar{a})$ against $\bar{a}$ for an isotropic material: comparison between known [3] and the author's FEM solutions. Also, $\overline{C}(\bar{a})$ against $\bar{a}$ for an orthotropic material with $\lambda = 0.902$ and $\rho = 7.92$: comparison between a previous FEM solution [5] and the author's FEM model.

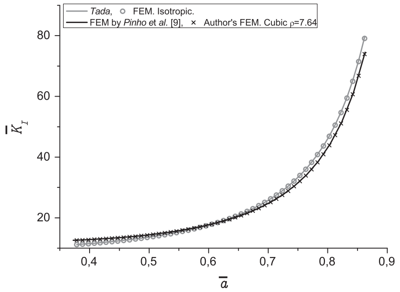

Fig. 5. Dimensionless SIF (Eq. (14)) against $\bar{a}$ for an isotropic material: comparison between known [3] and the author's FEM solutions. Also, SIF against $\bar{a}$ for a cubic material with $\rho = 7.64$: comparison between a previous FEM solution [9] and the author's FEM model.

the FEM model was compared with the FEM compliance solution of an orthotropic material computed by Laffan et al. [5]. The orthotropic material is a composite lay-up of T300/920 material, with a ply sequence of $[(0/90)_8/0]_s$. The mechanical properties of the unidirectional lamina in the longitudinal (L) and transverse (T) directions of the fiber are $E_{LL} = 135.10$ GPa, $E_{TT} = 8.88$ GPa, $G_{LT} = 4.54$ GPa and $\nu_{LT} = 0.32$ [5], with laminate values for λ and ρ being 0.902 and 7.92, respectively. Although not important to the overall results, in the FE model by Laffan et al. of Fig. 4, the specimen hole configuration is modeled as a point load applied directly to a node. Again, both FEM solutions are extremely similar, as is clearly shown in Fig. 4.

The FEM SIF was also compared with the isotropic solution [3]. In this case, the error was less than 0.66%, as can be appreciated in Fig. 5. Finally, the SIF of an orthotropic material was compared against a previously published FEM result by Pinho et al. [9]. In this case, the lamina properties are $E_{LL} = 131.7$ GPa, $E_{TT} = 8.88$ GPa, $G_{LT} = 4.6$ GPa and $\nu_{LT} = 0.32$. The laminate sequence is $[0/90]_8$, with $\lambda = 1.0$ and $\rho = 7.64$. Again, in the FEM model by Pinho et al., the loading is directly applied to a node. As Fig. 5 shows, the differences between both SIF FEM curves are trivial.

Once the numerical model had been validated, in order to obtain the compliance and SIF for different orthotropies, a total of 55 simulations were run, with different combinations of λ and ρ; there were 11 values of λ ranging from 0.03162 to 10.0 in constant logarithmic increments, and 5 values of ρ ranging from 0.1 to 10.0, also in logarithmic increments. The wide range of 55 combinations of λ and ρ cover most of the orthotropic materials.

4. Compliance and stress intensity factor parametric fitting

All the compliances obtained are fitted in an interpolating function to avoid computing $\overline{C}(\bar{a})$ from a FEM model. The dependence of the dimensionless compliance with respect to $\bar{a}$, λ and ρ can be approximated by a function of the form:

$$\overline{C}(\bar{a}, \lambda, \rho) = q(\bar{a}, \lambda, \rho) \cdot \lambda^B \cdot (1 + 0.22698 \cdot \rho^{0.53527}) \cdot \left(\frac{1+\bar{a}}{1-\bar{a}}\right)^2 \tag{13}$$

where $q(\bar{a}, \lambda, \rho)$ is a fourth order polynomial of $\bar{a}$, in which its coefficients depend on λ and ρ, and B is a polynomial that depends on the normalized crack length $\bar{a}$ and ρ. The coefficients can be found in A. Note that Eq. (13) is dimensionless and can be used for any size of w as long as the CT geometry of Fig. 1 is respected.

The interpolating function was obtained as follows: first, all the data points were divided by $((1+\bar{a})/(1-\bar{a}))^2$ to suppress the vertical asymptote of $\overline{C}$ when $\bar{a} = 1$ (the CT stiffness becomes 0 when the specimen is totally split). This asymptote is the same one previously published for the isotropic case [3]. When plotted in log–log scale, a near linear relationship is observed between $\overline{C}$ and λ for any $\bar{a}$ and ρ, with a slope B that depends on $\bar{a}$ and ρ. At the same time, when plotting $\overline{C}$ with respect to ρ in log–log scale, it can be seen that for small values of ρ the compliance is almost constant whereas for high values of ρ the compliance has a constant slope. This asymptote is described in Eq. (13) as $\overline{C} \propto (1 + c_1\rho^{c_2})$. The transition zone is determined as $\rho = (-1/c_1)^{1/c_2}$. The remaining tendency was fitted with the function q by using the least-squares method. This simple but rather long procedure can also be used to obtain $\overline{C}$ and *SIF* interpolating functions for other specimen geometries.

The fitting shows good agreement with the FEM model data, with a maximum error of less than 2.29% for a normalized crack length ranging from 0.2 to 0.9 and for the 55 combinations of λ and ρ. The fitted isotropic compliance curve differs by only 1.05% with respect to the known solution. Fig. 6 shows three examples of fitted compliances with their respective FEM data.

The SIF function of the orthotropic CT specimen is normalized as:

$$K_I = \frac{\bar{K}_I P}{h} \cdot \left(\frac{\bar{a}}{w}\right)^{1/2} \tag{14}$$

where $\bar{K}_I$ is the dimensionless SIF. Again, $\bar{K}_I$ is unique for a given $\bar{a}$, λ and ρ. It can be computed from the dimensionless compliance as:

$$\overline{K}_I^2 = \frac{1}{2\bar{a}}\sqrt{\frac{2\lambda^{3/2}}{1+\rho}}\frac{\partial\overline{C}}{\partial\bar{a}} \tag{15}$$

The $\overline{K}_I$ was fitted with a polynomial function to avoid computing the derivative of $\overline{C}$ with respect to $\bar{a}$. The $\overline{K}_I$ fitting function is as follows:

$$\begin{aligned}\bar{K}_I(\bar{a}, \lambda, \rho) &= p(\bar{a}, \lambda, \rho) \cdot \lambda^D \cdot \left(1 + 0.006689 \cdot \rho^{0.47151}\right) \\ &\cdot \frac{2(2+\bar{a})}{(1-\bar{a})^{3/2}} \cdot \frac{1}{\sqrt{\bar{a}}} \cdot \left(\frac{2\lambda^{3/2}}{1+\rho}\right)^{1/4}\end{aligned} \tag{16}$$

where $p(\bar{a}, \lambda, \rho)$ is a fourth order polynomial of $\bar{a}$, with coefficients that depend on λ and ρ, and D is a polynomial dependent on the normalized crack length $\bar{a}$ and ρ. The coefficients are also found

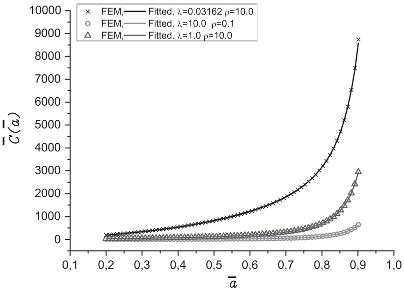

Fig. 6. Comparison between FEM and fitted $\overline{C}(\bar{a})$ curves for three examples of orthotropic materials.

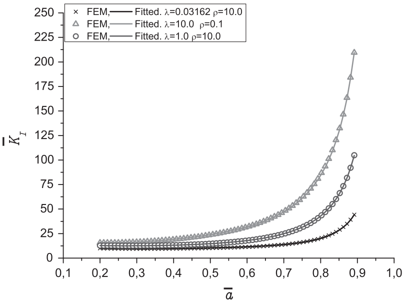

Fig. 7. Comparison between FEM and fitted SIF curves for three examples of orthotropic materials.

in A. Again, Eq. (16) is applicable to any size w where the normalization defined in Eq. (14) is used.

The procedure for obtaining the interpolating function is very similar to the one described for the dimensionless compliance. Again, the vertical asymptote is the same as the one for the isotropic case [3].

The SIF interpolating function has a maximum error of 2.37% with respect to the FEM data, for the same range of $\bar{a}$, λ and ρ as the compliance interpolating function. For the isotropic case, the fitted SIF differs by only 0.93% from the known solution. Fig. 7 shows good agreement of the dimensionless SIF for three orthotropic materials with their respective FEM data. It is important to recall, once more, that when using crack lengths shorter than 0.4, the SIF and compliance functions are affected by the pin loading configuration, as stated in Section 3. For $\bar{a} > 0.4$, the solutions remain unaltered. This is also true for the widely used classic isotropic solution, and not particular to the proposed expressions. Although this may be seen as an inconvenient for initial crack lengths shorter than 0.4, in reality, to obtain G_{Ic} or K_{Ic} from experimental results, the crack growth must be self-similar, that is, the FPZ must be completely developed. This occurs at longer crack lengths than the initial ones. Thus, it is possible to use an initial crack length shorter than 0.4 and use the proposed solution as soon as the crack grows in an self-similar way for $\bar{a} > 0.4$.

5. Stability of the crack growth

The CT specimen was specifically designed to measure the fracture toughness of a material under stable crack growth conditions. For this reason, it is very important to have a stable crack growth as long as possible. In this section, this stability is studied with reference to the crack length. Most standard procedures [1,2] recommend an initial crack $\bar{a}_0$ of 0.5, whereas in reality it can be shorter. It is important to remember that for $\bar{a} < 0.4$, the compliance and SIF are affected by the loading assumptions, as already stated in Section 3.

Assuming that the material is elastic and exhibits a brittle or quasi-brittle fracture propagation, a simple energy balance is sufficient to determine the initial crack length in which the crack growth is stable. From a LEFM point of view, the elastic ERR with respect to the displacement is defined as:

$$G_I = \frac{1}{2}\frac{u^2 E_{11}}{w}\frac{1}{\overline{C}^2(\bar{a})}\frac{\partial \overline{C}}{\partial \bar{a}} \tag{17}$$

The ERR with respect to the load can be found in Eq. (11). The condition of stability is satisfied while $\partial G_I/\partial a < 0$. This condition can be understood as follows: given a crack length a, if $\partial G_I/\partial a$ is negative this implies that in order to increase the crack, it is necessary to increase G_I. If the test is performed under controlled displacement, the stability condition is checked with Eq. (17), whereas if it is performed under controlled loading, the stability condition is checked with Eq. (11). In fact, very few geometries are stable under controlled loading conditions.

To verify the lowest $\bar{a}_0$ under stable growth conditions, $\partial G_I/\partial a < 0$ is evaluated with Eq. (17) in conjunction with Eq. (15):

$$\frac{\partial}{\partial \bar{a}}\left(\frac{1}{\overline{C}^2(\bar{a})}\frac{\partial \overline{C}}{\partial \bar{a}}\right) = \frac{\partial}{\partial \bar{a}}\left(\frac{2\bar{a}\overline{K}_I^2}{\overline{C}^2}\sqrt{\frac{1+\rho}{2\lambda^{3/2}}}\right) < 0 \tag{18}$$

The term $(1+\rho)/2\lambda^{3/2}$ is always greater than 0, and does not affect the positivity of the partial derivative. The condition is simply evaluated as:

$$\frac{\partial}{\partial \bar{a}}\left(\frac{2\bar{a}\overline{K}_I^2}{\overline{C}^2}\right) < 0 \tag{19}$$

Eq. (19) was reviewed for all the FEM compliance curves and produced some interesting results. All of the studied cases showed that a stable crack growth was achieved with an initial crack length smaller than $\bar{a} = 0.5$. For the majority of the 55 combinations of λ and ρ, the lowest observed initial crack length that ensured a stable test was $\bar{a}_0 = 0$ except for certain combinations of λ and ρ where the minimum crack length was slightly higher, $\bar{a} = 0.14$. This behavior is observed in orthotropic materials with relatively low values of λ and extremely high values of ρ, when $\lambda \leq 0.3162$ and $\rho \geqslant 10.0$.

Dimensionless load–displacement curve plots are useful to illustrate the effect of the crack growth stability. Assuming that the crack grows when $K_I = K_{Ic}$, the normalization of the load P can be obtained directly from Eq. (14) as:

$$\overline{P} = P\frac{1}{K_{Ic}h\sqrt{w}} = \frac{1}{\overline{K}_I\sqrt{\bar{a}}} \tag{20}$$

and given $\bar{u} = \overline{CP}$, the dimensionless displacement is defined as:

$$\bar{u} = u\frac{E_{11}}{K_{Ic}\sqrt{w}} = \frac{\overline{C}}{\overline{K}_I\sqrt{\bar{a}}} \tag{21}$$

Eqs. (20) and (21) depend only on known problem variables. Fig. 8 shows 3 examples of load–displacement curves: the isotropic case; $\lambda = 10$, $\rho = 0.1$; and $\lambda = 0.03162$, $\rho = 10$.

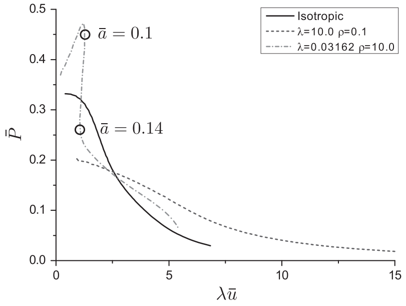

Fig. 8. Non-dimensional load ($\overline{P}$) displacement ($\bar{u}$) curve for various material orthotropies.

The normalized displacement has been scaled by λ in Fig. 8, in order to obtain comparable curves for the three examples. Notice that this scaling is introduced by replacing $E_{11} = E_{22}/\lambda$ in Eq. (21), and thus, obtaining the same displacement normalization but in terms of the elastic modulus in the loading direction. Observe in Fig. 8, in the first and second cases it can be clearly noticed that the crack grows under stable conditions. The third case represents a very stiff material in the x_1 direction with a very low shear modulus. It can be seen that the growth is stable until it reaches $\overline{P} = 0.45$. At this point crack growth becomes unstable and the load drops suddenly to 0.23. The minimum load that ensures a stable crack growth is $\overline{P} = 0.26$, which corresponds to $\bar{a} = 0.14$.

It is important to note that these recommendations are only valid for materials that behave elastically. If the material exhibits hardening, such as PMMA, the area ahead of the crack tip plasticizes before the crack growth start. The plastically hardened area usually stores a high amount of elastic energy prior to the crack initiation, which is released suddenly as the crack grows, resulting in an unstable test. This phenomenon is not contemplated by the recommendations in this section. Increasing the initial crack length or the specimen size can reduce the instability of the test due to the hardening of the material. In addition, the bearing effect on the holes of the CT has not been contemplated during this analysis, but will be covered in Section 6.

6. Design recommendations

Some undesired failure mechanisms may appear when testing a CT specimen, preventing the experiment from being performed properly. Blanco and Pinho [15] performed a FEM parametric analysis of the CT geometry for woven composite materials to avoid six non-desired failure mechanisms. Five failure mechanisms were predicted with failure criteria and the sixth was considered to be collapse due to buckling. Others authors have also proposed some failure mechanisms for CT of laminated composite material [16]. In this section, we present a proposal of failure criteria which take into account the orthotropy of the material, the specimen size, w, and the initial crack length, a_0.

6.1. Failure criteria

According to the Theory of Elasticity, the stress at any point of the specimen can be determined in terms of the load P being applied as $\sigma \propto P/(wh)$, for any component of the stress tensor. By using Eq. (14), it is possible to express the stress state normalized with respect to the fracture toughness and the specimen size as follows:

$$\sigma \frac{\sqrt{w}}{K_{Ic}} \propto \frac{1}{\overline{K}_{Ic}\sqrt{\bar{a}}} \tag{22}$$

The material failure can be expressed as a function of the crack length and the orthotropy, as follows:

$$\sigma_u \frac{\sqrt{w}}{K_{Ic}} = f_{MF}(\bar{a}, \lambda, \rho) \tag{23}$$

where f_{MF} is the function of the considered failure mode and σ_u is the material strength under a known stress state. It is important to highlight that, in order to use this type of failure criteria, the material toughness K_{Ic} must be known beforehand. To overcome this problem, it is possible to simply use an approximate expected fracture toughness of the specimen being tested.

Three failure criteria are considered in this study: two predict collapse under compression and the third contemplates buckling of the specimen.

6.1.1. Back end compression failure

Compression stresses at the back end of the CT appear during a fracture test and they tend to increase as the crack grows. This may cause the specimen to collapse under compression at the back end before it has been completely split [16]. For some composite materials this failure can occur in the form of ply delamination. Such phenomena have also been observed in some tougher materials with large initiation or propagation loads and also in low compression strength materials.

The compression stresses at the back end (BE) are obtained as follows:

$$\sigma_{BE} = \frac{K_I}{\sqrt{w}} \frac{r(\bar{a}, \lambda, \rho)}{\sqrt{\bar{a}}} \tag{24}$$

where $r(\bar{a}, \lambda, \rho)$ is the dimensionless back end compression stress function. The failure criterion for the back end compression (f_{BE}) can be expressed as:

$$\frac{\sigma_{uC}\sqrt{w}}{K_{Ic}} > f_{BE} \tag{25}$$

where $f_{BE} = r(\bar{a}, \lambda, \rho)/\sqrt{\bar{a}}$. This stress-based failure criterion predicts the initialization of the material failure at the back face of the specimen. For some materials, the failure may be controlled by a stable process due to the formation of a Fracture Process Zone (FPZ). When dealing with composite materials, the back end failure normally appears in the form of a kink-band. Hence, the failure criterion expressed in Eq. (25) is a conservative prediction of the failure.

The dimensionless back end stress $r(\bar{a}, \lambda, \rho)$ was obtained by fitting the results of the FEM models for a wide range of material orthotropies with the least-squares method and using the definition in Eq. (24). The function is defined as a fourth order polynomial of $\bar{a}$, with coefficients that depend on λ and ρ. The function $r(\bar{a}, \lambda, \rho)$ is applicable for any CT size that respects the geometry of Fig. 1, and can be found in A. The interpolating function is only valid for orthotropic materials ranging from $0.3162 \leqslant \lambda \leq 10.0$ and $0.3162 \leqslant \rho \leq 10.0$, and for crack lengths greater than $\bar{a} > 0.4$. The presented solution guarantees an error of less than 4.48% with respect to the FEM results.

6.1.2. Bearing load at the holes compression failure

It has been shown in Section 5 that the fracture test is stable for lower values of $\bar{a}_0 = 0.5$. When the crack length is very small, the bearing load required to propagate the crack may be so high that it causes the collapse under compression in the area surrounding the loading holes. The stress at the hole due to the bearing pin can be defined as

$$\sigma_{bearing} = \frac{P}{hd} < \alpha\sigma_{uC} \tag{26}$$

where d is the hole diameter and α is a parameter that depends on the stress distribution between the pin and the hole. The value of α is normally considered to be equal to 1 or $4/\pi$. The standard procedure recommends a hole diameter of $d = 0.25w$, but it has been demonstrated in Section 3 that the loading configuration does not affect the SIF of the CT specimen. Hence, the diameter can be defined as $d = w/n$ (with $n = 4$ in the standard recommendations). The failure criterion for the bearing load ($f_{bearing}$) can then be expressed as:

$$\frac{\sigma_{uC}\sqrt{w}}{K_{Ic}} > f_{bearing} \tag{27}$$

where:

$$f_{bearing} = \frac{n}{\alpha\overline{K}_{Ic}\sqrt{\bar{a}}} \tag{28}$$

Table 2
Laminate properties.

Laminate	E_{11} (GPa)	σ_{uC} (MPa)	K_{Ic} (MPa mm$^{1/2}$)	h (mm)
LC	42.3	392	1869	4.24
LG	16.0	405	1193	4.58

6.1.3. Buckling structural failure

The buckling criterion does not account for a material failure but for a structural failure. Thus, the buckling stress does not rescale as in Eq. (23). For a given crack length $\bar{a}$ and material orthotropy, the critical buckling load is proportional to:

$$P_{Buc} \propto \frac{D_{11}}{w} \tag{29}$$

where D_{11} is the material stiffness along direction x_1. The load P and the SIF are obtained using Eq. (14). The failure criterion is defined as:

$$\frac{D_{11}}{w^{3/2}} \frac{1}{hK_{Ic}} > f_{Buc} \tag{30}$$

where f_{Buc} depends on $\bar{a}$ and the in-plane orthotropic and bending constants, obtained from the roots of a characteristic polynomial similar to the one in Eq. (3). Although a solution for f_{Buc} has not been found, Eq. (30) can give some insight into how the specimen size affects the structural failure, given that $D_{11} \propto h^3$. For example, if the specimen size w is increased by a factor of 4, the buckling load decreases by a factor of 8. On the other hand, if the specimen thickness h is also increased by a factor of 4 the buckling load is reduced by half, rescaling as a stress-based criterion. It should be noted that any modifications of the thickness should be carried out with extreme caution, because fracture toughness normally depends on h, especially when dealing with materials that exhibit hardening. Also, to prevent this structural failure mode, one possible solution might be to use anti-buckling instrumentation devices [17].

6.2. Results and discussion

Two woven composite materials were tested to study the effectiveness of the compression failure criteria presented. The two woven materials used were Carbon (C) fabric type G0926 (5HS, 6 K, 370 gsm) and Glass (G) fabric type S2 (style 6781, Z-6040, 303 gsm). Both materials were supplied by Hexcel and were used with HexFlow® RTM6 mono-component epoxy system. A laminate of each woven composite material was manufactured. The laminate made from woven carbon fabric, LC, has a ply stacking sequence of $\left[\left(0^C/45^C\right)_3\right]_S$, whereas the laminate made from glass fabric, LG, has a stacking sequence of $\left[\left(0^G/45^G\right)_5\right]_S$. The laminates used were manufactured using a single material as described in the work of González et al. [18]. Each laminate was tested with a CT specimen respecting the dimensions of Fig. 1, with a size $w = 51$ mm and a hole diameter of 8 mm. The initial crack length in both cases was 26 mm, thus $\bar{a}_0 = 0.51$. The properties of the two laminates are given in Table 2. Due to the ply stacking sequence used, both laminates have in-plane quasi-isotropic properties ($\lambda = \rho = 1$).

The fracture toughness of each laminate was obtained from the CT fracture test. The load displacement curves of both laminates are shown in Fig. 9. The K_{Ic} of each laminate was obtained using Eq. (14), evaluated at the maximum load value.

According to Eq. (23), the specimen will fail under compression as soon as $f_{MF} > 1.49$ for the carbon fabric laminate LC and as soon

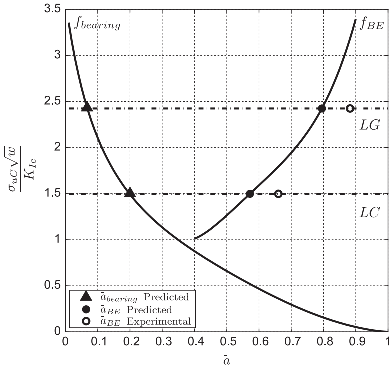

Fig. 10. $f_{bearing}$ and f_{BE} material failure criteria for both the carbon fabric laminate (LC) and the glass fabric laminate (LG).

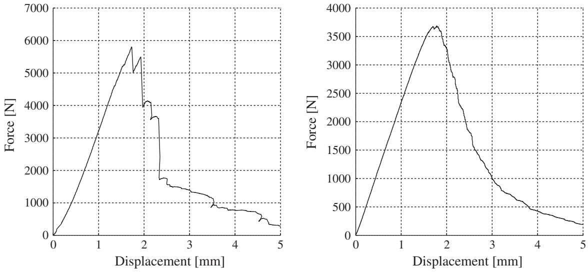

(a) LC laminate.

(b) LG laminate

Fig. 9. Load displacement curves of the CT fracture toughness test.

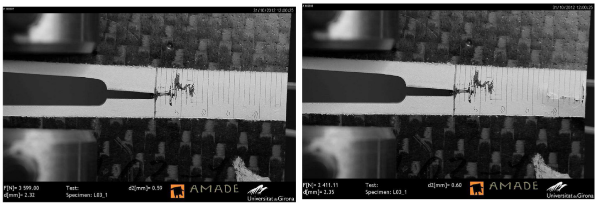

(a) LC prior to BE collapse **(b)** LC at the point of BE collapse

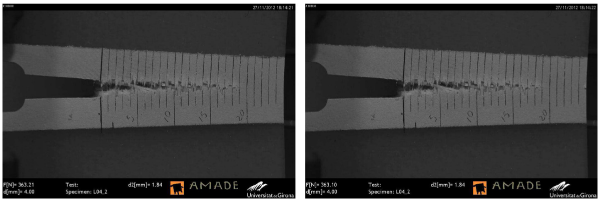

(c) LG prior to BE collapse **(d)** LG at the point of BE collapse

Fig. 11. CT specimens of woven carbon fabric laminate (LC) and glass fabric laminate (LG) at the instant of material failure due to the Back End (BE) compression stress. (For interpretation of the references to color in this figure legend, the reader is referred to the web version of this article.)

as $f_{MF} > 2.42$ for the glass fabric laminate LG. It was considered that $n = 51\ \text{mm}/8\ \text{mm} = 6.375$ and $\alpha = 1$ when computing the bearing failure criterion. The failures caused by the bearing load ($f_{bearing}$) and the compression at the back end (f_{BE}) are shown in Fig. 10.

According to the predictions, in the case of the LC and the LG laminates, the minimum initial cracks that will prevent the failure due to the bearing load are $\bar{a}_{bearing} = 0.2$ and $\bar{a}_{bearing} = 0.068$ respectively. Since the initial crack length is $\bar{a}_0 = 0.51$ in both CT specimens, neither will fail due to the compression at the holes. On the other hand, the failure at the back face will occur as soon as $\bar{a}_{BE} = 0.57$ and $\bar{a}_{BE} = 0.795$, respectively.

After the completion of the tests, the experimental results were found to be in accordance with the predictions. Neither of the tested materials failed due to the collapse under compression at the holes. Both specimens failed under back end compression stress before the end of the experiment. A few images taken at the instant of the BE failure are shown in Fig. 11.

The experimental BE failure occurred at a crack length of $\bar{a}_{BE} = 0.66$ for the LC and $\bar{a}_{BE} = 0.88$ for the LG. These results are in good agreement with the predicted results, which were slightly lower. In detail, in the case of the carbon fabric laminate, the predicted crack length was about 14% lower than the experimental result, while for the glass fabric laminate it was only about 10% lower. It should be noticed that the predicted results do not indicate when the material is actually going to collapse but rather when the stress is going to reach the σ_{uC} of the material. Beyond this point a stable FPZ starts to develop which is still capable of withstanding the stress and, therefore, the failure can occur at a greater crack length.

From the test results, it is clear that the carbon fabric CT specimen cannot be used to perform the test properly. Firstly, the initial crack length could have been smaller than $\bar{a}_0 = 0.5$ and the specimen would still be able to support the bearing load at the holes. In fact, the initial crack length could have been as small as $\bar{a}_0 = 0.2$. On the other hand, in order to increase the $\bar{a}_{BE}$, the size, w, should have been increased. For example, $\bar{a}_{BE}$ would be 0.74 with a specimen size of $w = 102$ mm.

As it has been shown, when designing a CT specimen, it is much simpler and time-efficient to decide the specimen size w and the pre-crack a_0, to avoid the mentioned failures, with the aid of the presented functions and proposed methodology, rather than by iterating several FEM models an adjusting the values by trial and error.

7. Conclusions

The compliance C and the stress intensity factor K_I functions of the CT specimen were obtained for a wide range of material orthotropies. These functions are applicable to any specimen size w as long as the geometry of Fig. 1 is respected. The proposed interpolating functions have been shown to be highly accurate with respect to the isotropic case as well as with previously published results of orthotropic materials.

Because of the introduction of the two dimensionless variables λ and ρ, it is no longer necessary to handle four elastic properties (E_{11}, E_{22}, ν_{12} and G_{12}) in order to fully describe the elastic state of the material. Due to the fact that C and K_I are completely defined by λ and ρ, the problem of computing two or more elastically equivalent solutions can now be avoided. Additionally, because of the introduction of the interpolating functions for C and K_I, it is no longer necessary to create a FE model every time a new orthotropic material needs to be tested and, consequently, less computing time is required. Even for other specimen geometries different from the standard CT, the same procedure presented in this paper may be used in order to obtain their compliance and ERR functions.

The second part of this work has focused on providing tools to help design CT specimens by varying the initial crack length a_0 and size w. The stability of the crack growth was discussed in terms of the initial crack length: it was proven, from a pure elastic point of view, that tests with initial crack lengths as short as 0 would still perform stably, for the majority of the material orthotropies and for the loading configuration defined in Fig. 1.

Stress failure criteria were introduced to take into account two material failure mechanisms: the failure at the holes caused by the bearing load, and the failure at the back end face caused by the compression stress that appears during the test. Both criteria are valid for a wide range of material orthotropies, have been shown to be in very good agreement with experimental results, and have proven to be a faster alternative that solving a FEM.

Acknowledgements

This work has been partially funded by the Spanish Government through the *Ministerio de Economía y Competitividad*, under contract MAT2012-37552-C03-03 (subprogram MAT). The first author would also like to thank the *Universitat de Girona* (UdG) for the BR pre-doctorate grant, reference BR2013/35.

Appendix A. Polynomial fitting functions

The polynomial function $q(\bar{a},\lambda,\rho)$ of Eq. (13) can be expressed in matrix form as follows:

$$q(\bar{a},\lambda,\rho)=\begin{bmatrix}1\\ \bar{\lambda}\\ \bar{\rho}\\ \bar{\lambda}^2\\ \bar{\lambda}\bar{\rho}\\ \bar{\rho}^2\\ \bar{\lambda}^3\\ \bar{\lambda}^2\bar{\rho}\\ \bar{\lambda}\bar{\rho}^2\end{bmatrix}^T\begin{bmatrix}1.6128 & 8.9466 & -20.688 & 18.786 & -5.5381\\ -3.2808 & 32.523 & -94.902 & 116.73 & -51.736\\ 0.71078 & 8.4546 & -11.629 & -3.8438 & 8.454\\ 0.34995 & 1.2604 & 15.834 & -37.624 & 20.129\\ -2.1383 & 12.246 & -29.195 & 37.859 & -18.884\\ -0.46023 & 15.616 & -34.155 & 25.156 & -7.1906\\ -1.4802 & 12.872 & -33.187 & 30.728 & -8.6936\\ -0.57399 & 7.1987 & -34.221 & 54.132 & -26.768\\ -3.0283 & 23.403 & -54.343 & 41.271 & -6.7808\end{bmatrix}\begin{bmatrix}1\\ \bar{a}\\ \bar{a}^2\\ \bar{a}^3\\ \bar{a}^4\end{bmatrix} \tag{A.1}$$

where:

$$\bar{\lambda}=\log\lambda,\quad \bar{\rho}=\log(\rho+1) \tag{A.2}$$

The polynomial function B of Eq. (13) is:

$$B=-0.24216+1.4018\bar{\bar{a}}-0.003505\bar{\rho}+1.4908\bar{\bar{a}}^2-0.058317\bar{\bar{a}}\bar{\rho} \tag{A.3}$$

where $\bar{\bar{a}}$ is:

$$\bar{\bar{a}}=\log\bar{a} \tag{A.4}$$

The polynomial function $p(\bar{a},\lambda,\rho)$ of Eq. (16) can be expressed in matrix form as follows:

$$p(\bar{a},\lambda,\rho)=\begin{bmatrix}1\\ \bar{\lambda}\\ \bar{\rho}\\ \bar{\lambda}^2\\ \bar{\lambda}\bar{\rho}\\ \bar{\rho}^2\\ \bar{\lambda}^3\\ \bar{\lambda}^2\bar{\rho}\\ \bar{\lambda}\bar{\rho}^2\end{bmatrix}^T\begin{bmatrix}0.30817 & 2.1609 & -5.72 & 6.2711 & -2.4512\\ 0.61118 & -4.5341 & 12.698 & -14.428 & 5.5896\\ 0.098042 & 2.3871 & -8.6206 & 10.742 & -4.3791\\ 0.1443 & 0.098426 & 0.47793 & -2.5788 & 1.9266\\ -1.2451 & 8.9848 & -22.996 & 26.09 & -11.037\\ 0.85309 & -3.104 & 7.3777 & -9.0334 & 4.0197\\ -0.14716 & 1.752 & -6.0346 & 7.7217 & -3.3098\\ -0.16912 & 0.82943 & -2.7216 & 4.5667 & -2.6053\\ 0.12556 & -0.35037 & -0.53346 & 0.90753 & -0.042327\end{bmatrix}\begin{bmatrix}1\\ \bar{a}\\ \bar{a}^2\\ \bar{a}^3\\ \bar{a}^4\end{bmatrix} \tag{A.5}$$

The polynomial function D of Eq. (16) is defined as:

$$D=-0.066112+0.75681\bar{\bar{a}}-0.015\bar{\rho}+0.58136\bar{\bar{a}}^2-0.08451\bar{\bar{a}}\bar{\rho} \tag{A.6}$$

The polynomial function $r(\bar{a},\lambda,\rho)$ of Eq. (24) can be expressed in matrix form as follows:

$$r(\bar{a},\lambda,\rho)=\begin{bmatrix}1\\ \bar{\lambda}\\ \bar{\rho}\\ \bar{\lambda}^2\\ \bar{\lambda}\bar{\rho}\\ \bar{\rho}^2\\ \bar{\lambda}^3\\ \bar{\lambda}^2\bar{\rho}\\ \bar{\lambda}\bar{\rho}^2\end{bmatrix}^T\begin{bmatrix}6.7195 & -47.349 & 129.7 & -150.03 & 66.291\\ -0.15366 & 4.1923 & -7.3129 & 1.6292 & 3.1257\\ -1.1389 & 6.2549 & -12.787 & 14.461 & -7.2961\\ 2.2165 & -14.813 & 32.255 & -28.591 & 9.0782\\ -3.0204 & 16.775 & -40.317 & 44.5 & -18.129\\ -1.4327 & 11.786 & -35.032 & 43.226 & -19.277\\ -0.25291 & 0.48823 & 1.7188 & -4.258 & 2.329\\ -3.2837 & 24.238 & -60.512 & 63.226 & -23.799\\ 4.5281 & -30.891 & 78.302 & -85.562 & 33.658\end{bmatrix}\begin{bmatrix}1\\ \bar{a}\\ \bar{a}^2\\ \bar{a}^3\\ \bar{a}^4\end{bmatrix} \tag{A.7}$$

References

[1] ASTM E399-06. Standard test method for linear-elastic plane-strain fracture toughness K_{Ic} of metallic materials; 2006.

[2] ASTM E1820-01. Standard test method for measurement of fracture toughness. American Society for Testing and Materials; 2001.

[3] Tada H, Paris PC, Irwin GR. The stress analysis of cracks handbook; 2000.

[4] Murakami Y. Stress intensity factors handbook, vol. 2. Pergamon Press; 1987.

[5] Laffan MJ, Pinho ST, Robinson P, Iannucci L. Measurement of the in situ ply fracture toughness associated with mode I fibre tensile failure in FRP. Part I: Data reduction. Compos Sci Technol 2010;70(4):606–13.

[6] Mostafavi M, Schmidt MJJ, Marsden BJ, Marrow TJ. Fracture behaviour of an anisotropic polygranular graphite (PGA). Mater Sci Eng A – Struct Mater Prop Microstruct Process 2012;558:265–77.

[7] Laffan MJ, Pinho ST, Robinson P, McMillan AJ. Translaminar fracture toughness testing of composites: a review. Polym Test 2012;31(3):481–9.

[8] Slepetz JM, Carlson L. Fracture of composite compact tension specimens. ASTM STP 593; 1975.

[9] Pinho ST, Robinson P, Iannucci L. Fracture toughness of the tensile and compressive fibre failure modes in laminated composites. Compos Sci Technol 2006;66(13):2069–79.

[10] Lekhnitskii SG. Theory of elasticity of an anisotropic body. Holdenday; 1963.

[11] Paris P, Sih G. Stress analysis of cracks, fracture toughness and applications. ASTM STP-381; 1969.

[12] Performance of continuum and shell elements for linear analysis of bending problems. In: ABAQUS/CAE 6.11-1 documentation; 2011.

[13] Newman JC. Stress analysis of the compact specimen including the effects of pin loading. In: Fracture analysis: proceedings of the 1973 national symposium on fracture mechanics (ASTM STP 560). Philadelphia: American Society for Testing and Materials; 1974. p. 105–21.

[14] Wetherhold R, Park S. Energy-release rate calculations for the compact tension specimen using brittle orthotropic materials. Compos Sci Technol 1986;25(3):219–30.

[15] Blanco N, Pinho ST. Parametric analysis of different compact tension specimens for fracture toughness characterisation in woven composite materials. Eng Fract Mech; 2013 [Submitted for publication].

[16] Minnetyan L, Chamis CC. The C(T) specimen in laminated composites testing. NASA Technical Memorandum. NASA-Technical Memorandum 4712; 1996.

[17] Li X, Hallett SR, Wisnom MR, Zobeiry N, Vaziri R, Poursartip A. Experimental study of damage propagation in over-height compact tension tests. Compos Part A – Appl Sci Manuf 2009;40(12):1891–9.

[18] González EV, Maimí P, Sainz de Aja JR, Cruz P, Camanho PP. Effects of interply hybridization on the damage resistance and tolerance of composite laminates. Compos Struct 2014;108(0):319–31.

[19] Laffan MJ, Pinho ST, Robinson P, Iannucci L. Measurement of the in situ ply fracture toughness associated with mode I fibre tensile failure in FRP. Part II: Size and lay-up effects. Compos Sci Technol 2010;70(4):614–21.

[20] Green DW, Winandy JE, Kretschmann DE. Mechanical properties of wood. Wood handbook: wood as an engineering material. Madison, WI: USDA Forest Service; 1999. p. 4.1–4.45.

[21] Suo Z. Delamination specimens for orthotropic materials. J Appl Mech – Trans Asme 1990;57(3).

PAPER B

Characterization of the translaminar fracture Cohesive Law

A. Ortega [a], P. Maimí [a], E.V. González [a], D. Trias [a]

[a]AMADE, Mechanical Engineering and Industrial Construction Department, Universitat de Girona, Campus Montilivi s/n, Girona, Spain

The paper has been published in *Composites Part A: Applied Science and Manufacturing Vol. 91, Part 2 (2016) 501-509.*

Composites: Part A 91 (2016) 501–509

Contents lists available at ScienceDirect

Composites: Part A

journal homepage: www.elsevier.com/locate/compositesa

Characterization of the translaminar fracture Cohesive Law

A. Ortega *, P. Maimí, E.V. González, D. Trias [1]

AMADE, Mechanical Engineering and Industrial Construction Department, Universitat de Girona, Campus Montilivi s/n, Girona, Spain

ARTICLE INFO

Article history:
Available online 16 February 2016

Keywords:
A. Laminates
B. Fracture toughness
D. Failure
D. Mechanical testing

ABSTRACT

Quasi-brittle materials such as fibre-reinforced composite materials develop a relatively large Fracture Process Zone where material toughening mechanisms such as matrix cracking, fibre-bridging and fibre pull-outs take place. The damage onset and damage propagation are well defined from a cohesive model point of view, although no standard procedure has been yet developed to characterize the translaminar Cohesive Law. The present work proposes an objective inverse method for obtaining the Cohesive Law with the use of an analytic model capable of predicting the load–displacement curve of a Compact Tension specimen for any arbitrary Cohesive Law shape. The softening law has been obtained for two laminates, providing an excellent agreement with the experimental results. With the obtained softening function, the nominal strengths of a Center Cracked Specimen and an Open Hole specimen have been predicted for a wide range of specimen sizes.

© 2016 Elsevier Ltd. All rights reserved.

1. Introduction

When a material exceeds its elastic range, it develops an energy dissipation zone where material toughening takes place. This zone can be divided into two main regions depending on the nature of the energy dissipation mechanisms. The first area, located ahead of the crack tip, is where the intrinsic toughening takes place, and it is primary associated with material plasticity. This is typical of ductile materials such as most metals, and takes place in a volume fraction of the material. The second area, located behind the crack tip, is where the extrinsic dissipation mechanisms lie, and it is the primarily source of toughening in brittle materials. In this case the damage zone is confined to a plane [1].

Quasi-brittle materials, such as fibre-reinforced composite materials, only exhibit extrinsic toughening, involving processes such as fibre-bridging, fibre pull-outs and matrix micro-cracking, which generally dissipate a high amount of energy [2]. This region is known in the literature as the Fracture Process Zone (FPZ). Classic fracture mechanics theories have tried to model this FPZ to predict the structural response of quasi-brittle materials through the use of Linear Elastic Fracture Mechanics (LEFM) in conjunction with Resistance curves ($\mathcal{R}$-curve) [3] or Bažant's Size Effect Law (SEL) [4]. Unfortunately these methodologies are only applicable when the FPZ is relatively small compared to other problem dimensions. In the case of Large-Scale Bridging (LSB), the $\mathcal{R}$-curve has proven to be Specimen Geometry (SG) and Size dependent [5–9].

In most quasi-brittle materials, LEFM cannot be applied, i.e., the fracture problem is not uniquely defined from a single material parameter such as the fracture toughness (G_c) or a variable fracture toughness defined by the $\mathcal{R}$-curve. Under these circumstances, more complex and usually non-linear models like the cohesive zone model are needed to predict the fracture of such materials. The cohesive model, derived from the works of Dugdale and Barenblatt [10–12], postulates that inside the FPZ there are cohesive stresses that tend to close the crack, and that they decrease as the crack opens. The relation between the crack openings and the cohesive stresses is known as the material Cohesive Law (CL) (or laminate CL, in the case of fibre-reinforced composites) [13]. An equivalent property related to the CL is the J-ω_{CTOD} curve, where ω_{CTOD} stands for the crack opening measured at the initial crack length, that relates the energy released inside the FPZ as the crack opens [14,8]. Numerically implemented cohesive models [13] have proven to properly match the experimental observations, while at the same time being size and geometry independent.

The experimental measurement of the CL is still a problem of interest to the scientific community, as there are still no standardized methodologies to perform it. Ideally, it could be obtained as the evolution of the stress measured at the initial crack tip position (a_0) as the crack opens, similarly to the methodology proposed by Zobeiry et al. [15]. In this method, the displacement field of the specimen is measured through the use of the Digital Image Correlation (DIC) technique, and the FPZ boundary is estimated where the material does not behave linear-elastically. The cohesive

---

* Corresponding author.
E-mail address: adri.ort@gmail.com (A. Ortega).
[1] Serra Húnter Fellow.

http://dx.doi.org/10.1016/j.compositesa.2016.01.019
1359-835X/© 2016 Elsevier Ltd. All rights reserved.

stresses are obtained by assuming the stress in the loading direction across the damaged material to be uniform and equal to the stress of the undamaged material adjacent to the FPZ. Finally, an optimization algorithm is used in order to find a softening function that best fits the experimental curves. Despite the fact that this method is time-consuming, it is capable of measuring any arbitrary CL during the FPZ formation as well as during the self-similar crack growth. Other common methods involve measuring the J integral, either by measuring the strain field using the DIC technique [16,17] or by using closed form solutions of the integral, in order to differentiate it with respect to ω_{CTOD} [5,18,19]. Finally, an alternative approach to measure the CL is through the use of an optimization algorithm to solve the inverse problem [20–24]. The inverse analysis consists of three steps: firstly an experimental u–P curve is recorded from laboratory tests or in situ tests; next, a computer simulation of the test (direct method) is performed in order to find the parameters that define the CL; finally, a suitable norm which quantifies the discrepancy between the experimental data and the corresponding values provided by the computer simulation is minimized, with respect to the mentioned parameters. The present work belongs to this last category of methodologies, and stands out with respect to other inverse analysis based methods in two aspects: the way the direct method is solved, and the approach in which the CL is found. In order to so, the CL is expressed as a piecewise function made of n linear segments, while the inverse analysis finds the slopes and amplitudes of each segment. This procedure will be further detailed in the next section.

The paper is structured as follows: Section 2 provides the analytic solution to obtain the P–u curve for any given CL shape, recently developed by the authors [9]. It also introduces the methodology used in order to solve the inverse problem. Section 3 exposes the experimental setup and the specifications of the tested laminates. Section 4 shows the results of the tests, as well as the measured CL for two different laminates. Section 5 discusses the results, and also proposes a simplified Cohesive Law shape for one of the laminates. Also, the proposed CL is used for predicting the nominal strength of a Center Cracked Specimen and an Open Hole Specimen for a wide range of specimen sizes. Lastly, Section 6 exposes the Conclusions of the present work.

2. Methodology

2.1. Direct method: Dugdale's condition

Before introducing the inverse methodology to obtain the CL, let us first introduce the direct method, that is, a tool capable of predicting the P–u curve for a given general Cohesive Law [9].

Given a standard CT specimen of size W, like the one shown in Fig. 1, under the action of a controlled displacement (u) and corresponding load (P) applied at the pin holes, the analytic solution presented here is capable of predicting the FPZ onset and development, while obtaining the whole cohesive stress profile σ_c and the crack opening profile ω inside the FPZ, by taking into account the laminate CL, as a crack grows in pure mode-I along the symmetry plane. The material is assumed to be isotropic, although the same procedure may be used for an orthotropic one. More details about this subject will be given at the end of this section.

The starting point of the problem solution comes from the Dugdale's condition, i.e., the global Stress Intensity Factor (SIF) of the problem, K, must be null. The problem SIF is a result of all the acting loads: P and σ_c. By applying the superposition principle, the SIF can be expressed as the superposition of the SIF caused by each load. Applying Dudgdale's condition, K of the global problem must be equal to zero:

$$K = K^P + K^{\sigma_c} = 0 \tag{1}$$

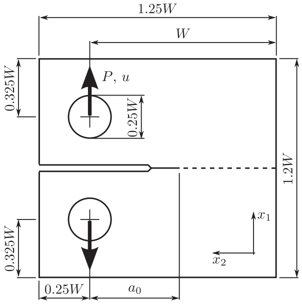

Fig. 1. Compact Tension (CT) Specimen Geometry, subjected to a load P under controlled displacement u.

where K^P is the SIF caused by the point load P and K^{σ_c} is the SIF caused by the whole cohesive stress profile σ_c. Although the σ_c is unknown and may change during the FPZ development, it can always be discretized as a series of small constant stresses of value equal to σ_i applied at the crack surface. The non-linear problem expressed as a superposition of linear problems is shown in Fig. 2.

Given $\sigma_N = P(Wh)^{-1} = s_N\sigma_u$ and $\sigma_i = s_i\sigma_u$, the SIF functions are defined as:

$$K^P = \sigma_u W^{1/2} s_N \bar{K}^P; \quad K^{\sigma_c} = \sigma_u W^{1/2} s_i \bar{K}_i^{\sigma} \tag{2}$$

where $\bar{K}^P$ is the non-dimensional function of the SIF caused by the point load P and $\bar{K}_i^{\sigma}$ is a vector that defines the non-dimensional function of the SIF due to a unitary constant stress σ_i of width equal to the discretization, and centred at a distance a_i from the load line. The length ℓ_{dam} is the damaged length of the material, measured from a_0, and combines the FPZ plus the traction free crack surface length, as shown in Fig. 2. Both SIFs are found in Appendix A. From Eqs. (1) and (2), if the cohesive stress profile σ_c is known, there is only one load P that satisfies the Dugdale's condition. Hence, using Eqs. (1) and (2) it is possible to obtain s_N by knowing the normalized cohesive stresses s_i

$$s_N = \beta_i s_i; \quad \beta_i = \bar{K}_i^{\sigma}/\bar{K}^P \tag{3}$$

with β_i being a vector that relates each normalized constant stress $s_i = \sigma_i/\sigma_u$ with the normalized load $s_N = P(Wh\sigma_u)^{-1}$ applied at the pin holes. The vector β_i is uniquely defined by the SG and the normalized length $\bar{a}_0 + \bar{\ell}_{dam}$.

In order to solve for the cohesive stress profile inside the FPZ, the crack opening profile must also be found. Again, it is possible to express the set of openings ω_i as a superposition of the opening caused by each acting load

$$\omega_i = \omega_i^P + \omega_i^{\sigma_c} \tag{4}$$

where ω_i, ω_i^P and $\omega_i^{\sigma_c}$ are the total crack opening, the crack opening caused by the point load P and the crack opening caused by the cohesive stress profile σ_c at a position a_i. These parameters can be expressed as:

$$\omega_i^P = \frac{\sigma_u W}{E'} s_N \hat{\omega}_i^P \tag{5}$$

$$\omega_i^{\sigma_c} = \frac{\sigma_u W}{E'} s_j \hat{\omega}_{ij}^{\sigma} \tag{6}$$

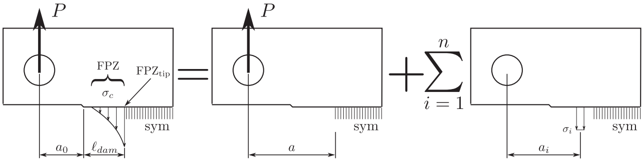

Fig. 2. Compact Tension (CT) specimen with a FPZ expressed as a superposition of linear problems.

where $\hat{\omega}_i^P$ is the non-dimensional function of the crack opening caused by the point load P and $\hat{\omega}_{ij}^\sigma$ is the non-dimensional function of the crack openings at a position i caused by the constant cohesive stress at a position j. Then, it is possible to express Eqs. (3)–(6) as:

$$\hat{\omega}_i = f_{ij}s_j; \quad f_{ij} = \beta_j\hat{\omega}_i^P + \hat{\omega}_{ij}^\sigma; \tag{7}$$

where $\hat{\omega}_i = \omega_i E'/(\sigma_u W)$ is the non-dimensional crack opening at position i and s_j is the non-dimensional stress at position j. At this point, by knowing the CL of the material and using Eq. (7) it is possible to obtain the normalized cohesive stresses s_j and the normalized crack opening $\hat{\omega}_i = \omega_i E'(\sigma_u W)$ at the FPZ for a given ℓ_{dam} and consequently any problem variable. The solution algorithm is outlined below. First, a ℓ_{dam} is selected. Then, from an iterative process Eq. (7) is solved for a given CL, and as a result the stress profile and the crack openings at the FPZ are obtained. At this point, the load P is obtained by means of Eq. (3). Lastly, the displacement u is defined as the crack opening at $a_i = 0$, using again Eq. (7).

In order to solve the direct problem for an orthotropic material, the SIF functions for the given orthotropy must be known. These can be obtained from an algebraic function (an example of the SIF function of a CT specimen subjected to a point load for an orthotropic material can be found in [25]) or by using a FE model [21]. Also, the load direction must be aligned with a principal direction of the material, in order to ensure that the crack grows along the symmetry plane.

2.2. Inverse method

The understanding of the FPZ formation within a cohesive crack model is needed in the development of the inverse method presented in this paper. The FPZ is initialized as soon as a point of the specimen reaches a stress equal to the material strength. Once the σ_u is reached, the FPZ grows as the displacement is increased, opening the cohesive crack and changing the cohesive stress profile in relation with the laminate CL. When the crack opening at $a = a_0$ reaches the critical opening ω_c, the FPZ ends its development. At this precise point the crack growth enters a steady state, meaning that it dissipates a constant energy G_c, while the FPZ moves along the crack path. During this steady state growth the cohesive crack opening profile and cohesive stress profile remain almost constant.

Since the peak load is reached while the FPZ is still being formed, the analysis of the cohesive stresses inside the FPZ along the crack growth is of great interest in predicting the nominal strength of structures. Fig. 3 gives some more accurate insight, as it depicts the progress of the FPZ growth, and its relation with the CL. Given the Point 1 of the P–u curve, the cohesive stresses range from σ_u at the FPZ tip (next to the undamaged material), where the crack opening is $\omega = 0$, to $\sigma = \sigma_1$ at a crack opening ω_1 measured at the end of the FPZ (next to the traction free crack), i.e., at a distance a_0 measured from the load line. In other words, to describe the crack growth and the FPZ development until the Point 1, only a part of the CL needs to be known, i.e, the CL shape beyond

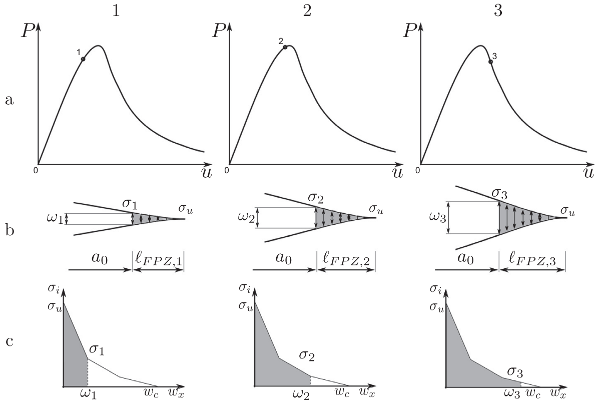

Fig. 3. Depiction of three states (1–3) during the FPZ growth: (a) the P–u position, (b) the FPZ stress and crack openings and (c) the dissipated energy inside the CL. The cracks openings ω_1, ω_2 and ω_3 are measured at the initial crack position a_0.

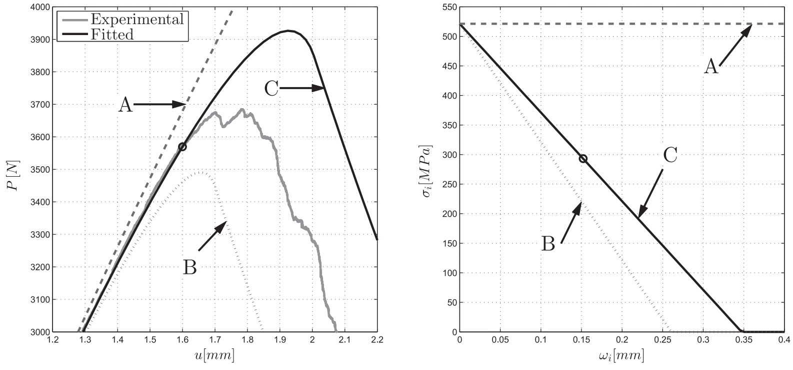

(a) (b)

Fig. 4. Inverse method approach: (a) three predicted *P*–*u* curves using the direct method obtained with (b) their corresponding Cohesive Laws. The experimental load is overestimated with (A), underestimated with (B) and best fitted with (C). The obtained branch has an amplitude of 0.152 mm.

the point ω_1–σ_1 is not needed. Observing Point 2, now the cohesive crack opening increases to ω_2 and the cohesive stress decreases to σ_2. In this case, to define the crack growth and the FPZ, the CL must be known up to ω_2–σ_2. The same can be applied to Point 3, and to every displacement increase. If all the cohesive model variables are known during the crack growth, each point of the *P*–*u* curve has a unique corresponding FPZ state, with the cohesive stresses defined between $0 \leqslant \omega \leqslant \omega_i$, where ω_i is the Crack Tip Opening Displacement (CTOD). In other words, every infinitesimal FPZ development increase needs an additional infinitesimal portion of the CL. This property allows to define a piecewise CL by fitting consecutive points in the *P*–*u* curve.

The inverse method takes advantage of the progressive FPZ development process, being able to determine the CL from a single CT fracture test, that is, there is no need to test other SG or sizes. Indeed, several additional factors need to be considered that may alter the local behaviour of the material, such as the presence of heterogeneities (voids or defects introduced during the manufacturing process, the fibre tow size, etc.) or the repeatability of the test, that may finally lead to the need of multiple repetitions of the test. For details on the tested materials, please see Section 3. A step-by-step algorithm to solve the inverse problem is given below:

- Select some experimental *P*–*u* points around the peak load, which will be used to fit the CL. The points must be picked while the FPZ is still being formed. That is, before the experimental *P*–*u* curve matches the LEFM one. As an example, in Fig. 4a the point that will be fitted is located at a displacement of 1.6 mm (marked with ∘).
- The unknown CL is initialized with the first point at $\sigma = \sigma_u$ when $\omega = 0$. The σ_u is the laminate strength, which must be obtained from an independent laminate tensile test. This is shown in Fig. 4b.
- The fitting process is illustrated in Fig. 4. The first branch of the CL is fitted using the first experimental point P_1–u_1 selected from the curve. The unknown branch is initialized with a slope of 0 MPa/mm (labelled with A in 4b). Then, the *P*–*u* curve (labelled with A in 4a) is predicted with the direct method of Section 2.1 for the given guessed slope. As it can be seen, the first trial slope overestimates the load for a displacement of 1.6 mm. The iterative process is continued by changing the slope to −2000 MPa/mm (labelled with B), resulting in a predicted load lower than the experimental one. The process is iterated by changing the slope until the predicted load matches the experimental one within a desired error (labelled with C). In this case, the slope found is −1500.9 MPa/mm. To automate this process, a numerical root-finding algorithm needs to be implemented. For the present work the secant-method was used, as the obtained convergence was fast enough.
- Once the slope is found, the crack opening that defines the first branch width ω_1 (marked with a ∘ in Fig. 4b) is obtained by computing the crack opening at the initial crack position $a = a_0$ with Eq. (4). In conjunction with the found slope, the stress σ_1 is obtained.
- The algorithm is continued for each selected point, until all the branches that define the CL have been found.

In this manner it is possible to obtain a piecewise laminate CL. Clearly, the number of branches obtained from this method will depend on the number of chosen points in the *P*–*u* curve, as will be shown in Section 4.

3. Experimental setup and test specimens

A standard Compact Tension specimen of size $W = 51$ mm, as the one shown in Fig. 1, was tested, with an initial crack length of $a_0 = 25$ mm and a pin hole diameter of $d = 8$ mm. As no standard procedure has been developed for the determination of the translaminar fracture toughness of fibre-reinforced composite materials using a Compact Tension specimen, the test was carried out following the recommendations by Pinho et al. [26]. The test was performed with a screw-driven universal testing machine, loading the specimens at rates of 0.5 mm/min. The crack tip notch was manufactured with a diamond coated disc, ensuring a radius lower than 250 μm, following the recommendations by Laffan et al. [27]. The load cell signal and the extensometer signal were acquired and recorded with a dedicated PC. The displacement was measured with a displacement transducer placed at the crack surface below the load line.

Table 1
Laminate properties.

Laminate	E (GPa)	σ_u (MPa)	h (mm)
LG	19.05	521.2	4.58
LCG	34.0	469.4	4.31

Two woven fibre-reinforced composite materials were tested in order to measure the translaminar Cohesive Law. The two woven materials used were Carbon (C) fabric type G0926 (5HS, 6 K, 370 gsm) and Glass (G) fabric type S2 (style 6781, Z-6040, 303 gsm). Both materials were supplied by Hexcel and were manufactured with HexFlow® RTM6 mono-component epoxy system, as described in the work by González et al. [28]. The first laminate (LG) was made only of Glass Fabric plies, with a stacking sequence of $\left[\left(0^G/45^G\right)_5\right]_S$. The second laminate (LCG) was an hybrid one, made of both Glass fabric and Carbon fabric plies, with a stacking sequence of $\left[\left(0^C/45^C\right)_2/0^G/60^G/-60^G\right]_S$. As it can be seen, both laminates are in-plane quasi-isotropic. The properties of the two laminates are given in Table 1.

During each specimen test the crack was optically measured with a videorecorder in order to observe any external damage. Fig. 5 show both CT specimen tested, LG and LCG, where the damage inside the FPZ is easily observable.

While performing the test and during the crack growth and crack propagation, no specimen buckling was observed. Once the tests were performed, the specimens were inspected by means of C-scan ultrasonic technique, using an Olympus Omni-Scan MX system. The inspection concluded that no significant delamination areas were present. With such observations, the assumption that there exists a Fracture Process Zone with closure stresses is appropriate for the studied specimens.

4. Results

In order to obtain the CL, two specimens of each laminate were tested. Although the inverse problem could have been applied to each of the tested specimens, the authors have decided to approach the problem in a different manner. Because the CL is supposed to be a material (or laminate) property, for each pair of tested specimens, the average P–u has been obtained. A Gaussian method is applied to the average curve to reduce the experimental scatter. The main benefit of using the Gaussian method is that, instead of averaging the values around a given experimental point, the used points in the smoothing are weighted according to a Gaussian function. In that manner, the end points at the data window have less influence on the averaged value than the ones near the centre. To ensure that only a slight smoothing is performed, the data window is set to 100 experimental points, while the total data curve is made of about 18,000 points.

As mentioned in Section 2.2, the number of branches of the obtained CL depends on the number of points from the P–u curve used to perform the fitting. In this manner, selecting just a single point of the curve will result in a linear CL, whereas selecting two points will result in a bi-linear CL. The influence of the number of branches and the CL shape has been studied for the LG laminate. The experimental P–u curves of both specimens are shown in Fig. 6a, along the smoothed average curves. Three CL have been obtained from the LG laminate, while changing the number of points used in the fitting. The curves obtained with three (□), five (○) and seven (×) points are shown in Fig. 6b. It is easily appreciated that the three curves resemble the same shape, although the higher number of points used, the more resolution the curve has. It is important to notice that the fracture toughness (G_c) of each measured curve, i.e., the area under the CL curve, is nearly identical regardless of the number of points used in the fitting. The measured G_c are 78.7 N/mm, 78.8 N/mm and 78.6 N/mm for the curves with three, five and seven points, respectively, proving that the proposed inverse method is sufficiently objective, and is not dependent on the number of used points as long as they are well distributed along the FPZ formation.

The CL has also been measured for the LCG laminate. Again, two specimens were fractured, while using the smoothed average P–u curve in the CL determination. The experimental curves and the corresponding smoothed curve are shown in Fig. 7a. Again, three different sets of points were used, with six (□), eight (▽) and nine (×) points. The CL measured with the inverse method are shown in Fig. 7b.

It is again appreciated that, regardless of the number of points used and their position, the average shape of the CL remains unaltered. Again, the fracture toughness was obtained from the area under the curve for each CL. The measured G_c are 105.0 N/mm, 103.8 N/mm and 105.0 N/mm respectively, once again proving the objectivity of the inverse methodology.

5. Discussion

To validate the accuracy of the measured CL obtained with the proposed inverse problem approach, a predicted P–u curve has been obtained for each laminate using the proposed direct method. In the calculation of the predicted P–u curves, the experimentally measured CL have been used. For both cases, the CL measured with the (×) set of points was used.

The predicted P–u curves are shown in Fig. 8. As it can be seen, the obtained curves for each laminate fit accurately the experimental data, thus precisely reproducing the maximum load during the FPZ formation.

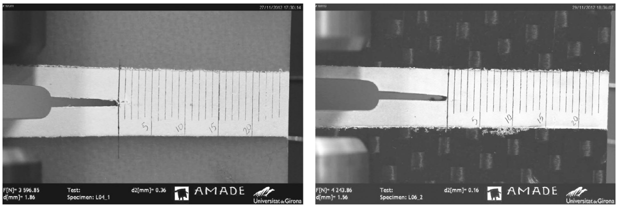

(a) (b)

Fig. 5. CT specimens of woven glass fabric laminate (LG), at a displacement of 1.86 mm and the hybrid laminate made of woven carbon fabric and woven glass fabric laminate (LCG) at a displacement of 1.56 mm, during the FPZ formation.

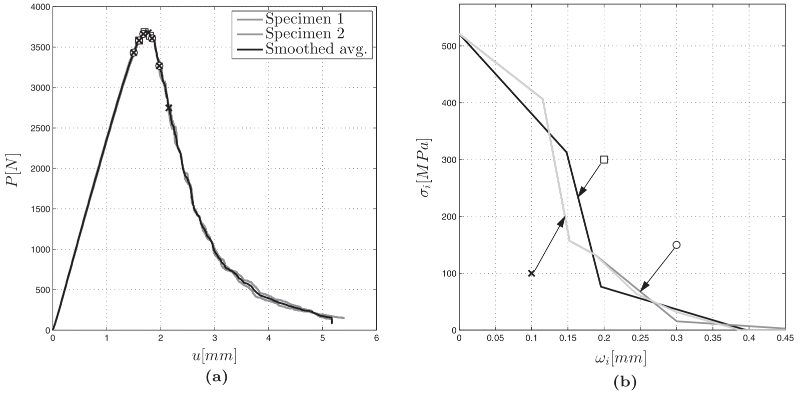

Fig. 6. (a) *P–u* curve for the two LG specimens and the corresponding smoothed average curve. (b) Three different CL obtained from three different sets of points.

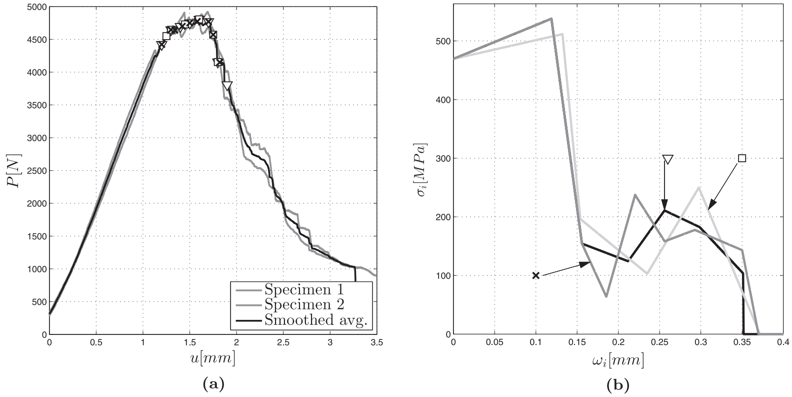

Fig. 7. (a) *P–u* curve for the two LCG specimens and the corresponding smoothed average curve. (b) Three different CL obtained from three different sets of points.

Although the experimentally determined CL are suitable for predicting structural strengths, as they provide accurate results, in general, they are not suitable to be implemented in any commercial Finite Element Modelling program. Similarly to the work of Zobeiry et al. [15], a better approach is to define a mathematical function that keeps the main CL shape characteristics, while only needing to define a few parameters. In this manner, an objective way of comparing similar CL shapes of different laminates is provided. In the case of the LG laminate, the CL can be easily adjusted with a trilinear CL. On the other hand, observing the LCG laminate CL shown in Fig. 7b, several characteristic traits are easily observable. Firstly, the stresses remain almost constant for relatively small crack openings. As soon as that certain crack opening is achieved, a sudden drop of stresses is observed, followed again by a second stress plateau value. The CL shape can be adjusted with a function of the form:

$$\sigma(\omega) = \begin{cases} \sigma_u & \omega \leqslant \omega_1 \\ (\sigma_u - \sigma_1)\exp\left[-A(\omega - \omega_1)\right] + \sigma_1 & \omega_1 \leqslant \omega \leqslant \omega_c \\ 0 & \omega \geqslant \omega_c \end{cases} \tag{8}$$

where σ_1 is the value of the second stress plateau-value, ω_1 is the crack opening that defines the end of the first stress plateau, ω_c defines the crack opening at which the FPZ is totally developed and A is a parameter that defines the exponential decrease of stresses after the first constant branch. The parameters of the CL defined in Eq. (8) have been chosen in order to adjust the LCG CL, taking the values $\sigma_1 = 180$ MPa, $\omega_1 = 0.125$ mm, $\omega_c = 0.35$ mm and $A = 50$.

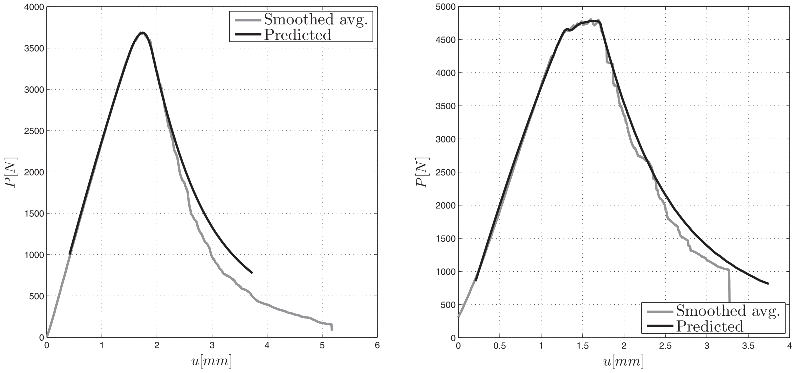

(a) (b)

Fig. 8. Predicted *P–u* curves using the experimentally measured CL for the (a) LG and (b) LCG laminates.

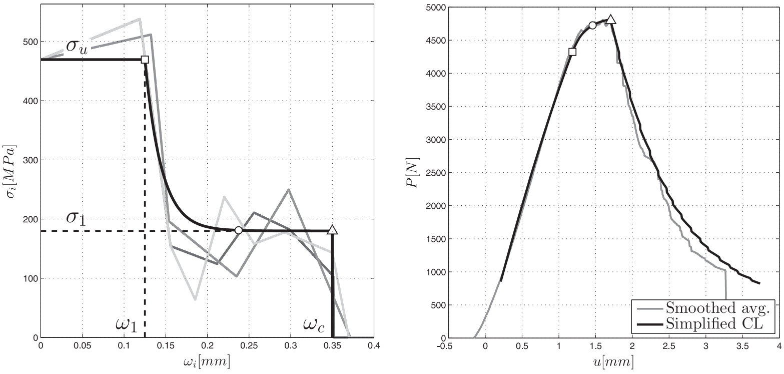

(a) (b)

Fig. 9. (a) Piecewise simplified CL shape for the LCG laminate along the experimental measured ones, with labelled crack openings at $\omega = 0.125$ mm, $\omega = 0.24$ mm and $\omega = 0.35$ mm. (b) Predicted *P–u* curve using the simplified CL, along the positions at which the crack opening at the initial crack length reaches the openings defined in (a).

With the selected parameters, the obtained G_c matches the experimental value of 105 N/mm. Fig. 9a shows the adjusted CL with Eq. (8) along the experimental measured curves. The predicted *P–u* curve using the suggested simplified CL is shown in Fig. 9b. As it can be seen, it accurately reproduces the experimental results, especially during the maximum load along the FPZ formation. Moreover, three characteristic cohesive crack openings have been labelled on the simplified CL in Fig. 9. The first crack opening at $\omega = 0.125$ mm (□) represents the end of the first stress plateau, the crack opening at $\omega = 0.24$ mm ($\circ$) has been chosen during the stress drop, and lastly the crack opening at $\omega = 0.35$ mm (△) shows when the FPZ has been fully developed. The three crack openings have also been plotted on the predicted *P–u* in Fig. 9b, showing the natural progress of the FPZ formation. As it can be seen, the deviation from the elastic compliance is first noticeable at (□). It is also remarkable to show that at (△) the FPZ has been fully developed, as the *P–u* curve meets the LEFM one. This property is true for almost all notched specimens, except for extremely small ones where the FPZ is not able to be fully developed before the specimen breaks apart.

The purpose of the CL determination using the present method is not only to reproduce the *P–u* curves of the tested CT specimens, but also to predict the structural strength of different specimen geometries and structures. In order to test the applicability of the measured CL, the nominal strength of an Open Hole specimen (OH) and the Center Cracked Specimen (CCS) has been predicted using the simplified LCG Cohesive Law. In order to do so, the direct method described in Section 2.1 has been applied to the OH [29] and the CCS [30] geometry and the maximum strength has been found for several specimen sizes. Both specimens are of infinite width, where R is the hole radius for the OH specimen or half the crack length for the CCS specimen. Fig. 10 shows the predicted nominal strengths of both specimens for a wide range of sizes.

The nominal strength σ_N represents the average stress at the failure plane of the undamaged material section when the maximum load is reached. The response of the CCS is typical of notched specimens modelled with a cohesive model, as illustrated by Maimí et al. [30]. For small specimens the response tends to the plastic limit response, i.e., the entire failure plane stress is equal to the material strength σ_u. From a cohesive model point of view this can be understood as a FPZ that spans the entire specimen width, with all the cohesive cracks placed at small openings with stresses close to σ_u. As the specimens size grows, the relative length of the FPZ with respect to the specimen width decreases, causing, at the same time, a decrease of the average stress at the failure plane. This tendency continues as the specimen size increases. For a very large crack length R, the relative FPZ is so small that it just takes a very small area ahead of the crack tip, having the stress field defined by a K-parameter. Hence, for big specimen sizes the crack growth can be explained by the LEFM theory. Fig. 10 also shows the point in which the initial crack opening for each nominal strength achieves the values marked in Fig. 9a ($\square, \circ, \triangle$). In concordance with the previous statements, is can be seen that for very small specimens the cohesive cracks openings are below $\omega = 0.125$ mm, i.e, the cohesive zone is defined only by the initial part of the CL. Also, the moment in which the nominal strength meets the LEFM limit is placed at the point in which the initial crack opening is equal to $\omega = \omega_c$.

For the OH specimen the response is typical of unnotched geometries [29]. Again, for small sizes the nominal strength is equal to the plastic limit. As the size is increased, the relative FPZ length at the maximum load decreases, along with a decrease of the nominal strength at the failure plane. In the extreme case of very large specimens, the nominal strength follows the elastic response, defined by a stress concentration factor. The FPZ is never fully developed at the maximum load regardless of the size. In fact, for the studied size spectrum the crack opening never exceeds $\omega = 0.125$ mm ($\square$). As highlighted by Maimí et al. [29], the nominal strength of such structures can by predicted by means of the initial part of the CL. In other words, the nominal strength could be predicted by just using a constant CL defined by the rectangle σ_u–ω_1, with a fracture toughness $G_1 = \sigma_u\omega_1$.

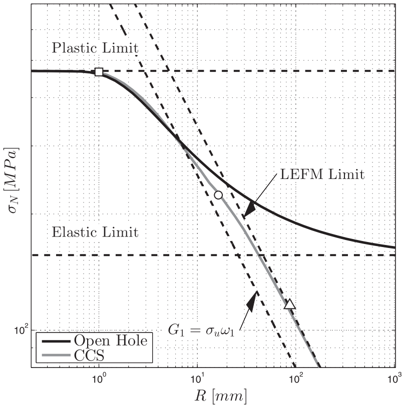

Fig. 10. Nominal strength of a CCS and an OH made of the LCG laminate against the specimen size, obtained using the simplified CL, where R is half the width of the initial crack length for the CCS and the hole radius for the OH.

6. Conclusions

A novel inverse methodology to measure the translaminar Cohesive Law has been proposed. The method is capable of obtaining the Cohesive Law from a single Compact Tension fracture test by fitting several points of the Load–Displacement distributed along the FPZ formation. In order to apply the method, the only laminate properties needed are the elastic modulus, the laminate strength and the specimen dimensions. The inverse method has been successfully implemented, being able to obtain any arbitrary Cohesive Law shape by just fitting the unknown CL shape in order to minimize the difference between the experimental and the predicted P–u curves. The proposed approach has been proven to be objective, as the obtained Cohesive Law and fracture toughness are independent of the location and number of the fitted points, provided that they are distributed along the Fracture Process Zone formation.

Two laminates have been tested in the present work. The Cohesive Law found for the first laminate (LG), made of woven Glass Fabric plies, can be adjusted with a trilinear piecewise function and with a G_c of 78.6 N/mm. The found Cohesive Law of the second laminate (LCG), made of woven Glass fabric and woven Carbon fabric plies, can be adjusted with a piecewise constant-stress function followed by an exponential decrease of the stresses. In this case, the measured G_c is 105.0 N/mm.

In order to objectively compare similar Cohesive Law shapes, a simplified softening function has been proposed for the second laminate, with only needing to define five parameters. The proposed simplified Cohesive Law is capable of predict accurately the P–u curve of the Compact Tension specimen, as the obtained results are in an excellent agreement with the experimental results.

Lastly, the nominal strength of a Center Cracked Specimen and an Open Hole specimen has been predicted using the simplified Cohesive Law of the LCG laminate. The Size Effect on the nominal strength has effectively been captured for both notched and unnotched geometries. In the case of the Center Cracked Specimen the response transitions from the plastic limit response for very small specimens to the LEFM limit for large specimens. On the other hand, for the Open Hole specimen, the geometry response for large specimens tends to the classic elastic solution defined by the stress concentration factor. It has also been concluded that only the initial part of the Cohesive Law is needed to predict the nominal strength of unnotched specimens, as the Fracture Process Zone is never fully developed at the maximum load regardless of the specimen size.

Acknowledgements

This work has been partially funded by the Spanish Government through the Ministerio de Economía y Competitividad, under contracts MAT2013-46749-R (subprogram MAT) and MAT2012-37552-C03-03.

Appendix A. Stress intensity factors equations

The non-dimensional stress intensity factor $\bar{K}^P$ caused by the load P is defined [31]

$$\bar{K}^P = \frac{2+\bar{a}}{(1-\bar{a})^{3/2}}F_1 \tag{A.1}$$

$$F_1 = 0.886 + 4.64\bar{a} - 13.32\bar{a}^2 + 14.72\bar{a}^3 - 5.6\bar{a}^4 \tag{A.2}$$

The stress intensity factor K_i^Q caused by a point load Q applied at the crack surface and at a distance of $\bar{a}_i$ from the load line is defined [32]

$$K_i^Q = \frac{Q}{W^{1/2}}\bar{K}_i^Q; \quad \bar{K}_i^Q = \left(\frac{2}{\pi(\bar{a} - \bar{a}_i)}\right)^{1/2} F_2 \tag{A.3}$$

$$F_2 = \left(1 + A_1\Delta + A_2\Delta^2\right)\left[1 - 1.05(1 - \bar{a})^9(\Delta/\Delta_0)^3\right]/(1 - \Delta)^{3/2} \tag{A.4}$$

$$\Delta = \bar{a} - \bar{a}_i; \quad \Delta_0 = 0.8\bar{a} + 0.2 \tag{A.5}$$

$$A_1 = 3.6 + 12.5(1 - \bar{a})^8;$$
$$A_2 = 5.1 - 15.32\bar{a} + 16.58\bar{a}^2 - 5.97\bar{a}^3 \tag{A.6}$$

The non-dimensional stress intensity factor $\bar{K}_i^\sigma$ caused by a constant cohesive stress of normalized width $\Delta\bar{a}$ and centred at a_i [33]

$$\begin{aligned}\bar{K}_i^\sigma = \frac{1}{(1 - \bar{a})^{3/2}(8\pi)^{1/2}}\Bigg[&2B(1 + A_1 + A_2)\sqrt{B^2 + (1 - \bar{a})B}\\ &+(1 - \bar{a})(5 + A_1 - 3A_2)\sqrt{B^2 + (1 - \bar{a})B}\\ &+(1 - \bar{a})^2(3 - A_1 + 3A_2)\ln\left(\sqrt{B} + \sqrt{B + 1 - \bar{a}}\right)\Bigg]\Bigg|_{B=\bar{a}-\bar{a}_i+\Delta a/2}^{B=\bar{a}-\bar{a}_i-\Delta a/2}\end{aligned} \tag{A.7}$$

The crack opening at a distance $\bar{a}_i$ caused by the load P is obtained

$$\hat{\omega}_i^P = \int_{\bar{a}_i}^{\bar{a}} 2\bar{K}^P\bar{K}_i^Q d\bar{a} \tag{A.8}$$

The crack opening at a distance $\bar{a}_i$ caused by a constant cohesive stress of normalized length $\Delta\bar{a}$ and centred at a_j is obtained

$$\hat{\omega}_{ij} = \int_{\bar{a}_i}^{\bar{a}} 2\bar{K}_j^\sigma\bar{K}_i^Q d\bar{a} \tag{A.9}$$

References

[1] Ritchie RO. The conflict between strength and toughness. Nat Mater 2011;10:817–22.

[2] Mai Yw. Cohesive zone and crack-resistance (R)-curve of cementitious materials and their fibre-reinforced composites. Eng Fract Mech 2006;69(2002):219–34.

[3] Irwin GR. Fracture mechanics. In: Structural mechanics. London: Pergamon Press; 1960.

[4] Bažant ZP, Kim J, Pfeiffer P. Continuum model for progressive cracking and identification of nonlinear fracture parameters. Appl Fract Mech Cementitious Compos 1984:197–285.

[5] Bao G, Suo Z. Remarks on crack-bridging concepts. Appl Mech Rev 1992;45(8):355–66.

[6] Suo Z, Bao G, Fan B. Delamination R-curve phenomena due to damage. J Mech Phys Solids 1992;40(1):1–16.

[7] Sørensen BF, Gamstedt EK, Østergaard RC, Goutianos S. Micromechanical model of cross-over fibre bridging Prediction of mixed mode bridging laws. Mech Mater 2008;40(4–5):220–34.

[8] Sørensen BF, Jacobsen TK. Large-scale bridging in composites: R-curves and bridging laws. Compos Part A: Appl Sci Manuf 1998;29(11):1443–51.

[9] Ortega A, Maimí P, González E, Trias D. Specimen geometry and specimen size dependence of the $\mathcal{R}$-curve and the size effect law from a cohesive model point of view. Submitted to Int J Fracture 2016.

[10] Dugdale D. Yielding of steel sheets containing slits. J Mech Phys Solids 1960;8:100–4.

[11] Barenblatt GI. The formation of equilibrium cracks during brittle fracture: general ideas an hypotheses, axially-symmetric cracks. J Appl Math Mech 1959;23:622–36.

[12] Barenblatt GI. The mathematical theory of equilibrium cracks in brittle fracture. Adv Appl Mech 1962;7:55–129.

[13] Hillerborg A, Modeer M, Petersson P. Analysis of crack formation and crack growth in concrete by means of fracture mechanics and finite elements. Cem Concr Res 1976;6(6):773–81.

[14] Bažant ZP, Planas J. Fracture and size effect in concrete and other quasibrittle materials. Boca Raton and London: CRC Press; 1998.

[15] Zobeiry N, Vaziri R, Poursartip A. Characterization of strain-softening behaviour and failure mechanisms of composites under tension and compression. Compos Part A: Appl Sci Manuf 2015;68:29–41.

[16] Catalanotti G, Camanho PP, Xavier J, Dávila C, Marques A. Measurement of resistance curves in the longitudinal failure of composites using digital image correlation. Compos Sci Technol 2010;70(13):1986–93.

[17] Bergan AC, Dávila CG, Leone FA, Awerbuch J, Tan Tm. Mode I Cohesive Law characterization of through-crack propagation in a multidirectional laminate. In: Proceedings of the American society for composites 2014-twenty-ninth technical conference on composite materials. San Diego; 2014.

[18] Paris AJ, Paris PC. Instantaneous evaluation of J and C*. Int J Fract 1988;38:19–21.

[19] Sørensen BF, Jørgensen K, Jacobsen TK, Østergaard RC. DCB-specimen loaded with uneven bending moments. Int J Fract 2006;141:163–76.

[20] Que NS, Tin-Loi F. An optimization approach for indirect identification of cohesive crack properties. Comput Struct 2002;80:1383–92.

[21] Silva FG, Xavier J, Pereira FA, Morais JJ, Dourado N, Moura MF. Determination of Cohesive Laws in wood bonded joints under mode II loading using the ENF test. Int J Adhes Adhes 2014;51(8):54–61.

[22] Roelfstra PE, Wittmann FH. Numerical method to link strain softening with failure of concrete. In: Wittmann FH, editor. Fracture toughness and fracture energy of concrete. B.V., Amsterdam: Elsevier Science Publishers; 1986. p. 163–75.

[23] Steiger T, Sadouki H, Wittmann FH. Simulation and observation of the fracture process zone. In: Proc of fracture mechanics of concrete structures, FRAMCOS II; vol. II. 1995. p. 157–68.

[24] Bolzon G, Fedele R, Maier G. Parameter identification of a cohesive crack model by Kalman filter. Comput Methods Appl Mech Eng 2002;191(25–26):2847–71. http://dx.doi.org/10.1016/S0045-7825(02)00223-2.

[25] Ortega A, Maimí P, González E, Ripoll L. Compact tension specimen for orthotropic materials. Compos Part A: Appl Sci Manuf 2014;63:85–93.

[26] Pinho ST, Robinson P, Iannucci L. Fracture toughness of the tensile and compressive fibre failure modes in laminated composites. Compos Sci Technol 2006;66(13):2069–79. http://dx.doi.org/10.1016/j.compscitech.2005.12.023. <http://linkinghub.elsevier.com/retrieve/pii/S026635380600011X>.

[27] Laffan MJ, Pinho ST, Robinson P, McMillan A. Translaminar fracture toughness: the critical notch tip radius of plies in CFRP. Compos Sci Technol 2011;72(1):97–102.

[28] González EV, Maimí P, Sainz de Aja JR, Cruz P, Camanho PP. Effects of interply hybridization on the damage resistance and tolerance of composite laminates. Compos Struct 2014;108(0):319–31.

[29] Maimí P, Trias D, González E, Renart J. Nominal strength of quasi-brittle open hole specimens. Compos Sci Technol 2012;72(10):12031208.

[30] Maimí P, González EV, Gascons N, Ripoll L. Size effect law and critical distance theories to predict the nominal strength of quasibrittle structures. Appl Mech Rev 2013;65:1–16.

[31] Tada H, Paris PC, Irwin GR. The stress analysis of cracks handbook. New York: ASME Press; 2000.

[32] Newman J, Yamada Y, James MA. Stress-intensity-factor equations for compact specimen subjected to concentrated forces. Eng Fract Mech 2010;77(6):1025–9.

[33] Mall S, Newman JC. The Dugdale model for compact specimen. In: Fracture mechanics: sixteenth symposium; 1985. p. 113–28.

PAPER C

Specimen geometry and specimen size dependence of the $\mathcal{R}$-curve and the Size Effect Law from a Cohesive Model point of view

A. Ortega [a], P. Maimí [a], E.V. González [a], D. Trias [a]

[a]AMADE, Mechanical Engineering and Industrial Construction Department, Universitat de Girona, Campus Montilivi s/n, Girona, Spain

The paper has been accepted for publication in *International Journal of Fracture, (2017)*

International Journal of Fracture manuscript No.
(will be inserted by the editor)

Specimen geometry and specimen size dependence of the $\mathcal{R}$-curve and the Size Effect Law from a Cohesive Model point of view

Adrián Ortega · Pere Maimí · Emilio V. González · Daniel Trias

Received: date / Accepted: date

Abstract An analytic model has been developed for a Compact Tension specimen subjected to a controlled displacement and corresponding load within a cohesive model framework. The model is able to capture the material response while the Fracture Process Zone is being developed, obtaining the evolution of multiple variables such as the crack opening and the cohesive stresses, for an arbitrary Cohesive Law shape. The crack growth prediction based on the $\mathcal{R}$-curve and the nominal strength prediction based on Bažant's Size Effect Law have been implemented using the output variables available from the proposed analytic model. The minimum specimen size has been found in order to properly apply $\mathcal{R}$-curve based methods. The study has concluded that only the cohesive model is able to properly capture the changes of the Specimen Geometry and Specimen Size, as unlike in other theories, no Linear Elastic Fracture Mechanics assumptions are made.

Keywords R-curves · Cohesive zone modelling · J-integral · Bridging · Crack growth

1 Introduction

During crack nucleation and crack growth within a continuum solid, most materials develop a relatively large Fracture Process Zone (FPZ) where energy is dissipated. Fig. 1 schematically describes the FPZ present between the traction free crack (between points a and b) and the elastic solid (beyond point d). This area is divided in two regions based on the nature of the dissipation mechanisms. The first region (bounded by points c and d) is located ahead of the crack tip, where non-linear material hardening takes place. Also known as intrinsic dissipation, it is typical of metals and other ductile materials. The second region (bounded by b and c) is located behind the crack tip, where material softening or extrinsic dissipation occurs. The latter region is typical of quasi-brittle materials, such as concrete, composite materials and advanced ceramics (Ritchie 2011). Depending on the relative sizes of these two zones and of the structure, one may distinguish between ductile behaviour (intrinsic dissipation is dominant), quasibrittle behavior (extrinsic dissipation is dominant) or brittle fracture (the FPZ is very small compared to the structure size). The present work focuses on quasibrittle materials.

Linear Elastic Fracture Mechanics (LEFM) considers that the entire FPZ (bounded by the points b and d

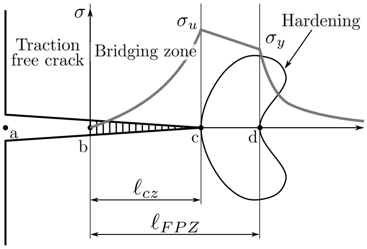

Fig. 1: Representation of the Failure Process Zone.

A. Ortega (✉) · P. Maimí · E. V. González · D. Trias [1]
AMADE, Mechanical Engineering and Industrial Construction Department, Universitat de Girona, Campus Montilivi s/n, Girona, Spain
[1] Serra Hnter Fellow
Tel.: +34 972 418 908
E-mail: adri.ort@gmail.com

in Fig. 1) lies at a single point at the crack tip while the rest of the solid behaves elastically, i.e., considers a brittle fracture. In reality this zone must have some finite size. Irwin estimated the FPZ length (ℓ_{FPZ}) using the elastic stress distribution around the crack tip, by assuming that the ℓ_{FPZ} is equal to the zone over which the tensile strength has been exceeded (Irwin 1960). Irwin also introduced the term equivalent crack length: a fictitious increase of the crack in order to maintain the force balance when assuming the new stress distribution inside the FPZ.

The non-linearities that take place at the crack tip while the FPZ is being formed can be predicted by using LEFM in conjunction with an $\mathcal{R}$-curve that defines the apparent increase of fracture toughness as the crack grows. This methodology can only be applied under small-scale bridging (SSB) conditions for quasibrittle materials or under small-scale yielding (SSY) for ductile materials, i.e., when the ℓ_{FPZ} is small compared to other problem dimensions, particularly when compared to the crack length. This limitation is obvious for laboratory sized specimens (Bažant 1992), and becomes especially true for some natural materials such as human bone (Yan et al 2007; Koester et al 2008b) or human dentin (Koester et al 2008a), whose natural size limits the specimen dimensions. This restriction is also present in some newly developed materials such as metallic-glasses and bioinspired ceramics (Bloyer et al 1998; Bouville et al 2014; Demetriou et al 2011) where the specimen size is limited by the manufacturing processes. In addition, it is known that the $\mathcal{R}$-curve is not a material property, as it depends on the specimen size as well as the Specimen Geometry (SG) (Bao and Suo 1992; Suo et al 1992; Sørensen et al 2008; Sørensen and Jacobsen 1998). Furthermore, the methodologies to predict the structural strength based on the $\mathcal{R}$-curve are only applicable for notched specimens, as they are not able to predict crack nucleation on smoothed surfaces.

An alternative approach to describe the FPZ formation is through the cohesive model by introducing the Cohesive Law (CL) of the material. This methodology goes back to the Dugdale's strip yield model (Dugdale 1960), who introduced a constant stress inside the FPZ, and Barenblatt (Barenblatt 1962a), who introduced a stress function with respect to the crack opening, and those implemented later with finite elements by Hillerborg by using cohesive elements (Hillerborg et al 1976) and Bažant in a smeared way (Bažant and Oh 1983). It should be mentioned that Dugdale's strip yield model was developed for perfect plasticity, although, in fact, the model is more suitable for quasibrittle fracture: the energy dissipation is confined in a plane (bridging stresses) instead of taking up a volume (material hardening). The use of the CL accounts for the extrinsic energy dissipation mechanisms typical of quasi-brittle materials, by introducing a relationship between bridging stresses and the crack opening.

The present paper is structured as follows: Section 2 defines an analytic cohesive model for a Compact Tension (CT) geometry, considering the cohesive stresses and crack openings inside the FPZ, that is used in further sections throughout the paper. Section 3 explores the characteristics of the FPZ formation and the relationship between the specimen size, the CL and how it influences the nominal strength of structures. Section 4 reviews currently available methodologies to obtain the CL from experimental results, and Section 5 compares the cohesive model with the fracture models based on the $\mathcal{R}$-curves and size effect theories. Lastly, Sections 6 and 7 are focussed on the results discussion and the conclusions, respectively.

2 Compact Tension cohesive model

2.1 Generalized Dugdale-Barenblatt model

An analytic model to solve the non-linear fracture problem has been implemented based upon the Dugdale-Barenblatt model (Dugdale 1960; Barenblatt 1959, 1962b), where the stress singularity at the crack tip is null due to the presence of cohesive stresses located at the FPZ. In this case, the model is adapted to consider any general cohesive stress profile. Although the procedure hereby described is applied to the CT specimen, the same method can be used to solve other Specimen Geometries (Maimí et al 2012; Newman 1983; Williams et al 2011).

Given a CT specimen of size W, as shown in Fig. 2, it experiences a crack growth along the symmetry plane, developing a FPZ with cohesive stresses σ_c, under the action of a controlled displacement (u) and corresponding load (P). The non-linear problem can be solved as a superposition of two linear problems: one case considering a CT specimen with a crack length of $a_0 + \ell_{dam}$ and a pair of loads P located at the pin holes and a second problem only considering the CT with closure cohesive stresses inside the FPZ. The superposition approach is shown in Fig.3, where the damaged length ℓ_{dam} is the length measured from the initial crack length a_0 to the FPZ tip. While the FPZ is growing, ℓ_{dam} is equal to the current length of the FPZ. Once the FPZ is fully developed and the crack growth is self-similar, ℓ_{dam} accounts for the FPZ length plus the traction free crack length.

Due to the the presence of cohesive stresses in the FPZ, no stress singularity is found in the model, in

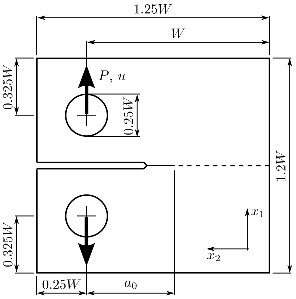

Fig. 2: Compact Tension (CT) Specimen Geometry, subjected to a controlled displacement u and corresponding load P.

other words, Dugdale's condition must be fulfilled, and the global SIF must be zero:

$$K = K^P + K^{\sigma_c} = 0 \tag{1}$$

where K^P is the Stress Intensity Factor (SIF) produced by the point load P and K^{σ_c} is the SIF caused by the whole cohesive stress profile. Although the σ_c is unknown and may change during the FPZ development, it can always be discretized as a series of small constant stresses of value equal to σ_i applied at the crack surface. Defining $\sigma_N = P\,(Wh)^{-1} = s_N \sigma_u$ and $\sigma_i = s_i \sigma_u$, where σ_u is the ultimate tensile strength of the material and h the specimen thickness:

$$K^P = \sigma_u W^{1/2} s_N \bar{K}^P \quad ; \quad K^{\sigma_c} = \sigma_u W^{1/2} s_i \bar{K}_i^{\sigma} \tag{2}$$

where $\bar{K}^P$ is the non-dimensional function of the SIF caused by a unitary point load P and $\bar{K}_i^{\sigma}$ is a vector that defines the non-dimensional function of the SIF caused by a unitary constant stress applied at the crack surface, of width equal to the one used in the σ_c discretization, and centred at a distance a_i measured from the load line, as shown in 3. The equations for both SIF can be found in A.

Using Eq. 1 and Eq. 2 it is possible to obtain s_N by knowing the normalized cohesive stresses s_i

$$s_N = \beta_i s_i \quad ; \quad \beta_i = \bar{K}_i^{\sigma} / \bar{K}^P \tag{3}$$

with β_i being a vector that relates the discretized cohesive stresses with the load being applied at the pin holes, uniquely defined by the SG and the normalized length $\bar{a}_0 + \bar{\ell}_{dam}$. These lengths are normalized with respect to the specimen size W as $\bar{a}_0 = a_0/W$ and $\bar{\ell}_{dam} = \ell_{dam}/W$.

In order to solve the cohesive stress profile inside the FPZ, the crack opening profile must also be found. It is possible to express the set of openings ω_i as a superposition of the opening caused by each acting load

$$\omega_i = \omega_i^P + \omega_i^{\sigma_c} \tag{4}$$

where ω_i, ω_i^P and $\omega_i^{\sigma_c}$ are the total crack opening, the crack opening caused by the point load P and the crack openings caused by the cohesive stress profile σ_c, respectively. Each crack opening is obtained as

$$\omega_i^P = \frac{W\sigma_u}{E'} s_N \hat{\omega}_i^P \tag{5}$$

$$\omega_i^{\sigma_c} = \frac{W\sigma_u}{E'} s_j \hat{\omega}_{ij}^{\sigma} \tag{6}$$

where E' is the equivalent plane stress or plane strain elastic modulus, $\hat{\omega}_i^P$ is the non-dimensional function of the crack opening caused by the unitary point load P and $\hat{\omega}_{ij}^{\sigma}$ is the non-dimensional function of the crack opening at a position i caused by the unitary constant cohesive stress at a position j. Both can be found in A. At this point, it is possible to re-write Eq. 3 to 6 as

$$\hat{\omega}_i = f_{ij} s_j \quad ; \quad f_{ij} = \beta_j \hat{\omega}_i^P + \hat{\omega}_{ij}^{\sigma}; \tag{7}$$

where $\hat{\omega}_i = \omega_i E' / (\sigma_u W)$ is the non-dimensional crack opening at position i and s_j is the non-dimensional stress at position j. By knowing $s_j\,(\hat{\omega}_j)$ of the material and using Eq. 7 it is possible to obtain the normalized cohesive stresses s_j and the normalized crack profile $\hat{\omega}_i$ inside the FPZ for a given $\bar{\ell}_{dam}$ and consequently any problem variable. The solution algorithm is outlined below. First, a $\bar{\ell}_{dam}$ is selected. Then, from an iterative process Eq. 7 is solved for a given CL, and as a result the stress profile and the crack openings at the FPZ are obtained. Then the load P is obtained by means of Eq. 3. Lastly, the displacement u is defined as the crack opening at $a_i = 0$, using again Eq. 7.

2.2 Cohesive Law and $J - w_{CTOD}$ curve

Matrix cracking, fibre-bridging and fibre pull-outs take place in fracture propagation of fibre-reinforced composites. In concrete, micro-cracks appear in the cement, and the aggregates produce friction as the crack faces are opening (Ouyang and Shah 1993). Such quasi-brittle materials do not exhibit hardening and have all the energy dissipation mechanisms confined in a plane. Under these circumstances, fracture is accurately-enough represented with the use of a cohesive model, with the only dissipation mechanisms taking place inside the FPZ

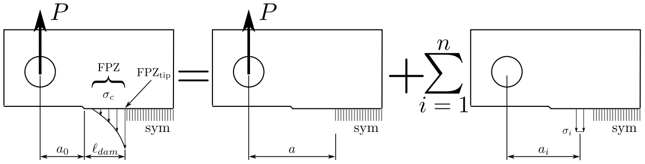

Fig. 3: Compact Tension (CT) specimen with a failure process zone as a superposition of linear problems.

(Mai 2006). This cohesive model is not only able to correctly reproduce the crack growth, but also to predict the crack onset and the structural strength. The Cohesive Law, considered to be a material property (Bao and Suo 1992), relates the cohesive stresses inside the FPZ with the cohesive crack openings. Because the energy being dissipated is entirely governed by the CL, it is a key property necessary to properly model the fracture mechanisms of quasi-brittle materials.

Some common CL shapes can be seen in Fig. 4a. Independently of the shape, some features are shared among all the possible CL types. The area under the curve must be equal to the material fracture energy G_{Ic}, to ensure the correct energy dissipation when the FPZ is fully developed. The onset point of the Cohesive Law must be equal to the material ultimate tensile strength σ_u, and the FPZ is totally developed once the crack opening at the initial crack tip has reached the critical value ω_c. Lastly, to ensure a localized crack, it is necessary that $\partial\sigma/\partial\omega \leq 0$, i.e. the softening function must be a non-increasing function, or, at least, that its local maxima are lower than σ_u. Otherwise, after the first crack had appeared, other crack would appear at neighbouring points (Elices et al 2002).

The J-ω_{CTOD} curve is a material property equivalent to the CL. This curve expresses the energy being dissipated inside the FPZ as the cohesive crack tip opens. Similar to the $\mathcal{R}$-curve, the energy dissipated grows as the FPZ is being formed, and achieves a plateau value once the FPZ has been completely developed. It is related to the CL as (Rice 1968):

$$J = \int_0^{\omega_{CTOD}} \sigma(\omega)\, d\omega \tag{8}$$

where ω_{CTOD} is the opening measured at the initial crack tip, i.e., the opening measured at a_0. Typical J-ω_{CTOD} curves can be seen in Fig. 4b, where J/G_{Ic} is the normalized J integral with respect to the total fracture toughness.

It is possible to define a normalized cohesive law by normalizing the stress $s = \sigma/\sigma_u$ and the crack openings $\bar{\omega} = \omega\sigma_u/\left(2G_{Ic}\right)$. Hence, it is possible to define several CL families classified by their general shape. In this manner, all the linear CL are defined: $s = 1 - \bar{\omega}$ for $\bar{\omega} < 1$; exponential: $s = \exp(-2\bar{\omega})$ or constant: $s = 1$ for $\bar{\omega} < 1/2$. It should be highlighted that the crack opening normalization used in the CL ($\bar{\omega}$) differs from the one introduced in Eq. 7 ($\hat{\omega}$). Both are related as $\hat{\omega} = 2\bar{\ell}_M\bar{\omega}$, where

$$\bar{\ell}_M = \frac{\ell_M}{W} \quad \text{where} \quad \ell_M = \frac{G_{Ic}E'}{\sigma_u^2} \tag{9}$$

ℓ_M is a material characteristic length.

2.3 Model output and normalization

Introducing the normalized material CL, it is possible to rewrite Eq. 7 as

$$2\bar{\ell}_M\bar{\omega}_i = f_{ij}s_j \quad ; \quad f_{ij} = \beta_j\hat{\omega}_i^P + \hat{\omega}_{ij}^{\sigma}; \tag{10}$$

It should be noticed that: (i) f_{ij} is a function that only depends on the Specimen Geometry, (ii) the relation $s\left(\bar{\omega}\right)$ is entirely defined by the CL shape and (iii) $\bar{\ell}_M$ defines the relation between the material characteristic length and the size of the structure. In other words, for a given SG and CL shape, the model response is only dependant on $\bar{\ell}_M$.

For a given $\bar{\ell}_{dam}$, the load, the displacement, the Fracture Process Zone length (ℓ_{FPZ}), the cohesive stresses, crack openings and the traction-free crack length are known. Furthermore, the whole model can be defined with just four inputs, hence, any dimensionless variable $\bar{\chi}$ can be expressed as a function $\bar{\chi}\left(\bar{\ell}_{dam}, \bar{\ell}_M, CL, SG\right)$. Being the CT a negative-geometry structure, the crack propagation is stable under controlled displacement, meaning that any dimensionless variable can also be expressed as $\bar{\chi}\left(\bar{u}, \bar{\ell}_M, CL, SG\right)$. The external load is defined as $P = s_N W h \sigma_u$, the displacements and crack openings are $\omega = \bar{\omega}2G_{Ic}/\sigma_u = \hat{\omega}\sigma_u W/E'$ and the crack and FPZ lengths are $\ell_{\text{FPZ}} = \bar{\ell}_{\text{FPZ}}W$. Actually, any variable can be rewritten as a function of m-times to the n-power of $\bar{\ell}_M$. This property is useful for comparing the model outputs with respect to other particular solutions.

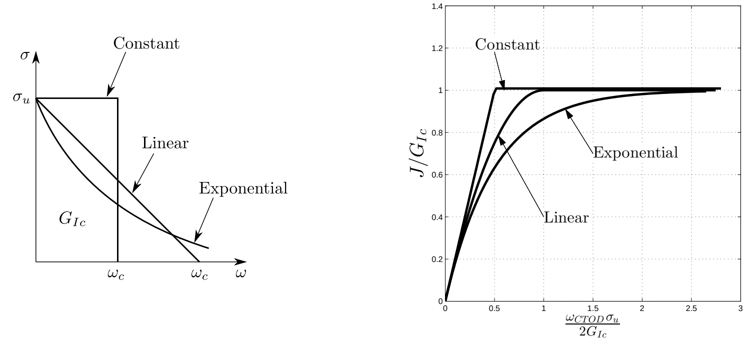

(a) (b)

Fig. 4: (a) Constant, linear and exponential Cohesive Laws, and (b) their corresponding J/G_{Ic} curves.

An interesting approach to normalize the load-displacement curve is by taking into account the LEFM theory. The load-displacement solution according to LEFM can be expressed as

$$\frac{P}{hK_{Ic}W^{1/2}} = \frac{1}{\bar{K}^P(\bar{a})} \quad \text{and} \quad u\frac{E'}{K_{Ic}W^{1/2}} = \frac{\bar{C}(\bar{a})}{\bar{K}^P(\bar{a})} \tag{11}$$

where $\bar{K}^P(\bar{a})$ and $\bar{C}(\bar{a})$ are geometrical functions presented in A and B, respectively. In order to obtain the same normalization with the available model outputs, the normalized load is obtained as $s_N/\sqrt{\bar{\ell}_M}$ while the normalized displacement is obtained as $2\sqrt{\bar{\ell}_M}\bar{u}$ or $\hat{u}/\sqrt{\bar{\ell}_M}$, where $\bar{u}$ and $\hat{u}$ are computed by evaluating the normalized crack openings $\bar{\omega}$ and $\hat{\omega}$, respectively, at load line $\bar{a}_i = 0$.

As previously mentioned, the response of the model depends on the normalized shape of the CL and on normalized material characteristic length $\bar{\ell}_M$. Fig. 4 shows several load-displacement curves normalized with respect to the LEFM solution, for various $\bar{\ell}_M$ and for a linear CL. As it can be seen, the response for small $\bar{\ell}_M$ (large W) tends to the LEFM particular solution. Each curve also features the point in which the crack tip opening reaches a certain series of values $\bar{\omega}_{CTOD} = 0.1$, 0.2 and 0.5. The corresponding position of each crack opening on the CL are seen in Fig. 5b. The load peak is achieved generally at small values of $\bar{\omega}_{CTOD}$, with a decreasing tendency as $\bar{\ell}_M$ increases, going as low as $\bar{\omega}_{CTOD} = 0.2$ for $\bar{\ell}_M = 10$. On the other hand, for extremely brittle responses, the peak load is achieved as soon as $\bar{\omega}_{CTOD} = 1$. Under these circumstances, the FPZ is small enough so that all the non-linearities can be neglected.

To show the influence of the cohesive law shape on material response, Fig. 6a shows three load displacement curves for a linear, constant and exponential CL when $\bar{\ell}_M = 0.5$. As it can be seen, the response around the load peak is very sensitive to the CL shape. The outputs related to the FPZ are also available for each point of the load-displacement curve using the proposed model. Fig. 6b illustrates the cohesive stress profile s_i and cohesive crack openings $\bar{\omega}_i$ for a CT with $\bar{a}_0 = 0.5$, $\bar{\ell}_M = 0.5$, $\bar{\ell}_{dam} = 0.25$ and a linear CL shape. It is easily observed that, in this precise moment, the FPZ has already been completely developed, and hence the crack growth has become self-similar. The FPZ length is obtained from measuring the cohesive crack surface length in which $s_i > 0$, that is, from $\bar{a}_i = 0.54$ to $\bar{a}_i = 0.75$. In the example showcased in the Fig. 6b, the $\bar{\ell}_{FPZ} = 0.21$ or $\ell_{FPZ} = 0.42\ell_M$. Notice that this length is lower than the predicted one for a Center Cracked Specimen (CCS), being in this case $\ell_{FPZ} = 0.732\ell_M$ (Bao and Suo 1992).

3 Measuring the Cohesive Law

Assuming the Cohesive Law as a material property, it could be characterized by means of the experimental measure of the function $\sigma - \omega$. Ideally, it could be obtained as the evolution of the stress measured at the initial crack tip a_0 position as the crack opens, similarly to the method applied to composite materials proposed by Zobeiry et al (2014). In this method, the displace-

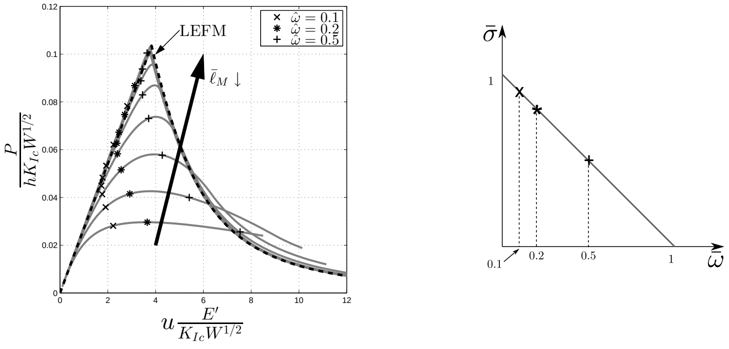

(a) (b)

Fig. 5: (a) Eight $\bar{P}$-$\bar{u}$ curves with a linear CL and $\bar{\ell}_M$ ranging from 0.01 to 10 in constant logarithmic increments and the normalized crack openings $\hat{\omega} = 0.1$, 0.2 and 0.5. (b) A linear Cohesive Law with the indicated crack openings at $\hat{\omega} = 0.1$, 0.2 and 0.5

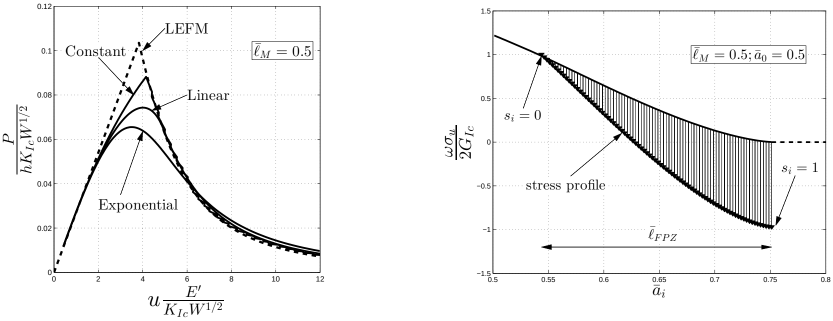

(a) (b)

Fig. 6: (a) Normalized load-displacement curves for a linear, constant and exponential CL. (b) Normalized crack opening profile $\omega\sigma_u/2G_{Ic}$ and cohesive stresses s_i for a specimen with $\bar{a}_0 = 0.5$, a linear CL, $\bar{\ell}_{dam} = 0.25$ and $\bar{\ell}_M = 0.5$.

ment field of the specimen is measured through the use of the Digital Image Correlation (DIC) technique, and the FPZ boundary is estimated where the material does not behave linear-elastically. The cohesive stresses are obtained by assuming the stress in the loading direction across the damaged material to be uniform and equal to the stress of the undamaged material adjacent to the FPZ. Finally, an optimization algorithm is used in order to find a softening function that best fits the experimental curves. Despite the fact that this method is time-consuming, it is capable of measuring any arbitrary CL during the FPZ formation as well as during the self-similar crack growth. In practice, some problems arise when trying to perform this experimental measurement. For instance, it is not feasible measure the strain inside an heterogeneous region such as the FPZ, where a material discontinuity is taking place, e.g. matrix cracking, fibre bridging and fibre pull-out. On the other hand, the crack opening could be measured with a displacement transducer placed at the ini-

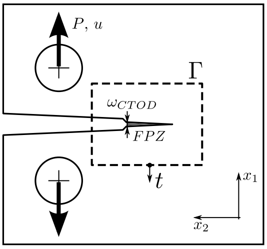

Fig. 7: Integration path Γ and normal traction vector t for the J-integral.

tial crack tip or with the use of the DIC, although the obtained data would probably suffer from high scattering.

Alternatively, instead of trying to obtain the stress, the CL could be obtained by means of the $\sigma(\omega)$ integration, that is, using the J-ω_{CTOD} curve (Sørensen and Jacobsen 2003), where J is the fracture energy dissipated inside the FPZ as the crack tip opens. The CL is obtained with Eq. 8 by differentiating J-ω_{CTOD}, obtaining $\sigma = dJ/d\omega_{CTOD}$. Experimentally, evaluating the J integral can be a difficult task. Ideally, one would like to measure the strain and stress field of the specimen during the whole crack formation and propagation. Then, it would be possible to directly apply the J definition

$$J = \int_{\Gamma} \left(\Phi dx_1 - t_i \frac{\partial u_i}{\partial x_2} ds \right) \tag{12}$$

where Φ is the elastic strain density, t_i is the surface traction vector and u_i is the displacement vector. The surface traction vector is obtained as $t_i = \sigma_{ij} n_j$, where n_j is a unitary vector normal to the path Γ and σ_{ij} is the stress tensor. The J defined in Eq. 12 is a path-independent integral, meaning that the measured energy that is being dissipated is invariant regardless of the path Γ, provided it encloses the FPZ, as seen in Fig. 7. As this method involves differentiating experimental measurements, it suffers from high scattering, and some sort of smoothing is normally needed. A sophisticated method to experimentally measure J is to use the DIC technique to obtain the strain field of the specimen during the whole fracture initiation and propagation, provided that the measurement is done sufficiently away from the FPZ (Catalanotti et al 2010; Bergan et al 2014). The stress is once again obtained with the measured strains in conjunction with the material elastic properties. Once J-ω_{CTOD} is known (some example curves are showed in Fig. 4b for a constant, linear and exponential softening curves), the CL is obtained by differentiating J with respect to the crack opening.

For some SG the closed form equation of the J-integral can be analytically obtained from Eq. 12, resulting in only needing to measure the acting load instead of measuring the stress and strain field. For instance, when evaluating J in a Double Cantilever Beam (DCB) subjected to a bending moment M in pure mode I loading the expression turns into a function of the form $J(M)$, with only needing to record the bending moment that is being applied as the FPZ progresses (Suo et al 1992). Similarly, J can expressed analytically for a DCB subjected to a pair of bending moments M_1 and M_2 in mixed mode I/II loading in the form $J(M_1, M_2)$ (Sørensen et al 2006). When applying a point load P in pure mode I loading, the expression is simplified as $J(P, \theta)$, where θ is the rotated angle at the loading end (Paris and Paris 1988; Olsson and Stigh 1989), meaning that in addition to measure P, θ needs also to be recorded experimetally (Andersson and Stigh 2004). Unfortunately, such closed-form J-integral expressions do not exist for a CT specimen. In this case, the only way to measure J would be by means of the more difficult and expensive DIC technique.

Finally, an alternative approach to measure the CL is through the use of an optimization algorithm to solve the inverse problem (Que and Tin-Loi 2002; Silva et al 2014; Ortega et al 2015; Roelfstra and Wittmann 1986; Steiger et al 1995; Bolzon et al 2002; Ortega et al 2016). The inverse analysis consists of three steps: an experimental u-P curve collected from experimental tests; a computer simulation of the test in order to find the parameters that define the CL; lastly, the minimisation of a suitable norm which quantifies the discrepancy between experimental data and the corresponding values provided by the computer simulation, with respect to the mentioned parameters. When addressing the problem in this fashion it is important to choose the correct specimen size W. The specimen needs to be sufficiently large so that at the end of the experiment the FPZ has been completely developed, and, at the same time, it must be sufficiently small so that its response differs enough from the LEFM one, allowing to properly capture the CL shape.

4 $\mathcal{R}$-Curve

The $\mathcal{R}$-curve is extensively used to predict the non-linear fracture properties of materials. It defines the apparent increase of the fracture toughness as a crack grows along a continuous solid given the presence of an initial notch. Instead of using a LEFM fracture criterion

$G = G_{Ic}$, the crack growth condition is computed with a variable toughness provided by the $\mathcal{R}$-curve. Although normally used as a material property, it is known that depends on the SG and size (Bao and Suo 1992; Suo et al 1992; Sørensen et al 2008; Sørensen and Jacobsen 1998). From a cohesive model point of view, the apparent increase of the fracture toughness of the material can be understood as the formation and propagation of the FPZ (Suo et al 1992; Jacobsen and Sørensen 2001). The increase of G_{Ic} takes place while the FPZ is growing. During this process the cohesive zone is being developed with the cohesive stresses and crack openings being related by the CL. As a consequence, even for the same $\bar{\ell}_M$ and SG, the $\mathcal{R}$-curve depends heavily on the CL shape (Gutkin et al 2011; Jacobsen and Sørensen 2001). When the FPZ has been completely developed the $\mathcal{R}$-curve achieves the fracture toughness plateau value G_{Ic}. At this point, the crack growth becomes self-similar with the FPZ moving along the crack path.

To measure the $\mathcal{R}$-curve, a fracture test needs to be carried out, along with the recording of the P-u curve and also some sort of crack length measure. The most common $\mathcal{R}$-curve is defined as a crack length function $\mathcal{R} - \Delta a$ (Irwin 1960; Krafft et al 1961), although other commonly used approaches to define the $\mathcal{R}$-curve are the $\mathcal{R} - \omega_{CMOD}$ and $\mathcal{R} - \omega_{CTOD}$ (Elices and Planas 1993; Planas et al 1993), where ω_{CMOD} stands for the opening at the crack mouth, that is, at the load line or $\bar{a} = 0$. A frequent practice is to use the LEFM definition of the Energy Release Rate (ERR) to measure the increase of $\mathcal{R}$, as in any fracture toughness reduction standard procedure (ASTM 2006, 2001)

$$G = \frac{1}{h}\frac{\partial U\,(P,a)}{\partial a} = -\frac{1}{h}\frac{\partial U\,(u,a)}{\partial a} = \mathcal{R} \tag{13}$$

Eq. 13 is based on the assumption that the specimen behaves elastically and that all the energy dissipation mechanisms lie in a very small area ahead of the crack tip, thus expressing the ERR as the crack length a increases. In reality, when large-scale bridging (LSB) occurs in quasi-brittle materials the stress field differs greatly form the LEFM one, as the FPZ takes a considerably large portion of the specimen. Thus, in such cases, the ERR is not well defined with Eq. 13.

Another problem arises when trying to measure a. Typically, in LEFM, the crack tip is defined as a sharp through-the-thickness edge perpendicular to the crack growth direction. In reality, even for brittle materials, the crack tip profile is not straight, and its shape usually depends on the specimen thickness. Additionally, taking the cohesive model as background, the definition of crack length looses its definition due the existence of the FPZ.

Generally, two methods for measuring the crack length exist: one based on an optical measure and one based on the equivalent elastic compliance. The main disadvantage of the optical measure of the crack tip position is that this is not an objective measure as the crack length itself is not well defined because of the presence of the FPZ. The second most typically used methodology to estimate a is through the equivalent crack length a_{eq}. The equivalent crack length is obtained by equalling the experimental compliance of the cracked specimen to the pure elastic case (Bažant and Planas 1998)

$$C = \frac{u}{P} = \frac{\bar{C}}{hE'} \tag{14}$$

where $\bar{C}$ is the normalized elastic compliance, uniquely defined given $\bar{a}$. The analytic expression of $\bar{C}$ is found in B for isotropic materials, and in (Ortega et al 2014) for orthotropic materials. For specimens with low values of $\bar{\ell}_M$ it would be acceptable to apply this methodology, as the FPZ length can be neglected, as is in the case of SSB and SSY. In this case, though, the measure would suffer from a high scatter, as the compliance $\bar{C}$ would remain almost constant during the FPZ development (see Fig. 5a for low values of $\bar{\ell}_M$).

Some $\mathcal{R}$-curves have been obtained in order to illustrate the $\bar{\ell}_M$ dependence. To obtain the curves, the output variables u and P have been obtained for a CT specimen with a linear CL for $\bar{\ell}_M = 0.05$, 0.5 and 1, using the analytic cohesive model defined in Section 2. First, the compliance obtained from the model is equalled to the elastic compliance of Eq. 14, in order to infer the equivalent crack length a_{eq}. Then, the fracture toughness is obtained from the LEFM definition of K_I^P, found in Eq. 2:

$$\mathcal{R} = \frac{\sigma_N^2}{E'} W (\bar{K}^P)^2 \tag{15}$$

Fig. 8a and Fig. 8b show how the change of $\bar{\ell}_M$ affects the $\mathcal{R}$-curve. It is clearly observed that neither $\mathcal{R}$-ω_{CTOD} nor $\mathcal{R} - \Delta a$ are material properties, as they are $\bar{\ell}_M$ dependant. There are several references in the literature that have also reflected this phenomena, either experimentally (Mai and Hakeem 1984; Bolzon et al 2002; Koester et al 2008b; Bloyer et al 1998; Bouville et al 2014; Demetriou et al 2011; Naglieri et al 2015) or numerically (Suo et al 1992; Jacobsen and Sørensen 2001; Brocks et al 2002). Comparing $\mathcal{R}$-ω_{CTOD} with the J-ω_{CTOD} curve of Fig. 4b, it is seen that both are equivalent only for small values of $\bar{\ell}_M$, that is, when the FPZ is so small that LEFM can be assumed and consequently $J = G$. On the other hand, for very small specimens, the material fracture toughness is overpredicted.

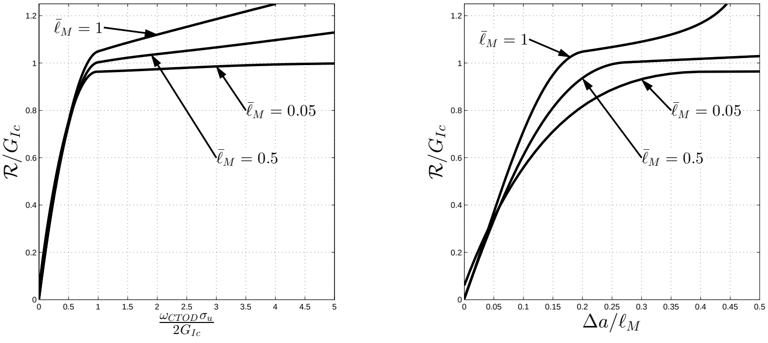

(a) (b)

Fig. 8: Three (a) $\mathcal{R}$-ω_{CTOD} and (b) $\mathcal{R}$-$\Delta a_{eq}/\ell_M$ curves with a linear CL for $\bar{\ell}_M = 0.05$, 0.5 and 1.

To be able to discern when large-scale bridging and small-scale bridging assumptions can be made, an additional plot has been obtained, observed in Fig. 9a. In this case the propagation values of $\mathcal{R}$, i.e. the maximum value $\mathcal{R}_{\max}$, has been obtained for several $\bar{\ell}_M$ values. As it can be observed in Fig. 9a, the $\bar{\ell}_M$ values for which the assumption of SSB is correct (and therefore LEFM is applicable) are influenced by the CL shape. When comparing the self-similar crack growth for a constant CL against a linear CL, the former exhibits a shorter FPZ length. Therefore, the assumption of SSB will be possible for greater values of $\bar{\ell}_M$ (smaller specimens). In general, the longer the tail of the CL shape is, the longer the fully developed FPZ length will be. On the other hand, as $\bar{\ell}_M$ increases, the $\mathcal{R}$ value becomes distorted when LEFM assumptions are made, as seen in the left region of Fig. 9a. Specifically, the standard procedure for the determination of the fracture toughness of metallic materials ASTM E399 (ASTM 1997) and of plastic materials ASTM D5045 (ASTM 1999) states that the procedure to determine the $\mathcal{R}$ can only be applied for $\bar{\ell}_M < 0.4\,(1 - \bar{a}_0)$, then for the CT specimen presented $\bar{\ell}_M^{-1} > 5$.
As it can be seen in Fig. 9a, for large enough specimens, it is correct to assume SSB, resulting in an $\mathcal{R}$-curve that is not size dependant. Fig. 9b shows three $\mathcal{R}$-curves for a linear, constant and exponential CL, for $\bar{\ell}_M^{-1} = 25$, in which case SSB can be assumed.

5 $\mathcal{R}$-curve from Size Effect Law

In order to prevent the dependence of $\bar{\ell}_M$ on the $\mathcal{R}$-curve determination, Bažant et al. (Bažant et al 1984) suggested an alternative approach. The method consisted on recording the structural strength of various specimens of the same geometry for a wide range of sizes, in order to obtain the resistance curve. As it has been shown in the results of Fig. 5a, for small specimens the peak load is achieved when the FPZ is barely developed, i.e. for small crack openings, whereas for large specimens the peak load is achieved when the FPZ has been fully developed, i.e. for large crack openings. This phenomenon is translated into an extremely different mean stress distribution at the failure plane for specimens of different sizes. Recording the nominal strength in such fashion makes Bažant's $\mathcal{R}$-curve a size-independent property. In addition, this methodology can also be applied to a SG unstable under controlled displacement. However, one of the main disadvantages of using this method is that several specimens of different sizes are needed in order to measure the $\mathcal{R}$-curve, while at the same the results are subjected to the experimental scatter.
From a set of experiments it is possible to obtain a function of the form $\sigma_N(W)$, defined as the Size Effect Law (SEL). For each experiment, the nominal strength is recorded and the ERR is computed using Eq. 15. Although the crack length defined in $\bar{K}^P$ is needed to compute $\mathcal{R}$, it can be inferred by imposing the invariability of $\mathcal{R}$ with respect to the specimen size, that is,

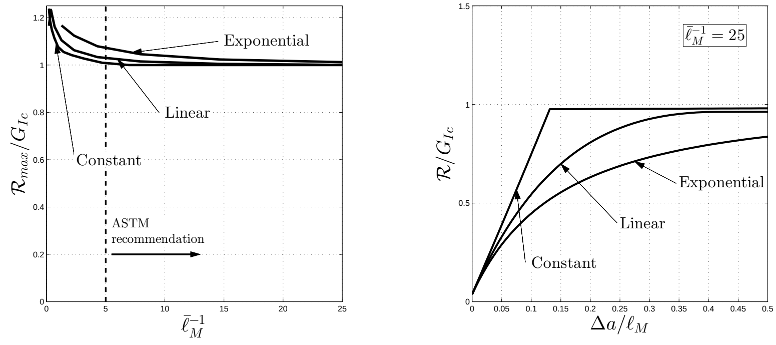

(a) (b)

Fig. 9: (a) Propagation values of $\mathcal{R}$ for several values of $\bar{\ell}_M$. (b) Three $\mathcal{R}$-curves with a linear, constant and exponential CL and with $\bar{\ell}_M = 0.04$.

$\partial\mathcal{R}/\partial W = 0$, which results in the condition:

$$\sigma_N \left(\bar{K}^P - 2\frac{\partial \bar{K}^P}{\partial \bar{a}} (\bar{a}_{eq} - \bar{a}_0) \right) + 2W\bar{K}^P \frac{\partial \sigma_N}{\partial W} = 0 \quad (16)$$

By solving this equation, it is possible to obtain $\bar{a}_{eq}$ and therefore the increase of crack length as $\Delta a = (\bar{a}_{eq} - \bar{a}_0)W$. Hence, by just obtaining the function $\sigma_N(W)$ it is possible to completely define the $\mathcal{R}$-curve for a given SG.

Bažant's Size Effect Law defines the nominal strength of a notched structure as (Bažant 1985, 1997):

$$\sigma_N = \sigma_u B \left(1 + \left(\frac{W}{W_0} \right)^r \right)^{\frac{-1}{2r}} \quad \text{or}$$

$$\left(\frac{B\sigma_u}{\sigma_N} \right)^{2r} = 1 + \left(\frac{W}{W_0} \right)^r \quad (17)$$

where B, W_0 and r are constants to be fitted from experimental observations. In the case of very small specimens $W \to 0$, hence $\sigma_N = B\sigma_u$. This limit represents the plastic limit solution, defined when the whole failure plane achieves a constant stress equal to σ_u. On the other hand, for very large specimens $W \to \infty$, thus obtaining the solution $\sigma_N = \sigma_u B \, (W/W_0)^{-1/2}$. This represents the LEFM nominal strength solution. Matching Eq. 17 with the CT limit solutions, the parameter B can be obtained from the moment balance at the failure plane with a constant stress equal to σ_u: $B = 1/2 \, (1 - \bar{a}_0)^2$. The parameter W_0 can be obtained through the use of the LEFM limit solution: $W_0 = \ell_M (B\bar{K}_0^P)^{-2}$, where $\bar{K}_0^P$ is $\bar{K}^P \, (\bar{a}_0)$. For comparative purposes, B and W_0 have been also obtained for a Center Cracked Specimen (CCS) of infinite width, being $B = 1$ and $W_0 = \ell_M (B\bar{K}_0^P)^{-2} = \ell_M/\pi$, taking into account that in this case W is defined as a_0 (Maimí et al 2012). As it can be seen, B is a scalar related uniquely with the Specimen Geometry, whereas W_0 is geometry and material dependent. The remaining parameter r defines the shape of the transition between the plastic and LEFM limits. It is usually defined as $r = 1$ since it gives good enough results for most of the experimental results (particularly when dealing with concrete, where a high experimental scatter is present). When fitting computer simulation results, however, they do not have random scatter, and so small deviations become noticeable. In this case, the values of r usually range from, although not restricted to, 0.5 to 2 depending on the SG and used CL.

Bažant's SEL for $r = 1$ (standard solution) is shown as a solid line in Fig. 10. The normalized variables $\sigma_N / (\sigma_u B)$ and $W/W_0 = (BK_0^P)^2/\ell_M$ are used, in order to being able to compare the solution with other SG and CL. Using these normalized variables, the representation of Bažant's SEL only depends on r. Furthermore, Bažant's SEL plotted in Fig. 10b results in a straight line for $r = 1$. The results obtained with the present cohesive model are also represented in the same figure for a CT and CCS specimens (Maimí et al 2013) with a linear and constant CL. The parameter r depends on the SG as well as the CL, and has been determined by best fitting Eq. 17 with the results obtained by the cohesive model. For the CT, $r = 0.54$ and $r = 0.9$ for a linear and a constant CL respectively. In the case of the

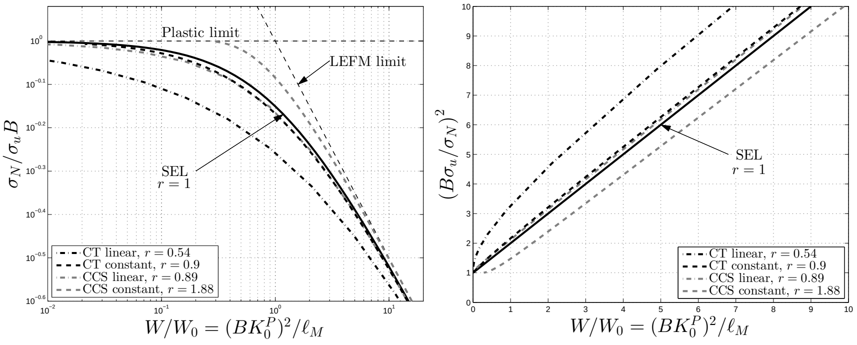

(a) (b)

Fig. 10: (a) Bažant SEL compared to the nominal strength of a CT and CCS of infinite width specimens with a linear and constant CL (b) and their respective linear representation.

CCS, it has been found that $r = 0.89$ and $r = 1.88$ best fit the data, again for a linear and a constant CL. The last value is in concordance with the value of $r = 1.99$ found by Bažant and Planas (1998).

The $\mathcal{R}$-curve obtained from Bažant's SEL is defined by means of Eq. 15 and Eq. 17:

$$\frac{\Delta a}{\ell_M} = \frac{\bar{a}_{eq}-\bar{a}_0}{(B\bar{K}_0^P)^2}\left(\frac{\bar{K}^P}{2\bar{K}^{P'}(\bar{a}_{eq}-\bar{a}_0)}-1\right)^{\frac{1}{r}} \quad ;$$
$$\frac{\mathcal{R}}{G_{Ic}} = B^2\left(2\bar{K}^{P'}(\bar{K}^P)^{2r-1}(\bar{a}_{eq}-\bar{a}_0)^{1-r}\right)^{\frac{1}{r}}\frac{\Delta a}{\ell_M} \quad (18)$$

Where $\bar{K}^{P'}$ is the derivative of the SIF with respect to the crack length. Fig. 11 shows the $\mathcal{R}$-curve obtained with Eq. 18. In the figure, the $\mathcal{R}$-curve has been computed for a CT and a CCS, again for a linear and a constant CL, using the corresponding parameter r found from the SEL. For the standard case of $r = 1$ the equation is reduced to:

$$\frac{\Delta a}{\ell_M} = \frac{1}{(BK_0^P)^2}\left(\frac{\bar{K}^P}{2\bar{K}^{P'}}-(\bar{a}_{eq}-\bar{a}_0)\right) \quad ;$$
$$\frac{\mathcal{R}}{G_{Ic}} = B^2 2\bar{K}^P\bar{K}^{P'}\frac{\Delta a}{\ell_M} \quad (19)$$

This particular solution is also featured in Fig. 11 with a solid line for the CT and the CCS specimens. As it can be seen, when comparing both specimen geometries for a given CL shape, the SEL results in very distinct $\mathcal{R}$-curves, concluding that the resistance curve determined by means of the SEL is not a material property. At this point, it is possible to compare the $\mathcal{R}$-curves of the CT specimen for a linear and a constant CL, computed from the classic LEFM definition (Section 4), seen in Fig. 9b, and the one defined by the SEL (Section 5), seen in Fig. 11. As it can be seen, the curve defined form the SEL slightly lies below the LEFM one. More concretely, for the CT specimen with a constant CL, the $\mathcal{R}$ achieves the propagation value G_{Ic} when $\Delta a/\ell_M = 0.125$ obtained from LEFM, whereas in the case of the SEL, the propagation is observed when $\Delta a/\ell_M = 0.15$. The same behaviour is appreciated in the case of the linear CL shape.

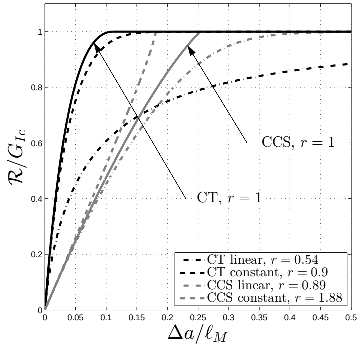

Fig. 11: Bažant's $\mathcal{R}$-curve for the CT and a CCS of infinite width with the found values of r.

Two advantages arise when obtaining the $\mathcal{R}$-curve through the SEL: first, it is not required for the SG to be stable under controlled displacement as only the maximum load needs to be recorded for each experiment; secondly, it is not required to measure any crack length during the experiments, since it is determined by the condition that the $\mathcal{R}$-curve is size-independent, that is, the condition defined in Eq. 16. However, some drawbacks appear during the use of this methodology. Firstly, multiple specimens of different sizes must be tested in order to measure the $\mathcal{R}$-curve, with costs increasing with the size. Also, it has been shown that ultimately, the shape of the curve is heavily dependent of the SG and other theories such as the Cohesive Model may predict more accurately the fracture of such materials. Therefore, the $\mathcal{R}$-curve should not be considered a material property.

6 Conclusions

An analytic solution has been presented in order to obtain the load-displacement curve for a Compact Tension specimen given any general Cohesive Law. The solution is completely defined by the Specimen Geometry, the normalized characteristic length $\bar{\ell}_M$ and the Cohesive Law. Along each point of the curve, several model outputs are obtained, such as: the Fracture Process Zone length, the cohesive crack openings, the cohesive stresses and the traction free crack length, as well as any other problem variable associated to the model. From the available load and displacement outputs of the proposed cohesive model, the $\mathcal{R}$-curve has been computed, from the load-displacement curve of a Compact Tension specimen with a linear, constant and exponential Cohesive Laws. By comparing the propagation values of the $\mathcal{R}$ against the specimen size, it has been determined the minimum specimen size for which it is possible to obtain an $\mathcal{R}$-curve independent of the specimen size, avoiding to over-predict the material fracture toughness. The specimen size recommendations proposed by the ASTM standard have proven to be sufficient for materials with a constant CL shape, although they are not big enough for materials with a CL shape with a long tail, such as the exponential shape, due to the increase of the FPZ length.

The $\mathcal{R}$-curve has been obtained from the Size Effect Law, following the approach suggested by Bažant. It has been shown that the results obtained from this methodology are dependent on the Specimen Geometry, while also differing from the results obtained from the load-displacement curve.

Lastly, it has been shown that the $\mathcal{R}$-curve its a property incompatible with the Cohesive Law. This disagreement is mainly caused by the use of LEFM assumptions in the $\mathcal{R}$-curve definition, and specially by the LEFM definition of the crack length. On the other hand, the cohesive model solved for the Compact Tension geometry does not assume any LEFM hypothesis.

Acknowledgements

This work has been partially funded by the Spanish Government through the *Ministerio de Economía y Competitividad*, under contracts MAT2013-46749-R (subprogram MAT) and MAT2015-69491-C3-1-R.

A Stress Intensity Factors equations

The Stress Intensity Factor $\bar{K}^P$ due the load P is defined Tada et al (2000)

$$\bar{K}^P = \frac{2+\bar{a}}{(1-\bar{a})^{3/2}} F_1 \tag{20}$$

$$F_1 = 0.886 + 4.64\bar{a} - 13.32\bar{a}^2 + 14.72\bar{a}^3 - 5.6\bar{a}^4 \tag{21}$$

The Stress Intensity Factor K_i^Q due a point load Q at a distance of $\bar{a}_i$ measured from the load line, positioned at the crack surface, is defined Newman et al (2010)

$$K_i^Q = \frac{Q}{hW^{1/2}} \bar{K}_i^Q \quad ; \quad \bar{K}_i^Q = \left(\frac{2}{\pi\left(\bar{a}-\bar{a}_i\right)}\right)^{1/2} F_2 \tag{22}$$

$$F_2 = \left(1 + A_1\Delta + A_2\Delta^2\right)\left[1 - 1.05\left(1-\bar{a}\right)^9\left(\Delta/\Delta_0\right)^3\right] / \left(1-\Delta\right)^{3/2} \tag{23}$$

$$\Delta = \frac{\bar{a}-\bar{a}_i}{1-\bar{a}_i} \quad ; \quad \Delta_0 = 0.8\bar{a} + 0.2 \tag{24}$$

$$A_1 = 3.6 + 12.5\left(1-\bar{a}\right)^8 \quad ; \quad A_2 = 5.1 - 15.32\bar{a} + 16.58\bar{a}^2 - 5.97\bar{a}^3 \tag{25}$$

The non-dimensional stress intensity factor $\bar{K}_i^\sigma$ caused by a constant cohesive stress of normalized width $\Delta\bar{a}$ and centered at a_i (Mall and Newman 1985):

$$\begin{aligned}\bar{K}_i^\sigma = &\frac{1}{(1-\bar{a})^{3/2}(8\pi)^{1/2}}\Big[2B\left(1+A_1+A_2\right)\sqrt{B^2+\left(1-\bar{a}\right)B}\\ &+\left(1-\bar{a}\right)\left(5+A_1-3A_2\right)\sqrt{B^2+\left(1-\bar{a}\right)B}\\ &+\left(1-\bar{a}\right)^2\left(3-A_1+3A_2\right)\ln\left(\sqrt{B}+\sqrt{B+1-\bar{a}}\right)\Big]\Big|_{B=\bar{a}-\bar{a}_i+\Delta\bar{a}/2}^{B=\bar{a}-\bar{a}_i-\Delta\bar{a}/2}\end{aligned} \tag{26}$$

The crack opening at a distance $\bar{a}_i$ caused by the load P is obtained

$$\hat{\omega}_i^P = \int_{\bar{a}_i}^{\bar{a}} 2\bar{K}^P\bar{K}_i^Q d\bar{a} \tag{27}$$

The crack opening at a distance $\bar{a}_i$ caused by a constant cohesive stress of normalized length $\Delta\bar{a}$ and centred at $\bar{a}_j$ is obtained

$$\hat{\omega}_{ij} = \int_{\bar{a}_i}^{\bar{a}} 2\bar{K}_j^\sigma\bar{K}_i^Q d\bar{a} \tag{28}$$

B Elastic CT compliance

The dimensionless elastic compliance for an isotropic material is defined (Tada et al 2000)

$$\bar{C} = \left(\frac{1+\bar{a}}{1-\bar{a}}\right)^2 \left(2.1630 + 12.219\bar{a} - 20.065\bar{a}^2 - 0.9925\bar{a}^3 \right. \\ \left. + 20.609\bar{a}^4 - 9.9314\bar{a}^5\right) \quad (29)$$

C Cohesive solution extended for orthotropic materials

The differential equation that defines the stress state of an orthotropic material with the principal directions aligned normal to the crack growth direction depends on the roots of the polynomial (Ortega et al 2014):

$$\lambda p^4 + 2\rho\sqrt{\lambda}p^2 + 1 = 0 \quad (30)$$

Defining the principal directions as in Fig. 2, in the plane stress case, λ and ρ are expressed as:

$$\lambda = \frac{E_{22}}{E_{11}} \ \ , \ \ \rho = \frac{\sqrt{\lambda}}{2G_{12}}\left(E_{11} - 2\nu_{12}G_{12}\right) \quad (31)$$

where E_{11} and E_{22} are the elastic moduli, G_{12} is the shear modulus, and ν_{12} is the Poisson's ratio. In the plane strain case, λ and ρ are obtained by replacing E_{11}, E_{22} and ν_{12} in Eq. (31) by:

$$E'_{11} = \frac{E_{11}}{1-\nu_{13}\nu_{31}} \ , \ E'_{22} = \frac{E_{22}}{1-\nu_{23}\nu_{32}} \ , \ \nu'_{12} = \frac{\nu_{12}+\nu_{13}\nu_{32}}{1-\nu_{13}\nu_{31}} \quad (32)$$

To ensure the positive definiteness of the strain energy, it must be ensured that:

$$\lambda > 0 \ \text{ and } \ \rho > -1 \quad (33)$$

The anisotropy of the material is easily described by the parameters λ and ρ. For an isotropic material, the parameters take the values $\lambda = \rho = 1$. However, for a cubic material, it only needs to be ensured that $\lambda = 1$ and that $\rho \neq 1$.

In order to solve the cohesive model for an orthotropic material, the SIF, and therefore, the other variables defined in Section 2 need to be expressed as a function of the geometry, λ and ρ.

$$\bar{K}^P\left(\bar{a},\lambda,\rho\right) \quad ; \quad \bar{K}_i^Q\left(\bar{a},\lambda,\rho\right) \quad ; \quad \bar{K}_i^\sigma\left(\bar{a},\lambda,\rho\right) \quad (34)$$

$$\beta_i\left(\bar{a},\lambda,\rho\right) \quad ; \quad \hat{\omega}_i^P\left(\bar{a},\lambda,\rho\right) \quad ; \quad \hat{\omega}_{ij}^\sigma\left(\bar{a},\lambda,\rho\right) \quad (35)$$

The equation $\bar{K}^P\left(\bar{a},\lambda,\rho\right)$ is found in (Ortega et al 2014), as for the rest of the Equations 34 and Equations 35, they can be obtained using the finite elements or equivalent method.

References

Andersson T, Stigh U (2004) The stress-elongation relation for an adhesive layer loaded in peel using equilibrium of energetic forces. International Journal of Solids and Structures 41:413–434

ASTM (1997) E399-90. Standard test method for plane-strain fracture toughness of metallic materials. 1991 Annual Book of ASTM Standards 3(Reapproved):451–485

ASTM (1999) D5045-99. Standard Test Methods for Plane-Strain Fracture Toughness and Strain Energy Release Rate of Plastic Materials. West Conshohocken, PA

ASTM (2001) ASTM E1820-01. Standard test method for measurement of fracture toughness. American Society for Testing and Materials

ASTM (2006) ASTM E399-06. Standard test method for linear-elastic plane-strain fracture toughness K_{Ic} of metallic materials.

Bao G, Suo Z (1992) Remarks on crack-bridging concepts. Applied Mechanics Reviews 45(8):355–366

Barenblatt GI (1959) The formation of equilibrium cracks during brittle fracture: general ideas an hypotheses, axially-symmetric cracks. Journal of Applied Mathematics and Mechanics 23:622–636

Barenblatt GI (1962a) The Mathematical Theory of Equilibrium Cracks in Brittle Fracture. Advances In Applied Mechanics 7:55–129

Barenblatt GI (1962b) The Mathematical Theory of Equilibrium Cracks in Brittle Fracture. Advances In Applied Mechanics 7:55–129

Bažant ZP (1992) Fracture Mechnaics of Concrete. In: First International Conference on Fracture Mechanics of Concrete Structures

Bažant ZP, Oh BH (1983) Deformation of Cracked Net-Reinforced Concrete Walls. Journal of Structural Engineering 109(2):93–108

Bažant ZP, Planas J (1998) Fracture and Size Effect in Concrete and Other Quasibrittle Materials. CRC Press, Boca Raton and London

Bažant ZP, Kim J, Pfeiffer P (1984) Continuum model for progressive cracking and identification of nonlinear fracture parameters. Application of Fracture Mechanics to Cementitious Composites pp 197–285

Bažant ZP (1985) Comment on Hillerborgs Comparison of Size Effect Law with Fictitious Crack Model

Bažant ZP (1997) Scaling of quasibrittle fracture : asymptotic analysis. International Journal of Fracture 83:19–40

Bergan AC, Dávila CG, Leone FA, Awerbuch J, Tan Tm (2014) Title: Mode I Cohesive Law Characterization of Through-Crack Propagation in a Multidirectional Laminate. In: Proceedings of the American Society for Composites 2014-Twenty-ninth Technical Conference on Composite Materials

Bloyer DR, Venkateswara Rao KT, Ritchie RO (1998) Fracture toughness and R-curve behavior of laminated brittle-matrix composites. Metallurgical and Materials Transactions A: Physical Metallurgy and Materials Science 29(10):2483–2496

Bolzon G, Fedele R, Maier G (2002) Parameter identification of a cohesive crack model by Kalman filter. Computer Methods in Applied Mechanics and Engineering 191(25-26):2847–2871

Bouville F, Maire E, Meille S, Van de Moortèle B, Stevenson AJ, Deville S (2014) Strong, tough and stiff bioinspired ceramics from brittle constituents. Nature Materials 13(5):508–514

Brocks W, Cornec a, Scheider I (2002) Computational Aspects of Nonlinear Fracture Mechanics. GKSS Forschungszentrum - Technical Note (July):2–187

Catalanotti G, Camanho PP, Xavier J, Dávila C, Marques A (2010) Measurement of resistance curves in the longitudinal failure of composites using digital image correlation.

Composites Science and Technology 70(13):1986–1993

Demetriou MD, Launey ME, Garrett G, Schramm JP, Hofmann DC, Johnson WL, Ritchie RO (2011) A damage-tolerant glass. Nature Materials 10(2):123–128

Dugdale D (1960) Yielding of steel sheets containing slits. Journal of Mechanics Physics of Solids 8:100–104

Elices M, Planas J (1993) The equivalent elastic crack: 1. Load-Y equivalences. International Journal of Fracture 61(2):159–172

Elices M, Guinea GV, Gómez J, Planas J (2002) The cohesive zone model: advantages, limitations and challenges. Engineering Fracture Mechanics 69(2):137–163

Gutkin R, Laffan ML, Pinho ST, Robinson P, Curtis PT (2011) Modelling the R-curve effect and its specimen-dependence. International Journal of Solids and Structures 48(11-12):1767–1777

Hillerborg A, Modéer M, Petersson PE (1976) Analysis of crack formation and crack growth in concrete by means of fracture mechanics and finite elements. Cement and Concrete Research 6:773–781

Irwin GR (1960) Fracture mechanics. In: Structural mechanics, Pergamon Press, London

Jacobsen TK, Sørensen BF (2001) Mode I intra-laminar crack growth in composites modelling of R-curves from measured bridging laws. Composites Part A: Applied Science and Manufacturing 32:1–11

Koester KJ, Ager JW, Ritchie RO (2008a) The effect of aging on crack-growth resistance and toughening mechanisms in human dentin. Biomaterials 29:1318–1328

Koester KJ, Ager JW, Ritchie RO (2008b) The true toughness of human cortical bone measured with realistically short cracks. Nature Materials 7(8):672–677

Krafft JM, Sullivan AM, Boyle RW (1961) Effect of Dimensions of Fast Fracture Instability of Notched Sheets. In: Proceedings of Cranfield Crack Propagation Symposium, pp 8–28

Mai YW (2006) Cohesive zone and crack-resistance (R)-curve of cementitious materials and their fibre-reinforced composites. Engineering Fracture Mechanics 69(2002):219–234

Mai YW, Hakeem MI (1984) Slow crack growth in bleached cellulose fibre cements. Journal of Materials Science Letters 3(2):127–130

Maimí P, Trias D, González E, Renart J (2012) Nominal strength of quasi-brittle open hole specimens. Composites Science and Technology 72(10):12031208

Maimí P, González EV, Gascons N, Ripoll L (2013) Size Effect Law and Critical Distance Theories to Predict the Nominal Strength of Quasibrittle Structures. Applied Mechanics Reviews 65:1–16

Mall S, Newman JC (1985) The Dugdale Model for Compact Specimen. In: Fracture Mechanics: Sixteenth Symposium, pp 113–128

Naglieri V, Gludovatz B, Tomsia AP, Ritchie RO (2015) Developing strength and toughness in bio-inspired silicon carbide hybrid materials containing a compliant phase. Acta Materialia 98:141–151

Newman J (1983) A nonlinear fracture mechanics approach to the growth of small cracks. In: AGARD, vol 5, pp No. 328, 6.1–6.26

Newman J, Yamada Y, James MA (2010) Stress-intensity-factor equations for compact specimen subjected to concentrated forces. Engineering Fracture Mechanics 77(6):1025–1029

Olsson P, Stigh U (1989) On the determination of the constitutive properties of thin interphase layers - An exact inverse solution. International Journal of Fracture 41(1):71–76

Ortega A, Maimí P, González E, Ripoll L (2014) Compact tension specimen for orthotropic materials. Composites Part A: Applied Science and Manufacturing 63:85–93

Ortega A, Maimí P, González EV (2015) Characterization of the intralaminar fracture cohesive law. In: 7th International Conference on Composite Testing and Model Identification COMPTEST 2015

Ortega A, Maimí P, González EV, Trias D (2016) Characterization of the translaminar fracture cohesive law. Composites Part A: Applied Science and Manufacturing

Ouyang C, Shah S (1993) Toughening Mechanisms in Quasi-Brittle Materials. Journal of Engineering Materials and Technology 115:300

Paris AJ, Paris PC (1988) Instantaneous Evaluation of J and C*. International Journal of Fracture 38:19–21

Planas J, Elices M, Ruiz G (1993) The equivalent elastic crack: 2. X-Y equivalences and asymptotic analysis. International Journal of Fracture 61:231–246

Que NS, Tin-Loi F (2002) An optimization approach for indirect identification of cohesive crack properties. Computer & Structures 80:1383–1392

Rice JR (1968) A Path Independent Integral and the Approximate Analysis of Strain Concentration by Notches and Cracks 35:379–386

Ritchie RO (2011) The conflict between strength and toughness. Nature materials 10:817–822

Roelfstra PE, Wittmann FH (1986) Numerical method to link strain softening with failure of concrete. In: Wittmann FH (ed) Fracture Toughness and Fracture Energy of Concrete, Elsevier Science Publishers, B. V., Amsterdam, pp 163–175

Silva FG, Xavier J, Pereira FA, Morais JJ, Dourado N, Moura MF (2014) Determination of cohesive laws in wood bonded joints under mode II loading using the ENF test. International Journal of Adhesion and Adhesives 51(8):54–61

Sørensen BF, Jacobsen TK (1998) Large-scale bridging in composites: R-curves and bridging laws. Composites Part A: Applied Science and Manufacturing 29(11):1443–1451

Sørensen BF, Jacobsen TK (2003) Determination of cohesive laws by the j integral approach. Engineering Fracture Mechanics 70:1841–1858

Sørensen BF, Jørgensen K, Jacobsen TK, Østergaard RC (2006) DCB-specimen loaded with uneven bending moments. International Journal of Fracture 141:163–176

Sørensen BF, Gamstedt EK, Østergaard RC, Goutianos S (2008) Micromechanical model of cross-over fibre bridging Prediction of mixed mode bridging laws. Mechanics of Materials 40(4-5):220–234

Steiger T, Sadouki H, Wittmann FH (1995) Simulation and Observation of the Fracture Process Zone. In: Proc. of Fracture Mechanics of Concrete Structures, FRAMCOS II, vol II, pp 157–168

Suo Z, Bao G, Fan B (1992) Delamination R-curve phenomena due to damage. Journal of the Mechanics and Physics of Solids 40(1):1–16

Tada H, Paris PC, Irwin GR (2000) The stress analysis of cracks handbook. ASME Press, New York

Williams TN, Newman Jr JC, Gullett PM (2011) Crack-surface displacements for cracks emanating from a circular hole under various loading conditions. Fatigue & Fracture of Engineering Materials & Structures 34(4):250–259

Yan J, Mecholsky JJ, Clifton KB (2007) How tough is bone? Application of elastic-plastic fracture mechanics to bone.

Bone 40(2):479–484

Zobeiry N, Vaziri R, Poursartip A (2014) Characterization of Strain-Softening Behaviour and Failure Mechanisms of Composites under Tension and Compression. Composites Part A: Applied Science and Manufacturing 68:29–41

PAPER D

Translaminar fracture toughness of interply hybrid laminates under tensile and compressive loads

A. Ortega [a], P. Maimí [a], E.V. González [a], J. R Sainz de Aja [b], F. M. de la Escalera [b], P. Cruz [c]

[a]AMADE, Mechanical Engineering and Industrial Construction Department, Universitat de Girona, Campus Montilivi s/n, 17003 Girona, Spain

[b]Aernnova, Engineering Solutions S. A., Structural Integrity Department, 20 Manoteras Avenue - Building B, 5th Floor, 28050, Madrid, Spain

[c]Applus IDIADA, Principal centro técnico, Santa Oliva, E-43710 Tarragona, Spain

The paper has been submitted for publication in *Composites Science and Technology, 2016*

Translaminar fracture toughness of interply hybrid laminates under tensile and compressive loads

A. Ortega[a,*], P. Maimí[a], E. V. González[a], J. R. Sainz de Aja[b], F. M. de la Escalera[b], P. Cruz[c]

[a] *AMADE, Mechanical Engineering and Industrial Construction Department, Universitat de Girona, Campus Montilivi s/n, 17003 Girona, Spain*
[b] *Aernnova Engineering Division S.A., Structural Integrity Department, 20 Manoteras Avenue - Building B, 5th Floor, 28050 Madrid, Spain*
[c] *Applus IDIADA, Principal centro técnico, Santa Oliva, E-43710 Tarragona, Spain*

Abstract

This paper presents an experimental study of the translaminar fracture toughness under tensile and compressive loads of interply hybrid polymer-matrix composite laminates. The studied laminates were obtained by combining two of three different reinforcements: woven carbon fabric, woven glass fabric and unidirectional carbon tape, manufactured using the Resin Transfer Molding (RTM) process. The resulting in-plane quasi-isotropic laminates were generated by changing each material location along the thickness.

Keywords: A. Laminate, B. Fracture toughness, C. Crack, C. Damage mechanics, C. Fibre bridging

---

1. Introduction

During their life cycle, structures are subjected to traction and compression loads, which are the most frequent cause of collapse. In the case of composite laminates under tensile and compressive loads, fibers are responsible for transferring most of the loads. A translaminar failure of a composite laminate is defined by the emergence of a crack that spans the entire thickness, leading to a structural collapse. This phenomenon is usually triggered by the fiber failure. Therefore, studying the fracture toughness of a translaminar crack is highly relevant

---

[*] Corresponding author
Email address: `adri.ort@gmail.com` (A. Ortega)

to determining the damage tolerance of composite laminates.

Several studies have attempted to understand the translaminar fracture under tensile [1–8] and compressive loads [9–13]. Some authors describe the crack growth in terms of the Resistance curve (or $\mathcal{R}$-curve, the rate of the dissipated energy with respect to the apparent increase of crack length), while others describe it using the Cohesive Law (CL) or its equivalent, the J-integral [14] (the rate of dissipated energy with respect to the crack opening). Both approaches assume that all the dissipation mechanisms are confined to the crack plane. Methods based on the $\mathcal{R}$-curve are also only valid when the Fracture Process Zone (FPZ) is very small compared to the rest of the problem dimensions.

Focusing on failure under tension, the damage onset is normally located at regions where the stress concentration is maximum, i.e. near holes, notches, or material imperfections. The damage mechanisms that take place at the FPZ involve fiber breakage, bridging and pull-out, matrix cracking and delaminations. These damage mechanisms are usually confined to a small region around the crack plane, although in some cases large matrix cracks and delaminations may appear, defining larger damage zones. This is especially true of ply-blocked laminates with unidirectional plies [15, 16].

On the other hand, failure under compressive loads is governed by micro-buckling of the plies oriented along the loading direction, followed by a formation of a kink band. According to experiments by Moran et al. [9] and Moran and Shih [10], three stages can be defined during kinking. The first stage, called incipient kinking, is defined by kink band initiation. When subjected to a critical load, fiber micro-bucking takes place, inducing the initiation of a kink band. During the second stage, called transient kinking stage, the kink band propagates across the specimen thickness, while the matrix undergoes severe shear strain. In the third stage, known as steady-state kinking, the fibers are locked in their orientation, and the kink band broadens by lateral propagation into softer (non-strain hardened) material. Early kinking models such as the one by Rosen [17] are based on using traditional energy methods to analyze the elastic buckling of fibers embedded in matrix, with a kink band normal to the fiber direction, ignoring the plastic or nonlinear shear deformations. On the other hand, Argon [18] based his model on the inherent fiber misalignment and shear yield strength of the matrix, still for a normal to the fiber direction kink band. Later, Budiansky [19] unified Rosen's and Argon's formulas for an elastic-ideally plastic composite, further generalized by Budiansky and Fleck [20] to contemplate inclined kink bands. These complex damage mechanisms that result in the kink-band initiation and broadening are localized in a region where the material softens. This characteristic suggests that the Cohesive Zone Model (CZM) can be an appropriate way to characterize the material response. Unlike in the case of tensile loads, the process of steady-state kink-band propagation is not defined by the formation of a new free crack surface, but by a constant transfer of stresses in the kink-band broadening regime.

Structural notch sensitivity is heavily influenced by translaminar fracture toughness, according to studies carried out since the early models of Waddoups et al. [21] and Whitney and Nuismer [22]. From a Cohesive Model point of view, the role of the translaminar Cohesive Law in the notch sensitivity and size effect of laminated composites has been analyzed under tensile loads in [23–27] and under compressive loads in [28–30]. These models completely define the characteristics of the Failure Process Zone for a given Cohesive Law. Additionally, determining the translaminar CL is crucial to feeding several constitutive damage models defined at the mesoscale, where the constitutive response is defined by means of the smeared crack band model [31–35].

In this work, a large experimental campaign was carried out to determine the fracture properties of several interply hybrid laminates under tensile and compressive loads. These are made from combining three different plies: unidirectional carbon tape, glass fabric, and carbon fabric. From these materials, thirteen quasi-isotropic laminates were manufactured: four made using plies of the same material (pure laminates) and nine with interply hybridization. The J curves of each of the thirteen laminates were obtained for both tensile (Compact Tension specimen) and compressive (Compact Compression specimen) loads. An in-depth analysis was performed, comparing the measured J curves for all the laminates, and how the position of certain plies along the laminate thickness can influence the global performance of the laminate.

The paper is structured as follows: in the next section the experimental campaign is presented, along with the material and specimen specifications. The Methodology section, the procedure used to obtain the J curve is explained. The following section contains the results of each of the tested laminates. In the Discussion, the most relevant results are analyzed, and the data are compared with the material response predicted by the mixing theory. Finally, the document ends with general conclusions derived from the present work.

2. Experimental setup and test specimens

2.1. Materials

Three composite materials were tested in the experimental campaign: two woven fabrics and a Unidirectional Carbon (UC) fiber tape, the same materials defined in the work of González et al. [36]. The three materials were supplied by Hexcel®. The fabric materials use HexFlow® RTM 6 mono-component epoxy system. All composites were supplied with epoxy binders on both sides (with the binder representing about 5% of the total fabric weight). The woven fabric plies are Carbon (C) fabric type G0926 (5HS, 6K, 370 gsm), and Glass (G) fabric type S2 (style 6781, Z-6040, 303 gsm), while the UC is type G1157 (UD, 6 K, 270 gsm).

The elastic properties of each lamina are given in Table 1. The ply thickness, which varies for each material (C = 0.353 mm, G = 0.229 mm and UC = 0.247 mm), was obtained from an average of six measurements of cured non-hybrid laminates.

Table 1: Ply properties of each composite material

Material	E_1 (GPa)	E_2 (GPa)	G_{12} (GPa)	ν_{12}	σ_{uT} (MPa)	σ_{uC} (MPa)
C	59.54	54.95	5.21	0.03	804.1	534
G	19.65	19.24	3.93	0.09	557.8	493
UC	116.73	8.31	4.67	0.26	1477.1	708

2.2. Laminates

By joining two different materials per laminate, the hybrid laminates were divided into three sets: C-G, C-UC and G-UC. Table 2 summarizes the stacking sequences, with the fiber direction of 0° aligned with the loading direction. In order to achieve a comparative analysis for each set, the ply sequences were chosen as symmetric, balanced and in-plane quasi-isotropic (although the G-UC laminates are not strictly quasi-isotropic). The number of plies of each material was also kept consistent. As a result, the in-plane stiffness is constant for each set, although the bending stiffness may vary from laminate to laminate. The C-G laminates are made of $n = 14$ plies, with a cured laminate thickness h of 4.31 mm. In the case of the C-UC laminates $n = 14$ and $h = 4.22$ mm, whereas for the G-UC, $n = 18$ and $h = 4.22$ mm.

For comparative purposes, a set of laminates made of a single material was also studied. The stacking sequences can be found in Table 3. The laminates denoted as LUC are made of UC plies, with $n = 16$ and $h = 4.25$ mm. The laminate LC is made of C plies, with $n = 12$ and $h = 4.36$ mm, while the laminate LG is made of G plies with $n = 20$ and $h = 4.56$ mm.

2.3. Test configurations

Tensile tests were performed on Compact Tension (CT) specimen geometries and compressive tests on Compact Compression (CC) specimen geometries. These geometries are depicted in Fig. 1, with a nominal size of $W = 51$ mm and a pin hole diameter of $d = 8$ mm. The initial crack length is $a_0 = 26$ mm for the CT and $a_0 = 20$ mm for the CC. The tests were carried out following recommendations by Pinho et al. [12], as no standard procedure has been developed for the determination of the translaminar fracture toughness of fiber-reinforced composite materials using a CT or CC specimen. The test was performed with a screw-driven universal testing machine, and the specimens were loaded at rates of 0.5 mm/min. The crack tip notch was manufactured with a diamond-coated disc, ensuring a radius lower than 250 μm, following the recommendations by Laffan et al. [4]. The load cell signal and the extensometer signal were acquired and recorded with a dedicated PC. The displacement was measured with a displacement transducer placed at the crack surface below the load line.

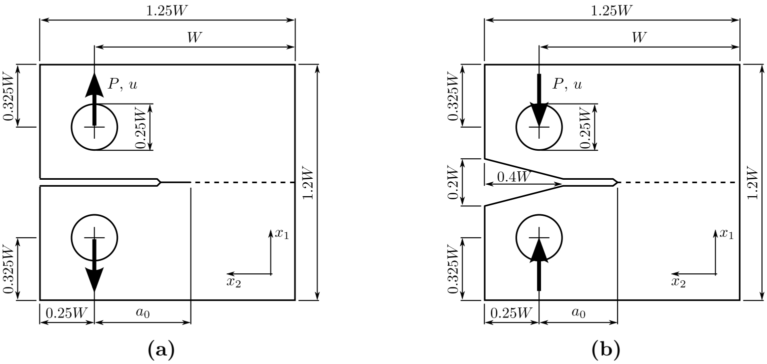

Figure 1: (a) Compact Tension (CT) and (b) Compact Compression (CC) specimen geometries.

Table 2: Hybrid laminates stacking sequences. The 0° direction is aligned with the loading direction.

Materials	Laminates
C-G	L01: $[0^{\mathrm{G}}/60^{\mathrm{G}}/-60^{\mathrm{G}}/(0^{\mathrm{C}}/45^{\mathrm{C}})_2]_{\mathrm{S}}$ L02: $[(0^{\mathrm{C}}/45^{\mathrm{C}})_2/0^{\mathrm{G}}/60^{\mathrm{G}}/-60^{\mathrm{G}}]_{\mathrm{S}}$ L03: $[0^{\mathrm{G}}/(45^{\mathrm{C}}/0^{\mathrm{C}})_2/60^{\mathrm{G}}/-60^{\mathrm{G}}]_{\mathrm{S}}$
C-UC	L04: $[90^{\mathrm{UC}}/-30^{\mathrm{UC}}/30^{\mathrm{UC}}/(0^{\mathrm{C}}/45^{\mathrm{C}})_2]_{\mathrm{S}}$ L05: $[(0^{\mathrm{C}}/45^{\mathrm{C}})_2/90^{\mathrm{UC}}/-30^{\mathrm{UC}}/30^{\mathrm{UC}}]_{\mathrm{S}}$
G-UC	L06: $[90^{\mathrm{UC}}/-45^{\mathrm{UC}}/0^{\mathrm{UC}}/45^{\mathrm{UC}}/(0^{\mathrm{G}}/45^{\mathrm{G}})_2/0^{\mathrm{G}}]_{\mathrm{S}}$ L07: $[(0^{\mathrm{G}}/45^{\mathrm{G}})_2/0^{\mathrm{G}}/-45^{\mathrm{UC}}/90^{\mathrm{UC}}/45^{\mathrm{UC}}/0^{\mathrm{UC}}]_{\mathrm{S}}$ L08: $[90^{\mathrm{UC}}/-45^{\mathrm{UC}}/0^{\mathrm{G}}/45^{\mathrm{G}}/0^{\mathrm{UC}}/45^{\mathrm{UC}}/0^{\mathrm{G}}/45^{\mathrm{G}}/0^{\mathrm{G}}]_{\mathrm{S}}$ L09: $[0^{\mathrm{G}}/45^{\mathrm{G}}/0^{\mathrm{G}}/0^{\mathrm{UC}}/45^{\mathrm{UC}}/0^{\mathrm{G}}/45^{\mathrm{G}}/90^{\mathrm{UC}}/-45^{\mathrm{UC}}]_{\mathrm{S}}$

Table 3: Single material laminates stacking sequences. The 0° direction is aligned with the loading direction.

Materials	Laminates
UC	LUC1: $[(90^{\mathrm{UC}}/-45^{\mathrm{UC}}/0^{\mathrm{UC}}/45^{\mathrm{UC}})_2]_{\mathrm{S}}$ LUC2: $[(90^{\mathrm{UC}})_2/(-45^{\mathrm{UC}})_2/(0^{\mathrm{UC}})_2/(45^{\mathrm{UC}})_2]_{\mathrm{S}}$
C	LC: $[(0^{\mathrm{C}}/45^{\mathrm{C}})_3]_{\mathrm{S}}$
G	LG: $[(0^{\mathrm{G}}/45^{\mathrm{G}})_5]_{\mathrm{S}}$

3. Determination of the translaminar Cohesive Law

When characterizing the resistance of a laminate to the growth of a crack, the most important parameter is the critical fracture energy (G_C). Since the fracture energy usually varies with the crack length, it is normally represented as the Resistance curve or $\mathcal{R}$-curve, as $\mathcal{R}(\Delta a)$. The $\mathcal{R}$-curve is not a material property, as it depends on the specimen geometry and size [37–39], which is especially true for laboratory sized specimens. According to the standard procedures, ASTM E399 [40] and ASTM D5045 [41], the specimen size must guarantee $0.2W\sigma_u^2 > EG_C$, where W is the normalized specimen size, shown in Fig. 1. Alternatively, this kind of fracture is well represented by the Cohesive Zone Model, where the key material property is the Cohesive Law ($\sigma(\omega)$) or the equivalent J-integral curve ($J(\omega)$) [14]. The first one defines the cohesive stresses that appear inside the Fracture Process Zone as the crack tip opening (ω) grows, while the second one defines the dissipated energy with respect to ω. Both properties are equivalent, and their relationship is defined as [14]:

$$J(\omega) = \int_0^{\omega} \sigma(\omega) d\omega \tag{1}$$

A method has been developed to measure the $J(\omega)$ or $\sigma(\omega)$ curve from a single load displacement curve. First, a semi-analytic model is used to obtain the load displacement curve for any given Cohesive Law shape. Second, the laminate Cohesive Law is obtained by means of the introduced model, by best-fitting some points of the experimental load displacement curve. A detailed explanation of the method is presented in [6, 42].

3.1. Generalized Dugdale-Barenblatt model

The Dugdale condition [43] states that the Stress Intensity Factor (SIF) of an elastic body in the presence of a Fracture Process Zone is null due to the existence of the closure stresses. Hence, it is possible to relate the SIF due to the external load (P) with the SIF due to the cohesive stresses (σ_c) as : $K^P = K^{\sigma_c}$. Each SIFs is expressed as:

$$K^P = \tfrac{P}{h\sqrt{W}}\bar{K}^P \quad \text{and} \quad K^{\sigma_c} = \sqrt{W}\sigma_i \bar{K}_i^\sigma \tag{2}$$

where σ_i is the cohesive stress at a position i inside the Failure Process Zone and $\bar{K}^P$ and $\bar{K}_i^\sigma$ are non-dimensional functions that depend on the geometry. The external load is, thus, related to the cohesive stresses as

$$P = \frac{hW}{\bar{K}^P}\sigma_i \bar{K}_i^\sigma \tag{3}$$

The crack opening displacements can be obtained as the superposition of the crack openings caused by each acting load as: $\omega_i = \omega_i^P + \omega_i^{\sigma_c}$, where

$$\omega_i^P = \tfrac{P}{hE}\hat{\omega}_i^P \quad \text{and} \quad \omega_i^{\sigma_c} = \tfrac{W}{E}\sigma_j \hat{\omega}_{ij}^\sigma \tag{4}$$

where $\hat{\omega}_i^P$ is the non-dimensional crack opening at position i caused by a unitary external load P and $\hat{\omega}_{ij}^\sigma$ is the non-dimensional opening at position i due to a unitary cohesive stress at position j. Again, $\hat{\omega}_i^P$ and $\hat{\omega}_{ij}^\sigma$ are non-dimensional functions that depend on the geometry. At this point, it is possible to define a set of algebraic equations such that:

$$\omega_i = \tfrac{W}{E} f_{ij}\sigma_j(\omega_j) \quad \text{where} \quad f_{ij} = \left(\bar{K}^P\right)^{-1} \bar{K}_j^\sigma \hat{\omega}_i^P + \hat{\omega}_{ij}^\sigma \tag{5}$$

These equations relate the crack opening displacements (ω_i) with the cohesive stresses profile (σ_j). Hence, for a given Cohesive Law, it is possible to solve Eq. 5 and obtain the cohesive stress and crack opening profiles at the Failure Process Zone. Lastly, once the cohesive stresses are known, the external load P is obtained with Eq. 3.

The algorithm capable of obtaining the load displacement curve for a given Cohesive Law is implemented as follows [42]: 1) an initial crack length is defined, which accounts for a_0 plus the FPZ length, 2) the cohesive stress and crack opening profiles inside the FPZ are obtained by numerically solving Eq. 5 , 3) the displacement u is obtained as the crack opening at the load line by solving Eq. 5, and the applied load P can be determined with Eq. 3, 4) the crack length is increased and the algorithm is repeated from point 2). This algorithm can be implemented as a standalone code, capable of obtaining the load-displacement curve in just a few seconds, provided that the geometrical functions of Eq. 2 and Eq. 5 are known.

3.2. Algorithm to define the translaminar Cohesive Law and the $J-$curve

The CL is obtained by means of an algorithm that is capable of solving the inverse problem, i. e., guessing the CL shape in order to best fit an experimental u-P curve [6]. The algorithm solves the inverse problem with the following strategy: first, some points from the u-P curve are selected around the peak load, since at this region the FPZ is still being developed. The selected points are used to fit the u-P curve. Taking into account that both the length of the Failure Process Zone and the crack tip opening displacements increase as the external displacement is applied, it is possible to adjust consecutive parts (or branches) of the Cohesive Law. The algorithm first fits a linear segment of the CL in order to fit the smaller of the displacements from the experimental curve. At this point, the first portion of the CL is found, and its width is determined by the cohesive crack opening at the initial crack tip a_0. The algorithm is continued by adding as many branches as points need to be fitted, until the whole shape is found.

3.3. Example of the process of fitting the Cohesive Law from the load displacement curve

The process of fitting the load displacement curve of a CT or CC specimen starts from properly selecting the points from the experimental response. The load displacement curve

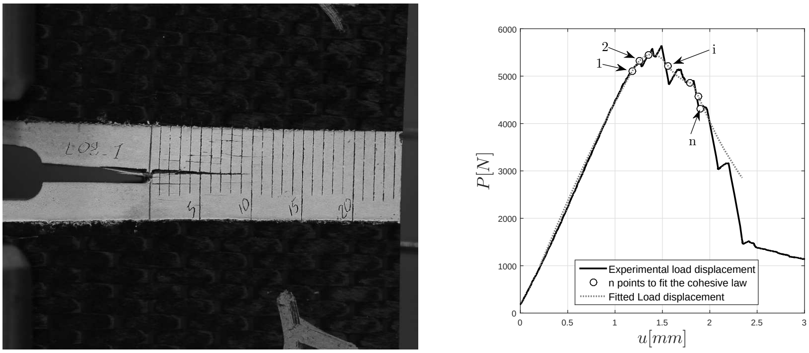

(a) **(b)**

Figure 2: CT specimen of Laminate L04: (a) specimen image at a $P = 4350N$, close to the last fitting point (n), where no back-end damage is observed. (b) Experimental load displacement curve with the points used to fit the Cohesive Law.

of the CT L04 specimen is shown in Figure 2b. As previously stated, the n points used in the fitting process must be selected according to several considerations. The only source of non-linearity in the experimental curve is caused by the cohesive stresses being developed inside the FPZ. The first point must be selected when the non-linearity in the load displacement curve is appreciated, as shown in Fig. 2b. The last point to select, n, must be chosen around the region where the FPZ has been completely developed and the crack growth enters the self-similar regime (for a CT specimen this point corresponds to a zero cohesive stress at the initial crack length a_0, whereas for the CC specimen it corresponds to a constant crushing stress that defines the kink-band broadening). In the present example, an image of the damaged specimen at point n is shown in Fig. 2a. As can be appreciated, the only visible damage is localized at the crack tip region. After this point the specimen fails due to back end compression, which results in a sudden drop of the load. Furthermore, the displacement at point n is small enough to consider small displacements while, at the same time, no buckling is observed. The rest of the points used to adjust the material response must be selected between the first and last point. Usually, the experimental curves have a saw-tooth shape. Since the present model is only capable of measuring the global softening of the material, it is necessary to smooth the experimental curves. This is done in two phases. First, all the experimental u-P curves of the same laminate are averaged. Second, a fine Gaussian smooth is performed in the resulting averaged curve. The used points are then selected from this smoothed experimental curve. In the example shown in Fig. 2b, $n = 7$ points are selected.

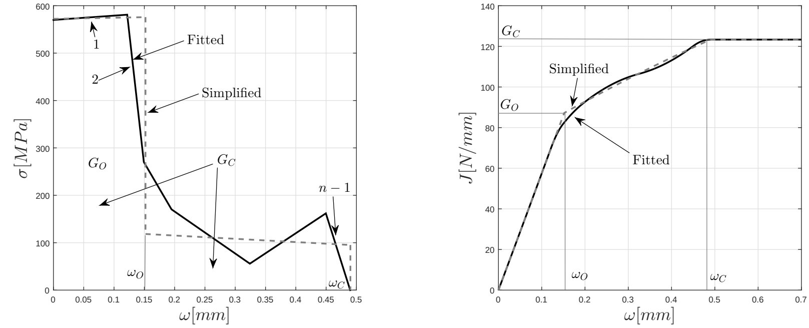

(a) **(b)**

Figure 3: Fitted and simplified (a) Cohesive Law and (b) $J(\omega)$ curve of the L04 CT specimen.

Once the points to be fitted have been selected, the algorithm presented in the previous section is applied. Initially, a first linear slope of the CL is found by fitting point 1. This corresponds to line 1 in Fig. 3a. A second segment of the CL is obtained by fitting point 2, and therefore obtaining the segment 2, also shown in Fig. 3a. Once the n points have been fitted the complete Cohesive Law, defined by n segments, is obtained. In the example, although seven points have been selected, the obtained curve is defined by only six segments, since the crack has already entered the self-similar growth regime after point six. The choice of a different set of points results in a slightly different CL. Once the Cohesive Law has been determined, the $J(\omega)$ curve of Fig. 3b is obtained by integrating $\sigma(\omega)$. The resulting $J(\omega)$ obtained through this method is quite independent of the selected points from the load displacement curve.

When observing the measured $J(\omega)$ curves from the CT specimens, they all share some features: firstly, large portions of energy are dissipated at relatively lower crack openings.

Also, from a certain crack opening, the rate of dissipated energy is more subtle, until reaching a plateau value that defines the total critical fracture energy G_{CT}. This response is translated as Cohesive Law with a region with high stresses for small crack openings and a region made of a long tail with small cohesive stresses. This response can be simplified as shown in Fig. 3. The most relevant parameters of the simplified law are: the total critical fracture energy (G_{CT}), the critical fracture energy dissipated at small crack openings (G_{OT}), which can be identified with the onset energy, the crack opening that defines the transition from the high to low cohesive stresses (ω_{OT}) and, finally, the ultimate crack opening that defines the opening required to create new net crack surface (ω_{CT}).

On the other hand, for the Compact Compression specimens, the $J(\omega)$ curves present a characteristic that stands out with respect to the Compact Tension specimens: after the first part of the curve, where large portions of energy are dissipated at small crack openings, a second region follows, characterized by never achieving a plateau value and always increasing the dissipated energy with a constant slope. This is translated in the Cohesive Law as a curve with a large tail of infinite length and with a constant stress (σ_C). This special characteristic is only present in the compressive specimens and is caused by the kink band broadening that is formed as the applied displacement is increased. To characterize the compressive response of the material, three parameters are considered: G_{OC} as the initial fracture toughness defined until crack opening displacement, w_{OC}, after which point a constant stress remains σ_C in the kink-band broadening regime.

4. Results

The methodologies introduced in the previous section were used to obtain the $J(\omega)$ curves under tensile and compressive loads of all the laminates of Section 2.2. Fig. 4 shows the experimental load displacement curves and the fitted J-curves for the single material (pure) laminates, found in Table 3. Figures 5, 6 and 7 show the experimental load displacement curves and the fitted J-curve of the C-G, C-UC and G-UC laminates, respectively. The laminate nomenclature is presented in Table 2. The black dots featured in all the load displacement experimental curves represent the first and last point used in the fitting process of the Cohesive Law. In the case of the CT specimens, a minimum of six points were used, whereas for the CC specimens more than fifteen points were used.

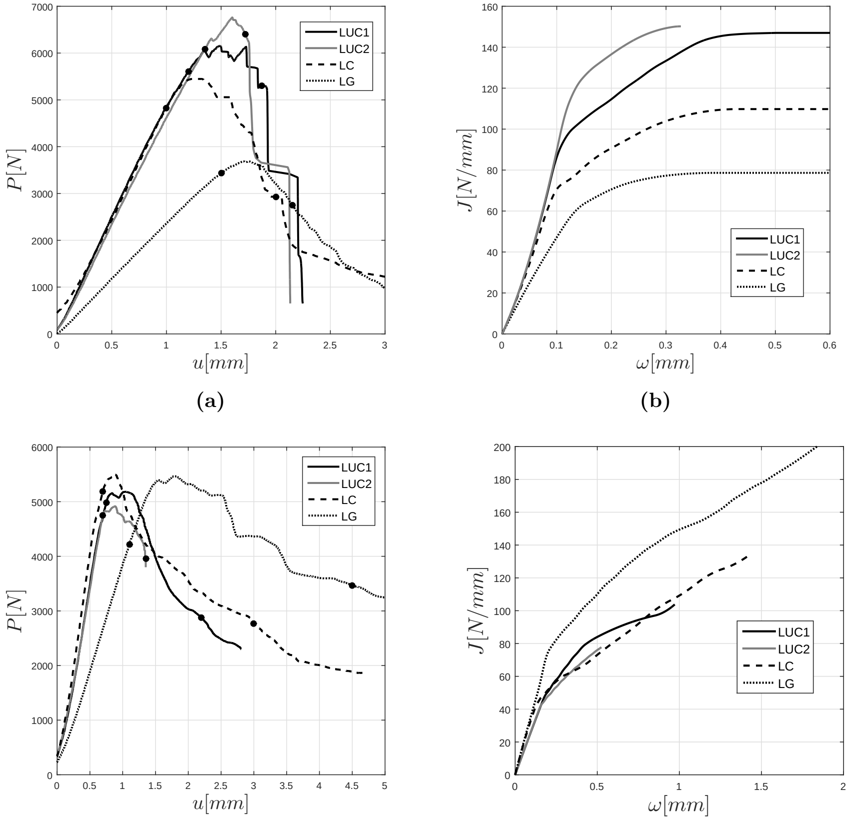

Figure 4: Experimental *P*-*u* curves of the (a) CT and (c) CC specimens, along their measured $J(\omega)$ curves, (b) and (d) respectively, for the single material laminates.

Table 4 summarizes the parameters that define the simplified $J(\omega)$ curves introduced in

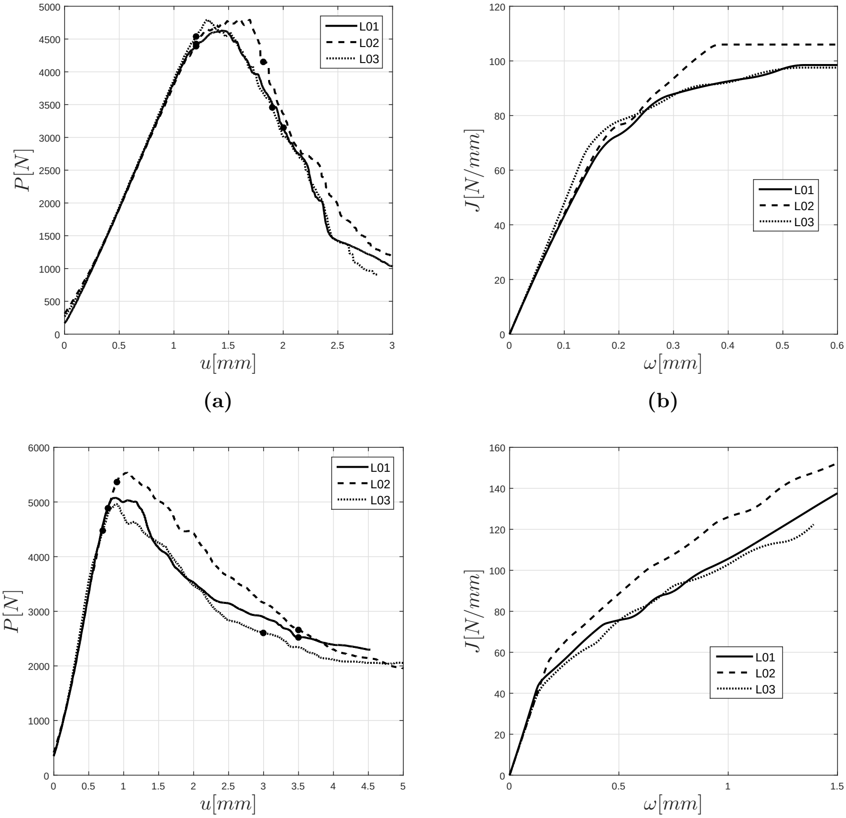

(a) **(b)**

(c) **(d)**

Figure 5: Experimental P-u curves of the (a) CT and (c) CC specimens, along their measured $J(\omega)$ curves, (b) and (d) respectively, for the C-G laminates.

Section 3. G_{OT} and G_{OC} are the onset energies and ω_{OT} and ω_{OC} are the critical crack openings where these onset energies end, for tensile and compressive loads, respectively. G_{CT} and ω_{CT} are the total fracture energy and the total crack opening under tensile loads, whereas σ_C is the constant stress in the kink-band broadening regime.

It is worth mentioning that the laminate LUC2 fails due to excessive compression at

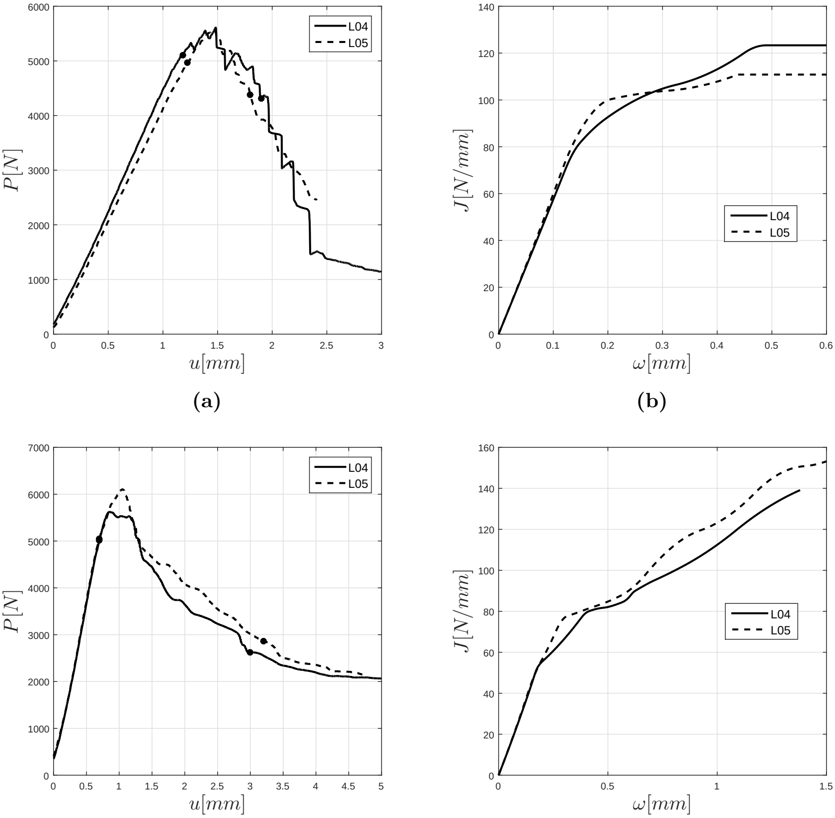

(a) **(b)**

(c) **(d)**

Figure 6: Experimental P-u curves of the (a) CT and (c) CC specimens, along their measured $J(\omega)$ curves, (b) and (d) respectively, for the C-UC laminates.

the back-end of the CT specimen before the Failure Process Zone at the crack tip has been completely formed. As a consequence, the $J(\omega)$ curve cannot be completely defined. The failure caused by the back-end compression has been observed in all the tested CT specimens, although in the rest of the cases, the FPZ was completely developed prior to the specimen failure. Because of this, the part of curve beyond the FPZ formation is not necessary to fit

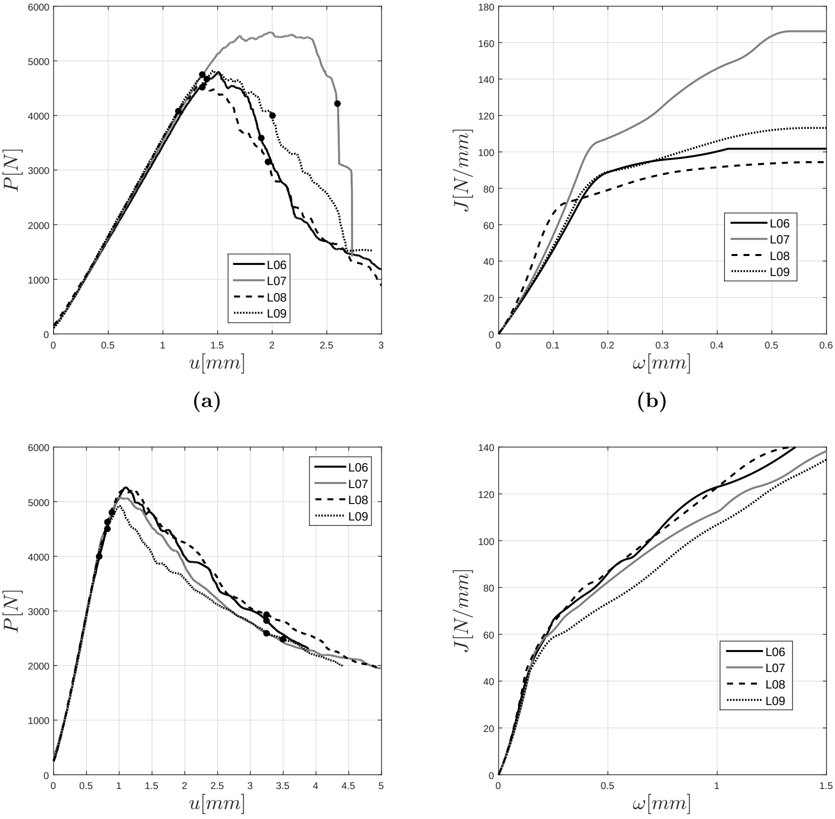

(a) **(b)**

(c) **(d)**

Figure 7: Experimental P-u curves of the (a) CT and (c) CC specimens, along their measured $J(\omega)$ curves, (b) and (d) respectively, for the G-UC laminates.

the tensile response of the laminate.

Observing the single material laminates shown in Fig. 4, the better performance of the unidirectional laminates with respect to the woven carbon specimens is noticeable under tensile loads. As for the compressive response, the woven glass fiber laminates stand out the most, as observed in the simplified curve parameters found in Table 4. Among the C-G

Table 4: Simplified Cohesive Law parameters for each laminate. Values with * were obtained prior to the fully formation of the FPZ.

Mat.	Lam.	G_{CT}	G_{OT}	ω_{OT}	ω_{CT}	G_{OC}	ω_{OC}	σ_C
UC	LUC1	147	94	0.10	0.40	75	0.41	50
	LUC2	*150	116	0.12	*0.33	46	0.17	93
C	LC	110	68	0.09	0.43	55	0.23	68
G	LG	78	62	0.14	0.35	107	0.43	67
C-G	L01	98	70	0.17	0.57	60	0.27	62
	L02	106	70	0.17	0.37	82	0.38	66
	L03	98	72	0.15	0.53	63	0.31	57
C-UC	L04	123	87	0.15	0.49	82	0.53	68
	L05	111	99	0.17	0.45	71	0.26	71
G-UC	L06	102	87	0.17	0.43	80	0.38	63
	L07	166	99	0.16	0.52	67	0.23	59
	L08	94	70	0.10	0.54	79	0.37	66
	L09	113	83	0.16	0.50	54	0.18	62

laminates shown in Fig. 5, laminate L02 presents the best performance. This laminate is characterized by having woven glass fibers in the central plies, whereas the laminate L01 has them in the outer plies. The worst performing laminate in this set, L03, has both material plies mixed along the thickness.

Regarding the response of the C-UC laminates presented in Fig. 6, no improvement is observed by the relative position of each type of ply in the laminate. Lastly, observing the G-UC set of laminates shown in Fig. 7, the excellent performance of L07 under tensile load is evident. The reason for this behavior is analyzed in the next section. Additionally, under compressive load, both laminates L06 and L08 perform slightly better than their counterparts L07 and L09. This is mainly because L06 and L08 have woven glass fiber plies in the center of the laminate, similar to the observed response of L02.

5. Discussion

When analyzing the results of the G-UC set, laminate L07 shows an outstanding response under a tensile load with respect to the rest of the laminates, which are made with the same plies but with different stacking sequences. The critical fracture energy of L07 is about 166N/mm, significantly larger than the rest of the G-UC specimens, with an average critical fracture energy of 100N/mm. The stacking sequence of the L07 has a unidirectional thicker 0^0 ply at the center of the laminate, resulting in outstanding performance, mainly caused by two phenomena. First, it is known that the fiber pull-out contributes to the laminate energy dissipation, being a desired failure mode when a translaminar crack is present. It is also known that thicker plies cause the fiber pull-out length to be increased, hence dissipating more energy [44], as is in the case of L07. The second damage mechanism phenomenon is the appearance of larger amounts of matrix cracks and delaminations in the presence of thicker plies [15, 16]. Fig. 8 shows the X-ray image of both laminates L06 and L07. In the case of L07, the damage zone is characterized by having larger matrix cracks and larger delaminations which are not present in the case of L06. These matrix cracks have two significant impacts during the damage process: first the matrix crack growth itself, which contributes to the laminate dissipated energy, and second, the laminate crack blunting produced by the presence of these matrix cracks, which leads to a reduction of the energy release rate of the specimen. It should be pointed out that the $J(\omega)$ curve and CL are obtained assuming that all the dissipation mechanisms are confined in the fracture plane. This hypothesis does not hold true for the laminate L07, where these cracks and delaminations occur outside the fracture plane. Hence, the determined J-curve, for this case, must be considered only qualitatively.

The mixing law, proposed by Camanho and Catalanotti [45], suggests a methodology to predict the tensile laminate fracture toughness from the properties of each ply that makes up the laminate. This hypothesis is also implicitly present when the fiber fracture toughness is defined from a cross-ply specimen [4, 12, 44], when it is considered that the plies in the loading direction are responsible for the energy dissipation, while the transverse plies only enforce the path of the crack. Observing the stacking sequences of the laminates of each set (L01 to L03 for C-G, L04 and L05 for C-UC, and L06 to L09 for G-UC), it can be appreciated that the only difference is the ply position along the thickness, while the number

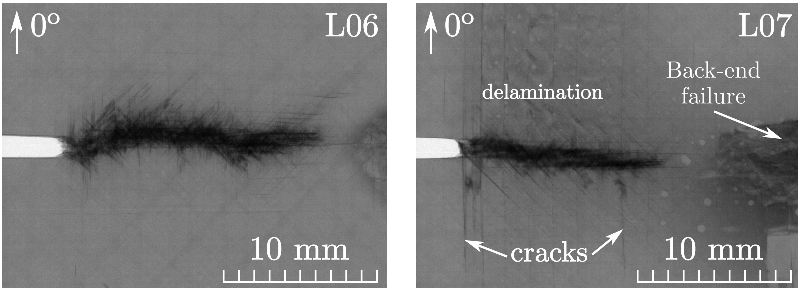

Figure 8: X-ray of the laminates L06 and L07 for the CT specimens. In the laminate L07 several matrix cracks can be observed.

of plies of each material and their orientations remain invariant. The measured J-curves show small differences between the laminates of each set, with the exception of the aforementioned L07. This suggests that the mixing theory will only give a rough estimate of the laminate toughness. Therefore, despite the differences originating from the relative position of each ply with respect to the others, it is still possible to define a mixing equation to predict the fracture properties as a combination of each ply. Based on the work of Camanho and Catalanotti [45], it is possible to define the mixing equation as:

$$J = \sum_{i}^{n} J_{Ply}^{i} \frac{h_P^i}{h_L} \frac{a_P^i}{a_L} \tag{6}$$

where J_{Ply} is the dissipated energy of a single ply, h_P/h_L is the relative thickness of each ply with respect to the whole laminate, and a_P/a_L is the ratio between the dissipated energy per unit crack length at the ply level with respect to the laminate. Camanho and Catalanotti [45] considered $a_P/a_L = 0$ for unidirectional 90^0 plies and 1 for any other ply orientation. This assumption is implicit when testing cross-ply laminates, where it is considered that only the 0^0 plies contribute to the energy dissipation [4, 12, 44]. In the present work, it is assumed that this ratio is proportional to the number of broken fibers with respect to a unitary increase of the translaminar crack. Therefore, the ratio of broken fibers can be defined as $a_P/a_L = \cos\theta$ for unidirectional plies, and $a_P/a_L = \cos\theta + \sin\theta$ for woven fabric plies (with cubic symmetry), where θ is the angle between the loading direction and the normal of the crack plane in absolute value. Focusing on the total fracture toughness G_{CT} of the single material laminates (LUC1, LC and LG), it is possible to determine the critical fracture energy under tensile load for each ply by means of Eq. 6: $G_{Ply}^{\text{UC}} = 244\text{N/mm}$, $G_{Ply}^{\text{C}} = 91\text{N/mm}$ and $G_{Ply}^{\text{G}} = 65\text{N/mm}$. With the values of each material ply toughness, it is possible to reuse Eq. 6 to predict the critical fracture energy of the hybrid laminates: $G_{CT}^{\text{C-G}} = 97\text{N/mm}$, $G_{CT}^{\text{C-UC}} = 123\text{N/mm}$ and $G_{CT}^{\text{G-UC}} = 107\text{N/mm}$. These values can be compared with the average critical energy of each set of hybrid laminates: 101N/mm, 117N/mm and 103N/mm (not including L07 laminate), for the C-G, C-UC and G-UC sets, respectively.

Additionally, it is possible to define a $J(\omega)$ curve using Eq. 6, if a relationship between the crack opening at the laminate level and ply level is assumed. When a translaminar crack grows the elongation of each fiber in the FPZ is equal to the total crack opening: $\omega = \omega_{Ply}$ regardless of the ply orientation. Then, using Eq. 6, it is possible to obtain the J-curve of each material ply from the pure laminate tests, while also obtaining the predicted J-curves of the hybrid laminates. Fig. 9 shows the experimental $J(\omega)$-curves from each specimen along the predicted $J(\omega)$-curve obtained from the mixing theory using the properties of each material ply. The results show that the mixing theory is able to produce a rough estimate of the hybrid laminate response. The only specimen that significantly deviates from the results obtained in this manner is the L07, because of the presence of the ply-blocking. For the compressive response, the mixing theory overestimates the material response for the C-G and G-UC laminates, and underestimates the response for the C-UC laminates.

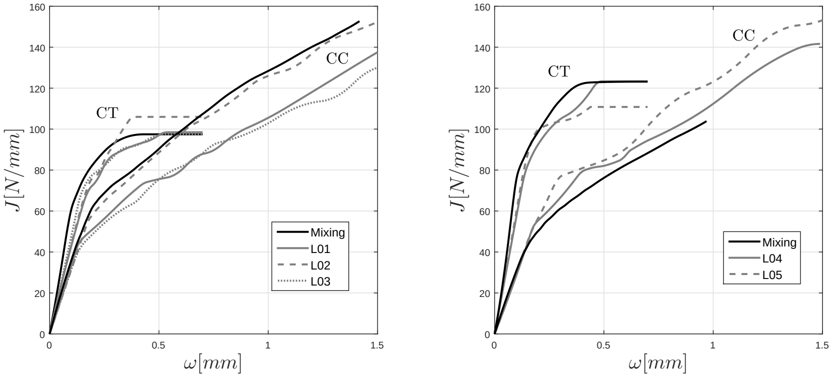

(a) C-G laminates **(b)** C-UC laminates

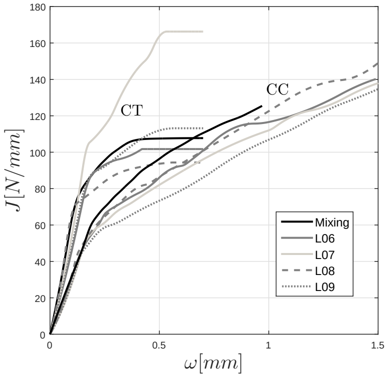

(c) G-UC laminates

Figure 9: Experimental and predicted with the mixing law $J(\omega)$-curves for G-C, C-UC and G-UC laminates, measured from the CT and CC specimens.

6. Conclusions

The translaminar fracture properties of nine interply hybrid laminates were studied experimentally. The laminates were obtained by mixing two of three different plies: woven carbon fabric, woven glass fabric and unidirectional carbon tape. The data reduction method utilized is capable of measuring the translaminar $J(\omega)$ and Cohesive Law from a single Compact

Tension and Compact Compression test.

An analysis of the obtained translaminar fracture properties was performed for all the specimens under tensile and compressive loads. The obtained response from the Compact Tension and Compact Compression specimens show that, in general, the influence of the position of each material ply along the thickness is minimal. When woven glass and woven carbon plies are mixed together, and the carbon fibers are placed in the outer plies of the laminate, a small improvement is appreciated for the case of the Compact Compression specimen. In the case of unidirectional plies, blocking several plies in the loading direction leads to an increase of the dissipated energy for the Compact Tension specimen. This phenomenon is explained by the increase of matrix cracks and larger delaminations when ply blocking is present, dissipating more energy during the formation, while at the same time, reducing the stress intensity factor at the crack tip.

The ability to use the mixing theory to predict the toughness of interply hybrid laminates, using single material ply properties, has been analyzed. The results show that the mixing theory roughly predicts the toughness of the hybrid laminates, although the methodology is limited, since it is not capable of capturing the influence of each material orientation with respect to the others and explaining how the laminate stacking-sequence impacts the overall translaminar crack growth.

Acknowledgments

This work has been partially funded by the Spanish Government through the *Ministerio de Economía y Competitividad*, under contracts MAT2013-46749-R and MAT2015-69491-C3-1-R.

References

[1] Sun CT, Prewo K. The Fracture Toughness of Boron Aluminum Composites. Journal of Composite Materials 1977;11(2):164–75. doi:10.1177/002199837701100204.

[2] Harris CE, Morris DH. Fracture Behavior of Thick, Laminated Graphite/Epoxy Composites. Tech. Rep.; NASA; 1984.

[3] Underwood JH, Kortschot MT, Lloyd WR, Eidinoff HL, Wilson DA, Ashbaugh N. Translaminar fracture toughness test methods and results from interlaboratory tests of Carbon/Epoxy laminates. 1995.

[4] Laffan M, Pinho ST, Robinson P, a.J. McMillan . Translaminar fracture toughness testing of composites: A review. Polymer Testing 2012;31(3):481–9. doi:10.1016/j.polymertesting.2012.01.002.

[5] Zobeiry N, Vaziri R, Poursartip A. Characterization of Strain-Softening Behaviour and Failure Mechanisms of Composites under Tension and Compression. Composites Part A: Applied Science and Manufacturing 2015;68:29–41. doi:10.1016/j.compositesa.2014.09.009.

[6] Ortega A, Maimí P, González EV, Trias D. Characterization of the translaminar fracture cohesive law. Composites Part A: Applied Science and Manufacturing 2016;:1–9doi:10.1016/j.compositesa.2016.01.019.

[7] Xu X, Wisnom MR, Mahadik Y, Hallett SR. Scaling of fracture response in Overheight Compact Tension tests. Composites Part A: Applied Science and Manufacturing 2015;69:40–8. doi:10.1016/j.compositesa.2014.11.002.

[8] Bergan A, Dávila CG, Leone FA, Awerbuch J, Tan TM. A Mode I cohesive law characterization procedure for through-the-thickness crack propagation in composite laminates. Composites Part B: Engineering 2016;94:338–49. doi:10.1016/j.compositesb.2016.03.071.

[9] Moran PM, Liu XH, Shih CF. Kink band formation and band broadening in fiber composites under compressive loading. Acta Metallurgica Et Materialia 1995;43(8):2943–58. doi:10.1016/0956-7151(95)00001-C.

[10] Moran PM, Shih CF. Kink band propagation and broadening in ductile matrix fiber composites: experiments and analysis. International Journal of Solids and Structures 1998;35(15):1709–22. doi:10.1016/S0020-7683(97)00138-8.

[11] Bažant ZP, Kim JjH, Daniel IM, Becq-Giraudon E, Zi G. Size effect on compression strength of fiber composites failing by kink band propagation. International Journal of Fracture 1999;95:103–41.

[12] Pinho ST, Robinson P, Iannucci L. Fracture toughness of the tensile and compressive fibre failure modes in laminated composites. Composites Science and Technology 2006;66(13):2069–79. doi:10.1016/j.compscitech.2005.12.023.

[13] Catalanotti G, Xavier J, Camanho PP. Measurement of the compressive crack resistance curve of composites using the size effect law. Composites Part A: Applied Science and Manufacturing 2014;56:300–7. doi:10.1016/j.compositesa.2013.10.017.

[14] Rice JR. A Path Independent Integral and Approximate Analysis of Strain Concentration by Notches and Cracks. Journal of Applied Mechanics 1968;35(2):379.

[15] Li X, Hallett SR, Wisnom MR, Zobeiry N, Vaziri R, Poursartip A. Experimental study of damage propagation in Over-height Compact Tension tests. Composites Part A: Applied Science and Manufacturing 2009;40(12):1891–9. doi:10.1016/j.compositesa.2009.08.017.

[16] Xu X, Wisnom MR, Hallett SR, Zobeiry N, Leslie S, Poursartip A, et al. Stacking Sequence Effects In Over-height Compact Tension Tests Of Quasi-isotropic Laminates. In: THE 19 TH INTERNATIONAL CONFERENCE ON COMPOSITE MATERIALS. 2016, p. 5004–11.

[17] Rosen BW. Mechanics of composite strengthening. In: Fiber Composite Materials; chap. 3. 1964, p. 37–75.

[18] Argon A. Fracture of Composites. In: Treatise on Materials Science & Technology. 1972, p. 79–114. doi:10.1016/B978-0-12-341801-2.50007-2.

[19] Budiansky B. Micromechanics. Computers & Structures 1983;16(1-4):3–12. doi:10.1016/0045-7949(83)90141-4.

[20] Budiansky B, Fleck NA. Compressive Failure of Fibre Composites. Journal of the Mechanics and Physics of Solids 1993;41:183–211.

[21] Waddoups ME, Eisenmann JR, Kaminski B. Macroscopic Fracture Mechanics of Advanced Composite Materials. Journal of Composite Materials 1971;5:446–54.

[22] Whitney JM, Nuismer RJ. Stress Fracture Criteria for Laminated Composites Containing Stress Concentrations. Journal of Composite Materials 1974;8(3):253–65. doi:10.1177/002199837400800303.

[23] Backlund J. Notch sensitivity of linearly softening materials exhibiting tensile fracture 1981;31(4):577–90.

[24] Backlund J. Fracture analysis of notched composites. Computers and Structures 1981;13(1-3):145–54. doi:10.1016/0045-7949(81)90119-X.

[25] Maimí P, Trias D, González EV, Renart J. Nominal strength of quasi-brittle open hole specimens. Composites Science and Technology 2012;72(10):1203–8. doi:10.1016/j.compscitech.2012.04.004.

[26] Maimí P, González EV, Gascons N, Ripoll L. Size Effect Law and Critical Distance Theories to Predict the Nominal Strength of Quasibrittle Structures. Applied Mechanics Reviews 2013;65(2):20802. doi:10.1115/1.4024163.

[27] Kabeel AM, Maimí P, González EV, Gascons N. Net-tension strength of double-lap joints under bearing-bypass loading conditions using the cohesive zone model. Composite Structures 2015;119:443–51. doi:10.1016/j.compstruct.2014.08.036.

[28] Soutis C, Fleck NA. Static Compression Failure of Carbon Fibre T800/924C Composite Plate with a Single Hole. Journal of Composite Materials 1990;24(5):536–58. doi:10.1177/002199839002400505.

[29] Soutis C, Curtis PT, Fleck NA. Compressive Failure of Notched Carbon Fibre Composites. Proceedings of the Royal Society A: Mathematical, Physical and Engineering Sciences 1993;440(1909):241–56.

[30] Soutis C, Curtis PT. A method for predicting the fracture toughness of CFRP laminates failing by fibre microbuckling. Composites Part A: Applied Science and Manufacturing 2000;31(7):733–40. doi:10.1016/S1359-835X(00)00003-8.

[31] Maimí P, Camanho PP, Mayugo JA, Dávila CG. A continuum damage model for composite laminates: Part II - Computational implementation and validation. Mechanics of Materials 2007;39(10):909–19.

[32] Maimí P, Camanho PP, Mayugo JA, Dávila CG. A continuum damage model for composite laminates: Part I - Constitutive model. Mechanics of Materials 2007;39(10):897–908.

[33] Lapczyk I, Hurtado Ja. Progressive damage modeling in fiber-reinforced materials. Composites Part A: Applied Science and Manufacturing 2007;38(11):2333–41. doi:10.1016/j.compositesa.2007.01.017.

[34] Mcgregor C, Zobeiry N, Vaziri R, Poursartip A. A Constitutive Model for Progressive Compressive Failure of Composites. Journal of Composite Materials 2008;42(25):2687–716. doi:10.1177/0021998308096330.

[35] Martín-Santos E, Maimí P, González EV, Cruz P. A continuum constitutive model for the simulation of fabric-reinforced composites. Composite Structures 2014;111:122–9. doi:10.1016/j.compstruct.2013.12.024.

[36] González EV, Maimí P, Sainz de Aja J, Cruz P, Camanho PP. Effects of interply hybridization on the damage resistance and tolerance of composite laminates. Composite Structures 2014;108:319–31. doi:10.1016/j.compstruct.2013.09.037.

[37] Zok F, Hom CL. Large scale bridging in brittle matrix composites. Acta Metallurgica Et Materialia 1990;38(10):1895–904. doi:10.1016/0956-7151(90)90301-V.

[38] Suo Z, Bao G, Fan B. Delamination R-curve phenomena due to damage. Journal of the Mechanics and Physics of Solids 1992;40(1):1–16.

[39] Bao G, Suo Z. remarks on crack bridging concepts. Applied Mechanics Reviews 1992;45(8):355–66.

[40] ASTM E 399 . Standard Test Method for Linear-Elastic Plane-Strain Fracture Toughness KIc of Metallic Materials. 2009.

[41] ASTM D 5045 . Standard Test Methods for Plane-Strain Fracture Toughness and Strain Energy Release. 1999.

[42] Ortega A, Maimí P, González EV, Trias D. Specimen geometry and specimen size dependence of the R -curve and the Size Effect Law from a Cohesive Model point of view. Submitted to International Journal of Fracture 2016;.

[43] Dugdale DS. Yielding of steel sheets containing slits. Journal of the Mechanics and Physics of Solids 1960;8(2):100–4.

[44] Laffan M, Pinho ST, Robinson P, Iannucci L. Measurement of the in situ ply fracture toughness associated with mode I fibre tensile failure in FRP. Part II: Size and lay-up effects. Composites Science and Technology 2010;70(4):614–21. doi:10.1016/j.compscitech.2009.12.011.

[45] Camanho PP, Catalanotti G. On the relation between the mode I fracture toughness of a composite laminate and that of a 0^{o} ply: Analytical model

and experimental validation. Engineering Fracture Mechanics 2011;78(13):2535–46. doi:10.1016/j.engfracmech.2011.06.013.